

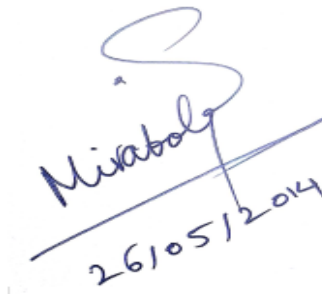
**SINGLE WALL TiO₂ NANOTUBES
FOR SENSITIZED SOLAR CELLS**

SEYED HAMED MIRABOLGHASEMI
M.Sc., Sharif University of Technology, Iran

**A THESIS SUBMITTED
FOR THE DEGREE OF DOCTOR OF PHILOSOPHY
DEPARTMENT OF MATERIALS SCIENCE AND ENGINEERING
NATIONAL UNIVERSITY OF SINGAPORE
2013**

Declaration

I hereby declare that this thesis is my original work and it has been written by me in its entirety. I have duly acknowledged all the sources of information which have been used in the thesis. This thesis has also not been submitted for any degree in any university previously.



Handwritten signature: S
Mirabolghasemi
26/05/2014

Seyed Hamed Mirabolghasemi

Acknowledgement

I would like to express my sincere gratitude to my supervisor, A/P Daniel John Blackwood for his supports and invaluable advices throughout my study at NUS.

I will also take this opportunity to express my utmost thanks to Professor Patrik Schmuki for giving me the opportunity to work in his lab in the Institute for Surface Science and Corrosion (LKO) at Friedrich-Alexander University. The support from the students and staffs in his research group especially Dr. Ning Liu and Kiyoug Lee is mostly appreciated.

My warmest thanks also go to my lab mates and colleagues in my department for their technical supports and advises; Fatemeh Safari Alamuti, Mohammad Reza Khajavi and Gui Yang.

Finally, my heartiest gratitude is due to my dear wife for her encouragement, help, support, and understanding throughout my study and research.

Table of Contents

Acknowledgement	ii
Table of Contents	iii
Summary	vii
List of Tables	x
List of Figures	x
List of Abbreviations	xviii
1. Introduction	1
1.1 Solar Energy Challenge	2
1.2 TiO ₂ Nanostructures in Dye and Semiconductor Sensitized Solar Cells (DSSCs and SSSCs) ...	3
1.3 Application of 1-D nanostructures in solar cells	5
1.4 Production of TiO ₂ nanotubes	7
1.4.1. Self-organized anodic TiO ₂ nanotubes	8
1.4.2. Role of electrolytes in anodization of TiO ₂ NTs	9
1.4.3. Organic solvents in anodization electrolytes	10
1.5 Mechanism of the formation of self-organized TiO ₂ NTs in organic electrolytes	12
1.6 The addressed problem of TiO ₂ NTs grown in the common EG electrolytes	13
1.7 Objectives and significance of the present thesis	15
2. Literature Review	18
2.1 Mechanism of nanotube array formation in anodization	18
2.2 Electro-oxidation of EG on metal surfaces	22
2.3 Electro-oxidation of dimethyl sulfoxide (DMSO)	25
2.4 Electro oxidation of the electrolytes on semiconductor surfaces	26
2.5 Tunnelling (Zener) breakdown	27
2.6 Heat treatment of TiO ₂ nanotubes	29
2.7 Formation of double wall TiO ₂ nanotubes in EG electrolytes	33
2.7.1 Annealing of double wall TiO ₂ nanotubes	35
2.8 Conductivity of TiO ₂ nanotubes	36
2.9 Photovoltage-photocurrent characterization of solar cell	39

2.10	Electrochemical Impedance Spectroscopy (EIS) of sensitized solar cells	42
2.10.1	Transport and recombination data obtained from EIS	44
2.10.2	Recombination resistance	45
2.10.3	Transport resistance	46
2.11	DSSCs fabricated from TiO ₂ nanotubes	47
3.	Experimental	49
3.1	Anodization materials and set-up	49
3.2	Heat treatment of nanotubes	52
3.3	Characterization techniques	52
3.3.1	SEM and TEM, and XRD of nanotubes	52
3.4	Conductivity Measurements of the as-formed and annealed nanotubes	53
3.5	DSC and TGA of the prepared nanotubes	54
3.6	FTIR experiments	54
3.7	Preparation of Dye Sensitized Solar Cells (DSSCs) and Backside illumination measurements	55
3.8	Nanotube decoration (TiCl ₄ treatment) of nanotubes	57
3.9	Preparation of Semiconductor (CdSe) Sensitized Solar Cells (SSSCs) and backside illumination measurements	57
3.10	Characteristic measurements of the backside illuminated DSSCs and SSSCs	58
3.11	Electrochemical Impedance Spectroscopy (EIS) Measurements	59
4.	Synthesis of single wall TiO₂ nanotubes	60
4.1	Anodization method	60
4.2	The double wall nanostructure of the TiO ₂ NTs grown from EG based electrolytes	63
4.3	Effect of anodization temperature on the nanostructure of DW- TiO ₂ NTs	66
4.4	The structure of TiO ₂ NTs grown in DMSO based electrolytes containing fluorine ions	68
4.5	Problems with single walls grown in pure DMSO based electrolytes	70
4.5.1.	Weak nanotubes with extremely slow growth rate	71
4.5.2.	Undesired geometry of the nanotubes from DMSO electrolyte	72
4.6	Kinetic studies of growth from mixed EG:DMSO electrolytes; current density versus time ..	78
4.7	Synthesis of single wall nanotubes from the mixed EG-DMSO based electrolytes	81
4.7.1	Effect of fluorine content:	82

4.7.2	Effect of voltage and temperature during anodization :	83
4.7.3	Effect of electrolyte composition; EG:DMSO in 2:1 ratio.....	84
4.7.4	Effect of electrolyte composition; EG:DMSO in 1:2 ratio.....	85
4.7.5	Effect of electrolyte composition; EG:DMSO in 1:1 ratio.....	86
4.7.6	Effect of water content	88
4.8	TEM studies of Single and double wall nanotubes	96
4.9	Mechanism of the electro-oxidation of EG during the anodization of TiO ₂	100
4.10	Conclusion.....	101
5.	Characterization of double and single wall nanotubes	103
5.1	FTIR characterization of the anodization electrolytes and the as-formed nanotubes	103
5.1.1	Characterization of the anodization electrolytes	103
5.1.2	Characterization of as-anodized nanotubes	108
5.2	The nature of the internal wall of DW nanotubes.....	112
5.3	XRD studies of the single and double wall nanotubes	114
5.4	Depth Profile XPS	118
5.5	Differential Scanning Calorimetric (DSC) Tests.....	120
5.6	Comparison of activation energies of amorphous to anatase transformations of DW and SW nanotubes from DSC results	126
5.7	Effect of heat treatment temperature on the conductivity of single wall nanotubes:.....	129
5.7.1	Variation of conductivity of amorphous nanotubes with temperature	129
5.7.2	Variation of conductivity of annealed nanotubes with temperature.....	134
5.7.2.1.	Effect of heating / cooling rate on the conductivity of nanotubes	134
5.7.2.2.	Effect of annealing temperature on the conductivity of single wall nanotubes	137
5.8	Diffuse reflectance UV-VIS of SW and DW nanotubes	139
5.8.1	Calculation of optical bandgap of SW and DW- TiO ₂ NTs	139
5.8.2	Diffuse reflectance UV-VIS of CdSe sensitized SW and DW nanotubes:	143
5.9	Conclusion.....	146
5.10	Effect of heat treatment ramping rates on the morphology of nanotubes.....	148
6.	Single wall nanotubes in dye and semiconductor sensitized solar cells.....	151
6.1	SW and DW nanotubes in dye sensitized solar cells.....	151

6.1.1	<i>j-V</i> characterization of SW and DW-DSSCs	151
6.1.2	Intensity modulated photocurrent spectroscopy (IMPS) and photovoltage spectroscopy (IMVS) of SW and DW-DSSCs	155
6.1.3	Electrochemical Impedance spectroscopy	159
6.2	SW and DW nanotubes in CdSe sensitized solar cells	169
6.2.1	<i>j-V</i> characterization of SW and DW-DSSCs	169
6.2.2	Electrochemical Impedance spectroscopy of SSSCs	171
6.2.3	IPCE of SSSCs	175
6.3	Conclusion.....	179
7.	Conclusions and Future Work.....	182
8.	References.....	191
9.	List of Publications and Presentations:.....	199

Summary

Electrochemical synthesis of TiO₂ nanotubes (NTs) leads to the best-aligned self organized arrays which are more favorable to fulfill the photovoltaic applications' requirements compared with NTs from other methods.

After more than a decade of investigation, *Ethylene Glycol (EG)*- based electrolytes became typical electrolytes to anodize high aspect ratio TiO₂ NTs. Nevertheless, those NTs consist of a *double shell wall*; a compact thin outside shell and a spongy inside shell containing high amount of carbon. The latter was thought to have negative effect on the properties of TiO₂ NTs.

This thesis is a complete report of synthesis, characterization and application of highly oriented high aspect ratio "*Single Wall (SW) NTs*". This study contains three main parts; Synthesis of *SW NTs*, Characterization of *SW NTs* and comparison to the regular "*Double Wall (DW) NTs* ", followed by application and characterisation of the newly synthesized SW NTs in dye and semiconductor (CdSe) sensitized solar cells.

In the first part, a detailed discussion is given about the anodization of TiO₂ NTs in *mixed EG:DMSO* organic baths that results in the successful elimination of the inside shell of DW NTs and growth of SW NTs.

In the second part, the characterization of the synthesized nanotubes by different methods such as SEM, TEM, XPS , XRD, DSC and TGA is reported. SEM and TEM prove the

complete exclusion of the internal shell of DWs and the successful growth of SW NTs. Moreover, FTIR experiments reveal that EG-based electrolytes decompose during high voltage anodization of TiO₂ nanotubes, ending up with contaminated double wall NTs, while adding DMSO to the electrolyte suppresses the decomposition and results in clean *single wall* NTs.

The conductivities of NTs were investigated and compared as well. The outcomes show that single walls are up to two orders of magnitude more conductive than the common DW NTs at different heat treatment temperatures and in their amorphous form.

Part two ends with diffuse reflectance UV-VIS studies and calculation of bandgaps of DW and SW NTs. It is discussed that diffusion of carbon to the internal nanoporous shell of DW NTs might happen during the heat treatment of NT arrays.

In the third part of this thesis, it is shown that dye sensitized solar cells (DSSCs) from SW NTs and TiCl₄ treated SW NTs are more efficient than their DW counterparts. *Modulated photocurrent and photovoltage spectroscopy measurements* (IMPS/IMVS) were used to show that the elimination of the inner shell leads to faster carrier transport and higher value of charge collection efficiency (η_{cc}) in SW DSSCs. Besides, *Electrochemical Impedance Spectroscopy* (EIS) demonstrated lower electron transport resistance and facilitated charge transport in SW DSSCs compared to DW DSSCs as well as higher recombination resistance that result in higher device performance.

In addition to DSSCs, 10-cycle CdSe deposited SW solar cells (SSSCs) displayed better photocurrent, incident photon to current efficiency (IPCE) and slightly better photo-conversion efficiency compared to DW SSSCs due to the better charge collection efficiency of SW NTs.

List of Tables

Table 4-1 Electrolytes' compositions, anodization conditions and the resulted length of nanotube arrays for (a) EG:DMSO 1:2 and EG:DMSO 2:1 by volume	92
Table 4-2 Electrolytes' compositions, anodization conditions and the resulted length of nanotube arrays for EG:DMSO 1:1 by volume.....	94
Table 5-1 Frequencies observed in FTIR of (EG) electrolyte (EG + 0.1M NH ₄ F+ 1M H ₂ O), Upper pointings are reactants and downwards are products	106
Table 5-2 Frequencies observed in FTIR of (EG/DMSO) electrolyte (1:1 vol. DMSO/EG + 0.1M NH ₄ F+ 1.5 M H ₂ O), Upper pointings are reactants and downwards are products.	107
Table 5-3 Frequencies observed in FTIR of as-anodized double wall (black) and single wall (red) TiO ₂ nanotube arrays plotted in Figure 5-4.	111
Table 6-1 The photovoltaic parameters of the DSSCs fabricated from plain and TiCl ₄ treated single and double wall nanotubes heat treated at 500°C with ramping rate of 1°C/s. (J _{sc} = short-circuit current density, V _{oc} = open-circuit voltage, <i>ff</i> = fill factor, and η = efficiency).....	153
Table 6-2 The photovoltaic parameters of the SSSCs fabricated from single nanotubes sensitized with different SILAR cycles of CdSe deposition. (J _{sc} = short-circuit current density, V _{oc} = open-circuit voltage, <i>ff</i> = fill factor, and η = efficiency)	170
Table 6-3 The data related to <i>j-V</i> characterization of SW and DW SSSCs sensitized by 10 SILAR cycles of CdSe deposition	171

List of Figures

Figure 1-1 a) Schematic representation of the principle of a dye sensitized solar cell, b) Schematic diagram of the electron excitation in a dye molecule and the electron injected from the LUMO of the dye to the conduction band of TiO ₂	4
Figure 1-2 Flow path of an electron in a) nanoparticulates, and b) nanotubular TiO ₂ films [11].....	6
Figure 1-3 SEM images of a) arbitrary oriented tubes from hydrothermal rout [22], and well oriented (b) hollow (c) nanotubes from electrochemical method.	8

Figure 1-4 General illustration of ions travelling in opposite directions during the anodization process.	12
Figure 2-1 a) Schematic representation of the five stages of nanotube formation [17], b) demonstration of changes in the current density during the time of anodization, and c) the flow directions of different ions through the oxide compact layer (grey) during the anodization [2, 18]	21
Figure 2-2 Effect of pH on the onset potential and the peak current density of EG electro-oxidation on Pd. CO ₂ is the main product at pHs lower than 12, while at higher voltages glyoxal and glycolates are produced [38].	23
Figure 2-3 <i>In-situ</i> FTIR spectra of an EG containing electrolyte obtained under potential step polarization at pH=6.4 [38].	24
Figure 2-4 Full reaction path of EG electro-oxidation proposed by Wang <i>et al</i> [38]	25
Figure 2-5 Voltage-induced formation of OH on the surface of an n-type semiconductor [37].	26
Figure 2-6 a) carrier flow in a typical pn junction connected to a power source, b) silicon diode and its I-V schematic characteristics [45].	28
Figure 2-7 Complete phase transformation path of TiO ₂ nanotubes from a) at 280 °C , b) above 280 °C, c) at 430 °C , d) above 620 °C , and e) above 620 °C [49].	31
Figure 2-8 SEM images of TiO ₂ nanotubes annealed at a) 350, and b) 450 °C showing the high level of cracks in the tube walls of the sample treated at 450 °C [50].	33
Figure 2-9 a) SEM images of top and side of tubes formed in EG before heat treatment showing a uniform structure. b) TEM image and SAED (selected area electron diffraction) pattern (inset) of an individual tube showing its double wall nanostructure and c) schematic demonstration of different parts of an anodically grown TiO ₂ from EG electrolyte [5].	34
Figure 2-10 Dependence of the morphology of DW tubes on the heating rate. a,d) 1°C/s, b,e) 25 °C/s, and c,f) 50 °C/s to 500 °C [5].	35
Figure 2-11 Electrical conductivity of TiO ₂ nanotubes (circles) , nanoporous anatase (squares) and nanocrystalline anatase (triangles) thin films [56].	37
Figure 2-12 Effect of annealing time and temperature on the specific resistivity of 2.5 hour and 20 hour annealed at 500 °C EG nanotubes [52].	38
Figure 2-13 <i>j-V</i> characteristic curve of a solar cell simulated based on the Shockley equation [58].	40
Figure 3-1 Experimental set-up for anodization[5].	50

Figure 3-2 a) Assembling steps of a DSSC with TiO ₂ NTs on foil for backside illumination, and b) a schematic of Newport solar diverging simulator for j-V measurements [79].	56
Figure 4-1 Schematic representation of the conventional nanotube anodization. a) formation of compact oxide layer immediately after the start, b) growth of tubes, c) formation of nanograss layer on top of the tubes as a result of chemical dissolution of tubes' walls near the top, and d) SEM image of nanograss on top of the anodized layer.	61
Figure 4-2 Schematic representation of double anodization method. The conventional tubes grown in the first stage (a-c) are removed from the surface by ultrasonication. d, e, f) second step of anodization. g) Schematic shape of the remaining top layer (golden) and the tubes underneath, and h) SEM top view image of a double anodized sample.	63
Figure 4-3 Schematic representation of double wall nanotubes , and b) SEM images of DW TiO ₂ NTs from top, middle and the bottom of the layer (adopted from reference [86])	64
Figure 4-4 a,b) TEM and SEM images of an as-grown double wall nanotube near the bottom of the tube, c) SEM image of an annealed sample at 450 °C, adopted from [87].	66
Figure 4-5 (a) SEM images of double wall TiO ₂ NTs from EG based electrolytes at different temperatures; and (b) Current-time (I-t) profiles of anodization of DW NTs in EG based electrolyte at different temperatures. Adopted from [87].	67
Figure 4-6 (a, b) TiO ₂ NT growth rate in (EG+0.1M NH ₄ F+1M H ₂ O) and DMSO (containing 2 wt% HF) electrolytes respectively; (c) current changes with time of the anodization for tubes grown in EG (top) and DMSO (bottom) at 60°C and room temperature; adopted from [87].	69
Figure 4-7 Nanotubes grown in DMSO + 2wt% HF in the a)as formed condition and b) after annealing at 450 °C, adopted from [81].	70
Figure 4-8 The growth rate of nanotubes in pure DMSO based electrolytes (DMSO + 2% HF) by two different methods at 60 V and room temperature. (Data points are the average of at least 5 measurements that were highly repeatable such that the error bars are too small to display).	72
Figure 4-9 SEM images of near top (a, b, c) middle height (d) and e) side view of an array anodized in a one-step process for 71 hours in pure DMSO + 2% HF at 60 V and room temperature	74
Figure 4-10 SEM image of top of a sample anodized in a two-step process for 6 hours in pure DMSO + 2% HF at 60 V and room temperature	75

Figure 4-11 SEM image of a) top, b) side, c, d) near bottom views of an array anodized in a two-step process for 15 hours in pure DMSO + 2% HF at 60 V and room temperature.....	76
Figure 4-12 SEM image of a sample anodized in a two-step process for 50 hours in pure DMSO + 2% HF at 60 V and room temperature and then annealed at 450°C for 1 hour.....	77
Figure 4-13 Variation of current density of anodization over time for a) EG + 0.1M NH ₄ F+1M H ₂ O electrolyte at room temperature (2nd step) , b) EG:DMSO + 0.1M NH ₄ F+1.5M H ₂ O electrolytes at 60 °C (2nd step), and c) anodization of simple foil in EG electrolyte at room temperature.....	81
Figure 4-14 Heavily nanograss top of a sample in 0.13M fluorine content (in 2:1 EG:DMSO, 1.3M H ₂ O).....	82
Figure 4-15 Fluorine rich cubic compounds formed from excess of fluorine ions in the solution	82
Figure 4-16 SEM images from the same height of TiO ₂ NTs anodized at different temperatures of -10°C (a), 0°C (b), and +30°C (c). d) Increase of the inner diameter of tubes (squares) with temperature while the outer diameter (circles) is almost constant, adopted from [35]......	83
Figure 4-17 a,b) Different views of the sample anodized in EG:DMSO, 2:1, NH ₄ F:0.1, and H ₂ O:1M, 60 V and 40 °C and c) double wall structure of the tubes.....	85
Figure 4-18 Different views of the sample anodized in EG:DMSO, 1:2, NH ₄ F:0.1, and H ₂ O:1M, 60 V and 60 °C.....	86
Figure 4-19 Different views of the sample anodized in EG:DMSO, 1:1, NH ₄ F:0.1, and H ₂ O:1.5M 60 V and 40 °C.....	87
Figure 4-20 SEM pictures of the double walled structure of the EG tubes after annealing at 500°C. for 30 minutes. a) Cross section of the tubes near bottom. b) Side view of the tubes near bottom showing the compact outer shell and porous inner shell of the nanotubes c) View of the tubes from bottom. (Electrolyte: 1M H ₂ O, 0.1 M NH ₄ F in EG).....	88
Figure 4-21 SEM pictures of the nanotubular structures from DMSO:EG, 1:1 electrolyte after annealing. a) Cross section of the tubes near the top, b, c) mid-height of the film, and d) very close to bottom of the tubes. (in 1.5 M H ₂ O, 0.1 M NH ₄ F / 1:1 EG and DMSO at 60 °C and heat treated at 500 °C).....	89
Figure 4-22 Effect of water content on the nanostructure of TiO ₂ NTs from 1:1 DMSO: EG, and 0.1 M NH ₄ F. a) with 1M H ₂ O, and b) with 1.5M H ₂ O.	90

Figure 4-23 Schematic representation of the effect of temperature and DMSO on the thickness of inner and outer shells of tubes. The numbers are the thickness of the outer shell. (RT= Room Temperature).....	90
Figure 4-24 TEM images of a,c) amorphous double wall TiO ₂ nanotubes anodized in 1M H ₂ O, 0.1 M NH ₄ F in EG, and b,d) as-formed single wall TiO ₂ nanotubes anodized in 1.5 M H ₂ O, 0.1 M NH ₄ F in 1:1 EG and DMSO.....	97
Figure 4-25 TEM images of a,c) annealed double wall TiO ₂ nanotubes anodized in 1M H ₂ O, 0.1 M NH ₄ F in EG, and b,d) annealed single wall TiO ₂ nanotubes anodized in 1.5 M H ₂ O, 0.1 M NH ₄ F in 1:1 EG and DMSO and heat treated at 500° C, 30 min	98
Figure 4-26 TEM images of a and c) double wall and b, d) single wall nanotubes. SEM images of TiO ₂ nanotubes close to the bottom of tubes for the double wall (e) and single wall (f) nanotubes. g, h)TEM images of the double wall and single wall nanotubes after annealing showing the grains (from the author's previous publication) [7].	99
Figure 4-27 Schematic representation of the mechanism of the voltage induced radical and hole formation and capture [37, 87], E _{fb} is the flatband potential.....	100
Figure 5-1 Full reaction path of EG electrooxidation proposed by Wang <i>et al.</i> [38]	104
Figure 5-2 FTIR spectrum of (EG + 0.1M NH ₄ F+ 1M H ₂ O) transmittance FTIR (in red) after anodization normalized against the fresh anodization electrolyte before anodization (as background)..	105
Figure 5-3 The FTIR plot of (1:1 vol. DMSO/EG + 0.1M NH ₄ F+ 1.5 M H ₂ O) transmittance FTIR (red) after anodization normalized against the fresh anodization electrolyte before anodization (as background)..	108
Figure 5-4 Simple(a) and base line corrected (b) absorbance FTIR spectra of as-anodized double wall and single wall TiO ₂ nanotube arrays. Typical FTIR spectra were recorded from at least 3 different samples with no significant differences being observed.	109
Figure 5-5 a, b) Schematic representation of double wall and single wall nanotubes respectively, c) TEM and SEM pictures of double wall tubes.	113
Figure 5-6 XRD patterns of a) single wall and b) double wall nanotubes on Ti foil annealed at 500 °C for 1 hour	114

Figure 5-7 XRD patterns of removed a) single wall TiO ₂ NTs heated at 5 °C /min, b) double wall nanotubes heated at 5 °C /min, c) single wall TiO ₂ NTs heated at 10 °C /min, and d) double wall nanotubes heated at 10 °C /min. All samples are annealed at 500°C for 1 hour	116
Figure 5-8 Comparison of XPS depth profiles of F1S in single and double wall tubes.....	117
Figure 5-9 a) XPS depth profile of F1S, b) XPS depth profile of C1S from the bottom of Double and Single Wall nanotubes , c) Schematic representation of different parts of TiO ₂ nanotube layers, and d) The outer shell thickness near the bottom of the tubes.....	119
Figure 5-10 a) DSC profile for double wall TiO ₂ NTs, b) Non-ambient XRD of double wall TiO ₂ NTs at different temperatures, (heating rate: 5 °C/s), c) DSC profile for the single wall TiO ₂ NTs, and d) The weight change of nanotubes with temperature (heating rate: 5 °C/s).....	122
Figure 5-11 DSC peaks (Black) and the deconvoluted peaks from the mathematical curve fitting technique (colorful) of a) DW and b) SW nanotubes (heating rate:15°C/s)	123
Figure 5-12 Weight change of double and single wall tubes during TGA; heating rate: 15 °C/s.....	124
Figure 5-13 Thermal desorption profile for M=44 (CO ₂), and M=18 (water) by TGA-MS analysis [7].....	125
Figure 5-14 The Kissinger plots of single and double wall nanotubes calculated from DSC data (Each experiment was repeated at least three times and error bars are too small to be seen).....	127
Figure 5-15 TEM images of heat treated double wall (a,b) and single wall (c,d) nanotubes at 500 °C for 1 hour [7].....	128
Figure 5-16 The distribution of grin sizes of single and double wall tubes [7].	129
Figure 5-17 a) Variation of the resistivity of as prepared double and single wall tubes with temperature, and linearly fitted curves of thermal desorption profiles of double and single wall nanotubes for b) Water and c) CO ₂ under 300°C (Re-plotted of the Figure 5-1)	131
Figure 5-18 Comparison of the electrical resistance of crystalline single wall and double wall nanotube layers of 15 μm thickness at different temperatures, a) single wall nanotube, treated at 500°C, with 1 °C/s heating/cooling rate, b) single wall nanotube, treated at 500°C, with 0.1 °C/s heating/cooling rate, c) double wall nanotube, treated at 500°C, with 1 °C/s heating/cooling rate, and d) double wall nanotube, treated at 500°C, with 0.1 °C/s heating/cooling rate. The dashed lines in the figure are a “guide to the eye”.....	135

Figure 5-19 XRD spectra of the annealed single wall TiO ₂ nanotubes (A = anatase, R = rutile and T = titanium) annealed at 500 °C with different heating/cooling rates.....	136
Figure 5-20 Comparison of the electrical resistance of crystalline single wall nanotube layers of 15 μm thickness at different temperatures, a) single wall nanotube, treated at 500°C, with 1 °C/s heating/cooling rate, b) single wall nanotube, treated at 400°C, with 1 °C/s heating/cooling rate, c) single wall nanotube, treated at 500°C, with 0.1 °C/s heating/cooling rate, and d) single wall nanotube, treated at 400°C, with 0.1 °C/s heating/cooling rate. The dashed lines in the figure are a “guide to the eye”.....	137
Figure 5-21 Comparison of the XRD patterns of annealed a) double wall, and b) single wall nanotubes at 400 and 500 °C.....	138
Figure 5-22 Diffuse reflectance UV-VIS spectra of single and double wall nanotubes heat treated at 500 °C for one hour.....	140
Figure 5-23 Tauc plot and b) derivative of $[F(R_{\infty})(h\nu)]^{1/2}$ versus photon energy for SW nanotubes	141
Figure 5-24 a) Tauc plot and b) derivative of $[F(R_{\infty})h\nu]^{1/2}$ versus photon energy for DW nanotubes	142
Figure 5-25 UV-VIS spectra of CdSe sensitized a) DW, b) SW nanotubes, and c) absorbance of 10 cycle CdSe sensitized SW and DW- TiO ₂ NTs	145
Figure 5-26 Effect of annealing with 10 °C/s ramp rates on the nanostructure of a) SW and b) DW nanotubes.	149
Figure 5-27 Effect of heating/cooling rates on the nanostructure of single walled nanotubes. a,b) 0.1°C/s. c) 1 °C/s, d,e) 10 °C/S, and f,g,h) 50 °C/s.The tubes are all kept at 500 °C, for 30 minutes. ..	150
Figure 6-1 <i>j</i> - <i>V</i> characteristics of DSSCs fabricated from plain and TiCl ₄ treated single and double wall nanotubes heat treated at 500°C with ramping rate of 1°C/s.	152
Figure 6-2 <i>j</i> - <i>V</i> characteristics of DSSCs fabricated from single wall nanotubes heat treated at 500°C with different ramping rates.....	154
Figure 6-3 XRD spectra of the annealed single wall TiO ₂ nanotubes (A = anatase, R = rutile and T = titanium) annealed at 500 °C/s with different heating/cooling rates.....	154

Figure 6-4 SEM images showing the effect of high (10 °C/s) ramp rate on the nanostructure of SW-TiO ₂ NTs. a) Tubes' walls and b) The top (almost) blocked surface. For comparison, an SEM of a sample annealed with a slow heating rate can be seen in Figure 4-4.....	155
Figure 6-5 IMPS responses of a) DW- TiO ₂ NT and b) SW- TiO ₂ NT DSSCs under different photon fluxes of 10 ¹⁴ , 10 ¹⁵ , and 10 ¹⁶ photons.cm ⁻² s ⁻¹ . f _{min} is the frequency of the minimum imaginary component of each curve	156
Figure 6-6 IMVS responses of SW and DW-DSSCs under different photon fluxes of a,d) 10 ¹⁴ , b, e) 10 ¹⁵ , and c, f) 10 ¹⁶ photons.cm ⁻² s ⁻¹ . f _{min} is the frequency of the minimum imaginary component of each curve.	157
Figure 6-7 Recombination time (a) and transport time (b) constants calculated from IMVS and IMPS for single and double walled DSSCs.	159
Figure 6-8 a) Nyquist, b) Bode and c) phase angle plots of single and double walled nanotube DSSC. d) Equivalent circuit used to fit the data; (dots represent experimental data and solid lines present the fitted data).....	162
Figure 6-9 Chemical capacitances of DW and SW DSSCs calculated from EIS spectra	164
Figure 6-10 SW and DW DSSCs (a) Charge transport resistance and (b) charge transfer resistance ..	166
Figure 6-11 Calculated electron Diffusion length (L _n) for SW and DW based DSSC at different V _{oc}	167
Figure 6-12 Electron lifetime in SW and DW-DSSCs.....	168
Figure 6-13 j-V characteristics of SSSCs fabricated from single nanotubes sensitized with different SILAR cycles of CdSe deposition.	169
Figure 6-14 Top view SEM images of a) heat treated blank SW nanotubes and b) 12 cycle CdSe deposited SW- TiO ₂ NTs showing blockage of the tubes in some parts.....	170
Figure 6-15 j-V characterization of SW and DW- TiO ₂ NT based solar cells sensitized by 10 SILAR cycles of CdSe deposition.....	171
Figure 6-16 Nyquist (a), Bode (b) and phase angle (c) plots of single and double walled nanotube SSSC sensitized by 10 SILAR cycles of CdSe deposition; (dots represent experimental data and solid lines present the fitted data). (To be continued in the next page)	172
Figure 6-17 Charge transfer resistance in both SW and DW SSSCs sensitized by 10 SILAR cycles of CdSe deposition.....	174

Figure 6-18 IPCE of DW and SW-SSSC sensitized by 10 SILAR cycles of CdSe deposition at different wavelengths..... 178

List of Abbreviations

SW- TiO₂ NT	Single Wall Titania Nanotube
DW- TiO₂ NT	Double Wall Titania Nanotube
OST	Outer Shell of the Nanotube
EG	Ethylene Glycol
DMSO	Dimethyl Sulfoxide
DSSC	Dye Sensitized Solar Cells
SSSC	Semiconductor Sensitized Solar Cell
SILAR	Successive Ionic Layer Adsorption and Reaction
IST	Internal Shell of the Nanotube
TGA	Thermal Gravimetric Analysis
DSC	Differential Scanning Calorimetry
EDX	Dispersive X-ray Spectroscopy
UV-VIS	Ultraviolet Visible Spectroscopy
IPCE	Incident photon-to-electron Conversion Efficiency
FTIR	Fourier transform infrared spectroscopy
EIS	Electrochemical Impedance Spectroscopy

TL	Transmission Line
IMVS	Intensity Modulated photovoltage Spectroscopy
IMPS	Intensity Modulated Photocurrent Spectroscopy

Chapter 1

Introduction

After the synthesis of carbon nanotubes by Ijima [1] in 1991 for the first time, the research came into the new era of *One dimensional (1-D)* nanostructures. Shortly after, a wide range of materials such as sulfides and transition metal oxides like *titanium oxide* were synthesized in 1-D form. These directionally oriented nanostructures including nanowires, nanorods and nanotubes have been subjects for several investigations as building blocks of numerous new applications like *Dye Sensitized Solar Cells (DSSCs)* in the past 20 years [2].

One dimensional (1-D) geometries provide a combination of advantageous properties in different applications. In photovoltaic devices for instance, employing 1-D nanostructures compared to their long-established nanoporous structures facilitates the electron transfer/transport and hence decreases the *exciton recombination* which is a crucial parameter to increase the efficiency of these devices[3]. In addition 1-Ds have high specific area, very high mechanical strength, and show high quantum confinement effects [4].

Among all semiconducting 1-D nanostructures, the most frequently investigated material for being utilized in solar cells is titanium dioxide nanotube (*TiO₂ NT*) [2]. TiO₂ NTs can be synthesized in a variety of methods such as *sol-gel method*, *template-assisted (TA) way*, *hydrothermal rout*, and *electrochemical process*. Among all, the electrochemical synthesis of TiO₂ NTs from non-aqueous electrolytes is shown to be the most successful method mainly

because of their high aspect ratio and superior alignment. However, some researchers have shown that the very common TiO_2 NTs from *Ethylene Glycol (EG)* have a *double wall* nanostructure with a detrimental effect on their properties [5, 6]. Therefore, synthesis of smooth, high aspect ratio *single wall TiO_2 NTs* could result in enhancing the properties of the TiO_2 NTs such as for charge carrier transport/transfer in *sensitized solar cells (SSCs)* [7].

To make the thesis easier to follow, the thesis opens with an introduction chapter that gives an overview of the principles of DSSCs, anodization of TNTs and their general properties. The chapter ends in the general objectives of the present thesis. Then the literature review chapter (chapter 2) goes into depth on the major research topics relevant to this thesis, which are the proposed mechanisms of TNT growth, electro-oxidation of EG on metallic and semiconductor surfaces, the phase transformation of TiO_2 during heat treatment and the conductivity of TNTs."

1.1 Solar Energy Challenge

The amount of energy that strikes the earth from the sun is up to 10000 times as much as the human's industrial needs [8]. This huge and long lasting source of energy not only provides a totally free and sustainable energy, but also could help to reduce serious problems like pollution made by the common fossil fuels. Therefore, development of effective *solar cells* to absorb the sun's energy and convert it to electricity could play a very unique role in the future of the energy market and hence the future of the human being. During several years of investigation several types of solar cells have been made, improved and commercialized by researchers and in industry.

The most highlighted commercial types of solar cells nowadays are solid junction solar cells such as GaAs based, crystalline silicon and thin film solar cells with conversion efficiencies roughly between 20 and 30%. However a lot of effort has been put in to increasing the efficiencies and lowering the final cost either by improving the above types or the invention of new types such as *perovskite, dye or quantum dot sensitized solar cells* in recent years [9].

The most important breakthrough in *Dye sensitized solar cells (DSSCs)* was reported by Graetzel and his coworkers in 1991 [10]. After their report a lot of investigations have been conducted on different aspects of DSSCs to improve them and increase their efficiencies. Although the achieved efficiencies are still low compared to the solid junction cells, the TiO₂ based SSCs are of great interest of researchers as not only is TiO₂ a rather cheap and very well studied semiconductor but also the whole solar cell is neither expensive, nor complicated to fabricate [11]. It is worth mentioning that more than 4000 papers and books have been published in 2012 until September 2013 according to *sciencedirect* database about different concepts related to *DSSCs*, this shows how hot the topic is.

1.2 TiO₂ Nanostructures in Dye and Semiconductor Sensitized Solar Cells (DSSCs and SSSCs)

A schematic representation of a TiO₂ based dye sensitized solar cell and its working principle is given in Figure 1-1a. It generally consists of 5 main parts. A platinized transparent conductive oxide (TCO) such as FTO glass (1), the redox medium (electrolyte) which is a hole-transmitting

means (2), the dye molecules as a light absorber (3) attached to the surface of the annealed TiO₂ phase as the photoanode (4) and the front TCO (5). In the common classic DSSCs, the photoanode is a film of nanocrystalline TiO₂ particles, which can also be substituted by one dimensional structures like TiO₂ nanotubes.

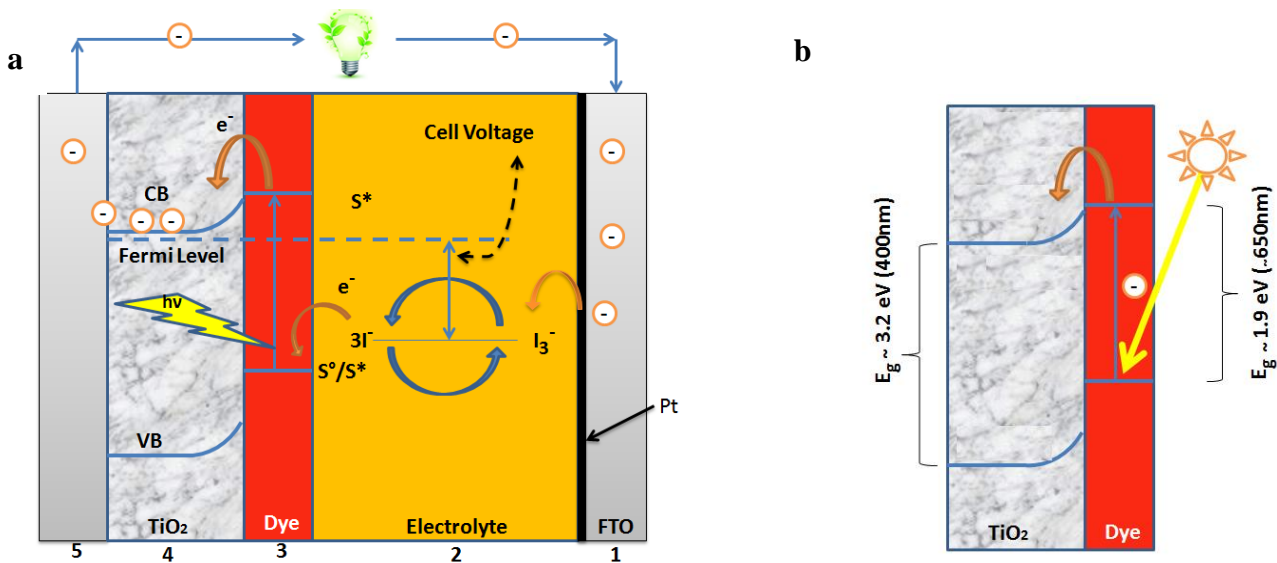


Figure 1-1 a) Schematic representation of the principle of a dye sensitized solar cell, b) Schematic diagram of the electron excitation in a dye molecule and the electron injected from the LUMO of the dye to the conduction band of TiO₂

In the dye molecules electrons excite to the LUMO energy level (S^{*}) under illumination, leaving holes behind in the HOMO level of the dye molecule (Figure 1-1b). The excited electrons then will be injected from the LUMO of the dye with a higher energy level to the conduction band of TiO₂ with a lower energy level. The oxidized dye molecule reduces by oxidizing the electrolyte. The electrolyte in DSSCs is usually the ionic I³⁻/I⁻ liquid, so the

oxidized dye oxidizes I^{3-} to I^- which will diffuse towards the platinized TCO electrode to get reduced to I^{3-} .

Another approach to fabricate organics-free cheaper solar cells is to replace the dye molecule with a semiconductor sensitizer to form semiconductor sensitized cell (SSSC). The working principle of SSSCs is similar to DSSCs and they are assumed as variation of DSSCs. Besides the cheap and simple synthesis method, semiconductor sensitizer offers exciting opto-electronic properties such as tunable band gap and the possibility to manipulate injection and recombination processes, high extinction coefficients and improved light absorption properties, impact ionization effect and multiple carrier generation [12, 13].

The semiconductor sensitizers (like InP, CdSe, CdS, and PbS) can be made in a colloidal solution or produced *in-situ* through chemical bath deposition (CBD) or successive ionic-layer adsorption and reaction (SILAR). The main advantage of these methods over the *ex-situ* methods is the high surface coverage of QDs on semiconductor layer [12, 14, 15].

1.3 Application of 1-D nanostructures in solar cells

A major problem in sensitized solar cells is the *charge recombination* that happens typically on the surface of the TiO_2 surface (with the excited dye molecule) or inside the TiO_2 film, if the charge diffusion and collection rate at the front electrode is not high enough.

The mechanism of charge flow in TiO_2 is a dynamic competition between the electron transport in the layer and the interfacial charge recombination [11, 16] The flow path of the electrons in nanoparticulate and nanotubular TiO_2 films are shown in Figure 1-2.

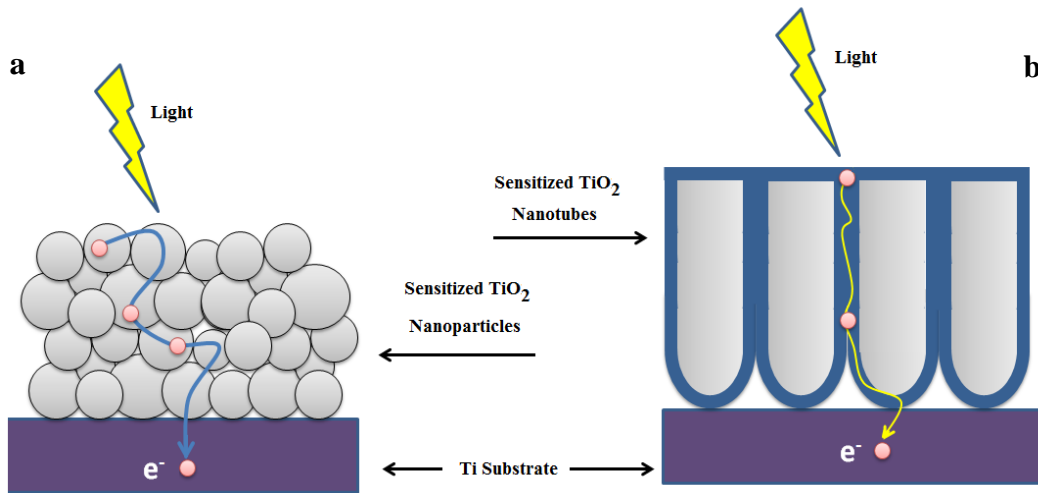


Figure 1-2 Flow path of an electron in a) nanoparticles, and b) nanotubular TiO_2 films [11]

The long travel distance, greater grain boundary area (a disordered high energy phase), and the surface states and defects in nanoparticles increase the probability of trapping the electrons and hence affect negatively on the charge diffusion flow in TiO_2 nanoparticles. These phenomena eventually result in less charge collection at the back contact and consequently lower efficiencies. The idea of "Straight paths", as shown in Figure 1-2b, has motivated researchers towards the synthesis and application of 1-D nanostructures like nanotubes, nanowires and nanorods to arrange a direct pathway to decrease the charge recombination. They have proved that this facilitates the electron travelling by directional mobility and lower the recombination likelihood [3, 11, 16]. Such an improvement may also improve the light harvesting of the solar cell, because higher diffusion coefficient of perpendicular TiO_2 nanotube array to the back

contact permits the utilization of thicker films, so the optical density will be increased which results in absorption of lower energy photons [17]. With similar reasoning, application of TiO₂ nanotubes in other applications like photocatalysis, electrochromism and in Li-batteries has shown better properties compared to nanoparticulate structures.[18]

1.4 Production of TiO₂ nanotubes

TiO₂ NTs have been synthesized through various methods such as *sol-gel*, *nanoporous alumina template-assisted (TA)*, *hydrothermal rout*, and *electrochemical process* [11, 19-21]. Except for the electrochemical method there is no precise control over the synthesized tubes' dimensions and orientations in other methods. Hydrothermal method, for example, results in loose agglomerates

or bundles of different sized individual nanotubes with an arbitrary orientation of the nanotubes as demonstrated by a sample image in Figure 1-3a.

For highly conductive single crystalline structures, the random orientation of TiO₂ NTs is not a key issue; however in most cases the synthesized nanotubes are poly-crystalline and the accidental orientation affects the electron directional flow unconstructively [11].

Yet the *electrochemical process* leads to a highly ordered and a very well aligned and well defined (length controllable) TiO₂ NTs as can be seen in Figure 1-3b and c. Such a structure is much more favorable to fulfill the charge dynamics' needed especially in photovoltaic devices. These tubes are self-organized and their vertical growth results in a favorable geometry and

shape for the fast electron mobility alongside the tubes in comparison to arbitrarily oriented TiO₂ NTs and TiO₂ nanoparticle films [2, 16].

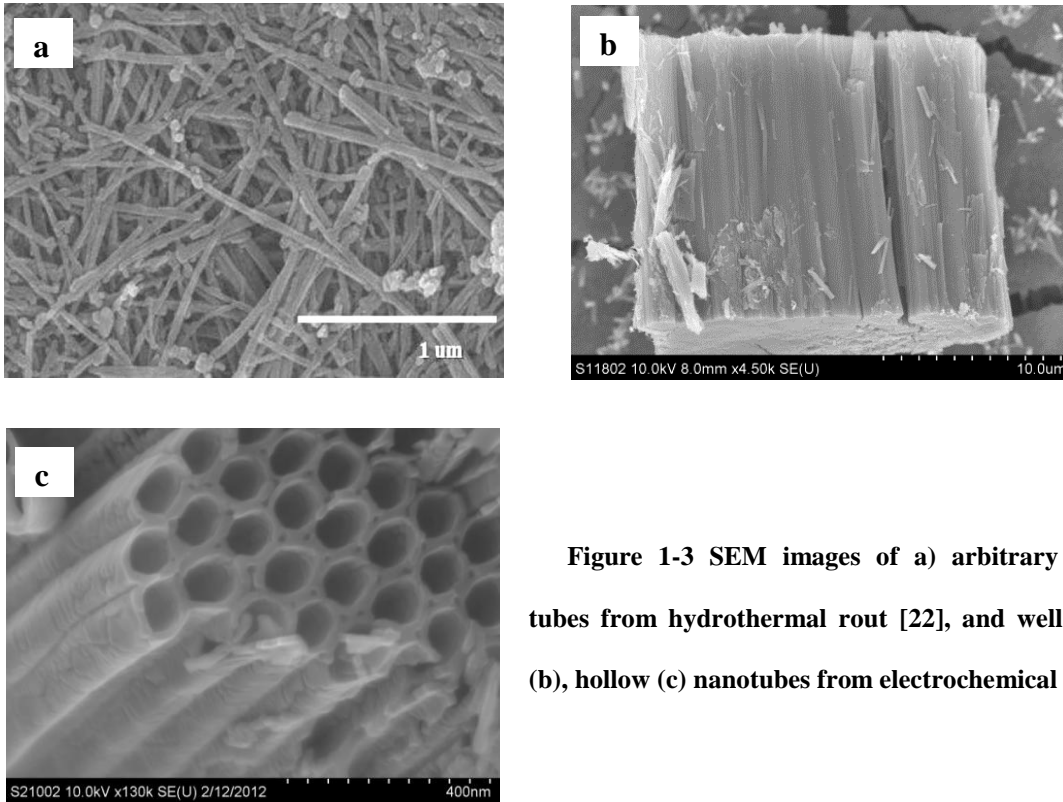


Figure 1-3 SEM images of a) arbitrary oriented tubes from hydrothermal route [22], and well oriented (b), hollow (c) nanotubes from electrochemical method.

1.4.1. Self-organized anodic TiO₂ nanotubes

Electrochemically anodized TiO₂ NTs were first synthesized and grown in chromic acid electrolytes containing HF on Ti foil by Zwilling *et al.* in 1999 [23]. Their successful report has been followed by several researchers in the past 14 years by a great effort to improve TiO₂ NTs' properties.

There are a number of factors that affect the structural properties of anodic TiO₂ NTs such as anodization electrolyte, time and temperature. The anodized TiO₂ NTs are classified to different generations with different properties based on the anodization electrolytes. This shows that the electrolyte plays the most important role in the synthesis of anodized TiO₂ NTs.

1.4.2. Role of electrolytes in anodization of TiO₂ NTs

Over these years of investigation, several aqueous electrolytes including acid based and neutral solutions with F⁻ ions, ionic liquids, and non-aqueous electrolytes have been widely exploited [2, 17, 24, 25].

The first tubes were grown in *acidic aqueous solutions (first generation electrolytes)* such as solutions containing HF, HF+HNO₃, HF+H₂SO₄, CH₃COOH + HF, or H₃PO₄+HF. The electro-etching rate in acidic aqueous solutions is high; therefore the tubes do not grow beyond 500 to 600 nm [25].

Synthesis of longer nanotubes to 2 μm is reported later in pH controlled *buffered aqueous electrolytes (second generation)*. Increasing pH to 5 in a potential window¹ of 5 to 25 was shown to increase the nanotube length. The best pH range was proven to be 3 to 5. In *neutral solutions* however, the TiO₂ NT array's length may reach up to 2-4 μm. In all aqueous solutions, water plays a key role in the chemical solution of the nanotubes during anodization, so the aspect ratio (length to diameter) of tubes grown in aqueous electrolytes is small. *Polar organic electrolytes*

¹ Potential window is the voltage range between a minimum voltage required for the electrochemical oxidation of Ti and a maximum voltage at which no TNT is formed upper than that because of the strong chemical dissolution

with water contents less than 5 percent were successful to overcome the limited aspect ratio problem, so *the third generation of TiO₂ NTs* came into existence. [2]

1.4.3. Organic solvents in anodization electrolytes

A considerable number of studies published by several researchers paved the way to show much better characteristics of TiO₂ NTs from organic electrolytes compared to others, like high degree of self ordering, length and shape control [6]

In the first attempts in formamide (FA) based electrolytes (35 V/48 hours) a 70 μm thick layer was produced. The potential window was 10 to 50 V which is much broader compared to aqueous electrolytes with KF or NaF. In this potential range increasing the voltage increases the ionic transport that results in longer nanotubes. It is shown that in these electrolytes the nanotubes reach a maximum length at a certain time and after that the dissolution rate overcomes the electrochemical oxidation rate, so tubes would be shortened after that [17].

As an interesting progress, Macak *et al.* showed that the smoothest (ripple-less), high aspect ratio TiO₂ NT can be achieved from electrolytes like *Ethylene Glycol (EG)*, *Glycerol* and *DMSO* [26].

In some later attempts, it was shown that the protophilic nature of DMSO causes the acceptance of a proton from HF and therefore decreasing the activity of the solution. This results in less chemical dissolution and hence thicker tube walls and longer tube arrays [27]. In DMSO solutions containing 1 to 6% HF, the potential window widens to 10 to 70 V with anodization time between 20 to 90 hours. The tubes grown in 60 V can reach 90 μm. A pre-anodization step

is shown to noticeably increase the growth rate [27]. An important problem of DMSO + HF electrolytes is that the adhesion of tubes to the underlying oxide layer is not good. For that purpose some researchers proposed adding water to increase the electrochemical conductivity of the electrolyte that results in more adhesive but shorter nanotubes [27]. Some other researchers proposed to make use of used (or aged) electrolytes. The electrolyte's aging step should be done in a low voltage for a long time. After aging, the conductivity of the electrolyte increases because of the increased amount of ions in it and results in more adhesive but shorter and thinner nanotubes [28]. Another drawback for the tubes grown in DMSO is that for short anodization times, unwanted precipitates block the tubes' mouths.

Some other organic solvents are also employed to grow nanotubes such as *diethylene glycol (DEG)* and *glycerol*. DEG is applied with HF, NH₄F or Bu₄NF. The advantage of the tubes from DEG is that they do not suffer from unwanted precipitates that clog the tubes. However, the tubes are completely separated so the surface area is less compared to more compact tubes from EG. Besides, the tubes' adhesion is not good [6, 29]. The other point to be mentioned is the slow growth kinetic of these tubes. In the best reported case for growing a 21 μm layer, 48 hours time is needed.

Nevertheless, the most successful anodization electrolytes with remarkable self alignments are *ethylene glycol (EG)* based electrolytes usually containing NH₄F (0.1 to 0.5 wt %) and water (1 to 4 wt %) [6, 30]. Its potential window is between 20 and 65 V. The longest nanotube for long time anodization of 17 hours at 60 V is found to be about 165 μm from 0.3 wt% NH₄F and 2 wt% H₂O. EG electrolytes with advantages like fast growth rate, high aspect ratio of the TiO₂

NTs, simplicity and good adhesion, have become the most common electrolyte used to synthesize high aspect ratio TiO₂ NTs [11].

1.5 Mechanism of the formation of self-organized TiO₂ NTs in organic electrolytes

The anodization of Ti foil to synthesize nanotubes is usually done in a single compartment electrochemical cell with Ti foil as the working electrode connected to the positive and Pt (in most of the cases) as the counter electrode connected to the negative side of the power source. The story of what happens to form TiO₂ nanotube layer, can be demonstrated briefly as follows. The schematic representation of the mechanism is also given in Figure 1-4.

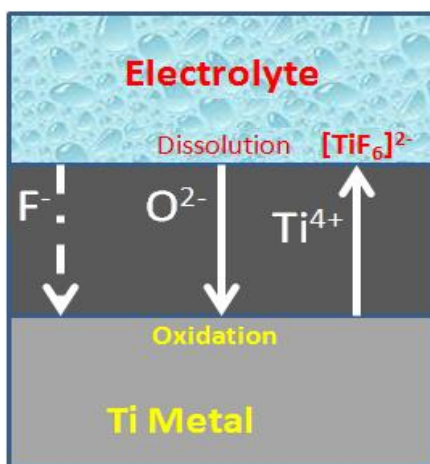


Figure 1-4 General illustration of ions travelling in opposite directions during the anodization process.

At first, under high anodic potentials, a layer of Ti atoms ionizes to Ti⁴⁺ and a thin compact layer of titanium oxide is formed. After a short time the TiO₂ compact layer gets thicker to a few nanometers, on one hand Ti⁴⁺ ions travels through the layer to reach the oxide/electrolyte

interface. On the other hand, O^{2-} and F^- ions migrate in the reverse direction from the oxide/electrolyte interface towards the oxide/metal interface. Basically the oxide can be formed at both interfaces. So, Ti^{4+} ions can react with O^{2-} to form oxide or react with H_2O/O_2 at the outer surface to form oxide or hydroxide compounds. Therefore the compact oxide layer continues to grow².

As a result of polarization in high electric fields, Ti-O bonds in oxide and hydroxide compounds are prone to the field assisted electrochemical dissolution which causes pitting in the compact layer. With increasing layer's thickness, the electrochemical dissolution decreases, but the dissolution of the layer continues by *chemical dissolution mechanism* based on the effect of fluorine ions in the electrolyte. Ti^{4+} reacts and forms $[TiF_6]^{2-}$, the pits transform to pores and then nanotubes after some time.

The rate of electrochemical oxide formation and chemical dissolution equalizes, and nanotubes continue to grow stably to form very long orderly TiO_2 NT layer even up to 2mm on both sides of a Ti foil to form a membrane nanostructure [31]. A more detailed explanation of the mechanism will be offered in *Section 2.1*.

1.6 The addressed problem of TiO_2 NTs grown in the common EG electrolytes

In an important work in 2008, Sergiu *et al.* provided an important insight that the TiO_2 NTs from EG and DEG electrolytes consist of a *double shell wall*: a compact thin shell outside, and a spongy shell inside tubes, like the sample image shown in Figure 1-5 [5]. The latter is shown to

² The formation of the oxide at each interface is basically dependant on their transfer numbers. In TiO_2 the ratio of the transfer number for Ti^{4+} is 0.4

be a less defined layer of precipitated titanium oxy-hydroxide from the reaction of Ti^{4+} with water during the anodization. The layer is shown to contain a high amount of carbon. Besides, the existence of surface hydroxide(s) in the inside shell has been proven by XPS profiles. Burning and thermal decomposition of carbon containing compounds during the heat treatment of tubes leaves a nanoparticulate shell inside the tubes. They discussed that the presence of carbon could be due to the voltage-induced Schottky breakdown and the decomposition of the EG during anodization at high voltages, while it is not the case for the tubes from aqueous electrolytes and electrolytes based on pure dimethyl sulfoxide (DMSO) [6, 32-35]. However, as stated before in *Section 1.4.3*, the aspect ratio of the tubes from aqueous electrolytes is too small compared to the tubes from organics. Moreover, as will be discussed and shown later in *Chapter 4*, the morphology of TiO_2 NTs from DMSO is not fine enough especially for applications like solar cells. Therefore, nanotubes with characteristics similar to tubes from EG without the internal shell, would be of much higher quality. This is the first investigation on the so called *high aspect ratio single wall TiO_2 NTs* with higher quality [6, 27].

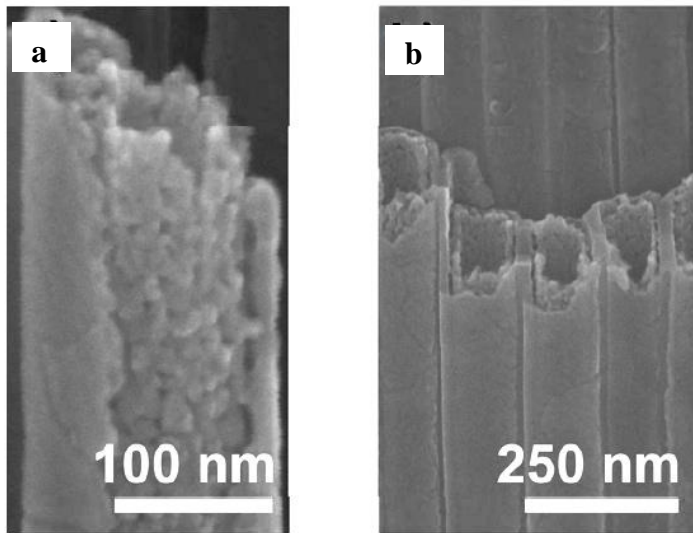


Figure 1-5 SEM images of nanotubes from ethylene glycol electrolyte showing the double wall structure of the tubes after heat treatment at 500°C [5].

1.7 Objectives and significance of the present thesis

The foremost aim of this study was synthesis of single wall nanotubes and their application in SSCs and the main problems that will be acknowledged and discussed in the subsequent chapters are as follows.

- Although ethylene glycol (EG) is known to be the best electrolyte to grow TiO₂ NTs, it decomposes at high anodization voltages which may have a negative effect on the tubes' properties.
- The TiO₂ NTs from EG have a double wall structure. It is discussed that the inside wall may form as a result of the decomposition of the electrolyte and could be harmful for electron transfer and charge injection because of the nanoparticulate shape of the inside layer and probable effects of carbon contamination on the properties of TiO₂ NTs.

- Before this study, no report had been published on the probable elimination of the decomposition of the electrolyte and synthesis of high aspect ratio single wall TiO₂ NTs and its effect on the electron transfer properties in DSCs is not yet reported.

To solve the above mentioned problems the main purposes of this study were to synthesize “single wall TiO₂ NTs” and investigate its electronic properties and effects in DSCs and the specific objectives of this study were:

- Determination of the best anodization condition to synthesize single wall TiO₂ NTs (Chapter 4)
- Characterization of the intrinsic properties of the single wall TiO₂ NTs such as their electrical resistance and band gap and make a comparison with the conventional tubes from EG electrolytes (Chapter 5).
- Efficiency comparison between DSSCs and SSSCs fabricated by single wall and double wall TiO₂ NTs (Chapter 6)
- The contrast in electron transport/transfer properties between single wall and double wall TiO₂ NTs in DSSCs and SSSCs by impedance spectroscopy and intensity modulated photocurrent and photovoltage spectroscopy (IMVS/IMPS) experiments (Chapter 6).

The improvement of the physical properties of TiO₂ NTs, as a major result of our study, may be a highly promising platform for development of nanotube applications in photovoltaic devices such as DSSCs, SSSCs and water splitting photoelectrodes. In addition to photoelectrochemical applications, the highly defined single wall tube structure should also be able to act as a much better defined

secondary material deposition (templates) or serve in membrane applications where a much more defined profile (constant inner tube diameters) is highly desired.

Chapter 2

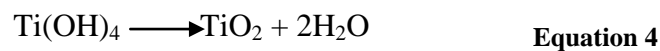
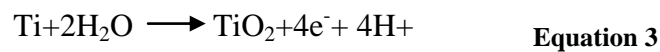
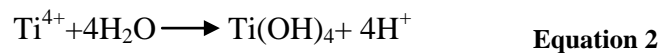
Literature Review

In this chapter an overview of the proposed mechanism of growing TiO₂ NTs and electro-oxidation of EG on metallic and semiconductor surfaces will be presented. Subsequently the phase transformation of TiO₂ during heat treatment and conductivity of TiO₂ NTs will be reviewed based on the literature. Finally the chapter ends with a brief theory of nanotube based solar cells.

2.1 Mechanism of nanotube array formation in anodization

In general, the nanotube growth in a two compartment anodization process (*see Section 3.1*) occurs in 5 main steps shown schematically in Figure 2-1 and explained as follows:

a) At first Ti ionizes to Ti⁴⁺ and then reacts with O²⁻ from de-protonation of H₂O and/or OH⁻ ions in the electrolyte to form an oxide layer forms through equations 1 to 4 on the surface of the foil (step 1 in Figure 2-1a).



As the oxide layer grows over time and becomes thicker at a fast rate, the current density drops sharply (region I in Figure 2-1b).

b) Migration of O^{2-} and OH^- ions happens from oxide/electrolyte surface towards the metal and Ti^{4+} from the metal/oxide towards the surface under the electrical field (Figure 2-1c).

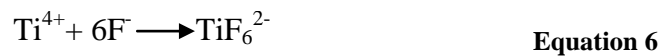
c)

1- The Ti-O bond in TiO_2 tetragonal lattice structure will be polarized under a high electric field which activates the electrochemical dissolution reaction of the layer as well as the chemical dissolution in presence of fluorine ions according to Equation 5. The current density increases in this step (region II in Figure2-1b). So small pits immerge in the thin oxide layer.



2- As a result of the O^{2-} ions migration towards the metal/oxide interface, TiO_2 barrier layer forms and thickens under the pores. Therefore, the current density slows down in this stage (region III in Figure2-1b).

d) As the field assisted dissolution reduces the Ti^{4+} ions reaching the oxide/electrolyte interface dissolve chemically (Equation 6) in fluorine containing electrolyte (chemical dissolution, steps 2 and 3 in Figure2-1a)



e) After sometime the rate of electrochemical oxide formation at the oxide/metal interface and the electrochemical and chemical dissolutions (Equation 5 and Equation 6) at the pore bottom become equal and stable pore growth continues to form orderly nanotubes (steps 2 and 3 in Figure2-1a, and region III in Figure 2-1b) [2, 17, 18].

Several parameters affecting the growth and properties of nanotubes have been studied in detail in numerous works such as the effect of the applied voltage, anodization time and temperature and the anodization electrolyte. Among all, the effect of the anodization electrolyte's composition (such as the solvent, amount of water and fluorine) on the morphology and characteristics of nanotubes has been studied in detail [2, 11, 17, 18, 25, 27, 36, 37]. However, it is worth mentioning that in the proposed nanotube growth mechanisms, the probable intervention of the electrolytes on the tubes' properties is ignored and all researchers have just supposed that the electrolyte's composition remains unchanged during the anodization process.

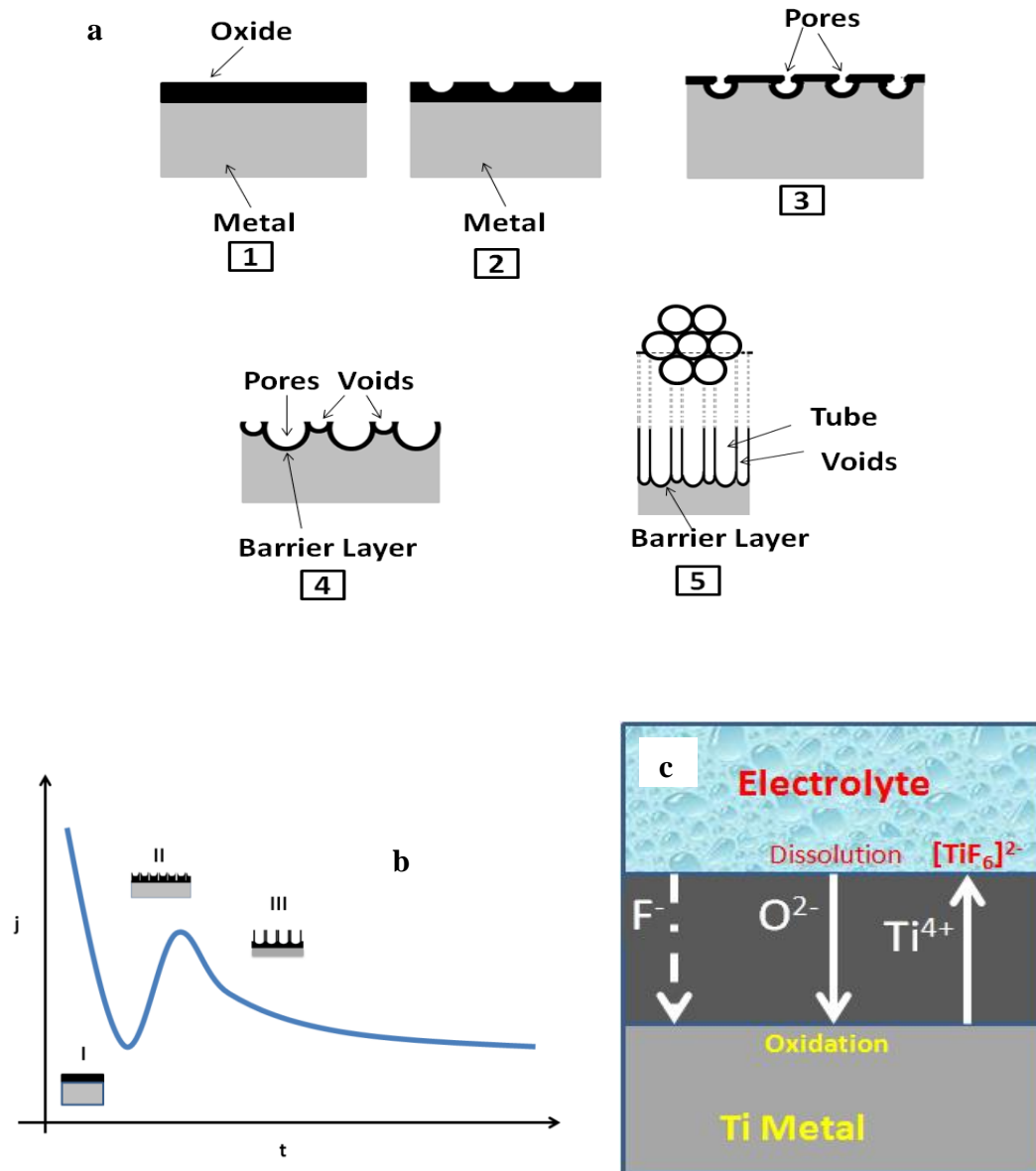


Figure 2-1 a) Schematic representation of the five stages of nanotube formation [17], b) demonstration of changes in the current density during the time of anodization, and c) the flow directions of different ions through the oxide compact layer (grey) during the anodization [2, 18]

2.2 Electro-oxidation of EG on metal surfaces

Electro-oxidation of EG on metallic surfaces has been the subject of several studies in recent years as EG has always been an attractive choice for direct alcohol fuel cells (DAFCs).

In an ideal condition the full oxidation of EG produces CO_2 . However, an EG molecule needs 10 electrons for full oxidation, hence the electro-oxidation process has several steps, resulting in formation of several in-between products such as glycolaldehyde, glyoxal, glycolic acid, oxalic and formic acids through a number of other intermediate compounds [38].

In a detailed investigation Wang *et al* have shown that the electro-oxidation chain reaction of EG in aqueous solutions depends strongly on the pH of the solution [38]. On a polycrystalline Pd metal electrode, glycolate, glyoxal, glyoxylate, oxalate, formate and carbonate form in basic solutions [38]. In solutions with pH less than 12, CO_2 is the ultimate product (Figure 2-2).

The electro-oxidation of EG is shown to be stronger in strong acids (pH near 0) and strong basis (pH near 15). The data presented in Figure 2-2 is collected from cyclic voltammetric experiments revealing that the oxidation potential of EG is higher in acidic solutions.

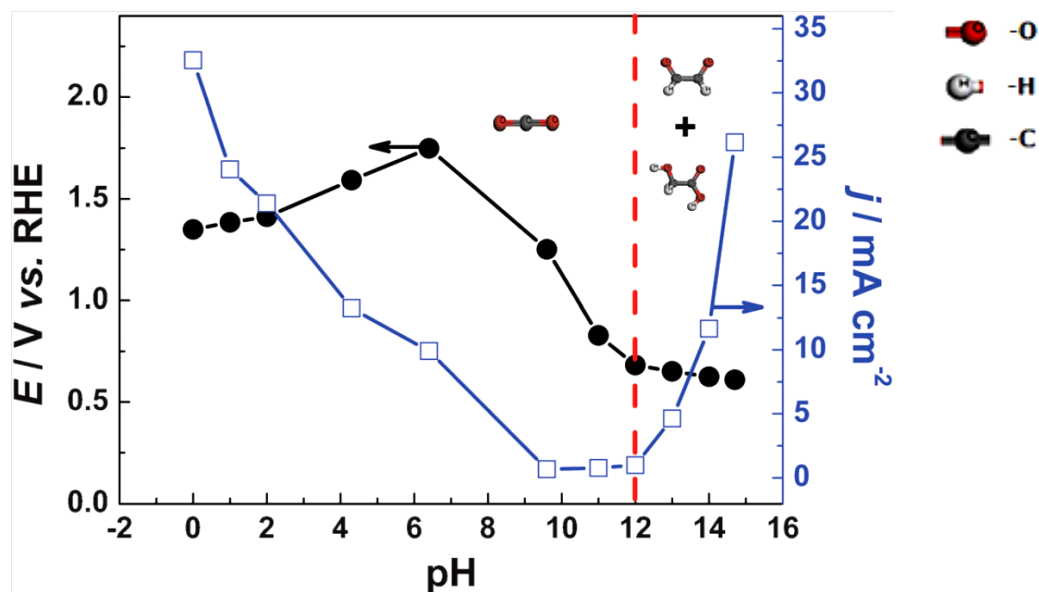


Figure 2-2 Effect of pH on the onset potential and the peak current density of EG electro-oxidation on Pd. CO₂ is the main product at pHs lower than 12, while at higher voltages glyoxal and glycolates are produced [38].

In Figure 2-3 the *in-situ* FTIR results of the electro-oxidation of EG is demonstrated. The important points to note here is the broad band between 1600 and 3000 cm⁻¹ that becomes deeper as the voltage increases and is due to the production of molecular water and formation of CO₂ at higher voltages (2343 cm⁻¹ peak) during the electro-oxidation of EG. Another species is -OOC-COOH that is an intermediate production of oxidation of EG (1220 and 1070 cm⁻¹).

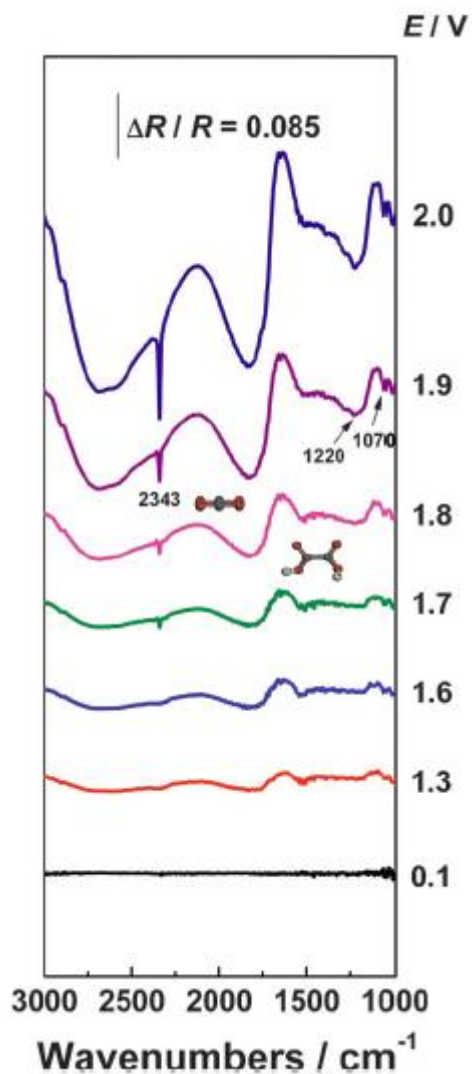


Figure 2-3 *In-situ* FTIR spectra of an EG containing electrolyte obtained under potential step polarization at pH=6.4 [38]

Based on their findings, Wang *et al* proposed the general pathway shown in Figure 2-4 for the EG electro-oxidation [38]. It should be mentioned that this is the complete sequences of the EG electro-oxidation and depending on the pH, one or more of the compounds can be detected in the products.

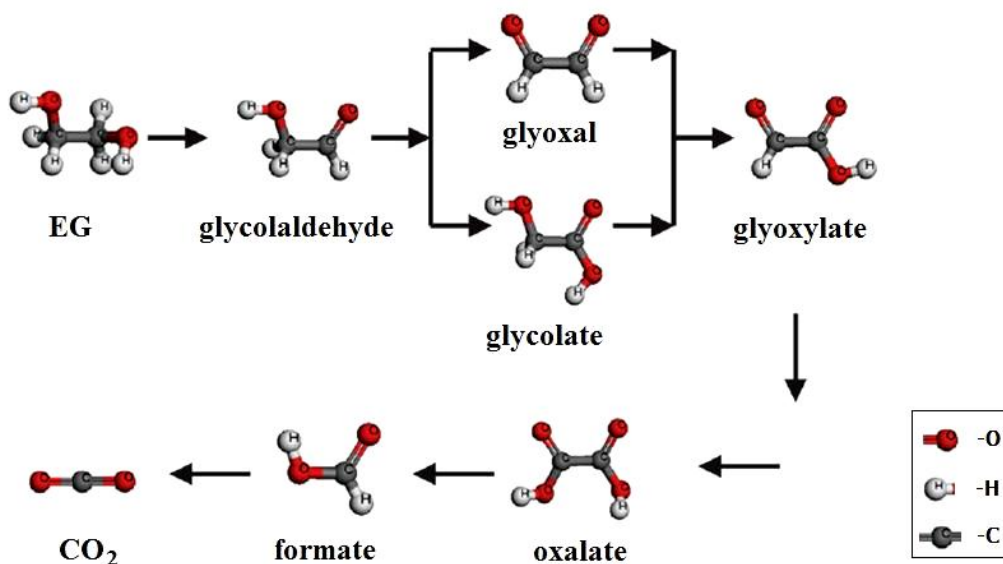
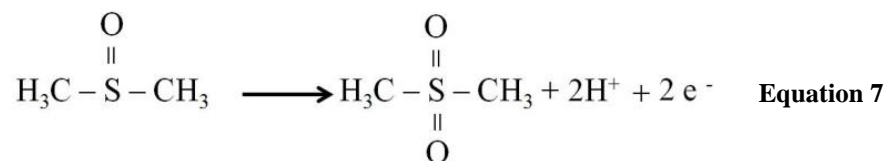


Figure 2-4 Full reaction path of EG electro-oxidation proposed by Wang *et al* [38]

2.3 Electro-oxidation of dimethyl sulfoxide (DMSO)

In an attempt to show why DMSO based electrolytes cannot be used in photoelectrochemical devices, Krtil *et al* revealed that the electrolyte (containing small amount of H₂O) is not stable above 1 V vs. SCE. The anodic and photoanodic oxidation of the DMSO based electrolytes on Pt, glassy carbon and anatase TiO₂ produces dimethyl sulfone [(CH₃)₂SO₂] and two protons as demonstrated by Equation 7.



Hence, in FTIR characterizations the production of dimethyl sulfone can be detected from the production of peaks around 1300 and 1150 cm⁻¹ corresponding

to asymmetric and symmetric stretches of SO₂ in dimethyl sulfone respectively [39].

2.4 Electro oxidation of the electrolytes on semiconductor surfaces

The voltage induced carrier generation in silicon and electro-oxidation of electrolytes on silicon substrates for metal electrodeposition is reported by researchers [40-42]. In 2010 Song *et al* used this phenomenon to explain the pseudo-photocatalytic reaction on highly doped anatase TiO₂ substrates [37]. The doping level of the annealed titania nanotube layer is shown to be about $1 \times 10^{19} \text{ cm}^{-3}$ [43]. When such an n-type semiconductor is in contact with an electrolyte, a Schottky junction can be established [37]. Under voltages higher than its band gap, valence band hole generation is likely to happen. A schematic representation of this phenomenon is demonstrated in Figure 2-5.

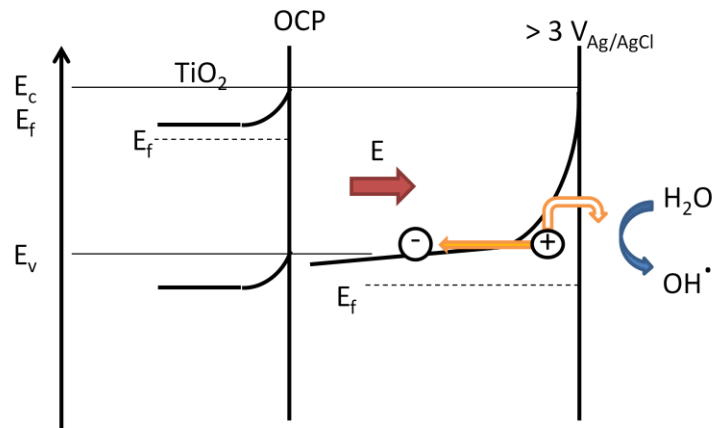


Figure 2-5 Voltage-induced formation of OH on the surface of an n-type semiconductor [37]

Under high anodization voltages the semiconductor will be polarized, making its Fermi level lower towards higher potentials until it reaches the valence band edge of TiO₂. The applied voltage to reach this point will be as in Equation 8 in

which E_{appl} , E_{fb} and E_{g} are effective applied voltage, flat band potential and band gap of the material respectively. For TiO_2 , $E_{\text{appl}} \approx -0.4 \text{ V}$ versus Ag/AgCl at $\text{pH}=7$ and E_{g} is 3 to 3.2 eV (3 -4 V versus Ag/AgCl).

$$E_{\text{appl}} \approx E_{\text{F}} + E_{\text{g}} \quad \text{Equation 8}$$

At this point Schottky barrier break-down may take place; holes will be generated at the surface of the semiconductor (band ionization). The holes then can oxidize the species in the electrolyte such as H_2O to form OH . It is noteworthy that for valence band ionization the voltage should be high enough to let the *tunneling breakdown* of Schottky barrier occur, otherwise just deep depletion will be favored [44].

2.5 Tunnelling (Zener) breakdown

When there is a p-n junction between heavily doped semiconductors, if the n side is connected to the higher potential side of a power source, for a thin depletion layer, the electric field is:

$$E_{\text{t}} = E_{\text{i}} + E_{\text{ext}} \quad \text{Equation 9}$$

Where E_{t} is the total electric field, E_{i} is the internal electric field (due to pn junction) and E_{ext} is the external electric field in the opposite direction.

Briefly, as the field over the space-charge layer is reversely proportional to its thickness ($E = \frac{V}{d}$), in case of high voltages, the field will go very high and is likely to reach the breakdown voltage. The energy then is enough to excite electrons from valence to conduction band leaving an electron- hole pair in the layer (valence band ionization). The electrons will be drifted to the negative side

and holes will be pushed towards the surface of the semiconductor (Figure 2-6a). This phenomenon can continue and increases exponentially³ the concentration of electron-hole pairs, similar to what happens for a silicon diode, is illustrated in Figure 2-6b (quadrant III). The phenomenon is called tunnelling or Zener breakdown.

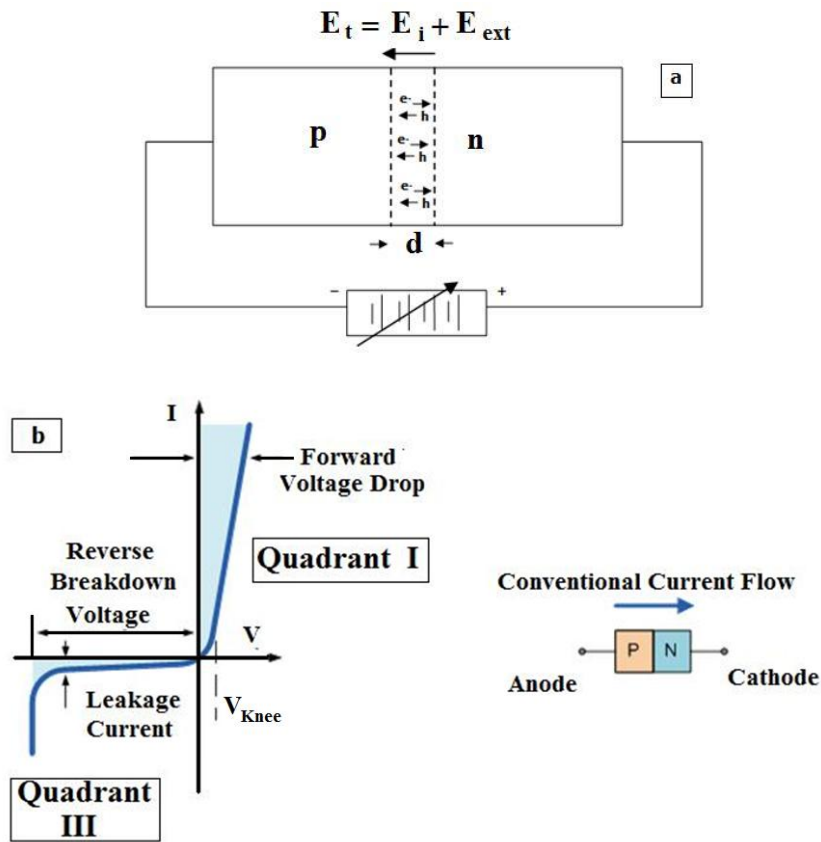


Figure 2-6 a) carrier flow in a typical pn junction connected to a power source, b) silicon diode and its I-V schematic characteristics [45].

³ This case is similar to a diode structure in which $I = I_s \left(e^{V_D/nV_T} - 1 \right)$, where I is the diode current, I_s is the reverse bias saturation current (or scale current), V_D is the voltage across the diode, V_T is the thermal voltage, and n is the ideality factor

2.6 Heat treatment of TiO₂ nanotubes

The TiO₂ nanotube layers from electrochemical techniques are generally amorphous in their as-synthesized form. According to some researchers the as-prepared nanotubes consist of an amorphous gel of hydroxylated / oxide TiO₂ containing small dispersed anatase crystals of 1-3 nm [5, 46, 47]. The amorphous nanotubes have to convert to crystalline structures to become functional for most of applications. For that purpose, the amorphous structure is usually heat treated to give the atoms the needed energy to rearrange to an orderly crystalline manner.

In the crystalline form, the TiO₂ atoms may form different polymorphs mostly *rutile*, *anatase* and *brookite*. Each of these atomic structures has its special characteristic properties and potentials, so in general TiO₂ may be utilized in a wide range of applications, depending on its crystal structure.

In dye sensitized solar cells and catalysts for instance, anatase phase is generally preferred; while rutile phase is favored for high temperature oxygen gas sensing applications and use in dielectrics [2, 11, 16, 48].

The atomic arrangement of rutile and anatase are very similar, both crystallize in tetragonal bravais system with the same degree of symmetry, but different interfacial angles.

The amorphous nanotubes generally transform to anatase first during the heat treatment of the layer following by a transformation of anatase or amorphous to rutile at higher temperatures. By means of XRD diffraction patterns of nanotubes grown on Ti foils, it is shown that the amorphous tubes transform to anatase at

about 280 °C by Varghese *et al* or 300°C [49] by other researchers [46, 50, 51]. This transformation temperature is shown to be insensitive to the ambient atmosphere.

By further heating, Varghese *et al* believe that the rutile phase starts to appear at near 430°C and ends between 620 °C to 680 °C [49]. However there is a dispute over the start temperature of the transformation. Schmuki *et al* and some other researchers believe that the rutile phase starts to form at temperatures higher than 500 °C [5, 52, 53]. All these data are driven by means of XRD analysis. Nevertheless, the anatase to rutile transformation temperature window, driven from *differential scanning calorimetry* (DSC) tests was 641 to 682 °C depending on the heating rate. This difference is thought to be because the XRD profiles are taken from almost isothermally heat treated samples at different temperatures; however the DSC test is a non-isothermal experiment which might affect the transformation temperature range.

It is noteworthy that in XRD results of the tubes on foils, the metallic Ti peaks from the foil are also observed as the penetration depth of X-ray beams is almost 9µm [54]. These peaks also fade away between 620 °C to 680 °C, because of the oxidation of the foil [49].

The schematic phase transformation path proposed by Varghese *et al* is shown in Figure 2-7 [49]. At 280 °C, the anatase crystals start to form at the center of the nanotubes' walls and also in the oxide compact layer underneath the tubes (Figure 2-7a) which has been verified by other researchers [50, 51]. Then the crystals

grow (Figure 2-7b) and rutile crystals come to existence at around 430 °C at the compact oxide layer under the tubes, but not in the tubes' thin walls (Figure 2-7c). Similarly, in small TiO₂ particles (14 nm), Zhang *et al* [55] showed that the anatase to rutile transformation will not happen as there is not enough volume for the transformation to happen. The fact is also confirmed by Schmuki *et al* [50] for the nanotubes, but for the samples annealed at higher temperatures (500°C). Besides, the detailed TEM study of Jaroenworarluck *et al* also proves that only anatase lattice spacing can be found in the wall of detached tubes from the foil and then treated at 600 °C [51].

As annealing process continues, the rutile crystals grow and the anatase crystals transform to rutile up to 620 °C (Figure 2-7d) and continue to grow (Figure 2-7e) but the near surface part hardly transforms to crystalline.

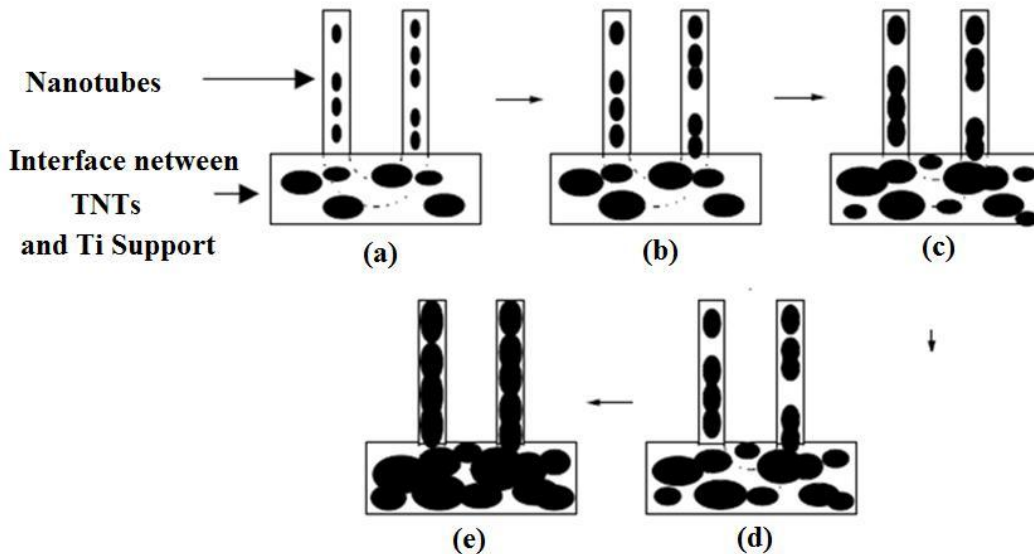


Figure 2-7 Complete phase transformation path of TiO₂ nanotubes from a) at 280 °C , b) above 280 °C, c) at 430 °C , d) above 620 °C , and e) above 620 °C [49].

Sergiu *et al* showed that the anatase crystals have a cylindrical shape elongated in the direction of nanotubes axes [50]. Regonini *et al* argued that at all heat treatment temperatures (between 400 and 600 °C), the outer surface of the nanotubes remains amorphous and a layer of amorphous TiO₂ covers the crystals in the middle [51].

Another issue to raise is that the sizes of the anatase crystals are independent of heat treatment temperature and have comparable sizes in samples annealed at 350 and 450°C. However (independent of heating and cooling rates), annealing at 450°C results in numerous cracks at grain boundaries in the tube wall, while the tubes annealed at 350°C have a much smoother surface. This is evident from SEM images in Figure 2-8. This might have arisen from the transformation, heating, and cooling stresses. This fact along with the thick rutile layer formed beneath the nanotubes at high temperatures can be the reason for a considerable slower electron transport for the tubes annealed at 450°C. Therefore, one may assume that for such a reason the lower temperature annealed sample is better for applications based on transport of electrons such as dye sensitized solar cells (DSSCs). However, it is shown that in the 450°C annealed cells, the defects help to increase the amount of dye adsorption which compromises the negative effect of lower charge transport in those nanotubes [43].

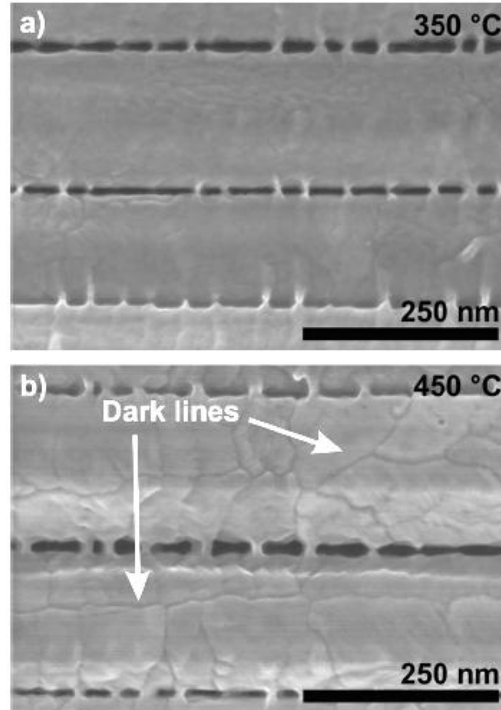


Figure 2-8 SEM images of TiO₂ nanotubes annealed at a) 350, and b) 450 °C showing the high level of cracks in the tube walls of the sample treated at 450 °C [50]

2.7 Formation of double wall TiO₂ nanotubes in EG electrolytes

In most of research publications about TiO₂ nanotubes synthesized in EG the shape of the nanostructure is shown in SEM images of anodized tubes which are very smooth and uniform nanotubes similar to the image shown in Figure 2-9a. However in 2008 Sergiu *et al* published their work to show in detail that the TEM images of the TiO₂ NTs from EG and DEG electrolytes have a double wall structure; an outside compact thin shell which is uniform in thickness and surrounds an internal conical less compact shell (Figure 2-9b) [50].

As can be seen in the schematic presentation in Figure 2-9c, the thickness of the outer shell tube (OST) is almost constant and about 20 to 25 nm, while the

internal shell of the tube (IST) has a conical shape with thickness varying from a few nanometers near the top to about 50 nm near the bottom of the tubes.

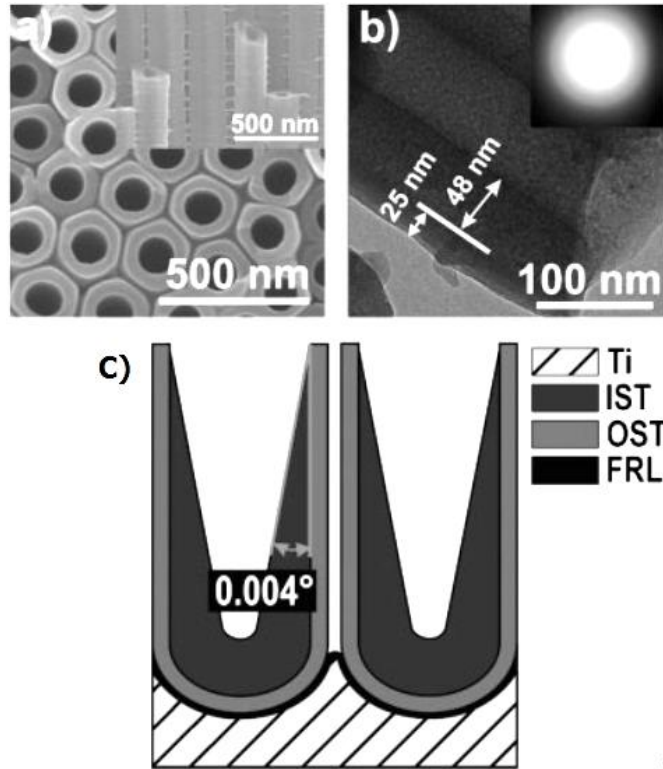


Figure 2-9 a) SEM images of top and side of tubes formed in EG before heat treatment showing a uniform structure. b) TEM image and SAED (selected area electron diffraction) pattern (inset) of an individual tube showing its double wall nanostructure and c) schematic demonstration of different parts of an anodically grown TiO_2 from EG electrolyte [5]

Sergiu *et al's* dispersive X-ray spectroscopy (EDX) detailed investigation also reveals that a considerable amount of contaminating elements of carbon and fluorine is detected in DW nanotubes. The amount of carbon contamination is proportional to the thickness of the inside shell. With not much experimental evidence, they discussed that the contamination source could be the decomposition of EG during the anodization resulting in entrapment of electrolyte species in the internal shell of the tubes (IST) [5], so the amount of C-

contamination is proportional to the IST thickness along the tubes. The conical shape of the IST is mainly because the tubes are more prone to be etched by fluorine ions near their mouths (*see Section 4.1*) [50].

2.7.1 Annealing of double wall TiO₂ nanotubes

In general, the amorphous structure of TiO₂ nanotubes must be transformed through annealing to a crystalline structure first to be used in different applications such as solar cells. As discussed before in *Section 2.7*, the carbon species are mainly entrapped in the internal shell of DW nanotubes. During heat treatment, carbon burns and leaves a porous annealed shell inside the TiO₂ NTs. It also should be noted that the overall morphology of the porous IST also depends on the rate of the heat treatment which is demonstrated in Figure 2-10 in which it can be observed that at very high heating rates such as 25 °C/s, and 50 °C/s, the internal and external shells will not be separated, while as is evident this happens at low heating rates of 1 °C/s (Figure 2-10a,d).

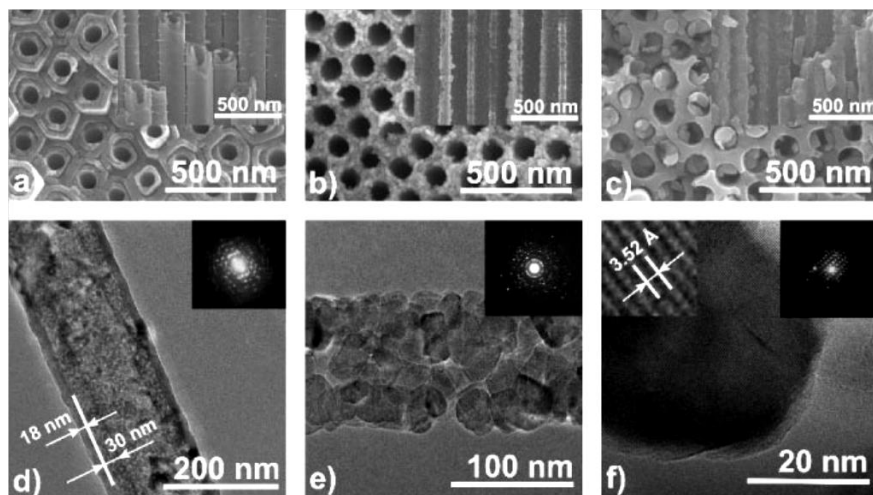


Figure 2-10 Dependence of the morphology of DW tubes on the heating rate. a,d) 1 °C/s, b,e) 25 °C/s, and c,f) 50 °C/s to 500 °C [5].

2.8 Conductivity of TiO₂ nanotubes

Although the solid state electrical conductivity of TiO₂ nanotubes play a key role, especially in applications like photovoltaics, very few investigations have been published either on the measurement of the conductivity of TiO₂ NTs or on the effect of nanotube characteristics, such as length and heat treatment condition, on the tubes' conductivity. In the first report, Asmatulu *et al* measured and reported the axial electrical conductivity of 60 to 80 μm TiO₂ NTs grown in EG electrolytes by means of impedance spectroscopy over the temperature range of 225 to 400 °C [56]. They calculated the conductivity from the interception point of the impedance curve with X-axis considering the sample dimensions [56]. The Arrhenius plot of $\log(\sigma) - (1/T)$ is shown in Figure 2-11 for TiO₂ NTs heated from the amorphous condition to 400 °C. The open circles represent the amorphous sample's conductivity at 225°C. It can be seen that $\log(\sigma)$ changes linearly from 250 to 350 °C.

Another point to mention is that the conductivity of EG- TiO₂ NTs lies between the conductivities of thin film TiO₂ samples (triangles) and nanoporous particles (squares) that all approach together at high temperatures as 500°C (Figure 2-11).

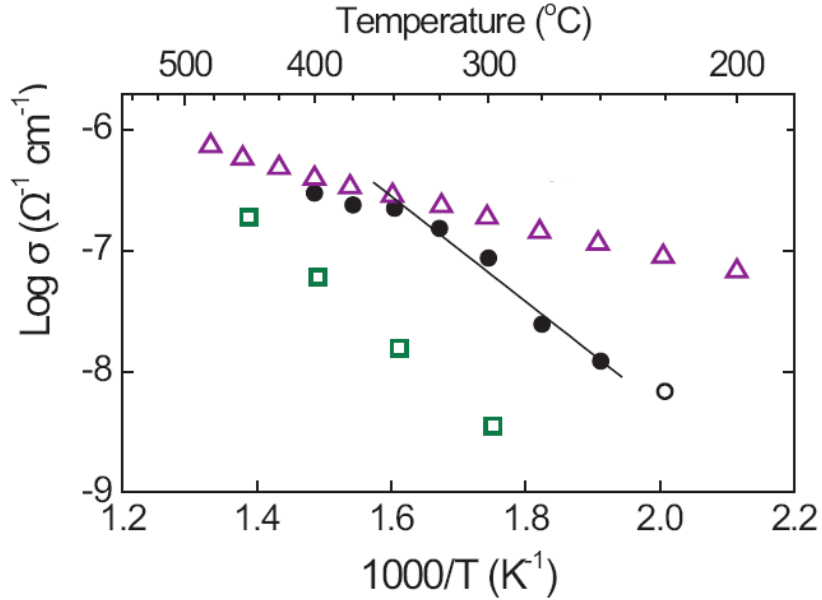


Figure 2-11 Electrical conductivity of TiO₂ nanotubes (circles) , nanoporous anatase (squares) and nanocrystalline anatase (triangles) thin films [56].

From the Arrhenius relationship between the conductivity and temperature, Asmatulu *et al* found that the thermal activation energy for carrier transport is about 0.87 eV in TiO₂ NTs from EG electrolyte [56]. While, based on the two other sets of data for nanoparticulate TiO₂ and thin films, their thermal activation energies can be calculated to be 1.25 and 0.22 eV respectively. These activation energies are reasonable as there we expected to be much higher energy defects like interfaces in nanoparticles; hence an increase in the activation energy is required.

Later on in a systematic study, Alexei *et al* [52] investigated the effect of the heat treatment conditions on the solid state electrical conductivity of TiO₂ NTs. They found specific resistivity values of 1.2 to 17 μm EG tubes to be 10⁹ to 10¹⁰ Ωcm in amorphous form which drops to 10⁴ to 10⁵ Ωcm in their annealed state.

Moreover, the resistivity of tubes grown in glycerol/water is proved to be similar to those grown in EG electrolytes.

Alexei *et al's* experiments have also revealed the effects of the length of TiO₂ NTs and their annealing time and temperatures on the resistivity. The specific resistivity of tubes increases with their length. Besides, Figure 2-12 shows the effect of annealing time and temperature on the specific resistivity of EG nanotubes.

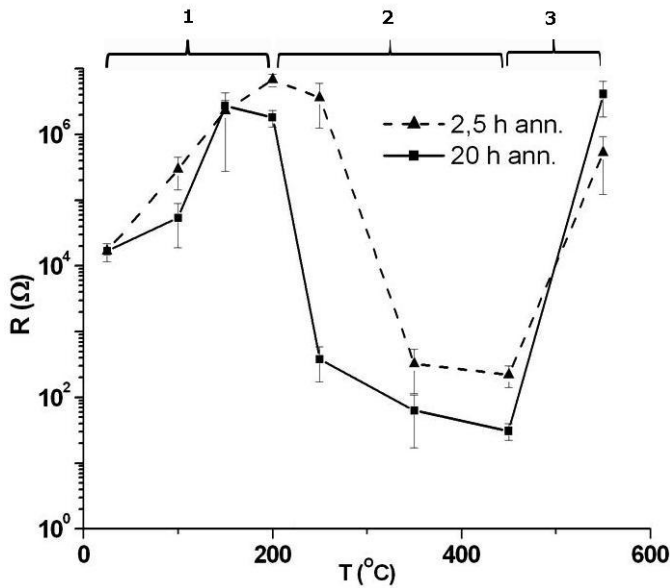


Figure 2-12 Effect of annealing time and temperature on the specific resistivity of 2.5 hour and 20 hour annealed at 500 °C EG nanotubes [52].

As it can also be observed in Figure 2-12, longer annealing times (20 hours) results in lower specific resistivities at almost all temperatures. The other point to be mentioned here is the trend of the changes with the temperature. The resistivity curves in Figure 2-12 have three different regions. In the first region it increases due to loss of absorbed water and fluoride in the TiO₂ NTs. From about 250 °C it drops sharply and this can be attributed to the transformation of the amorphous

TiO₂ phase to crystalline anatase. Up to 450°C the dominant phase is anatase. Finally, rutile formation happens and a sharp increase in resistivity is evident in region 3.

2.9 Photovoltage-photocurrent characterization of solar cell

A photovoltaic cell can be modelled as a current source connected with a rectifying diode in parallel [57]. In the dark PV cell performs like a diode and when the light is illuminated on the cell, current is generated. The Shockley equation describes the corresponding j - V characteristic, which is equivalent to the generated current minus the diode current.

$$j(V) = j_{sc} - j_0 \left(e^{\frac{qV}{mTK_B}} - 1 \right) \quad \text{Equation 10}$$

In this equation q is the elementary charge, V is the voltage at the terminals of the cell, m ($1 < m < 2$) is the diode ideality factor, K_B is the Boltzmann constant, T is the absolute temperature, J_0 is the diode saturation current density and j_{sc} is the short circuit photocurrent density defined by the incident photon flux.

The j - V characteristic curve of a typical solar cell is presented in Figure 2-13. As depicted, the maximum value of photocurrent in the cell is represented by the short circuit photocurrent density (j_{sc}) which corresponds to the short circuit condition when the voltage is zero. Likewise, the maximum photovoltage generated in a cell is shown by open circuit photovoltage (V_{oc}) which occurs when the current passing through the cell is zero. It is clear that the values of j_{sc} and V_{oc} cannot be achieved simultaneously.

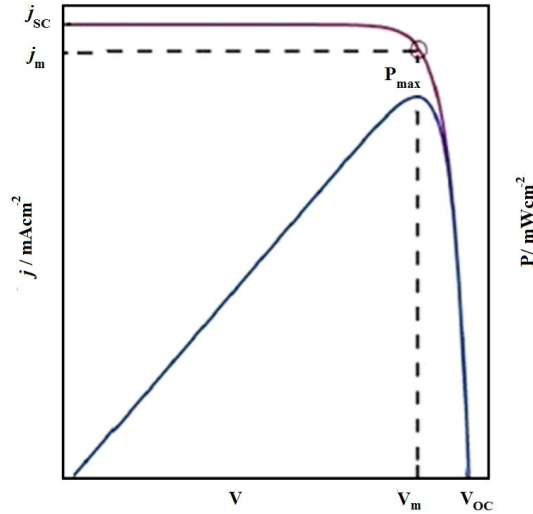


Figure 2-13 j - V characteristic curve of a solar cell simulated based on the Shockley equation [58].

Instead, optimized performance of the cell is presented by a maximum power point (P_{max}) corresponding to a maximum photocurrent density (j_m) and maximum photovoltage (V_m). The overall photoconversion efficiency (η) of the cell could be calculated as follows:

$$\eta = \frac{j_m V_m}{P_{in}} = \frac{j_{sc} V_{oc}}{P_{in}} ff \quad \text{Equation 11}$$

In Equation 11, P_{in} is the incident irradiance ($W\ m^{-2}$) and ff is the fill factor which indicates the solar cell's quality.

Solar cell efficiency is reduced during the operation by power dissipation across the internal resistances which are typically represented by a shunt (R_{sh}) and series resistance (R_s). A higher value of R_{sh} , that represents a leakage current in the cell, is desired. While, a lower value of R_s is desired for the device performance as it determines the current flow through the device. The series resistance includes the charge transport resistance through the photoanode and

FTO contact, charge transfer resistance at the counter electrode and the resistance of the electrolyte.

The standard spectrum for testing solar cell current-voltage performance is the AM 1.5G (Air Mass 1.5 Global) spectrum. It is nearly equal to the total power of the photon distribution when the absorption band of the atmosphere and a dilution factor of 1.56×10^{-5} are considered for blackbody spectrum at temperature 5800 K. The AM 1.5G matches sunlight spectral intensity distribution at the earth's surface with 48.2° incident angle and with an integrated power density of 100 mW cm^{-2} .

Theoretical maximum photocurrent generated by the solar cell can be calculated from the integration of incident photon-to-current conversion efficiency and incident photon flux of the standard spectral irradiation spectra AM 1.5G.

$$j_{sc} = q \int b_s(\lambda) IPCE(\lambda) d\lambda \quad \text{Equation 12}$$

In this equation, q is the elementary charge, b_s is photon flux and IPCE is incident photon-to-current conversion efficiency.

IPCE (λ) or external quantum efficiency is equivalent to the number of photogenerated electrons in the external circuit divided by the number of incident photons at different wavelengths. It is also identical to multiplication of light harvesting, charge separation and charge collection efficiency at different wavelengths as described by equation 13:

$$IPCE(\lambda) = \frac{\text{photogenerated current}}{\text{photon flux} \times \lambda} = \eta_{th}(\lambda)\eta_{sep}(\lambda)\eta_{col}(\lambda) \quad \text{Equation 13}$$

Light harvesting efficiency is attributed to the light absorption coefficient of the sensitized photoanode, the charge separation efficiency can be calculated by multiplying the carrier injection efficiency (from the excited sensitizer into the conduction band of metal oxide) and the sensitizer regeneration efficiency and finally, the charge collection efficiency (that defines how efficiently the injected carrier can be collected at the external circuit) can be determined by the impedance spectroscopy measurement [57].

$$\eta_{sep}(\lambda) = \eta_{inj}(\lambda)\eta_{reg}(\lambda) \quad \text{Equation 14}$$

2.10 Electrochemical Impedance Spectroscopy (EIS) of sensitized solar cells

Electrochemical impedance spectroscopy (EIS) is one of the well-established and powerful measurement techniques to characterize the electrochemistry systems [58]. In 1970s EIS has been extensively applied to investigate the photoelectrochemistry [59, 60] phenomena in crystalline electrodes used for solar energy conversion [61].

By the advent of the DSSC and other new generation of solar cells, EIS had been successfully used to study different features of solar cell devices. In these studies frequency based models were applied to nanostructured wide band gap semiconductors used in the device [62]. Later, the model was expanded for both nanostructured and bulk semiconductors based solar cells [63]. The EIS results

were also compared with other available techniques examined earlier [64] and similar trends were observed in both characterization methods.

Basically, EIS measures the AC electrical current at defined angular frequency (ω) under a certain AC voltage. Likewise, the AC voltage can be measured for system under defined AC current. Impedance is represented by $Z(\omega)$ and is equal to the ratio of AC voltage to AC current [58]. Application of EIS for characterization of DSSC and more recently for characterization of semiconductor sensitized solar cell (SSSC) [65] has become predominant. More explicitly, EIS characterization has become the most widespread method as it offers applicable information regarding the different device features simultaneously e.g. transport and recombination related parameters [58, 64, 66].

To simulate the performance of a cell under device conditions, the impedance measurement is performed under illumination and light with different intensity is imposed on the system and constrains the system at the steady state point. Then, $Z(\omega)$ is measured within the selected frequency window. Frequency is related to ω by $f = \omega/2\pi$ and the frequency range is determined mainly based on the device specifications and by the experiment. Typically the order of magnitude of frequency includes several decades from mHz to 10 MHz. Performing EIS measurements at lower frequencies are considerably time consuming, while indispensable for accurate interpretation of the system behaviour. The system performance is measured and recorded at different steady state point by changing the intensity of imposed light. Then the recorded frequency dependent impedance data ($Z(\omega)$) is related to an electrical circuit model usually defined as an

equivalent circuit. The equivalent circuit model relates the impedance parameters to the physical properties of solar cell and make it possible to track changes in the solar cell properties at different conditions [67]. The combination of EIS measurements and equivalent circuit model interpretation has shed light into the unknown physical properties of cells which cannot be acquired directly.

When the EIS characterization technique is applied, typically the cell potential is used as a reference to report the data and to compare the performance of different cells. However, it must be noted that material preparation methods and electrolyte composition could potentially shift the conduction band edge of a wide band gap semiconductor with respect to its Fermi level. Therefore, the cell potential is not always an accurate reference. Indeed, it is more accurate to report the measured data with respect to the relative position of the Fermi level and the conduction band to ensure that the comparison is made under the equivalent number of charge carriers [58].

Besides the characterization of a solar cell, EIS measurements have been used by several researchers to monitor the trend of photophysical properties of the cell upon applying a different modification in order to find the best solar cell performance.

2.10.1 Transport and recombination data obtained from EIS

In conventional DSSCs and SSSCs, the sensitizer deposited into the semiconductor material (TiO_2 or SnO_2) absorbs light and the wide band gap semiconductor material acts as the electron transporting material (ETM). To

complete the circuit, a hole transporting material (HTM) is required which could be liquid redox electrolyte or solid hole transporting material such as Spiro-OmeTAD deposited into the semiconductor/sensitizer film [58, 68]

Although several electronic processes happen in DSSC, EIS measurements and data analysis is predominantly focused on the electronic processes in the electron transporting material e.g. TiO₂ film. This fact is justified by researchers [42] that bias hardly affects the redox electrolyte due to the very high carrier concentration of an electrolyte. Moreover drift transport limitations in an electrical field is also diminished by the large conductivity of electrolyte offered by the salt molecules in the liquid phase [58, 62]. However, the electron concentration in ETM is very sensitive to potential displacement and can change by several orders of magnitude.

2.10.2 Recombination resistance

When a solar cell operates under illumination, photocurrent generation is always in competition with a loss mechanism called recombination that produces a current in the opposite direction [58, 67]. In order to fabricate a high performance solar cell the recombination must be controlled. The recombination process in the device has a different pathway and it is reported that the predominant loss mechanism in DSSC is the recombination of the electron injected into the TiO₂ film with the hole in the hole transporting material [42]. It should be noted that both energetics and kinetics determine the recombination rate and recombination resistance. The quantity that describes the recombination in EIS measurement is recombination resistance, R_{ct} (charge transfer resistance). A distribution of

recombination (r_{ct}) is more commonly used and related to the overall resistance by $R_{ct} = r_{ct}/Ad$ where d and A are the thickness and projected area of semiconductor film respectively [58].

2.10.3 Transport resistance

When an incident photon is absorbed electron is injected into the wide band gap metal oxide film, photogenerated carriers must travel a distance inside the film to reach the contact in order to be collected. At the same time, the carrier extraction into the external circuit is always in competition with the recombination process. Thus, efficient carrier transport properties of the electron/hole transporting media are of great importance. The transport resistance, R_t is the quantity that describes the transport properties of the film in EIS measurements.

It should be emphasized that the both electron and hole transporting media contribute to the overall transport resistance of the cell. Similar to recombination, reporting of distributed parameters of transport resistance (r_t) is more common and is related to the total resistance by $r_t = R_t A/d$. It is believed that a nanotube conformation of semiconductor film improves the electron transporting features and results in the better DSSC device. Besides the transport and recombination resistances, other effective parameters such as diffusion length and lifetime can be also measured based on the data acquired from EIS.

Electron effective diffusion length (L_n) shows the average distance charge carrier diffuse before being recombined and is determined by recombination and transport resistances obtained from EIS spectra as [69]:

$$L_n = d \sqrt{\frac{R_{ct}}{R_t}} \quad \text{Equation 15}$$

A diffusion length larger than the film thickness indicates good collection efficiency. Electron lifetime (τ_n) is a widespread quantity used to determine the recombination dynamics in the solar cell and can be measured by several techniques. It is shown that from EIS data, the product of the chemical capacitance and recombination resistance results in τ_n .

$$\tau_n = R_{ct} C_\mu \quad \text{Equation 16}$$

Good solar cell necessitate that the carrier collection time should be shorter than the lifetime, or recombination time [69].

2.11 DSSCs fabricated from TiO₂ nanotubes

As discussed in section 1.4.2, different generations of TiO₂ NTs have different properties such as length, pore diameter, and morphological structure that affects the properties of the DSSCs made from them. The first DSSC was fabricated by 500 nm to 2.5 μ m TiO₂ NTs from the first generation of NTs sensitized by N3 dye. The efficiency of the cell was reported to be 0.036% [70]. However, by advances in the fabrication of high aspect ratio NTs by using organic solvents like Glycerol and Ethylene Glycol, the efficiency of these solar cells drastically increased to 2 to 3% under AM 1.5 illumination [11, 71, 72]. In a few cases higher efficiencies of up to 5% have also been reported [11, 73] . It should be noted that most of the fabricated and reported solar cells have been back side illuminated cells.

It was shown by Frank et al that compared to DSSCs with nanoparticles, the NT-DSSCs show similar transport properties, but 10 times slower recombination constants [3]. Later, Jennings et al demonstrated that 20 μm tubes result in the highest IPCE and the diffusion length of the electrons in that cell is of the order 100 μm which is much longer than the tube length [71]. It is also revealed that 15 to 20 μm tubes result in the highest efficiencies [2].

To further improve the efficiency and properties of the DSSCs, different modifications has been proposed such as synthesis of new dyes, synthesis of NTs with advanced geometries like "bamboo-type" geometry [74], modification of tube tops and increasing the surface area of TiO_2 NTs by methods like particle infiltration and TiCl_4 treatment [16, 73, 75]. TiCl_4 treatment is reported to increase the efficiency to about 7% [75].

The tube tops of those NTs synthesized from EG based electrolytes, usually is covered by a "nanograss structure" due to the strong effect of chemical etching. This layer is shown to have probable detrimental effect on directional flow of electrons [72, 76, 77]. (See Section 4.1)

To conclude, further modification of NTs from the common ethylene glycole solvent to prepare NTs with better properties in DSSCs like charge collection, electron transfer, and recombination resistant would be of interest and have been a motivation of the present research

Chapter 3

Experimental

3.1 Anodization materials and set-up

Electrochemical synthesis of TiO₂ nanotubes possesses advantages like very well alignment of the tubes and high aspect ratio over other synthesis methods. In this research both types of nanotubes (single wall and double wall) are grown electrochemically through the anodization of titanium foils (99.6% purity, Goodfellow) with a thickness of 0.1 mm. Before the anodization step, the foils were cut in to small pieces and cleaned by ultrasonication in acetone, ethanol and de-ionized (DI) water in sequence for about 10 minutes each and dried in a stream of nitrogen gas. The anodization processes were carried out by *Voltcraft VLP 2403 pro* power supply in the common two electrode configuration. For measuring and recording the current during the anodization, a *Keithley 236* source meter was used.

Different set-ups have been used by different investigators for growing nanotubes, such as in beaker or in closed setup made of polymers like polytetrafluoroethylene (PTFE), in which a window is available to expose the Ti foil to the electrolyte [36, 78]. The main trouble with the first method is that it is hard to mask the parts of the foil which should not be anodized. In the second method the volume of container and the distance between the foil and the counter electrode is invariable and besides, as the container is a closed vessel the gas

evolved during the anodization, sometimes does not find a way out and causes cracks in the TiO₂ NT layer and removal from the foil. To avoid the above problems, all anodization processes in this thesis were performed in a two electrode configuration and the tubes were grown vertically in as a set-up shown in Figure 3-1[5].

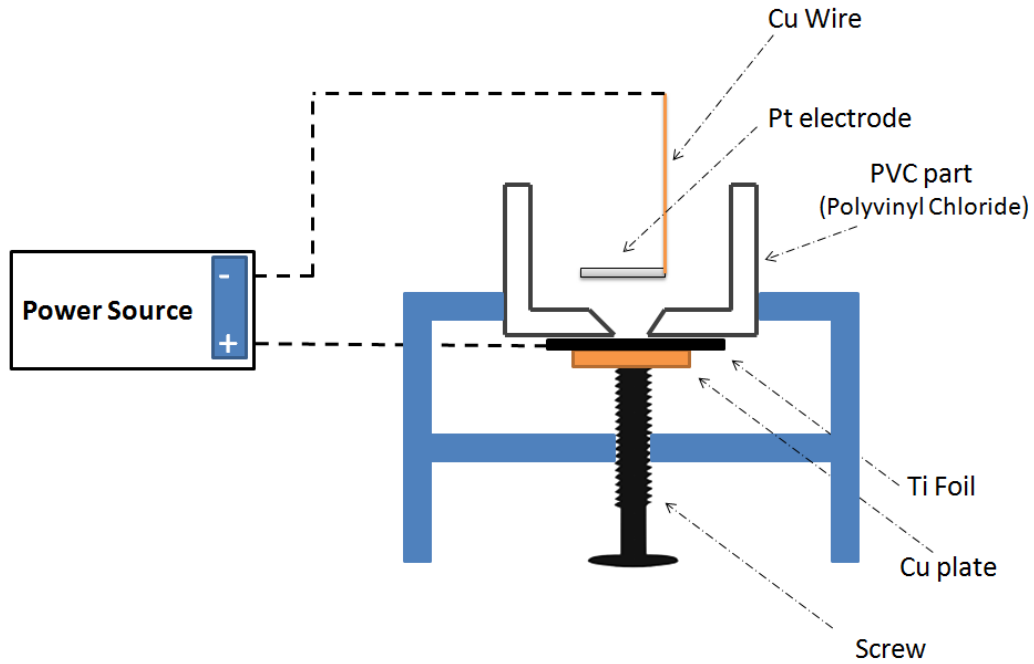


Figure 3-1 Experimental set-up for anodization[5]

The size of the Ti cut foils were $1.5 \times 2.5 \text{ cm}^2$, the counter electrode in all anodization processes was $1 \times 1 \text{ cm}^2$ platinum gauze, and the distance between electrodes were 1.5 cm in all experiments. 50 ml of fresh electrolyte were prepared and used for each sample. The typical electrolyte for double wall TiO₂ nanotubes was *ethylene glycol* (EG, Sigma–Aldrich, containing less than 0.2 wt% H₂O) containing 1 M de-ionized H₂O and 0.1 M NH₄F (Sigma–Aldrich, 98%). The electrolytes were prepared by adding EG to the pre-prepared (NH₄F+H₂O)

followed by stirring the solution for a few hours. The best electrolyte for single wall TiO₂ nanotubes in all cases -unless otherwise indicated- was 1:1 EG and dimethyl sulfoxide (DMSO, Sigma–Aldrich, containing less than 0.2 wt% H₂O) by volume ratio, containing 1.5 M de-ionized water and 0.1 M NH₄F. To prepare it EG was first added to the pre-prepared (NH₄F+H₂O) solution, then DMSO was added to it gradually while it was stirring followed by stirring the solution for a few hours. The electrolyte for the samples anodized in pure dimethyl sulfoxide was DMSO with 2 wt% HF (Sigma-Aldrich, 40%).

The anodization of Ti foils in EG and EG:DMSO baths generally results in nanotube layers with nanograss on top of the it. As the nanograss layer may affect the properties of the tubes especially in applications such as solar cells, a double anodization method was chosen to synthesize nanotubes with clean top without nanograss [77]. The details of the method is explained in *section 4.1*.

In all cases the first anodization was performed at 60V for 60 min in the EG/H₂O/NH₄F electrolyte at room temperature, and then the layer was removed by strong ultrasonication. Subsequently the double wall nanotubes were grown in the same electrolyte for 60 min at room temperature. The single walls were anodized at 60 V for 16 min while the foil is heated up to 60 °C. The foils were heated using a heating water bath connected to the set-up (Figure 3-1). The bath heated up the foils by means of hot water circulated copper tubes placed between Ti foil and Cu plate in figure 3-1. After the anodization, the nanotube array was kept at the same temperature in the electrolyte for 50 minutes (*post anodization treatment*). After the anodization, samples were cleaned with ethanol and DI

water thoroughly and dried with a gentle stream of nitrogen gas. Under these conditions, double wall and single wall TiO₂ nanotube layers of a thickness of about 15 μm were obtained [7].

3.2 Heat treatment of nanotubes

To transform the amorphous nanotubes to anatase, they were heat treated on a programmable hot plate first to 200°C to reduce the cracks, kept for 15 minutes, and then to 500 °C and kept for 1h. The surface temperature of the hotplate was also monitored by an infrared temperature sensor.

Wherever a precise heating / cooling rate was needed, the heat treatments of the nanotubes were carried out in air using a *Rapid Thermal Annealer* (Jipelec JetFirst 100) at 500 °C with the mentioned heating/cooling. The samples were annealed at 500 °C for 1 h.

3.3 Characterization techniques

Several characterization techniques were employed in this investigation to determine the properties of the synthesized SW nanotubes and compare them with their DW counterpart. It should be mentioned that each experiment and measurement in this study- unless otherwise mentioned - was repeated at least three times.

3.3.1 SEM and TEM, and XRD of nanotubes

The morphology of nanotube samples was studied using *Hitachi S4800* and *Zeiss FE SUPRA40* field-emission scanning electron microscopes. SEM was employed

to check the single or double wall nature of nanotubes. Besides, different parameters of nanotubes such as length, wall thickness and diameter of the nanotubes were directly found from SEM inspections. In addition, EDAX Genesis, fitted to SEM chamber was used for local chemical analysis.

XRD patterns were collected using a *Bruker D8 Advanced Thin Film XRD* with a fixed incidence angle of 3° and using CuK α radiation ($\lambda = 1.54056\text{\AA}$).

Non-ambient XRD investigations were also performed using X-ray powder diffraction (*PANalytical, X'Pert Pro MPD*) equipped with a high temperature chamber (*ANTON PAAR, HTK 1200*) to study the crystal phase evolution of the nanotubes. The heating rate was set to $6^\circ\text{C}/\text{min}$.

Further morphological and structural characterization of the TiO $_2$ nanostructures was carried out with a TEM (*Philips CM30 TEM/STEM*).

3.4 Conductivity Measurements of the as-formed and annealed nanotubes

To measure the solid-state conductivity, a 300 nm thick Au dot through a 2.1 mm wide opening in a shadow mask was deposited on the surface of the tubes by evaporation. Resistivity values were obtained from I-V curves [52]. The conductivity 2-point measurement setup consisted of a micromanipulator and Agilent 4156C precision semiconductor parameter analyzer, where the reference electrode is connected to the metallic substrate, and the working electrode to the aluminum contact. The resistance values were extracted from IV-slopes obtained by cycling the potential from -2 to +2 V, with a sweep-rate of 0.01 V/s and

measuring the currents. All measurements were done by a teammate at LKO institute in University of Erlangen-Nuremberg in Germany.

3.5 DSC and TGA of the prepared nanotubes

Thermogravimetry combined with a mass spectrometer (TGA-MS) was done using on a *Netzsch STA 409 CD* instrument equipped with a *Skimmer QMS 422* mass spectrometer (MS/EI). The annealing was done in air at a rate of 20 °C/min to 600 °C, holding for 60 min and then ramping back to RT with 20 °C/min.

3.6 FTIR experiments

All FTIR experiments were performed on a Shimadzu, FTIR 8400. In all runs, a sum of 64 interferograms were collected and co-added into one spectrum and the spectral resolution was 4 cm⁻¹.

Two KBr disc windows were used for FTIR of the electrolytes. A very thin layer of electrolyte (about 10 µl) was dropped each time in between the two windows and screwed. FTIR radiation passed through the set-up (KBr windows with a thin-layer solution in between). As a result, dissolved substances in the electrolyte solution could be identified.

The FTIR spectrums of the used electrolytes were collected using the fresh electrolyte as the background. Therefore, the resulting spectrum for the electrolytes would be $\Delta S = \frac{(S_{el} - BG)}{BG}$ where S_{el} is the used electrolyte's spectrum and BG is the background's (fresh electrolyte) spectrum. Hence the downward bands represent the produced and upward ones stand for the consumed species.

In case of nanotubes, the reflectance mode of the FTIR was implemented. The IR radiation hits and is reflected from the electrode surface. Therefore the adsorbed species on the electrode surface can be detected. For nanotubes, a gold plated glass mirror was used to record the background spectrum.

3.7 Preparation of Dye Sensitized Solar Cells (DSSCs) and Backside illumination measurements

After the heat treatment of nanotubes (*Section 3.2*) for use in dye sensitized solar cells (DSSCs), the samples were immersed in a 300 μM Ru-based dye (cis-bis (isothiocyanato) bis (2,2-bipyridyl 4,4-dicarboxylato) ruthenium(II) bis-tetrabutylammonium (D-719, Eversolar, Taiwan) solution in a mixture of acetonitrile and tert-butyl alcohol (volume ratio: 1:1) for 3 days at 40 °C.

Thereafter, the samples were rinsed with acetonitrile to remove non-chemisorbed dye molecules and dried with gentle stream of nitrogen gas.

To prepare the counter electrode, a drop of H_2PtCl_6 solution (2 mg Pt in 1 ml ethanol) was spread on the cleaned FTO substrate (TCO22-15, Solaronix) and then heat treated at 400°C for 15 minutes.

In the next step, the sensitized nanotubes were sandwiched together with the Pt coated FTO glass (as counter electrode), using a polymer spacer (Surlyn, Dupont) in between. An electrolyte (Iodolyte R50, Solaronix) was introduced into the space between the sandwiched cells through a hole made in the TCO (Figure 3-2a).

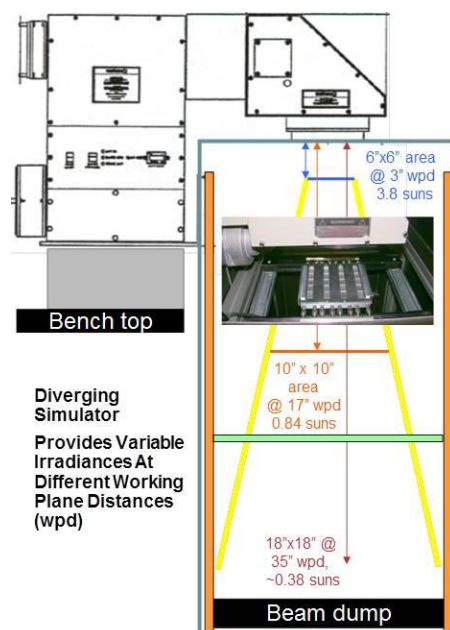
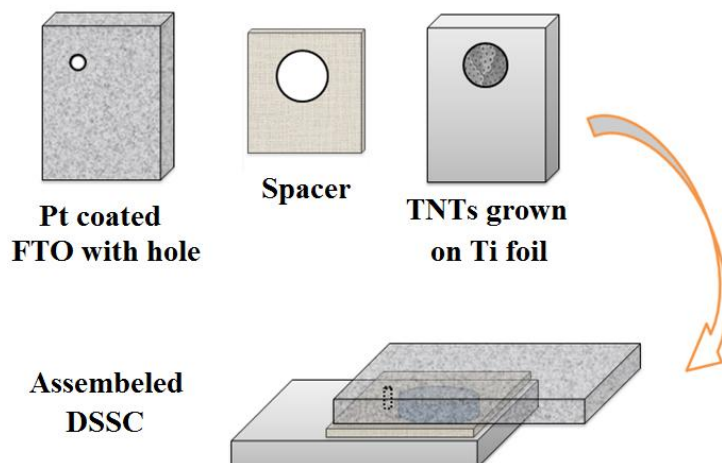


Figure 3-2 a) Assembling steps of a DSSC with TiO_2 NTs on foil for backside illumination, and b) a schematic of Newport solar diverging simulator for j-V measurements [79].

To measure the effective amount of the adsorbed dye to the nanotubes, dye desorption measurements of sensitized nanotubes were carried out by immersing the samples in 5 ml of 10 mM KOH for 1 day. Then the concentration of the desorbed dye from the tubes was measured by a Lambda XLS UV/VIS spectrophotometer (PerkinElmer) at 520 nm.

3.8 Nanotube decoration (TiCl₄ treatment) of nanotubes

For fabrication of DSSCs, the nanotubes were also decorated with TiO₂ particles through the following method. 0.2 M aqueous solutions of TiCl₄ was prepared under ice-cooled conditions. Then the heat treated TiO₂ NTs were treated in a closed vessel at 70 °C for 30 minutes. Afterwards, the samples were washed with DI water and rinsed with ethanol to remove any excess TiCl₄ and finally dried in a N₂ stream. After the treatment, TiO₂ nanotube samples were annealed again at 450 °C for 30 min to crystallize the attached nanoparticles.

3.9 Preparation of Semiconductor (CdSe) Sensitized Solar Cells (SSSCs) and backside illumination measurements

As a part of this study, semiconductor sensitized solar cells were also fabricated to study the probable difference between double wall and single wall nanotubes in charge transport and injection in SSSCs.

To do sensitization, CdSe was deposited through several cycles of *Successive Ionic-Layer Adsorption and Reaction* (SILAR) method [80, 81] One deposition cycle consists of the following 4 main steps, done in a glove box:

- 1) Immersion of the nanotube layer in a solution of cadmium nitrate tetrahydrate (0.02 M) (Cd(NO₃)₂·4H₂O , (Fluka, >99.0%) in ethanol for 1 min to deposit Cd²⁺
- 2) Rinsing in ethanol for 1 min to remove excess Cd²⁺
- 3) Immersion of the nanotube layer in a solution containing 0.03M Se²⁻. The solution is prepared by mixing selenium dioxide (SeO₂,

Sigma-Aldrich, 99.9%), sodium borohydride (NaBH_4 , Sigma Aldrich) and ethanol following the literature [82].

- 4) Rinsing in ethanol for 1 min to remove the excess ions.

All samples were dried after the second and fourth steps in an argon atmosphere

This procedure was repeated several times in order to achieve the desired CdSe deposition.

3.10 Characteristic measurements of the backside illuminated DSSCs and SSSCs

The current-voltage characteristics of the assembled cells were measured under simulated AM 1.5 (100 mW/cm^2) illumination provided by a solar simulator (300 W Xe with optical filter, Solarlight), applying an external bias to the cell and measuring the generated photocurrent with a Keithley model 2420 digital source meter. The light incident intensity on the cell was measured before each characterization by a calibrated Si photodiode.

To investigate the charge transfer and injection characteristics of the TiO_2 NTs, Intensity modulated photovoltage and photocurrent spectroscopy (IMVS and IMPS) measurements were performed. The experiments were done under modulated light (10 % modulation depth) from a high power green LED ($\lambda = 530 \text{ nm}$). The modulation frequency was controlled by a frequency response analyzer (FRA, Zahner) and the photocurrent or photovoltage of the cell was measured using an electrochemical interface (Zahner) and fed back into FRA for analysis.

The incident photon-to-current conversion efficiency (IPCE) of the DSSCs were measured by a DC method with a 300W Xenon Lamp (Oriental 6258) as source

of light and a monochromator with a resolution of 10 nm (Cornerstone 260 Oriel 74125) to select a single wavelength.

3.11 Electrochemical Impedance Spectroscopy (EIS) Measurements

An autolab potentiostat/galvanostat and the Nova 1.6 software package were used to perform the EIS measurements. To accomplish the experiment, the solar cell was illuminated under a red LED (centre wavelength $\lambda = 627$ nm) and biased by illumination induced V_{oc} . The highest light intensity was adjusted to be sufficient to produce an open circuit photovoltage approximately equal to the value obtained under AM 1.5 1 Sun illumination. The incident photon flux was approximately in the order of 10^{17} cm^{-2} S^{-1} and the frequency range was adjusted between 10^5 to 0.1 Hz with 15 mV rms voltage perturbation rate. Neutral density filters mounted in an automated filter wheel system (Newport) were used to achieve different illumination intensities and Nova 1.6 software controlled the wheel. The EIS data were fitted to an equivalent circuit, details of which are provided in *Section 6.1.3* using ZVIEW software provided by *Scribner Associates*.

Chapter 4

Synthesis of single wall TiO₂ nanotubes

This Chapter starts with the details of the synthesis method implemented in this study, continues with the characterization of the nanostructure of DW and SW nanotubes obtained from EG and pure DMSO based electrolytes respectively. Subsequently, after explaining the limitations and the problems with the DMSO-nanotubes, a new method to synthesize high aspect ratio SW-TiO₂ NTs from mixed organic (EG+DMSO) electrolytes will be presented. Finally a mechanism for the formation of double wall nanostructure in anodization of Ti in EG-based electrolytes is proposed.

4.1 Anodization method

An important point about the anodized TiO₂ nanotubes in all experiments is the morphology of the tube tops. The morphology varies depending on the anodization method and the growth sequence [77]. In the common method of growing nanotubes in EG containing fluorine ions, the tubes' tops are covered by a nanograss layer which is shown schematically with a high resolution SEM picture of a real sample in Figure 4-1. The process, by which this nanograss forms in a simple anodization method, is that first a compact oxide layer forms immediately after the start of the anodization process (Figure 4-1a). This compact layer breaks down under the strong electrical field forced by high voltage, and the tubes start growing underneath and the compact layer gets dissolved during the

anodization as shown in Figure 4-1b (*see also Section 2.1 for more details*). The concentration of fluorine ion is higher near the tube openings as the ions are consumed inside the tubes to form TiF_6^{2-} and also penetrate through the bottom of the tube towards the oxide/metal interface [2]. Thus the tube walls dissolve over time and get thinner. As top parts of the tubes are exposed to high fluoride levels, they collapse and a so called “nanograss” forms (Figure 4-1c). During heat treatment of the tubes, those weak parts bundle together.

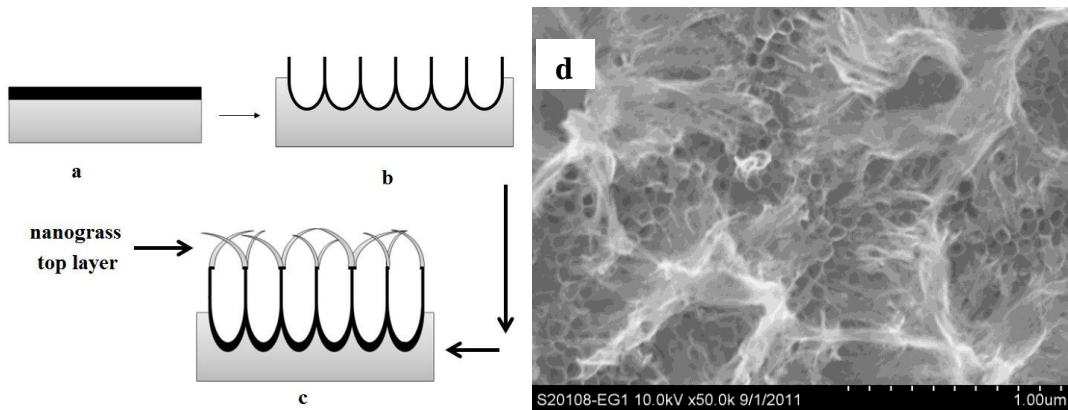


Figure 4-1 Schematic representation of the conventional nanotube anodization. a) formation of compact oxide layer immediately after the start, b) growth of tubes, c) formation of nanograss layer on top of the tubes as a result of chemical dissolution of tubes’ walls near the top, and d) SEM image of nanograss on top of the anodized layer.

It has been shown by some researchers that for applications like DSSCs, this kind of irregularity may be disadvantageous [72], hence some methods have been proposed to eliminate the nanograss from the top of the TiO_2 NT layer such as double anodization process [83, 84] and photoresist technique [77, 85].

To keep the surface condition the same and eliminate the probable effect of nanograss top layer, a double anodization method was chosen to prepare the

samples in all cases. This method is described schematically in Figure 4-2. As can be seen, the conventional nanotube layer (grown on the Ti foil) is removed by ultrasonication. The compact oxide layer beneath the tubes remains and will act as an initiation compact layer for the second step of the anodization (Figure 4-2d). During the second step, this layer will break and the tubes grow beneath (Figure 4-2e and f). Depending on the conditions of the anodization (time, temperature and the electrolyte's concentration), the thickness of the remaining "net shape" layer changes (Figure 4-2g, f).

Another important point about choosing the double anodization method is that, besides the elimination of nanograss from top of the tubes, the initiation layer prevents collapsing the nanotube tops in high temperature anodization (Figure 4-2g). Without such a benefit of the initiation layer it is almost impossible to grow nanotubes with a clean top surface at high temperatures such as 60 °C.

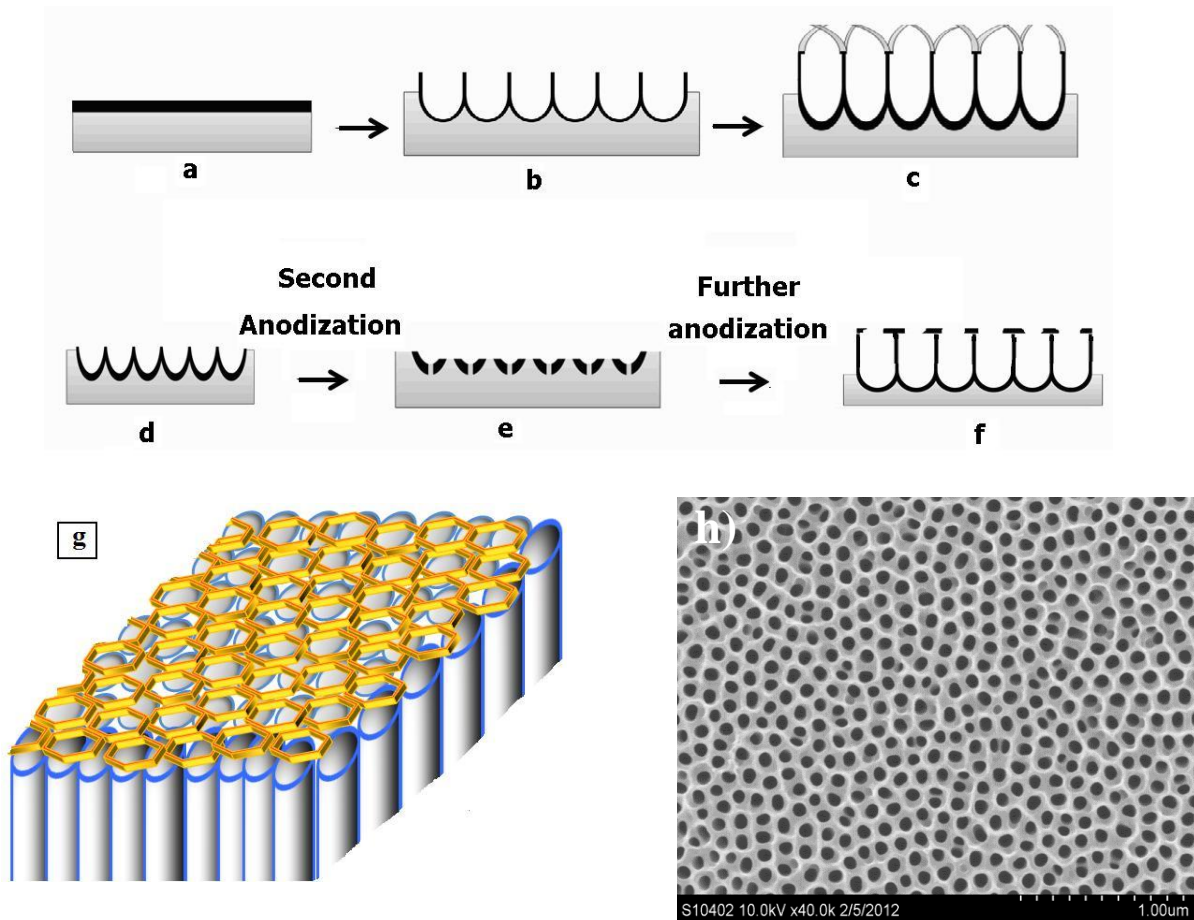


Figure 4-2 Schematic representation of double anodization method. The conventional tubes grown in the first stage (a-c) are removed from the surface by ultrasonication. d, e, f) second step of anodization. g) Schematic shape of the remaining top layer (golden) and the tubes underneath, and h) SEM top view image of a double anodized sample.

4.2 The double wall nanostructure of the TiO_2 NTs grown from EG based electrolytes

Synthesis of highly ordered self-organized TiO_2 nanotubes (TiO_2 NTs) from ethylene glycole (EG), the widest used solvent results in a double wall nanostructure[5, 6], a thin outside shell tube (OST) and an internal shell in the tube (IST) with varying thickness.

According to Sergiu *et al* [5], as stated in *Section 2.7*, the formation of the IST is mainly because of the migration and diffusion characteristics of cations and anions moving inward and outward through the oxide during the anodization process

Figure 4-3a shows the general nanostructure of double wall (DW) TiO₂ NTs schematically. As can be deduced from Figure 4-3b, the inner hollow space of the tube is not cylindrical, but an inverted pyramidal, so it has a V-like shape in the cross section in Figure 4-3a. The tubes' inner walls gets thicker as one moves from the top of the tubes towards the bottom.

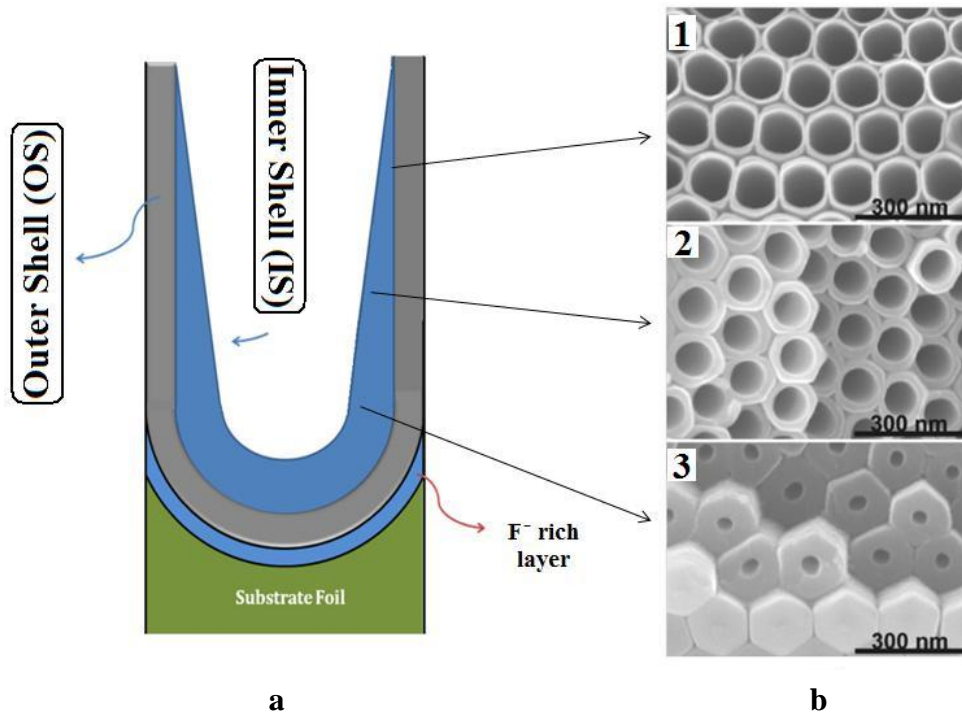


Figure 4-3 Schematic representation of double wall nanotubes, and b) SEM images of DW TiO₂ NTs from top, middle and the bottom of the layer (adopted from reference [86])

Enachi *et al* showed that increasing or decreasing the HF by 20% in EG/HF electrolytes, results in an almost 30% decrease or increase in the inner diameter of the tubes respectively [35]. It is discussed in *Section 2-1* and shown in Figure 2-1 that in the steady state growth part of anodization (the last and longest part of tube growth), the rate of chemical dissolution of the tubes from the top is equal to the rate of the electrochemical anodization of the foils at the bottom of nanotubes. Under such a condition the thickness of the tubes' walls near top becomes thinner because these are more prone to chemical etching by fluorine ion during the anodization and formation of TiF_6^{-2} (*Equation 6* in *Chapter 2*. See also *Section 4.1*) [35, 87]. The concentration of fluorine ion decreases from top (near the bulk electrolyte) to the bottom of tubes as it is consumed during the tube formation process at the bottom. Another point, as will be shown in *the next Chapter* is that the internal shells of DW tubes are rich in impurities such as carbon, making these more vulnerable to dissolution by fluorine ions than the external shell [87].

It is noteworthy that the as-grown double wall shape of the TiO_2 NTs formed in EG based electrolytes can only be distinguished by means of TEM (Figure 4-4a). In SEM images of the as-grown tubes (Figure 4-4b) the shells appear smooth and attached together as the double wall shape is not clearly discernible. However, after heat treatment the internal shell transforms to a very finely porous layer that can be seen under the SEM, as shown in Figure 4-4c.

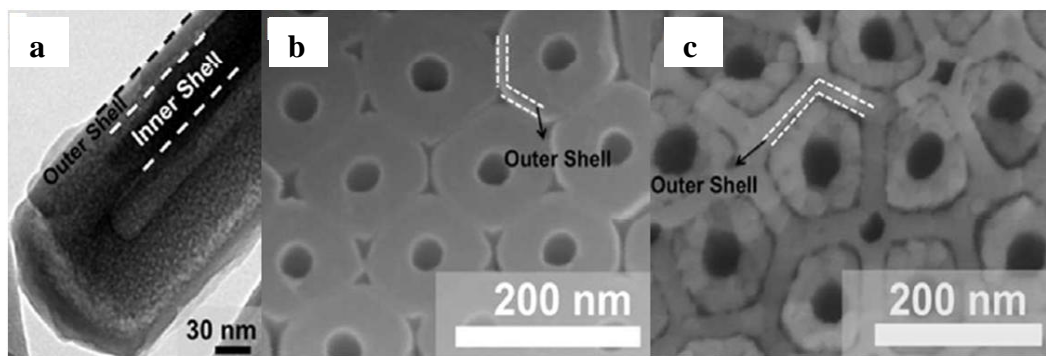


Figure 4-4 a,b) TEM and SEM images of an as-grown double wall nanotube near the bottom of the tube, c) SEM image of an annealed sample at 450 °C, adopted from reference [87].

The internal layer in DW tubes was predicted by Albu *et al* to have negative effects on the properties of the TiO₂ NT layer for many applications mainly because of the contamination uptake of this shell [5] however no investigation had been published before the current author’s work [7, 87] to study the probable effect of this layer on the tubes’ characteristics. To tackle the issue the main idea was the elimination of the internal layer to form called “single wall” TiO₂ nanotubes. It should first be determined that whether the formation of the double wall nanostructure is an inborn phenomenon to the EG electrolyte or if it is because of the anodization conditions such as temperature and time.

4.3 Effect of anodization temperature on the nanostructure of DW-TiO₂ NTs

It is shown by several researchers that increasing the anodization temperature boosts the anodization current density [18, 35, 36] and hence the etching effect of the fluorine ions. Therefore, the inner shell will dissolve more rapidly. In the present case, the effect of anodization temperature on the nanostructure and the

current density of the anodization are shown detail in Figure 4-5. As can be seen in Figure 4-5b the current density increases considerably with increasing temperature. Figure 4-5a shows the nanostructure of tubes at the same position near the bottom of the tube layer for three different temperatures. As can be distinguished, at higher temperatures the internal diameters of the tubes are larger because of the stronger dissolution ability of the fluorine ions at higher temperatures. The basic question here is whether by just increasing the temperature one will be able to eliminate the internal shell or not.

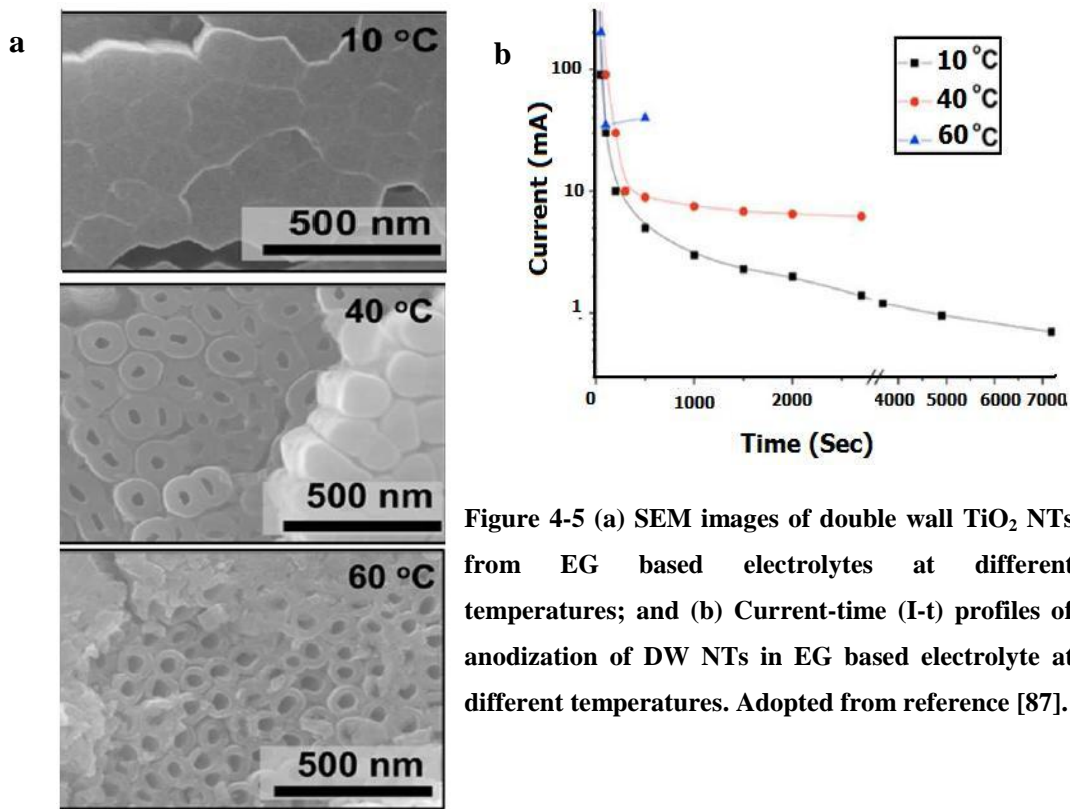


Figure 4-5 (a) SEM images of double wall TiO₂ NTs from EG based electrolytes at different temperatures; and (b) Current-time (I-t) profiles of anodization of DW NTs in EG based electrolyte at different temperatures. Adopted from reference [87].

The results of the present work show that although the wall thickness of the tubes is reduced at higher temperatures, the inner wall cannot be eliminated completely. Besides, it is also not possible to get long enough and good quality

nanotubes at high anodization temperatures in EG because of the high chemical etching power of the electrolyte. Anodization at high temperatures in EG is detrimental especially to the surface of the formed TiO₂ NT layer. Thus elimination of the inside shell is not possible by heating alone. The next step then would be to investigate the influence of changing the medium of the tube growth in anodization.

4.4 The structure of TiO₂ NTs grown in DMSO based electrolytes containing fluorine ions

Ethylene glycol is a protic solvent that is able to donate a hydrogen bond, however DMSO is a strong protophilic solvent [27]. It captures radicals at least 4 times faster than EG [88]. Therefore, based on this reason and the probable electro-oxidation of EG on Ti metal substrates (*see Section 2.2*) nanotubes grown in DMSO was studied in detail. The study shows that the tubes anodized in DMSO based electrolytes, lack the common internal shell to double wall TiO₂ NTs from EG based electrolytes regardless of the temperature used. The high resolution SEM pictures are shown in Figure 4-7a and b.

Figure 4-6a and b are thickness- time curves of the tubes grown in EG and DMSO respectively. Although the tubes from DMSO are single wall, it is evident that the growth rate of so called “single wall” tubes from DMSO is too slow. One may suppose that the main reason for the elimination of the inner shell in DMSO is its slow ion flux as indicated by low current density (Figure4-6c), so that there is enough time at room temperature for the inner shell to get dissolved by the fluorine containing electrolyte. Nonetheless, the results show that even at a high

temperature (60 °C), in which the current density of anodization is similar to EG at room temperature, no inner shell forms in the tubes from DMSO (Figure4-6c) [87]. It should also be noted that in anodization of Ti in EG, it is known that after a few seconds at room temperature and after a few minutes at higher temperatures the growth rate becomes almost constant (Figure 4-6c). Therefore, the linearly change of the thickness with time in Figure 4-6a (general linearity on a 60 minute range) is not un-realistic.

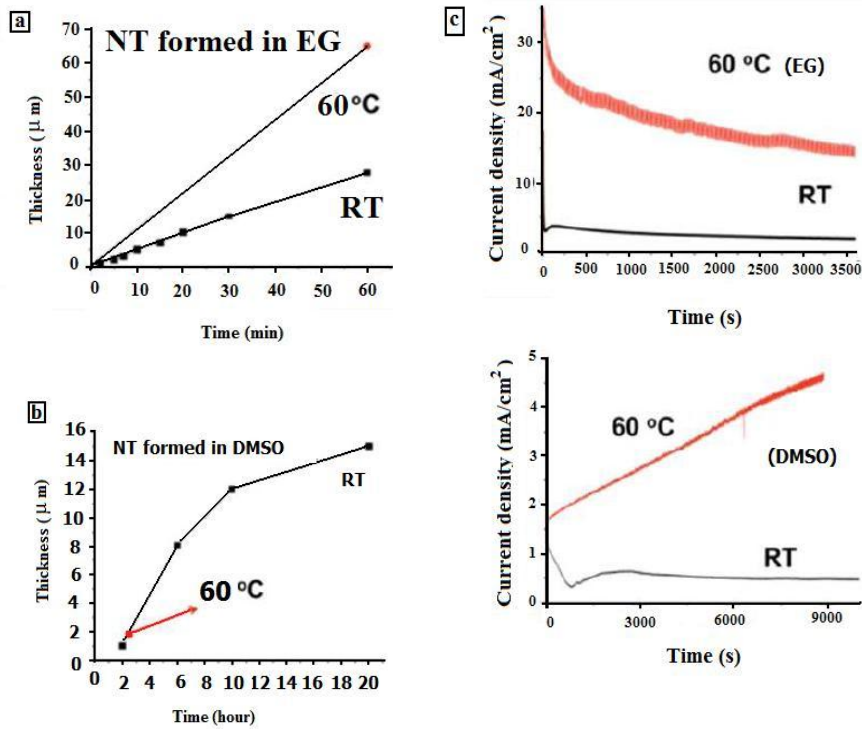


Figure 4-6 (a, b) TiO₂ NT growth rate in (EG+0.1M NH₄F+1M H₂O) and DMSO (containing 2 wt% HF) electrolytes respectively; (c) current changes with time of the anodization for tubes grown in EG (top) and DMSO (bottom) at 60 °C and room temperature; adopted from reference [87].

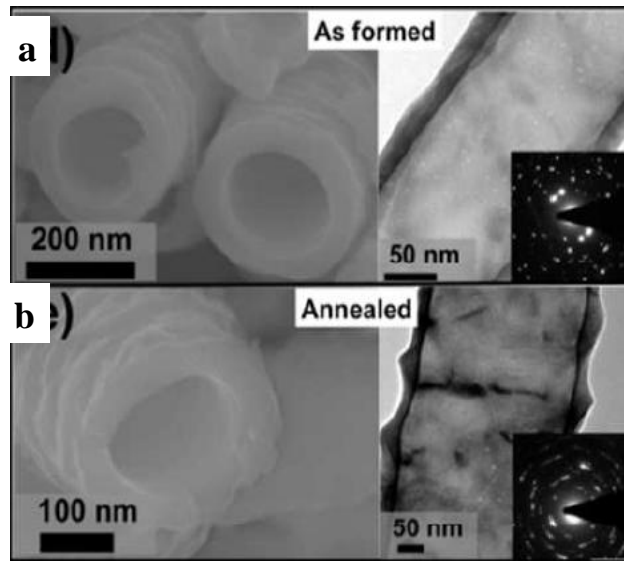


Figure 4-7 Nanotubes grown in DMSO + 2wt% HF in the a)as formed condition and b) after annealing at 450 °C, adopted from [81].

Therefore the formation of “single wall” tubes in DMSO is very likely to be related to the inherent characteristics of DMSO compared to EG, such as its ability to capture radicals and the stability of products of its electro-oxidation during the anodization at high voltages. In *Section 4.9* a mechanism based on hole formation and capture phenomena at high voltages will be proposed to justify the formation of DW nanotubes.

4.5 Problems with single walls grown in pure DMSO based electrolytes

As stated in the previous section, unlike the tubes from EG, those from DMSO are single wall, however because of the following reasons they are not suitable for deployment in photovoltaic devices like solar cells.

4.5.1. Weak nanotubes with extremely slow growth rate

The first point about the single wall tubes grown in DMSO is that they are not robust and the tube- to-foil, as well as the tube-to-tube adhesion, is very weak. The second practical problem with tubes from DMSO is that the kinetics of the growth is extremely slow such that growing a 10 μm thick layer in a one step anodization at 60 V take 3 days thus the tubes are neither long enough, nor easy to fabricate. The thickness-time plots of tubes grown in 1-step in DMSO based electrolysis shown in Figure 4-6b and Figure 4-8 (red point).

To solve the slow growth rate problem of DMSO, some researchers proposed a two-step method [27]. The first step is a short time anodization of Ti foil (20 minutes) in an electrolyte containing a low HF concentration (0.5%), and then continuing the process in the more common electrolyte with 2% HF. In this method, the growth rate is much faster as can be observed in Figure 4-8. However, compared to EG based electrolytes it is still much longer as it needs more than 10 hours to grow a roughly 15 μm thick TiO_2 NT layer (depending on the ambient changes like temperature variation during the whole process), while it takes about 1 hour in EG electrolyte.

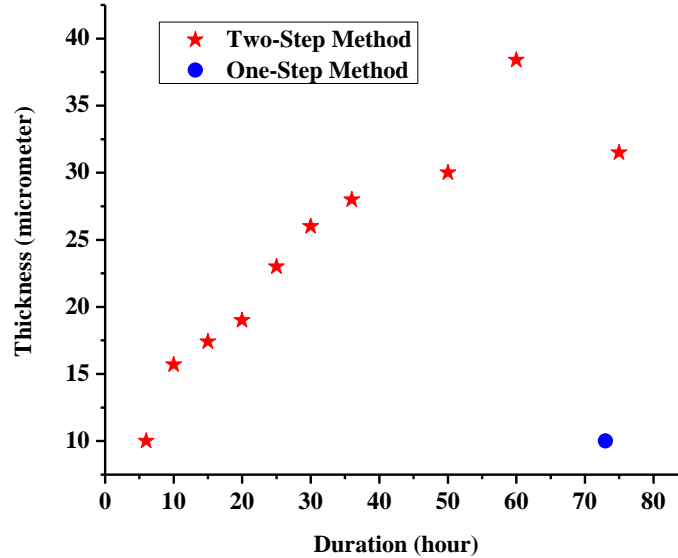


Figure 4-8 The growth rate of nanotubes in pure DMSO based electrolytes (DMSO + 2% HF) by two different methods at 60 V and room temperature. (Data points are the average of at least 5 measurements that were highly repeatable such that the error bars are too small to display).

4.5.2. Undesired geometry of the nanotubes from DMSO electrolyte

Besides the two practical problems mentioned in *Section 4.5.1*, there are also a few problems with the nano-geometry of the tubes grown in DMSO that means these are inappropriate to be utilized in solar cell applications.

A selected series of SEM images of nanotube arrays grown in pure DMSO are shown in Figures 4-9 to 4-12. Figure 4-9 shows different views of nanotubes grown in a long one-step procedure. The length of the tubes reaches only about 10 microns after 72 hours (Figure 4-9 e). Figure 4-10 is a top view of a sample grown in a two-step procedure in 6 hours. In Figure 4-11 nano-images of a similar sample grown for 15 hours is shown and Figure 4-12 demonstrates the SEM images of a 50 hour anodized sample after heat treatment.

As can be noticed from the SEM top views, with long anodization times the tubes are not real tubes near the top of the sample having a very thin ‘spring-like’ nature (Figure 4-9a, b, c, and Figure 4-12c). This structure cannot bear the heat treatment required for crystallization and would be very fragile and easily broken after annealing (Figure 4-12c). Furthermore, from SEM cross sections it can be seen that at middle height the tubes are solid (Figure 4-11d) and loosely brought together in a “mesoporous matrix” (Figure 4-9e, Figure 4-11c, d, and Figure 4-12a,d), something that was previously reported by other researchers as well [6]. In general, the tubes’ shape is not uniform as their morphology on top is completely different than their bottom especially when the anodization time is long (Figure 4-9e, and Figure 4-11 b).

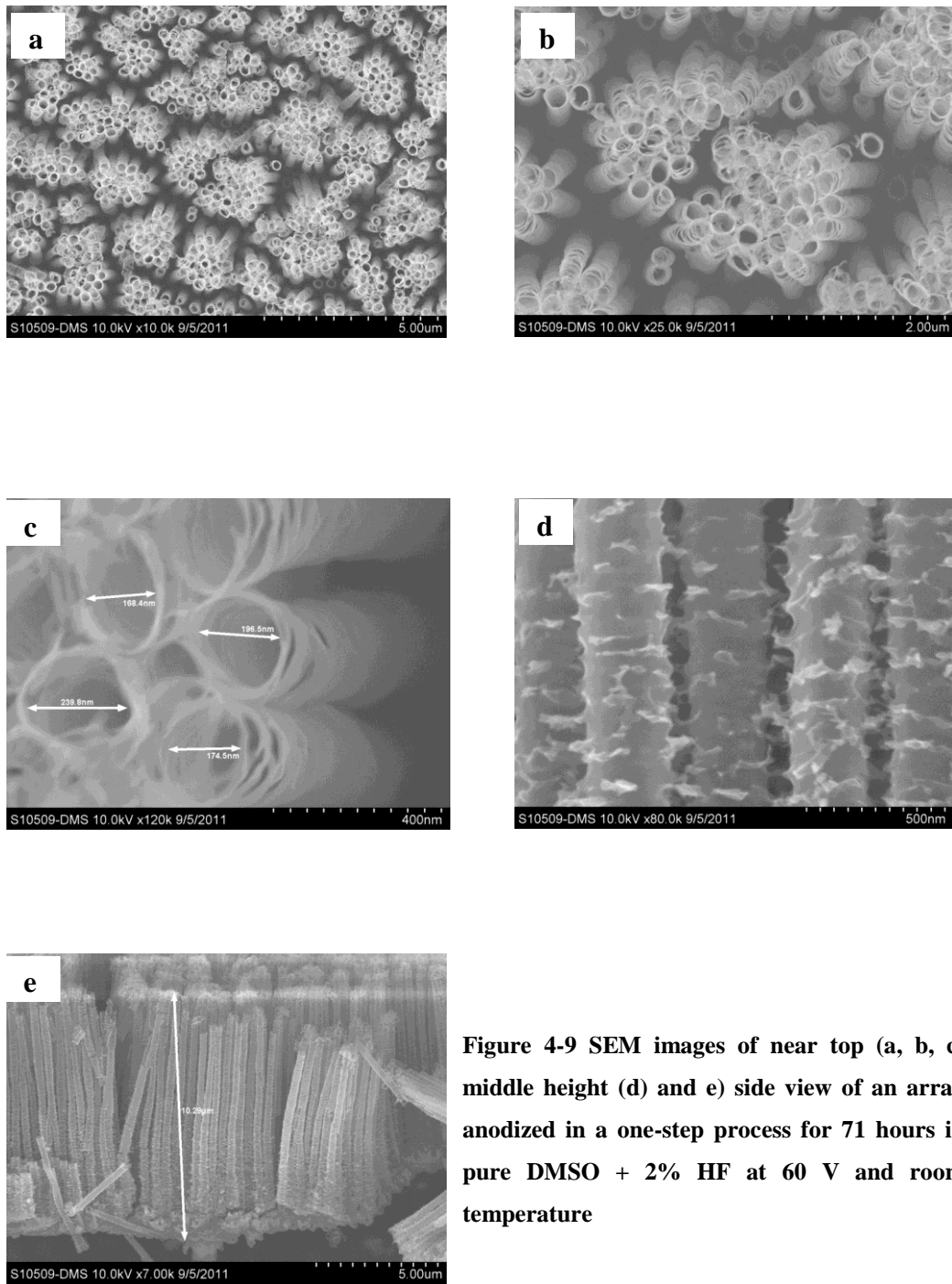


Figure 4-9 SEM images of near top (a, b, c) middle height (d) and e) side view of an array anodized in a one-step process for 71 hours in pure DMSO + 2% HF at 60 V and room temperature

As mentioned before, some researchers proposed a two-step anodization method to shorten the anodization time and increase the tubes' length (Figure 4-8). However, in the two-step method, although the anodization time is shorter, in

most cases the tubes are clogged on top which can be either from an initiation layer which is not etched yet or from solution precipitates [25] (Figure 4-10, and Figure 4-11a). According to Grimes *et al* for etching times shorter than 40 hours precipitates from the solution clog the tube openings, however at longer times, because the electrolyte becomes more acidic (according to *Equation 2* and *Equation 3, Chapter 2*), the clogging layer easily gets dissolved [25]. Therefore it is practically hard to manage for instance, to grow an open-top layer which is 15 to 20 μm thick.

The other problem about these tubes is their weak tube-to-tube adhesion which makes them fall down during annealing (Figure 4-12 a, b). So there will be a lot of cracks grown and extended in different directions in the layer.

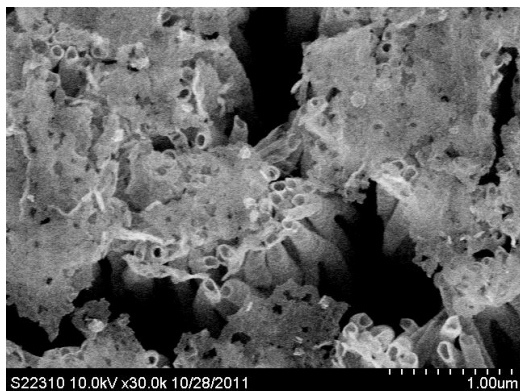


Figure 4-10 SEM image of top of a sample anodized in a two-step process for 6 hours in pure DMSO + 2% HF at 60 V and room temperature

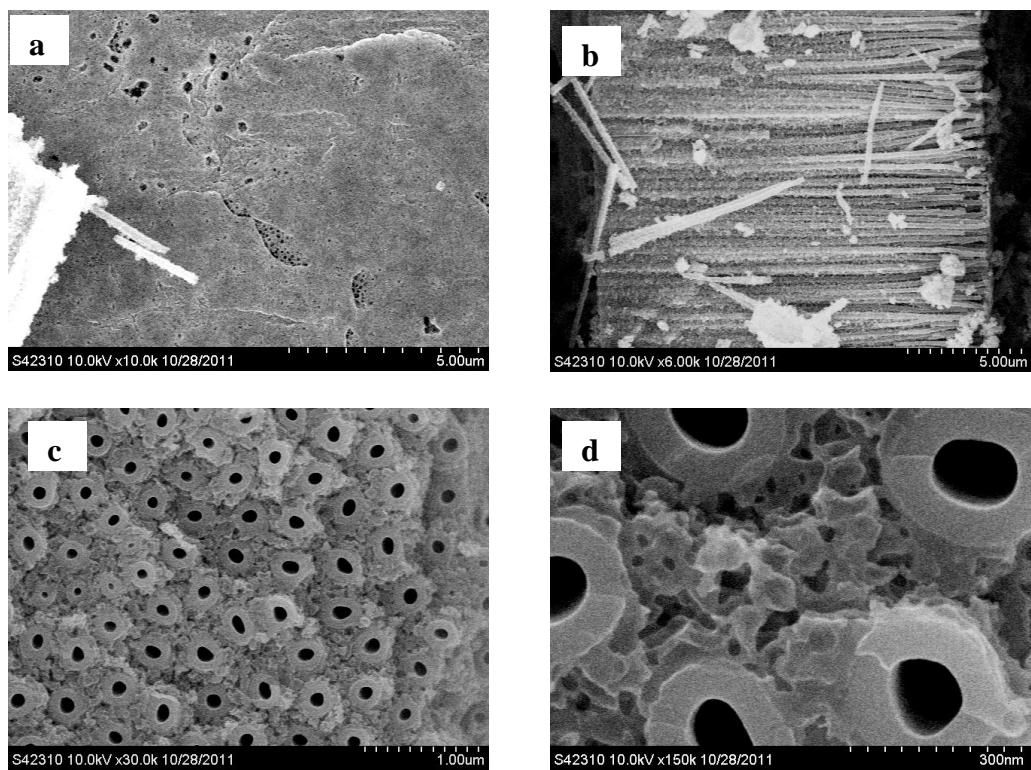


Figure 4-11 SEM image of a) top, b) side, c, d) near bottom views of an array anodized in a two-step process for 15 hours in pure DMSO + 2% HF at 60 V and room temperature

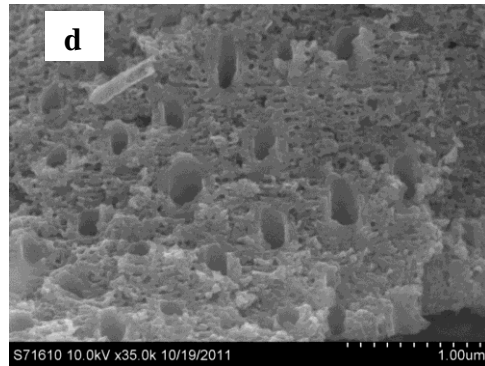
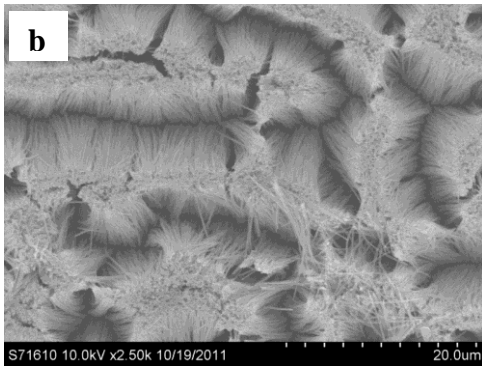
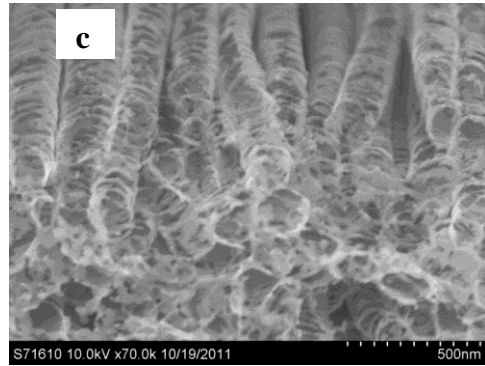
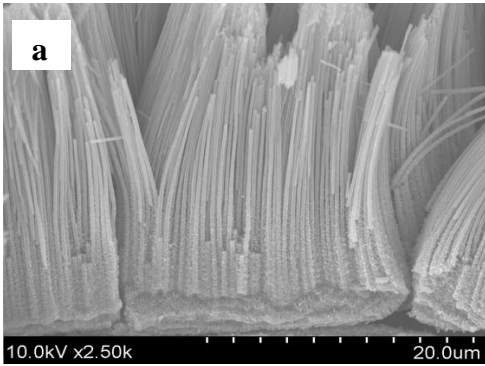
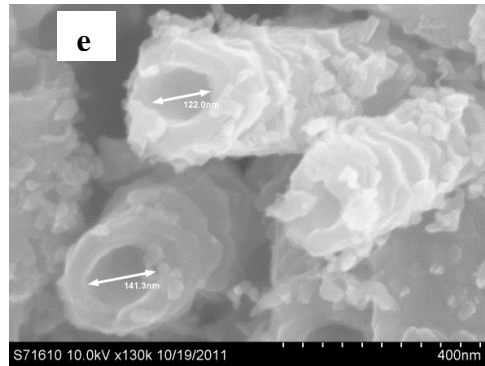


Figure 4-12 SEM image of a sample anodized in a two-step process for 50 hours in pure DMSO + 2% HF at 60 V and room temperature and then annealed at 450°C for 1 hour



Finally it is noteworthy that the tubes' diameter and thickness are much greater than that of their counterparts anodized under similar conditions in EG based electrolytes (Figure 4-9c and Figure 4-12e). The TiO₂ NTs from EG are about 90 nm wide with thicknesses between 15 and 20nm (see Figure 4-3b for instance)

probably because of slower ion flux in DMSO (Figure 4-6). The greater diameter and thicker separate tubes makes them less dense and hence lessens the wettable surface area in DMSO tubes. As the surface area is an important factor especially when we need to sensitize it in photovoltaic applications like DSSCs, the nano-geometry of DMSO single wall tubes are not desirable, as it has a great impact on the current density produced by the device .

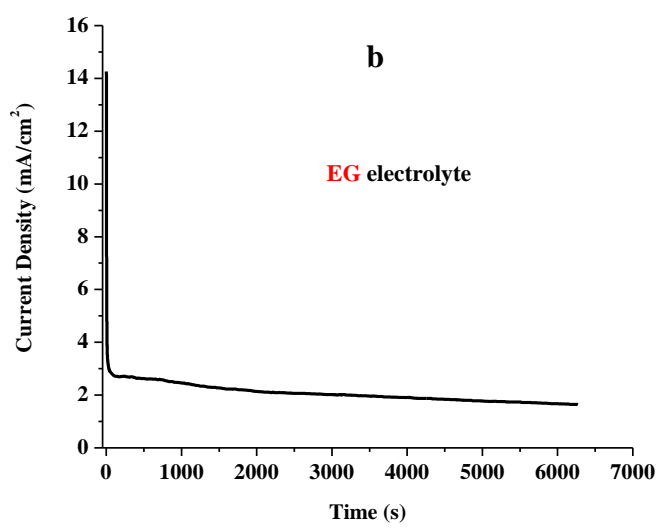
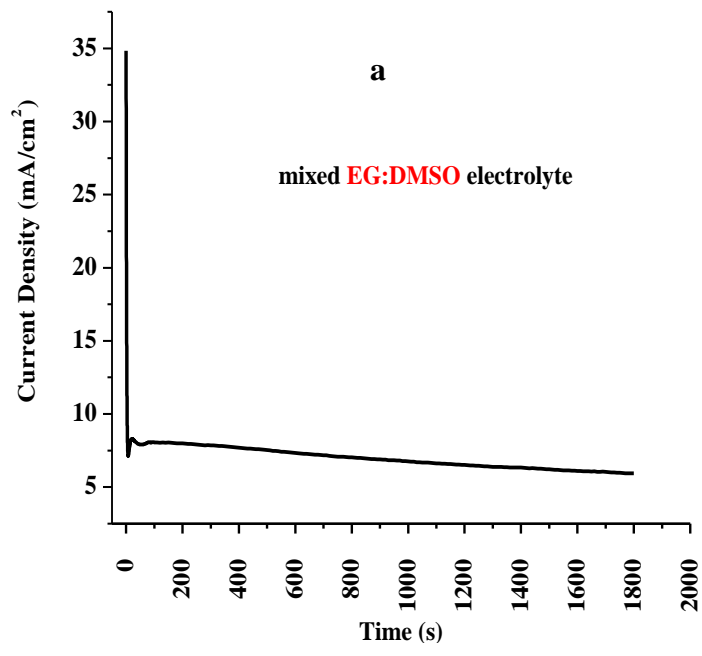
All the above mentioned disadvantages and limitations of the tubes produced from pure DMSO, although being single wall, makes them not of practical interest as a good replacement for the conventional double wall tubes from EG. Therefore in this work a new idea of using a mixture of EG-DMSO solvents to maintain the benefit of using both of solvents is proposed.

4.6 Kinetic studies of growth from mixed EG:DMSO electrolytes; current density versus time

It is explained in detail in *Section 4.1* that for growing nanotubes the double anodization method is performed mainly to get rid of the formation of the nano-grass irregularities on top of the tubes. In the first step a tube layer is grown in pure EG, which will be removed by ultrasonication before the second step in EG or EG:DMSO electrolytes. The current density variations of the growth of nanotubes from EG electrolyte and from EG:DMSO mixed electrolyte at 60 °C in the second anodization step (See *Section 4.1*) are shown in Figure 4-13a and b. As can be seen, the general trends of variation in current densities for both EG and EG:DMSO electrolytes in the second step (Figure 4-13a,b) are the same. However, as it is evident from Figure 4-6c, the anodization current density of the

pure DMSO electrolyte at high temperatures clearly changes differently than EG, so it is not surprising that different nano-structures are obtained as discussed in the previous section (4.4.2). Similarity of the J-t curves of EG:DMSO and EG shows that the growth mechanism of the tubes could be the same or at least very similar in these two cases.

It is noteworthy that the current density in the steady state growth stage in DMSO:EG is higher than EG, meaning a faster growth rate. Figure 4-13c shows the j-t curve for anodization of a simple foil in EG electrolyte at room temperature (first anodization step). As explained by Sergiu *et al* [18], stage I is related to the formation of the initial compact layer under a high applied field. Stage II is the pore formation step in the compact layer formed, which will continue to stage III, which is pore growth and widening step (See *Section 2.1* for more detail). The current densities of stage III of the anodization in EG for both simple and pre-anodized foil are almost the same (Figure 4-13b, c). However, the first stages' (I) slopes are different. This reveals that the formation of the compact initial oxide layer takes up to 400 seconds in case of a simple foil while in the second anodization the current drops in less than 10 seconds due to the presence of the pre-formed compact layer.



(To be continued in the next page)

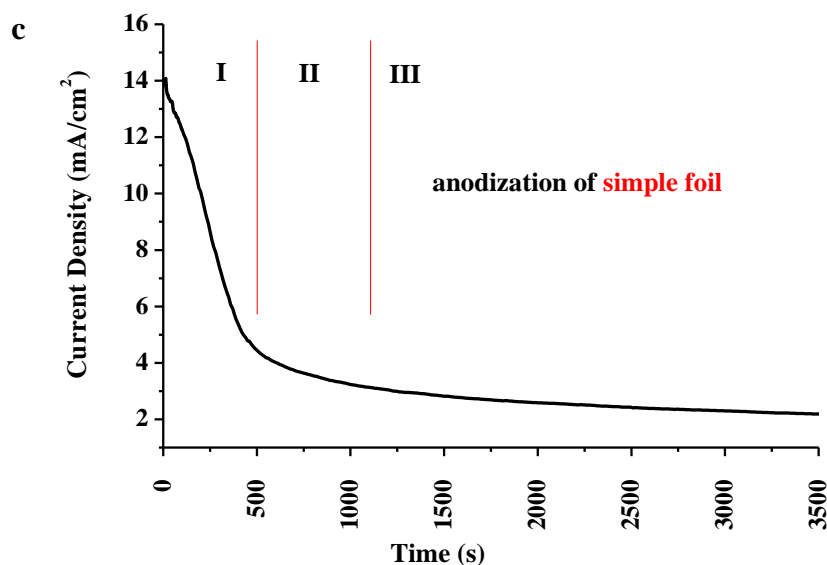


Figure 4-13 Variation of current density of anodization over time for a) EG + 0.1M NH₄F+1M H₂O electrolyte at room temperature (2nd step) , b) EG:DMSO + 0.1M NH₄F+1.5M H₂O electrolytes at 60 °C (2nd step), and c) anodization of simple foil in EG electrolyte at room temperature

4.7 Synthesis of single wall nanotubes from the mixed EG-DMSO based electrolytes

Anodization of Ti in mixed organic electrolytes is a topic that has not been previously investigated. As discussed and shown in previous sections of this chapter, using DMSO results in single wall tubes, however because of the problems with the array obtained from pure DMSO electrolyte, a systematic investigation of the effect of adding DMSO to ethylene glycol was made. For that reason, several experiments in different conditions were performed to find the best way to rapidly synthesize nanotubes with similar characteristics to the robust tubes from EG such as length, diameter and strength yet without the inside shell that is single wall nanotubes.

4.7.1 Effect of fluorine content:

To find the best concentration of fluoride ions, 0.05, 0.075, 0.1, and 0.13 M NH_4F were tried. As shown in Table 4-1, increasing fluoride content in the electrolyte increases the growth rate, however too much fluoride results in heavy nanograss formation on top of the tubes, as shown in Figure 4-14. Besides, when the ratio of DMSO to EG is higher than 1 or in case of high amount of fluoride, crystallization of fluoride-rich compounds may happen. So, in high concentrations of fluoride as can be seen in Figure 4-15, some cubic shape compounds remain on the surface of the nanotubes after anodization checked by EDX. The anodization is done at high temperatures and these compounds might appear because of the lower solubility of NH_4F in presence of DMSO after anodization at room temperature. Fluoride ion may get oxidized (resulting in F_2 gas bubbles) and/or react with other elements during the anodization. As a result, a moderate amount of 0.1 M NH_4F seems to work more effectively.

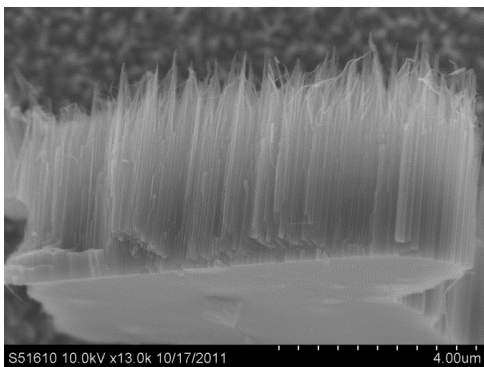


Figure 4-14 Heavily nanograss top of a sample in 0.13M fluorine content (in 2:1 EG:DMSO, 1.3M H_2O)

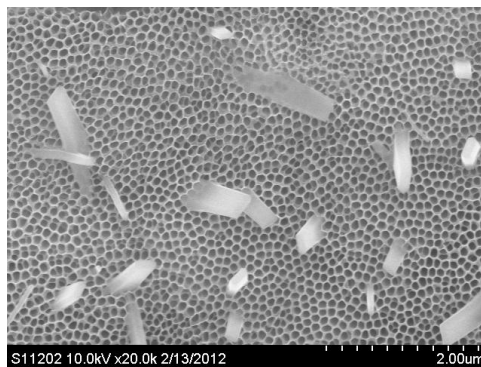


Figure 4-15 Fluorine rich cubic compounds formed from excess of fluorine ions in the solution

4.7.2 Effect of voltage and temperature during anodization ⁴:

In an investigation published in 2010, Enachi *et al* showed that for EG based electrolytes with HF, the outer diameter of TiO₂ NTs and their number in the unit area (density) is independent of anodization temperature, while the temperature has an enormous effect on the internal diameter of the tubes (Figure 4-16d). As can be distinguished in Figure 4-16, the inner diameters of the tubes increase from a few nanometers to about 250nm, when the temperature is increased from -20 to +50 °C. [35]

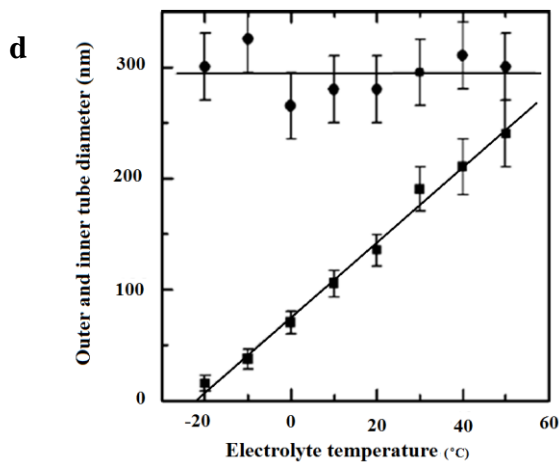
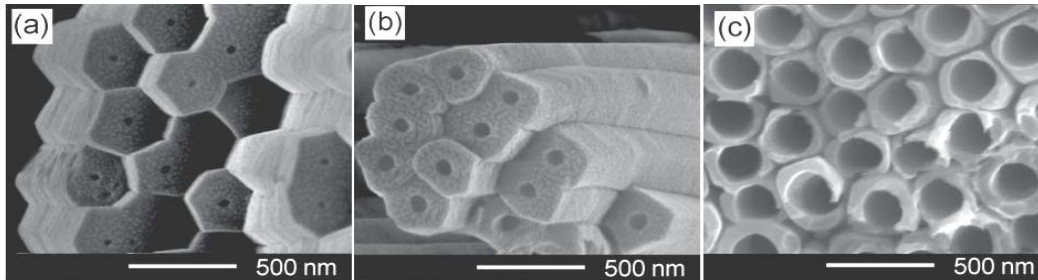


Figure 4-16 SEM images from the same height of TiO₂ NTs anodized at different temperatures of -10°C (a), 0°C (b), and +30°C (c). d) Increase of the inner diameter of tubes (squares) with temperature while the outer diameter (circles) is almost constant, adopted from [35].

⁴ It should be noted that temperature in these results means the temperature of a heating element (bath) which was used to warm the foil up during the anodization process (*See Chapter 3*).

It should be pointed out that in the case of using EG based electrolytes, due to the joule heating phenomenon, high anodization temperatures cause a very high increase in the anodization current density and the steady state condition will not be reached, so growing long nanotubes in such a condition is not possible [18]. Moreover, the present investigation shows that even the tubes grown at high temperatures have double wall nanostructure; therefore the mixed solvents was tried to investigate the effects of temperature and voltage.

As presented in Table 4-1, anodization at low voltages (30 and 40 V) results in slow growth kinetics, which is mainly attributed to the presence of DMSO in the electrolyte. The same effect is seen for growing nanotubes at lower temperatures. So, growing at 60 °C under 60 V was preferred.

4.7.3 Effect of electrolyte composition; EG:DMSO in 2:1 ratio

In a series of experiments, the amount of NH_4F and water were kept at 0.1 M and 1M respectively and other parameters were allowed to vary. All parameters such as length and diameters of nanotubes were checked to determine whether a single wall structure is successfully formed or not. For that purpose all samples were heat treated and checked thoroughly by means of SEM. The tube lengths obtained at different voltages and temperatures are summarized in Table 4-1 and two sample SEM pictures of one condition are shown in Figure 4-17. The results show that in all conditions with 2:1 EG:DMSO electrolyte, although the internal shell of the tubes (IST) are less and thinner than tubes from pure EG, the structure after

anodization is still double walled (Figure 4-17c), so it can be concluded that this amount of DMSO is not enough to suppress the formation of the IST.

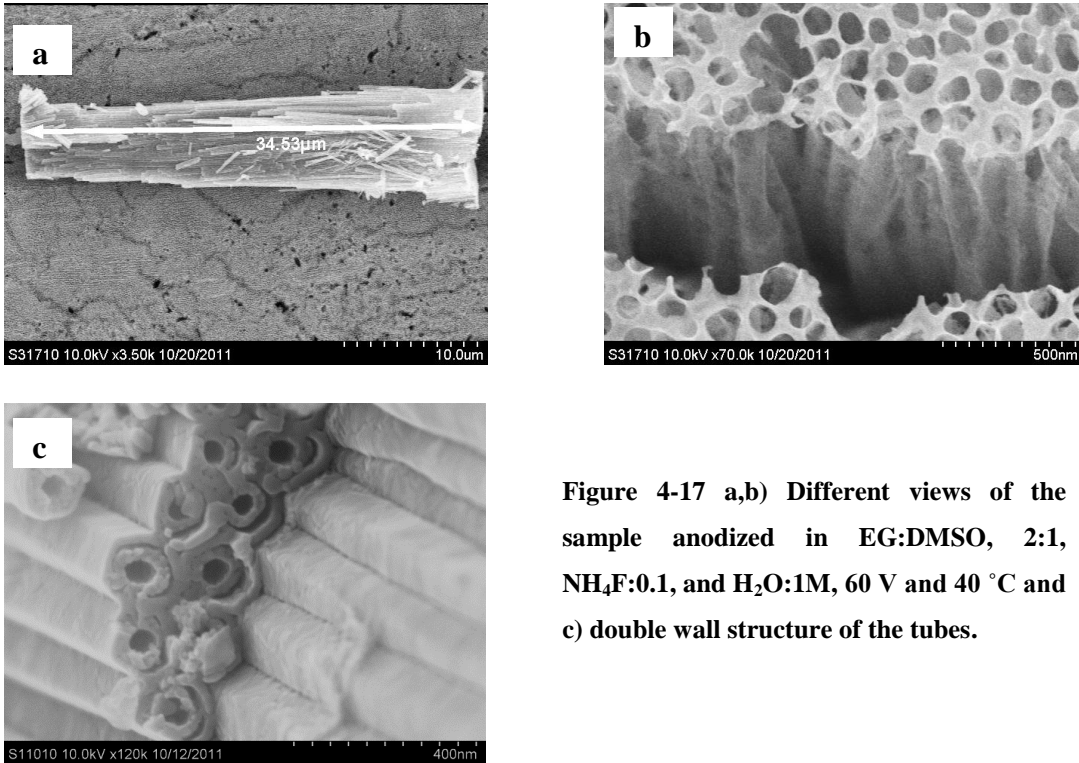


Figure 4-17 a,b) Different views of the sample anodized in EG:DMSO, 2:1, NH₄F:0.1, and H₂O:1M, 60 V and 40 °C and c) double wall structure of the tubes.

4.7.4 Effect of electrolyte composition; EG:DMSO in 1:2 ratio

As it is displayed in Figure 4-18, when there is more DMSO than EG in the electrolyte, the top initiation layer is thick and in some cases blocks the tubes. It seems that the dissolution ability of the electrolyte is directly related to the amount of EG in the mixture. Besides, cubical particles rich in fluorine are seen on top of the TiO₂ layer from more DMSO electrolytes, most probably because of the low solubility of NH₄F in DMSO similar to the condition in which the amount of NH₄F is high (Figure 4-14).

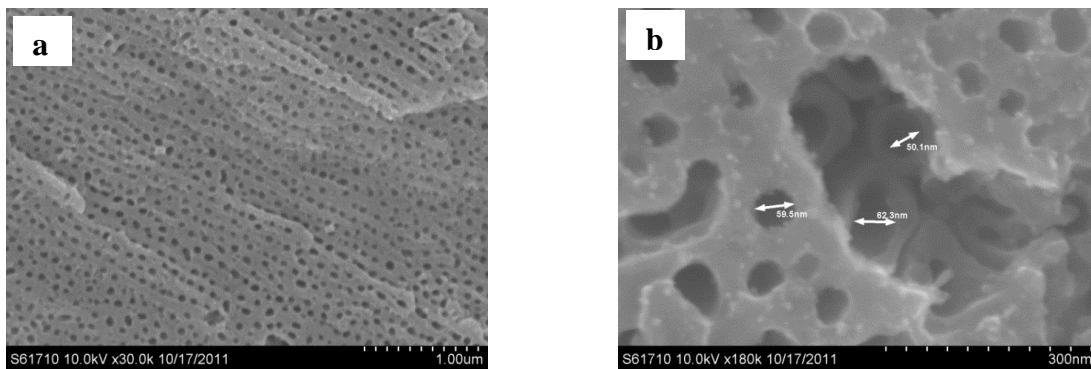


Figure 4-18 Different views of the sample anodized in EG:DMSO, 1:2, NH_4F :0.1, and H_2O :1M, 60 V and 60 °C

4.7.5 Effect of electrolyte composition; EG:DMSO in 1:1 ratio

Figure 4-19 shows the nanostructure of a TiO_2 NT layer from 1:1 EG:DMSO electrolyte. On one hand by increasing the EG ratio the problems of thick initiation top layer and the cubical species were solved. On the other hand, this composition, unlike for the tubes from pure EG based electrolytes (Figure 4-20), yields fully “single Wall” nanotubes at 60°C (Figure 4-21). The sample was kept at 60 °C after anodization in its electrolyte to dissolve the inside layer formed very close to the bottom of the tubes.

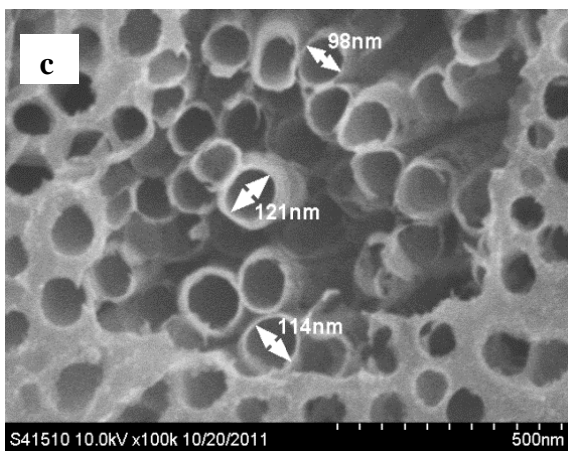
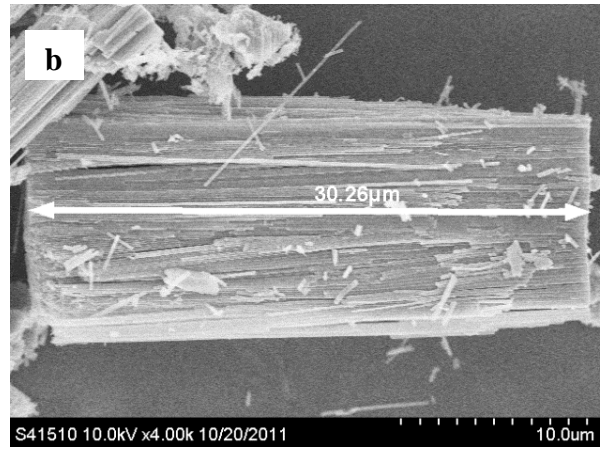
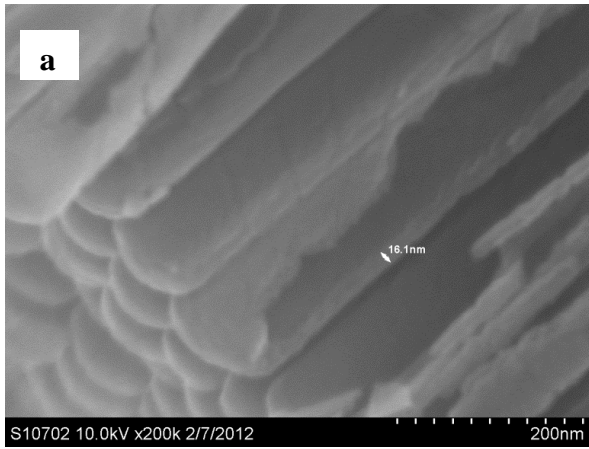


Figure 4-19 Different views of the sample anodized in EG:DMSO, 1:1, NH_4F :0.1, and H_2O :1.5M 60 V and 40 °C

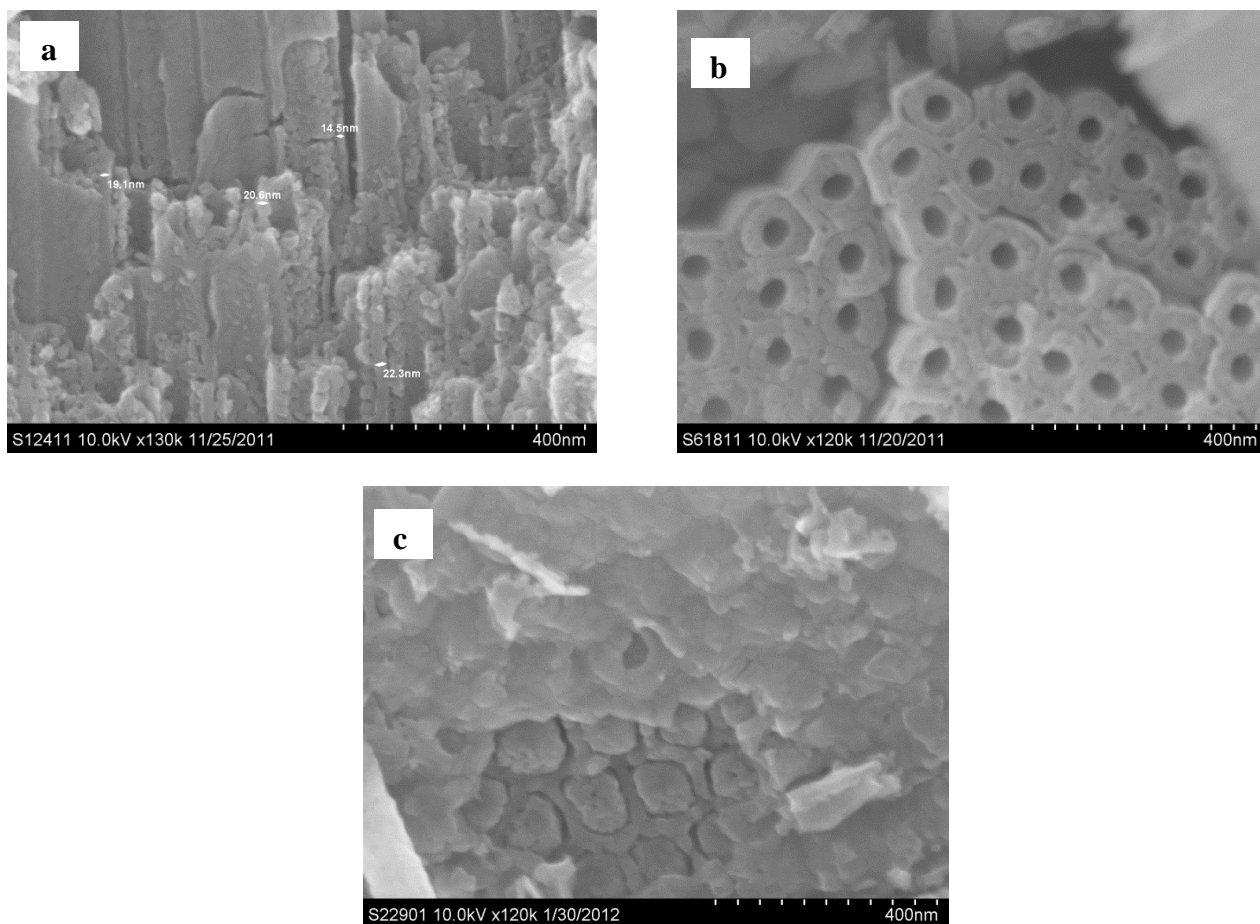


Figure 4-20 SEM pictures of the double walled structure of the EG tubes after annealing at 500°C. for 30 minutes. a) Cross section of the tubes near bottom. b) Side view of the tubes near bottom showing the compact outer shell and porous inner shell of the nanotubes c) View of the tubes from bottom. (Electrolyte: 1M H₂O, 0.1 M NH₄F in EG)

4.7.6 Effect of water content

It was shown by Wei *et al* that [89] in very low water content the anodized layer has nanopore shape rather than nanotube. Increasing the amount of water causes the solution of the boundaries between the tubes and results in nanotube shape structure. In the present case, for the single walls, the same effect was observed as well. While a water content less than 1M yields in a thick top-layer (initiation layer) with small openings, 1M concentration results in a nanopore structure in

which the tubes are not separated well. Increasing the amount of water from 1 M to 1.5 M, results in a better tube separation as shown in Figure 4-22.

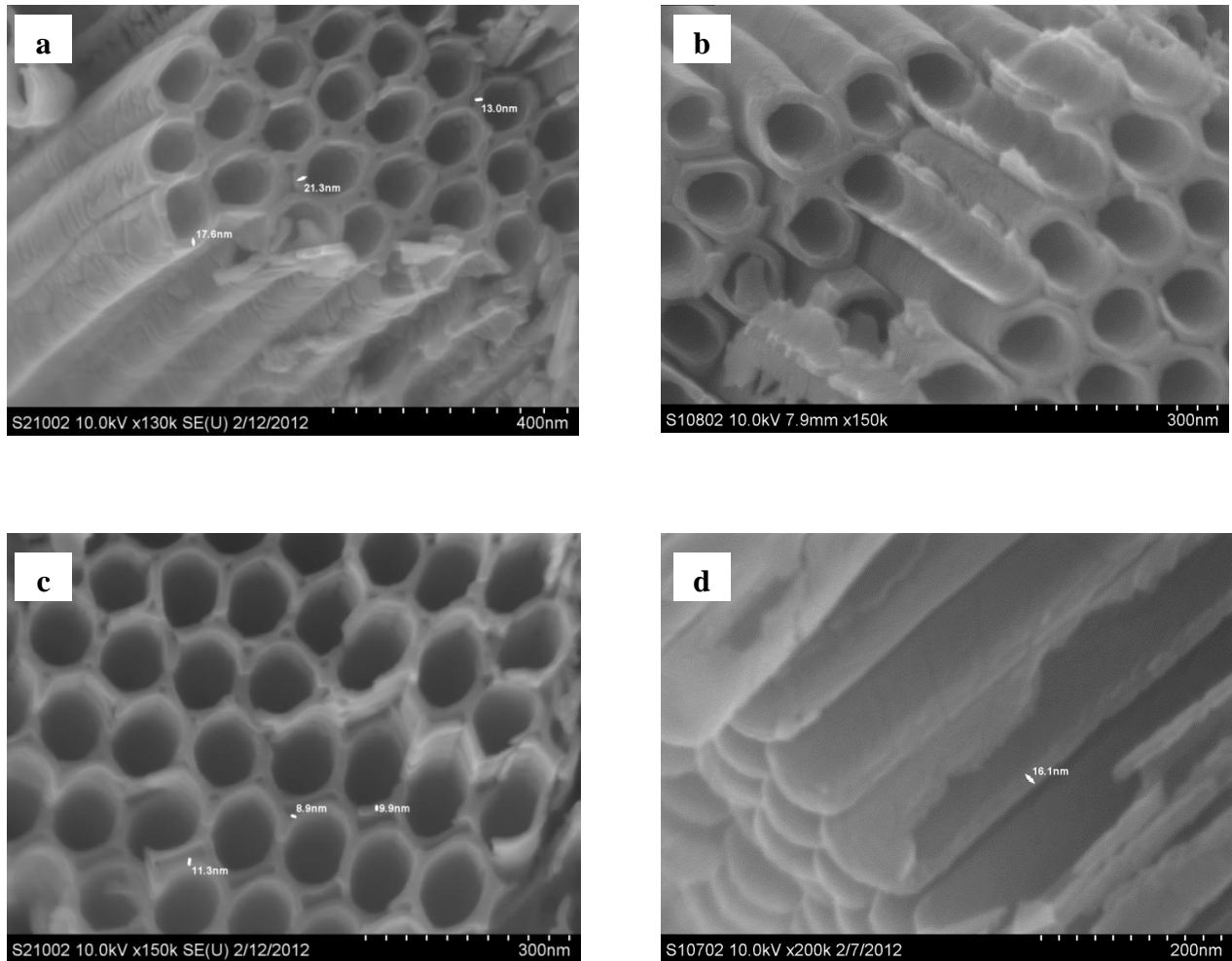


Figure 4-21 SEM pictures of the nanotubular structures from DMSO:EG, 1:1 electrolyte after annealing. a) Cross section of the tubes near the top, b, c) mid-height of the film, and d) very close to bottom of the tubes. (in 1.5 M H₂O, 0.1 M NH₄F / 1:1 EG and DMSO at 60 °C and heat treated at 500 °C)

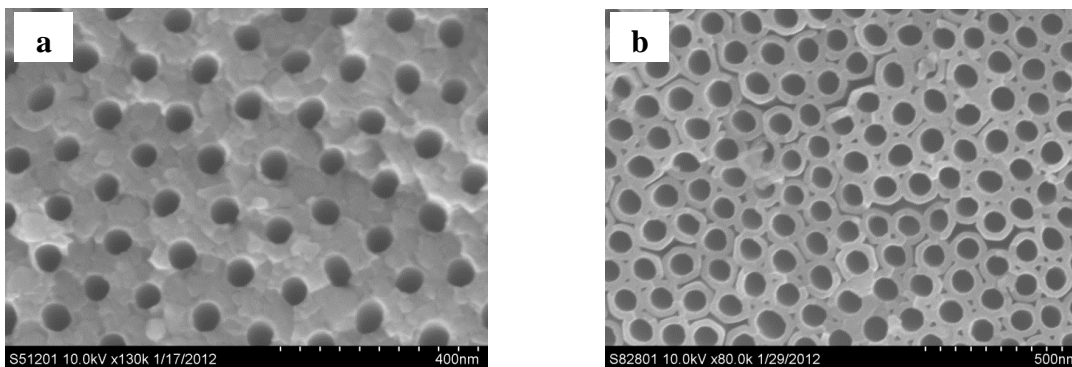


Figure 4-22 Effect of water content on the nanostructure of TiO₂ NTs from 1:1 DMSO: EG, and 0.1 M NH₄F. a) with 1M H₂O, and b) with 1.5M H₂O.

All in all, from a complete investigation and several SEM images, the effect of temperature and amount of DMSO on the geometry of TiO₂ NTs grown in mixed electrolytes, and removal of the inner shell can schematically be summarized as in Figure 4-23.

Increasing DMSO content →			Increasing Temperature ↓
EG based electrolyte	EG:DMSO, 1:1	EG:DMSO, 1:2	
 8-10 nm at RT	 15-20 nm at RT	 40-50 nm RT	
	15 nm at 45 °C 10-15 at 60 °C 	35 nm at 45 °C 	

Figure 4-23 Schematic representation of the effect of temperature and DMSO on the thickness of inner and outer shells of tubes. The numbers are the thickness of the outer shell. (RT= Room Temperature)

In Tables 4-1 and 4-2 summarize all the electrolytes' compositions, anodization times and tubes' lengths screened to find the best condition. It is worth noting that the growth rates are calculated based on the assumption that the growth is linear, however this assumption may not be valid as after sometime the growth stops and the length of the NTs will not change anymore.

It should be noted that besides the abovementioned parameters, a number of other parameters were also investigated. These included the effect of the volume of the electrolyte on the final structure, and the effect of post anodization in blank EG under a small applied voltage. Additionally, heating and cooling of the electrolyte during the post anodization was also inspected. After all, the best method to synthesize the best single wall tubes with uniform channel size from top to bottom, was found to be the one shown in the *Section 4.7.5; anodization in 1.5 M H₂O, 0.1 M NH₄F / 1:1 EG and DMSO at 60 °C, following by a post anodization step in the same electrolyte and temperature condition.*

Table 4-1 Electrolytes' compositions, anodization conditions and the resulted length of nanotube arrays for (a) EG:DMSO 1:2 and EG:DMSO 2:1 by volume (from the author's previous publication) [7]

Electrolyte Composition				Anodization condition			Approximate Growth rate ($\mu\text{m}/\text{min}$)	Tubes' Length (μm)	Description
EG Volume Ratio	DMSO Volume Ratio	$\text{NH}_4\text{F}(\text{M})$	$\text{H}_2\text{O}(\text{M})$	Time (min)	Voltage (V)	Temperature ($^\circ\text{C}$)			
1	2	0.07	0.7	120	60	40	0.05	6	<ul style="list-style-type: none"> ➤ Tube walls are rough. ➤ Porous nanostructure (tubes are not separated well). ➤ Small-hole size porous initiation layer on top
				120	30	60	0.017	2	
				120	60	60	0.5	60	
				60	60	60	0.65	39	
				40	60	60	0.7	28	
				20	60	60	0.68	13.7	
1	2	0.1	1	10	60	60	1.5	15	<ul style="list-style-type: none"> ➤ Nano-cubic shape particles seen on the top surface. ➤ Porous nanostructure (tubes are not separated well) ➤ Small-hole size porous initiation layer on top.
				15	60	60	1.25	18.8	
				20	60	60	1.3	26	
				30	60	60	-	-	
				120	60	40	0.05	5.8	
				180	60	40	0.033	6	

To be continued in the next page.

Table 4-1 (Continued) Electrolytes' compositions, anodization conditions and the resulted length of nanotube arrays for (a) EG:DMSO 1:2 and EG:DMSO 2:1 by volume (from the author's previous publication) [7]

Electrolyte Composition				Anodization condition			Approximate Growth rate ($\mu\text{m}/\text{min}$)	Tubes' Length (μm)	Description
EG Volume Ratio	DMSO Volume Ratio	$\text{NH}_4\text{F}(\text{M})$	$\text{H}_2\text{O}(\text{M})$	Time (min)	Voltage (V)	Temperature ($^\circ\text{C}$)			
1	2	0.1	1.5	20	60	60	0.72	14.3	<ul style="list-style-type: none"> ➤ Rough and grainy tube walls. ➤ Small-hole size porous initiation layer on top ➤ Nano-cubic shape particles seen on the top surface.
2	1	0.13	1.3	120	30	60	0.033	Less than 4	<ul style="list-style-type: none"> ➤ Nano- grass formed on top of the tubes.
				120	60	40	0.3	36	
				120	60	60	0.38	45	
2	1	0.1	1	5	60	60	1.14	5.7	<ul style="list-style-type: none"> ➤ Porous nanostructure (tubes are not separated well)
				10	60	60	1.17	11.7	
				15	60	60	1.27	19	
				40	60	40	0.675	27	
				30	60	40	0.7	21	
				20	60	40	0.75	15	

To be continued in the next page.

Table 4-1 (Continued) Electrolytes' compositions, anodization conditions and the resulted length of nanotube arrays for EG:DMSO 3:1 by volume (from the author's previous publication) [7]

Electrolyte Composition				Anodization condition			Tubes' Length (μm)	Description
EG Volume Ratio	DMSO Volume Ratio	$\text{NH}_4\text{F}(\text{M})$	$\text{H}_2\text{O}(\text{M})$	Time (min)	Voltage (V)	Temperature ($^{\circ}\text{C}$)		
3	1	0.075	0.75	60	60	RT	15	➤ Very thick initiation layer on top.
				120	60	RT		

Table 4-2 Electrolytes' compositions, anodization conditions and the resulted length of nanotube arrays for EG:DMSO 1:1 by volume (from the author's previous publication) [7]

Electrolyte Composition				Anodization condition			Approximate Growth rate ($\mu\text{m}/\text{min}$)	Tubes' Length (μm)	Description
EG Volume Ratio	DMSO Volume Ratio	$\text{NH}_4\text{F}(\text{M})$	$\text{H}_2\text{O}(\text{M})$	Time (min)	Voltage (V)	Temperature ($^{\circ}\text{C}$)			
1	1	0.05	0.5	120	60	RT	0.01	11.6	➤ Thick porous initiation layer on top ➤ Lower growth rate.
				240	60	RT	0.07	17.3	
				120	60	60	0.25	30	
				120	60	40	0.12	14.3	
				120	40	40	0.07	8	

Table 4-2 (Continued) Electrolytes' compositions, anodization conditions and the resulted length of nanotube arrays for EG:DMSO 1:1 by volume (from the author's previous publication) [7]

Electrolyte Composition				Anodization condition			Approximate Growth rate ($\mu\text{m}/\text{min}$)	Tubes' Length (μm)	Description
EG Volume Ratio	DMSO Volume. Ratio	$\text{NH}_4\text{F}(\text{M})$	$\text{H}_2\text{O}(\text{M})$	Time (min)	Voltage (V)	Temperature ($^{\circ}\text{C}$)			
1	1	0.1	1	60	60	RT	0.12	7.35	➤ Porous nanostructure (tubes are not separated well)
				120	30	40	0.033	4	
				120	30	60	0.017	2	
				120	60	60	> 0.83	More than 100	
				120	60	40	0.25	30	
				40	60	40	0.475	19	
				30	60	40	0.53	16	
				10	60	60	1.1	11	
				60	60	60	-	-	
				35	60	60	0.94	33	
				10	60	60	1.5	15	
				15	60	60	1.27	19	

To be continued in the next page.

Table 4-2 (Continued) Electrolytes' compositions, anodization conditions and the resulted length of nanotube arrays for (a) EG:DMSO 1:2 and EG:DMSO 1:1 by volume (from the author's previous publication) [7]

Electrolyte Composition				Anodization condition				Tubes' Length (μm)	Description
EG Volume Ratio	DMSO Volume. Ratio	$\text{NH}_4\text{F}(\text{M})$	$\text{H}_2\text{O}(\text{M})$	Time (min)	Voltage (V)	Temperature ($^{\circ}\text{C}$)			
1	1	0.1	1.5	15	60	60	0.93	14	➤ Tubes are well separated.
				16	60	60	0.94	15	➤ The structure is double wall near to bottom after anodization. ➤ The structure is fully single wall after "Post anodization treatment"

4.8 TEM studies of Single and double wall nanotubes

As stated earlier, the single or double wall nature of amorphous TiO_2 nanotubes can only be examined with TEM. The TEM images of double wall tubes from EG electrolyte and single wall tubes from EG: DMSO based electrolytes prior to annealing are shown in Figure 4-24. Unlike SEM images of amorphous tubes, the inner and outer shell of double wall tubes can easily be distinguished in TEM

observations. Figures 4-24b and d are further confirmation for the successful synthesis of single wall tubes with the mixed electrolyte/solvent method.

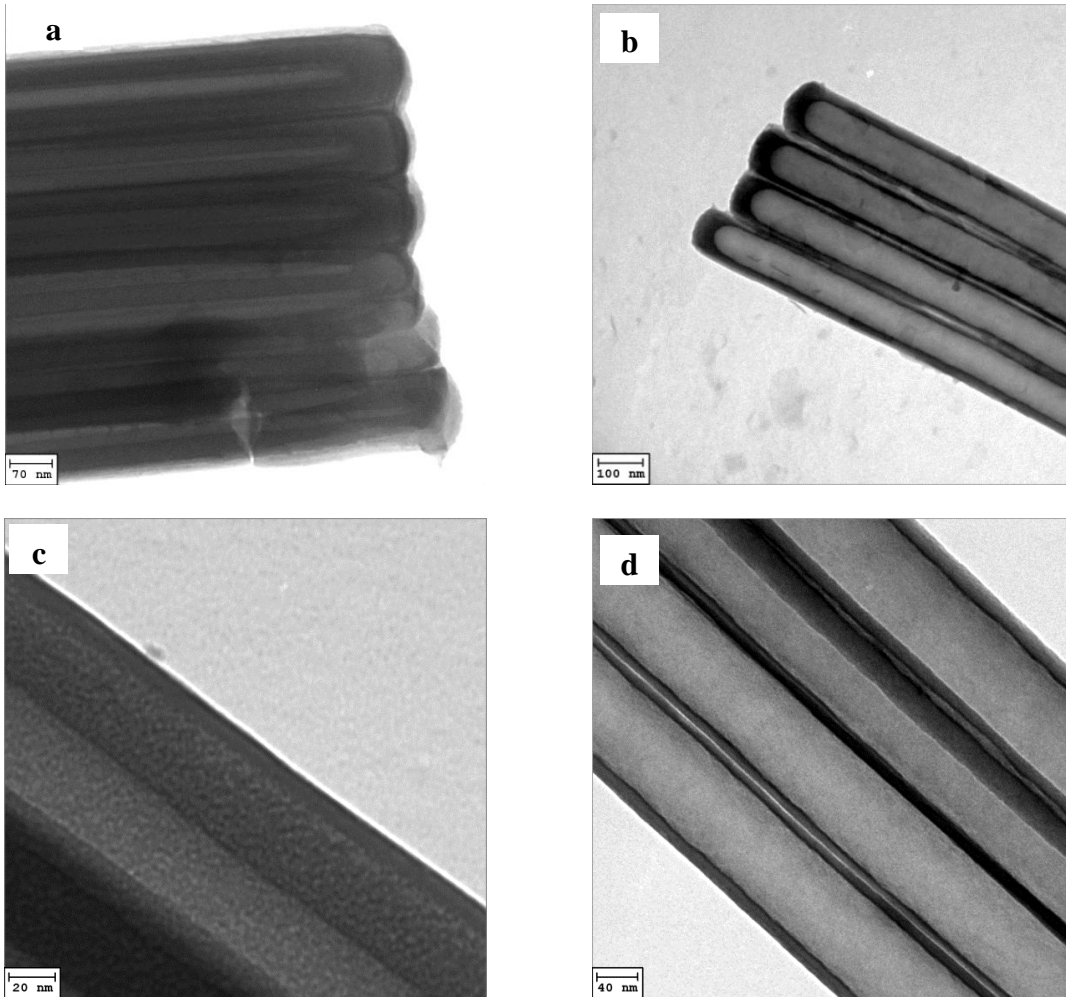


Figure 4-24 TEM images of a,c) amorphous double wall TiO₂ nanotubes anodized in 1M H₂O, 0.1 M NH₄F in EG, and b,d) as-formed single wall TiO₂ nanotubes anodized in 1.5 M H₂O, 0.1 M NH₄F in 1:1 EG and DMSO

Figure 4-25 shows the TEM images of double and single wall tubes after heat treatment. As can be observed, there is a considerable difference between the two kinds in the internal structure and grain sizes.

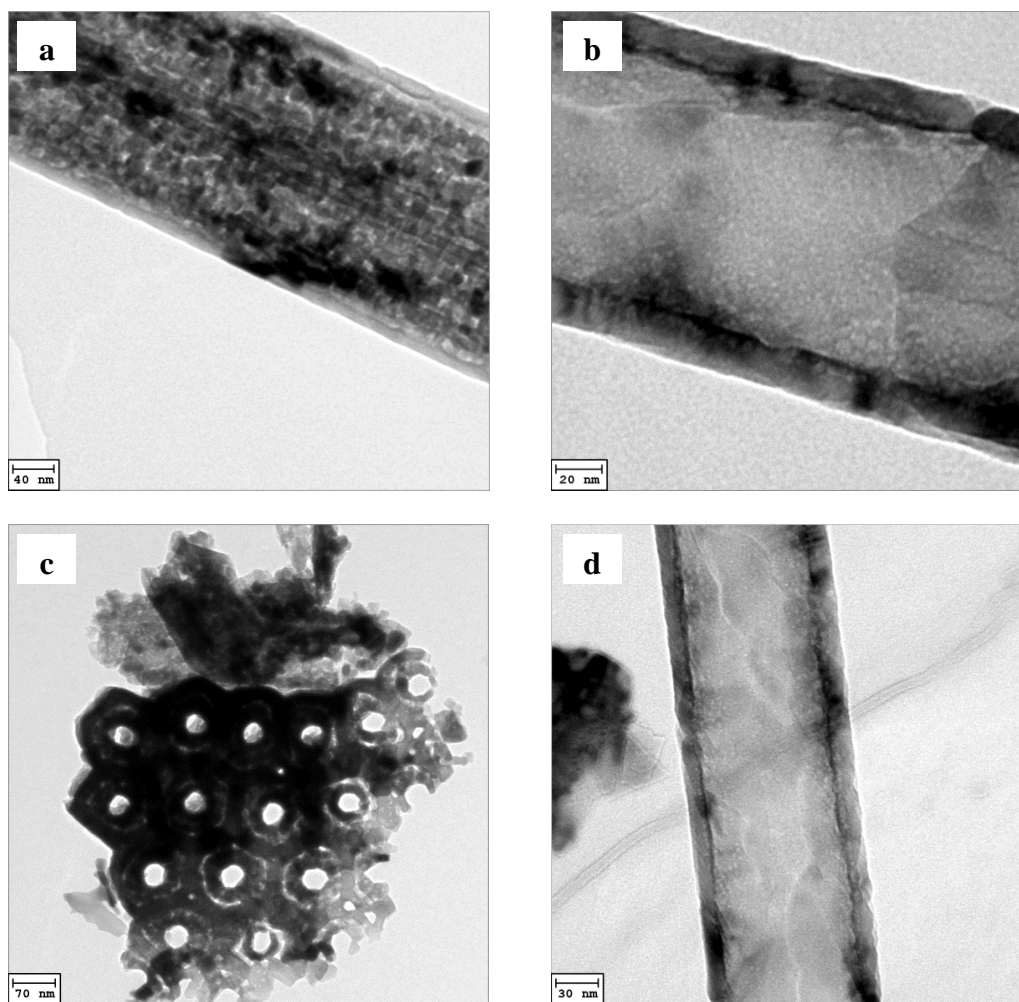


Figure 4-25 TEM images of a,c) annealed double wall TiO₂ nanotubes anodized in 1M H₂O, 0.1 M NH₄F in EG, and b,d) annealed single wall TiO₂ nanotubes anodized in 1.5 M H₂O, 0.1 M NH₄F in 1:1 EG and DMSO and heat treated at 500° C, 30 min

In Figures 4-26a to d a detailed comparison is made between the inner and outer shell sizes of the tubes near the bottom and mid-height of tubes. The nanotubes' grain sizes are also compared in Figures 4-26g and h which shows a considerable difference. The greater grain sizes of single wall nanotubes means they have less defects like grain boundaries and atomic voids, vacancies and dislocations that may result in significant dissimilarity in characteristics such as conductivity of the tubes, phase transformation thermodynamics / kinetics and

carrier transport for applications like photovoltaics. This issue will be discussed in more detail in *Chapter 6*.

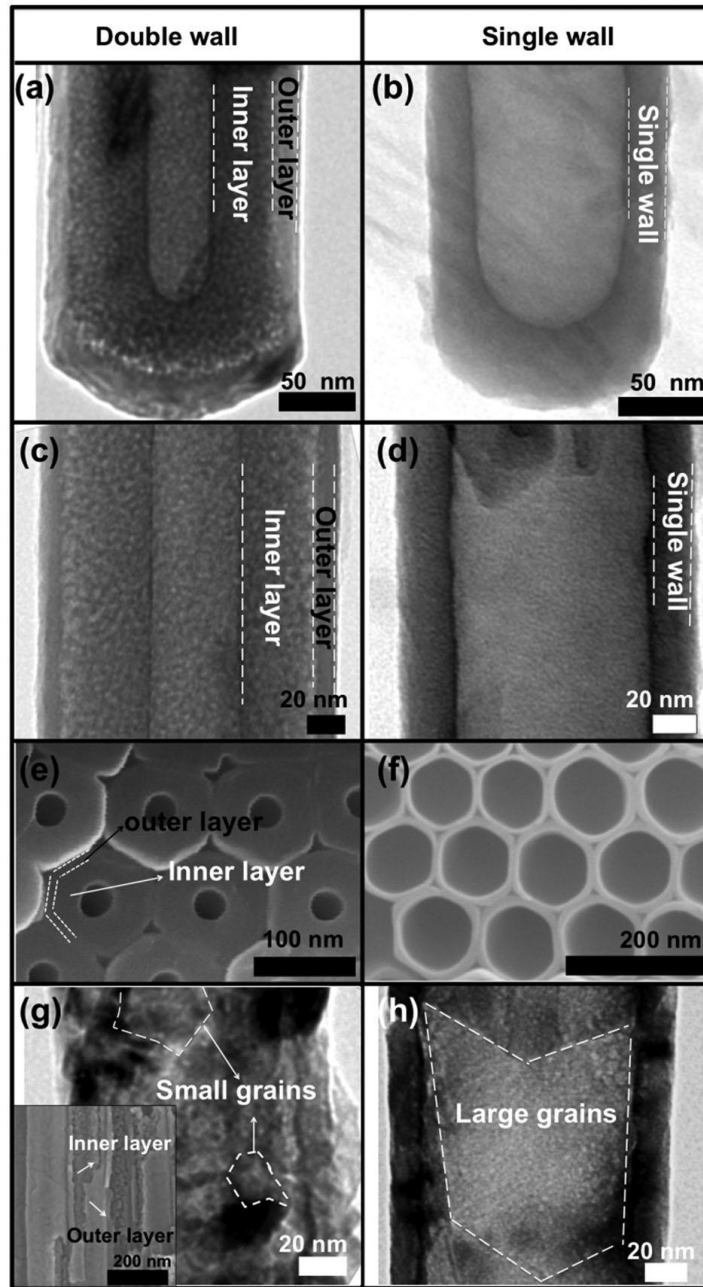


Figure 4-26 TEM images of a and c) double wall and b, d) single wall nanotubes. SEM images of TiO_2 nanotubes close to the bottom of tubes for the double wall (e) and single wall (f) nanotubes. g, h) TEM images of the double wall and single wall nanotubes after annealing showing the grains (from the author's previous publication) [7].

4.9 Mechanism of the electro-oxidation of EG during the anodization of TiO₂

The formation of double wall nano-structure can be explained by the “voltage induced radical and hole formation and capture” mechanism. [87]

Under high anodization voltages after the formation of the first TiO₂ layer, the TiO₂ becomes polarized in the positive direction. A schematic representation of what happens at high voltages is given in Figure 4-27 (Repeat of Figure 2-5 given again to aid the reader, See *Section 2.4*). The polarization decreases the Fermi level until it reaches to the valence band edge causing valence band ionization [37, 87]. This occurs when the effective applied voltage almost reaches $E_{fb} + E_g$, where E_{fb} is the flatband potential (≈ -0.4 V vs. KCl saturated Ag/AgCl) and the E_g is the band gap (3.4 eV) of TiO₂.

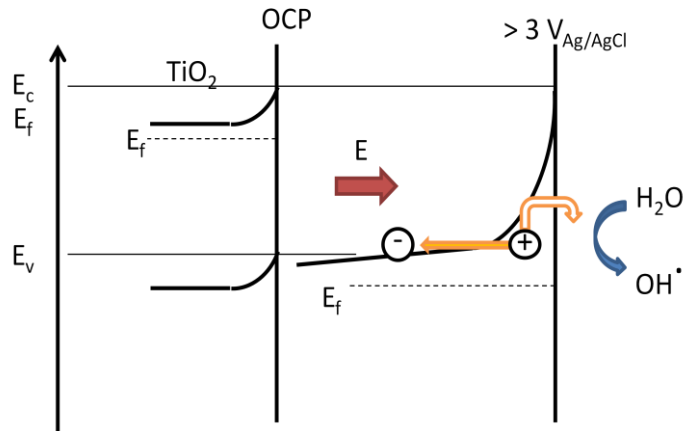


Figure 4-27 Schematic representation of the mechanism of the voltage induced radical and hole formation and capture [37, 87], E_{fb} is the flatband potential.

As TiO₂ nanotubes are in amorphous form, they are highly defective (doped) and the tunnelling breakdown of the Schottky junction is likely to happen as explained by Tiginyanu. (See *Section 2.5*) [90, 91].

Based on the above two phenomena, there will be a number of valence band holes generated on the semiconductor surface. These holes can react with any species from the electrolyte, water, for instance can be radicalized ($\text{H}_2\text{O} \rightarrow \text{OH}^\cdot$) on the surface.

The FTIR results discussed in *Section 5.1* will show that at such a high voltage, electro-oxidation of EG occurs and oligomerized products are formed by radical or hole capture oxidation. The products can adsorb on the TiO_2 electrode's surface and form a layer containing a mixture of TiO_2 particles and organic species. It is also known that DMSO can capture radicals 10 times faster than EG therefore in a mixed electrolyte of EG+DMSO it is likely that DMSO prevents the adsorption of the products of electro-oxidation of EG to TiO_2 and hence suppress the formation of the internal wall inside the tubes. The issue is discussed further in detail in *Chapter 5*.

4.10 Conclusion

The nanostructure of titania nanotubes grown in the conventional EG-based electrolytes containing fluoride ion is shown to be double walled by means of SEM and TEM characterizations. Performing anodization at higher temperatures can reduce the internal shell of the DW- TiO_2 NTs but not eliminate it completely.

Changing the electrolyte to DMSO results in single wall TiO_2 NTs, however their mechanical and geometrical properties and problems with their anodization process, makes the DMSO-based SW nanotubes undesirable. They are not robust

enough, the nanostructure is not uniform, the anodization time is too long and the tubes are very likely to be blocked by a thick layer.

Anodization of Ti-foils in mixed EG:DMSO solvents has been investigated thoroughly and shown that they have the benefit of both EG and DMSO solvents; rapid synthesis of TiO₂ nanotubes which are uniform in their nanostructure like the TiO₂ NTs from EG-based electrolytes, and single wall like those TiO₂ NTs from DMSO-based electrolytes. The details of the effects of the ratio of EG to DMSO, water and fluorine contents of the electrolyte and the voltage and temperature of the anodization process on the nanostructure of the TiO₂ NT film has been presented. The best route to grow SW- TiO₂ NTs is proposed to be anodization in 1.5 M H₂O, 0.1 M NH₄F in 1:1 EG and DMSO at 60 °C, following by a post anodization step in the same electrolyte at the same temperature.

Finally, the mechanism of the formation of the internal shell in double wall TiO₂ NTs has been explained based on voltage induced hole formation on the surface of TiO₂ nanotubes during the anodization process.

Chapter 5

Characterization of double and single wall nanotubes

After demonstration of the synthesis properties of high aspect ratio SW- TiO₂ NTs, in this chapter the detailed properties of these nanotubes through XRD, depth profile XPS, FTIR, DSC, conductivity measurements and UV-VIS characterization methods will be presented and a comparison between them and the conventional DW- TiO₂ NTs will also be made. Moreover the effect of the internal shell of the tubes (IST) in DW- TiO₂ NTs on the properties of the tubes such as their phase transformation activation energy, band gap and conductivity will be discussed.

5.1 FTIR characterization of the anodization electrolytes and the as-formed nanotubes

5.1.1 Characterization of the anodization electrolytes

EG can be fully oxidized to CO₂ in an electrochemical process through a chain of products (Figure 5-1)⁵. It is also shown by Wang *et al* that in the electrooxidation process of EG, water is produced with a feature appearing as a broad peak in FTIR between 1600 and 3000 cm⁻¹ [38].

⁵ The figure is repeat of Figure 2-4 given again to aid the reader.

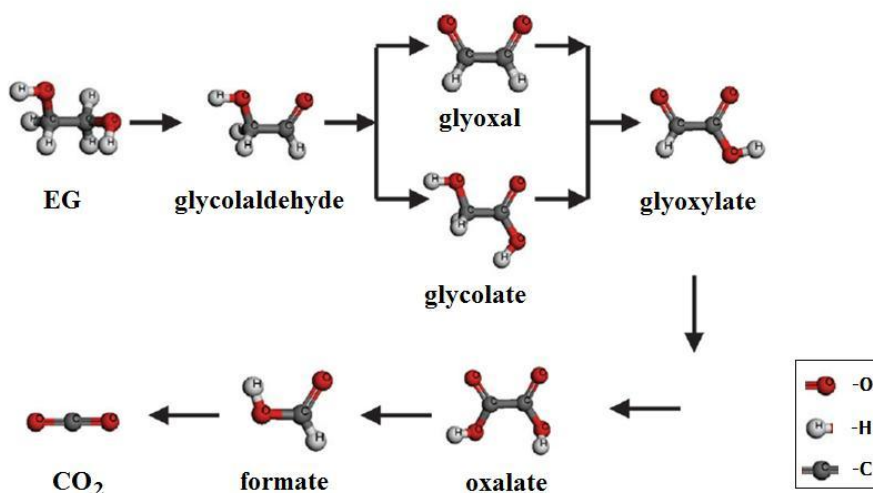


Figure 5-1 Full reaction path of EG electrooxidation proposed by Wang *et al.* [38]

FTIR studies of the electrolytes and as-formed nanotubes were performed to investigate the probable electro-oxidation of electrolyte species during the anodization process.

Figure 5-2 shows the FTIR spectra of the common ethylene glycol (EG) electrolyte widely used to synthesize TiO₂ nanotube arrays after anodization process with respect to the electrolyte before anodization (as FTIR background). The major band frequencies and their corresponding bonds are summarized in Table 5-1.

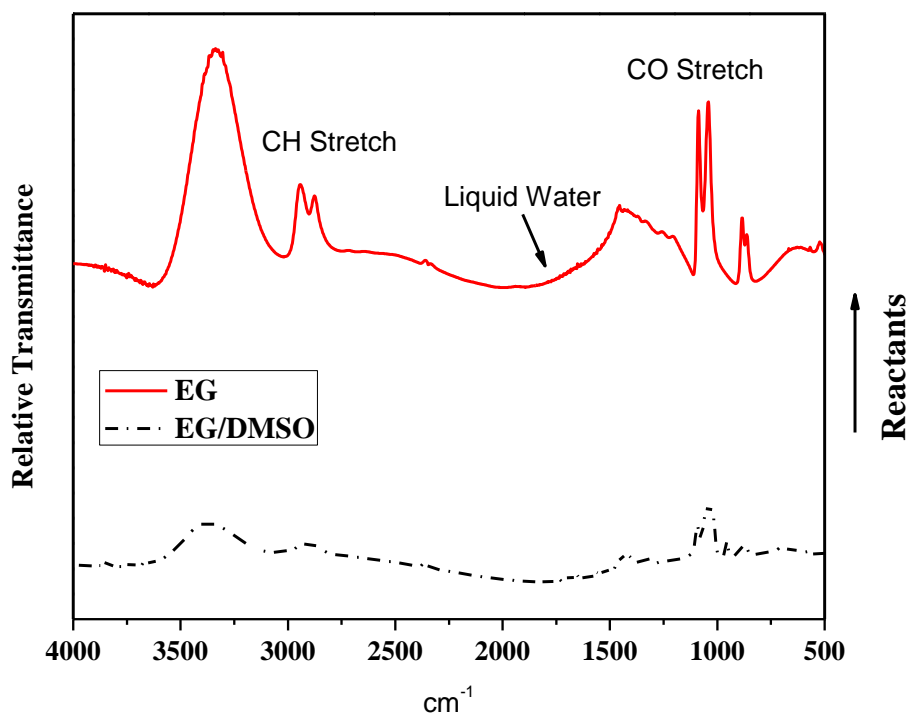


Figure 5-2 FTIR spectrum of (EG + 0.1M NH₄F+ 1M H₂O) transmittance FTIR (in red) after anodization normalized against the fresh anodization electrolyte before anodization (as background). The FTIR response of the EG/DMSO- based electrolyte (dotted black) is also plotted for comparison using a difference zero so that the two spectrum are clearly separated. Typical FTIR spectra were recorded from at least 3 different samples with no significant differences being observed.

As can be seen in Figure 5-2, the CH₂ Rocking peak at 886 cm⁻¹, CO stretch peaks at 1042 cm⁻¹, and 1089 cm⁻¹, CH₂ bending at 1455 cm⁻¹, CH stretch peaks at 2879 cm⁻¹ and 2942 cm⁻¹, and the peak for the stretch of OH group at around 3340 cm⁻¹ are all pointing upwards showing that they are consumed during the anodization process. This fact in addition to the rather wide downward pointing peak of water indicates the likely electro-decomposition of EG on the anode surface (the TiO₂ formed on the Ti foil) during the electrochemical anodization.

Table 5-1 Frequencies observed in FTIR of (EG) electrolyte (EG + 0.1M NH₄F+ 1M H₂O), Upper pointings are reactants and downwards are products [92].

EG based electrolyte cm ⁻¹	Assignment
886	EG- CH ₂ Rocking
1042	EG CO stretch
1089	EG- CO Stretch
1423	EG-C—O—H bending
1455	EG-CH ₂ bending
2336	CO ₂ (ν ₃ , asymmetric stretch)- P branch
2362	CO ₂ (ν ₃ , asymmetric stretch) - R branch
2879	EG-CH stretch system
2942	EG-CH stretch anti-system
3343	stretch region of OH groups and molecularly chemisorbed water

Figure 5-3 shows the FTIR spectra of the mixed EG/DMSO based electrolytes used to grow single wall nanotubes after the electrochemical anodization versus the fresh electrolyte (as FTIR background). The major band frequencies and their corresponding bonds are summarized in Table 5-2.

As can be distinguished by comparing Figure 5-2 and 5-3, the amount of organics produced is much less (shorter peaks) in the electrolyte containing DMSO. Besides, the amount of water produced during the anodization is also

much less. These results show that DMSO suppresses oxidation of EG such that less water and organics are formed during the anodization process.

Table 5-2 Frequencies observed in FTIR of (EG/DMSO) electrolyte (1:1 vol. DMSO/EG + 0.1M NH₄F+ 1.5 M H₂O), Upper pointings are reactants and downwards are products [92].

Electrolyte EG/DMSO cm⁻¹	Assignment
886	EG- CH ₂ Rocking
953	DMSO perpendicular CH ₃ rocking vibration
1042	EG CO stretch
1095	EG- CO Stretch
1325	DMSO-symmetric bending of CH ₃
1434	DMSO- asymmetric bending of CH ₃
2336	CO ₂ (ν ₃ , asymmetric stretch)
2362	CO ₂ (ν ₃ , asymmetric stretch)
2873	EG-CH stretch system
2936	EG-CH stretch anti-system
3380	stretch region of OH groups and molecularly chemisorbed water

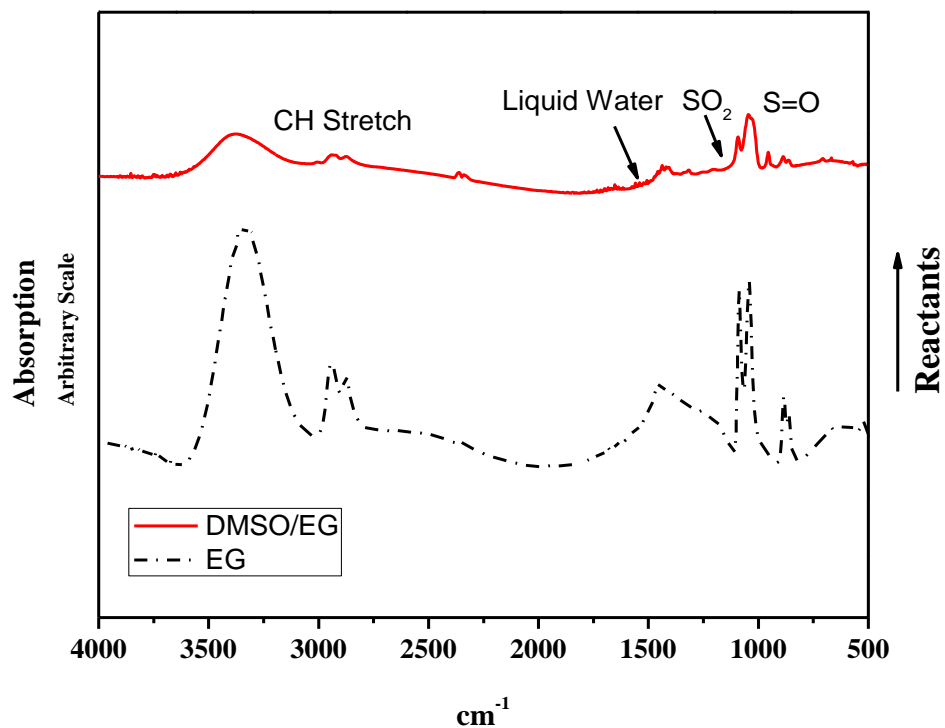


Figure 5-3 The FTIR plot of (1:1 vol. DMSO/EG + 0.1M NH_4F + 1.5 M H_2O) transmittance FTIR (red) after anodization normalized against the fresh anodization electrolyte before anodization (as background). The FTIR response of the EG-based electrolyte (dotted black) is also plotted for comparison using a difference zero so that the two spectrum are clearly separated. Typical FTIR spectra were recorded from at least 3 different samples with no significant differences being observed.

5.1.2 Characterization of as-anodized nanotubes

The FTIR spectra of as-anodized SW and DW nanotubes, after cleaning and drying, are shown in Figure 5-4 and their important peaks are listed in Table 5-3. It can be deduced that the DW have higher amount of carbon containing compositions (including CO_2) adsorbed on / incorporated on DW tubes. It can be observed that in the product spectrum, the CO_2 has only a single peak. This suggests an absence of rotational fine structure that usually causes the P and R-branches. The lack of rotation can be taken to indicate that the CO_2 is adsorbed to

the nanotube walls. It should be noted that the SO_2 downward peak around 1150 cm^{-1} can be attributed to the symmetric stretches of SO_2 in dimethyl sulfone which is the product of the oxidation of DMSO remained in the electrolyte (See Section 2.3).

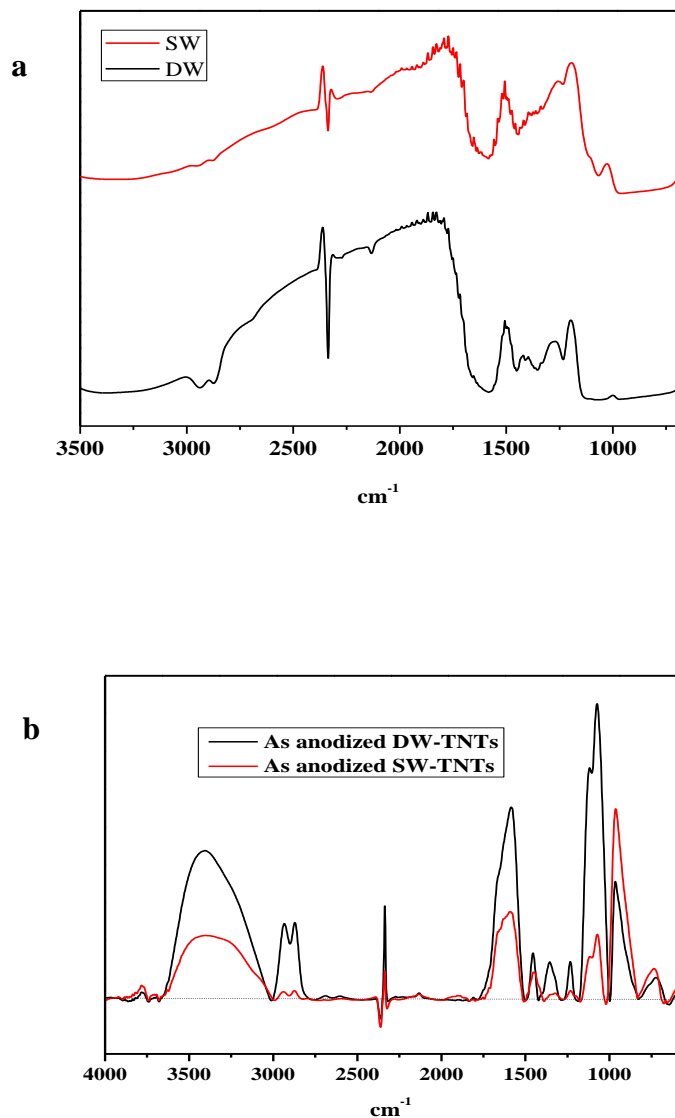


Figure 5-4 Simple(a) and base line corrected (b) absorbance FTIR spectra of as-anodized double wall and single wall TiO_2 nanotube arrays. Typical FTIR spectra were recorded from at least 3 different samples with no significant differences being observed.

As can be seen in Figure 5-4, the common double wall tubes have much higher C-OH stretch peak at 1080 cm^{-1} , CH_2 bending peak at 1455 cm^{-1} , CO_2 peak at 2340 cm^{-1} , CH stretch at 2880 and 2940 cm^{-1} , and OH stretch peak at around 3400 cm^{-1} . These higher peaks can be attributed to the full and partial electro-oxidation of -mainly - ethylene glycol and adsorption to the surface of the anodized nanotubes.

The peak at 1120 cm^{-1} could be arise from C-O-C bond from carbonaceous organic material contaminations [93].

It should also be mentioned that the oxidized product of DMSO (dimethyl sulfone) can theoretically be detected from the production of peaks around 1150 and 1300 cm^{-1} which are located in the ranges of CO stretches and liquid water peaks and overlap with them.

Table 5-3 Frequencies observed in FTIR of as-anodized double wall (black) and single wall (red) TiO₂ nanotube arrays plotted in Figure 5-4.

DW TiO ₂ NT cm ⁻¹	Assignment	SW TiO ₂ NT cm ⁻¹	Assignment
964	O-H bend from Carboxylic acids from Electrooxidation of EG[38]	959	DMSO perpendicular CH ₃ rocking vibration[94] + O-H bend from Carboxylic acids from Electrooxidation of EG [38]
1079	EG-CO Stretch [95]	1074	EG- CO Stretch (C-O-H) [95]
1121	C-O-C bond from carbonaceous organic materials [93]	1115	C-O-C bond from carbonaceous organic materials [93]
1236	HOOC-COOH[38]	1196	EG-CH ₂ twist
1356	glyoxilate at higher potentials	1230	HOOC-COOH[38]
1455	EG-CH ₂ bending[95]	1321	DMSO-symmetric bending of CH ₃
1585	glyoxal and glycolate [38]	1453	EG-CH ₂ bending[95]

1665	OOC-COOH	1596	glyoxal and glycolate at pH= 13 [38]
2133	N-O stretch	2133	N-O stretch
2336	CO ₂ (ν ₃ , asymmetric stretch)	2336	CO ₂ (ν ₃ , asymmetric stretch)
2362	CO ₂ (ν ₃ , asymmetric stretch)	2362	CO ₂ (ν ₃ , asymmetric stretch)
2873	EG-CH stretch system	2869	EG-CH stretch system
2936	EG-CH stretch anti- system	2936	EG-CH stretch anti-system
3406	stretch region of OH groups and molecularly chemisorbed water	3390	stretch region of OH groups and molecularly chemisorbed water
3708	CO ₂ (ν ₁ +ν ₃)	3620	CO ₂ (2ν ₁ +ν ₃)
		3713	CO ₂ (ν ₁ +ν ₃)

5.2 The nature of the internal wall of DW nanotubes

As shown in *Chapter 4*, SEM observations reveal that the inner layer of double wall TiO₂ nanotubes shows - under most annealing conditions - a distinct granular morphology (Figure 5-5) that can be ascribed to the extremely high carbon content compounds - shown in FTIR results in *Sections 1.3* and *1.4* - from electro-oxidation of EG during the anodization in these tubes. For EG based electrolytes the decomposition products are a range of EG oxidation products and oligomerized EG. These, can strongly adsorb on anodic TiO₂ nanotubes layer. The formed Ti oxides and/or oxy-hydroxides then pick up the electrolyte

oxidation products, water and species as molecules adsorbed at the oxide/electrolyte interface. Evaporation and oxidation decomposition of these compounds to CO_2 during the annealing process leads to voids in the structure and leaves a porous layer behind.

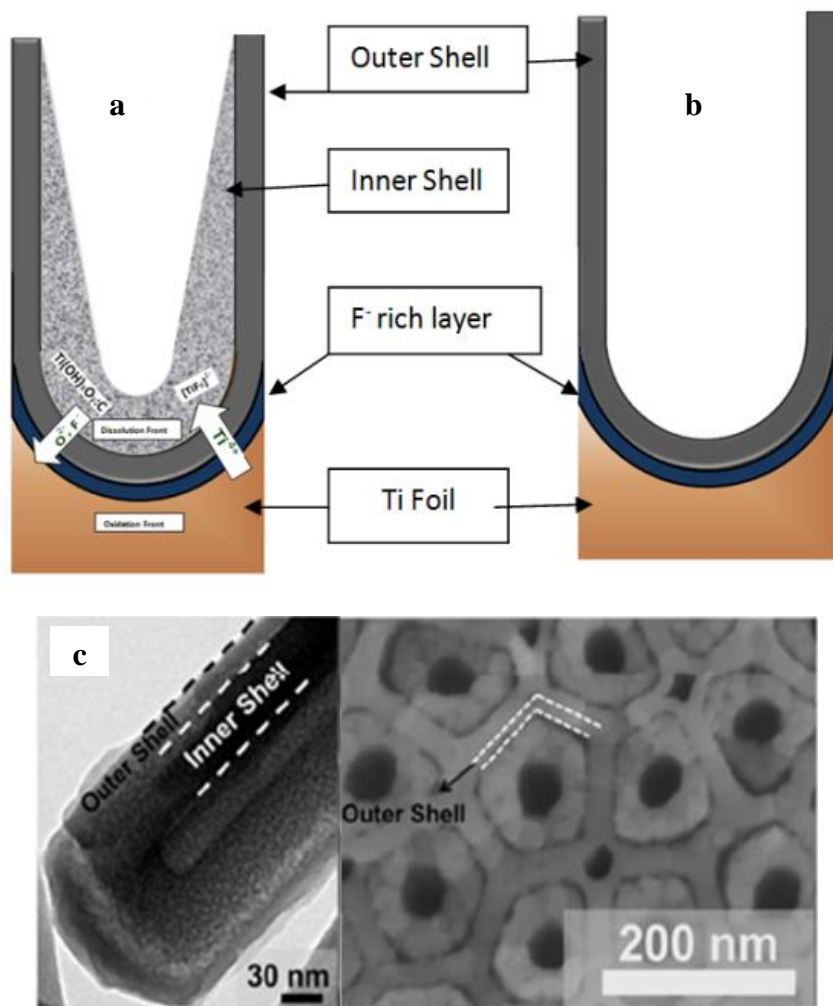


Figure 5-5 a, b) Schematic representation of double wall and single wall nanotubes respectively, c) TEM and SEM pictures of double wall tubes.

Adding DMSO to EG, as it captures radicals at least a factor of 4 faster than EG, suppresses the electro-oxidation of EG, resulting in nanotubes with less significant internal wall (single walls). DMSO is known as a powerful scavenger

of the highly reactive hydroxyl free radical -with strong redox properties- to the extent that has been used as an OH radicals probe in biological systems [88, 96, 97].

5.3 XRD studies of the single and double wall nanotubes

The crystal structure of the nanotubes in different conditions was investigated using XRD method. XRD profiles of SW and DW nanotubes on Ti foil, annealed at 500 °C for 1 hour are shown in Figure 5-6. In this figure T stands for the peaks from the Ti substrate foil and R stands for rutile. The remaining are anatase peaks that have been assigned to their corresponding planes (JCPDS Card No. 21–1272).

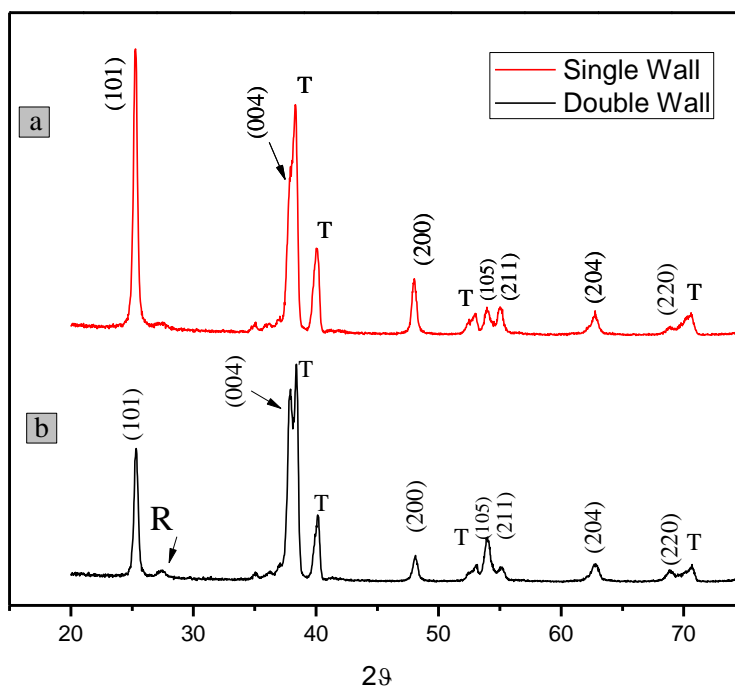


Figure 5-6 XRD patterns of a) single wall and b) double wall nanotubes on Ti foil annealed at 500 °C for 1 hour

As can be seen, in both cases there are small amounts of rutile phase formed at 500°C. Another point is that in single wall tubes the low index (101) peak is more intense than (004), while it is the reverse for double wall anatase nanotubes. The relatively high intensity of (004) plane points out that the structure of the tubes are exposed by {001} facets [98].

Figure 5-7 shows XRD patterns of nanotubes removed from the surface, annealed at 500 °C for 1 hour but heated at different rates of 5 and 10 ° C/min. As can be seen all peaks can be indexed to the anatase TiO₂ according to JCPDS Card No. 21-1272.

A comparison of the XRD patterns in Figure 5-6 and Figure 5-7 reveals that the intensity of the (101) plane of the removed nanotubes is stronger than (004) compared to the annealed tubes on foils. This significant difference shows that the preferred growth direction is not the same for the free nanotubes and those on the foil. This fact could be arise from the probable effect of the foil on the final exposed facets of the nanotubes. The surface energy of {001} facets is higher than {101} facets, so in a normal growth condition it is much favorable for {101} facets to be exposed as can be observed for the *removed* (free) nanotubes from the foil in Figure 5-7 [99]. However, Yang *et al* [100] showed that the presence of fluoride ions can decrease the surface energy of {001} facets lower than {101} as the ions can adsorb preferentially onto {001} facets. Besides, thermal expansion of the tubes and Ti to TiO₂ crystal volume change can be sources of stress that may result in the special orientation growth of nanotubes on foils. It is worth noting that the {001} facet is highly reactive and more desirable for applications

such as photovoltaics and photo catalyses [98]. Therefore, anodization of the foil in presence of fluoride plays a positive role and helps the growth of {001} facets.

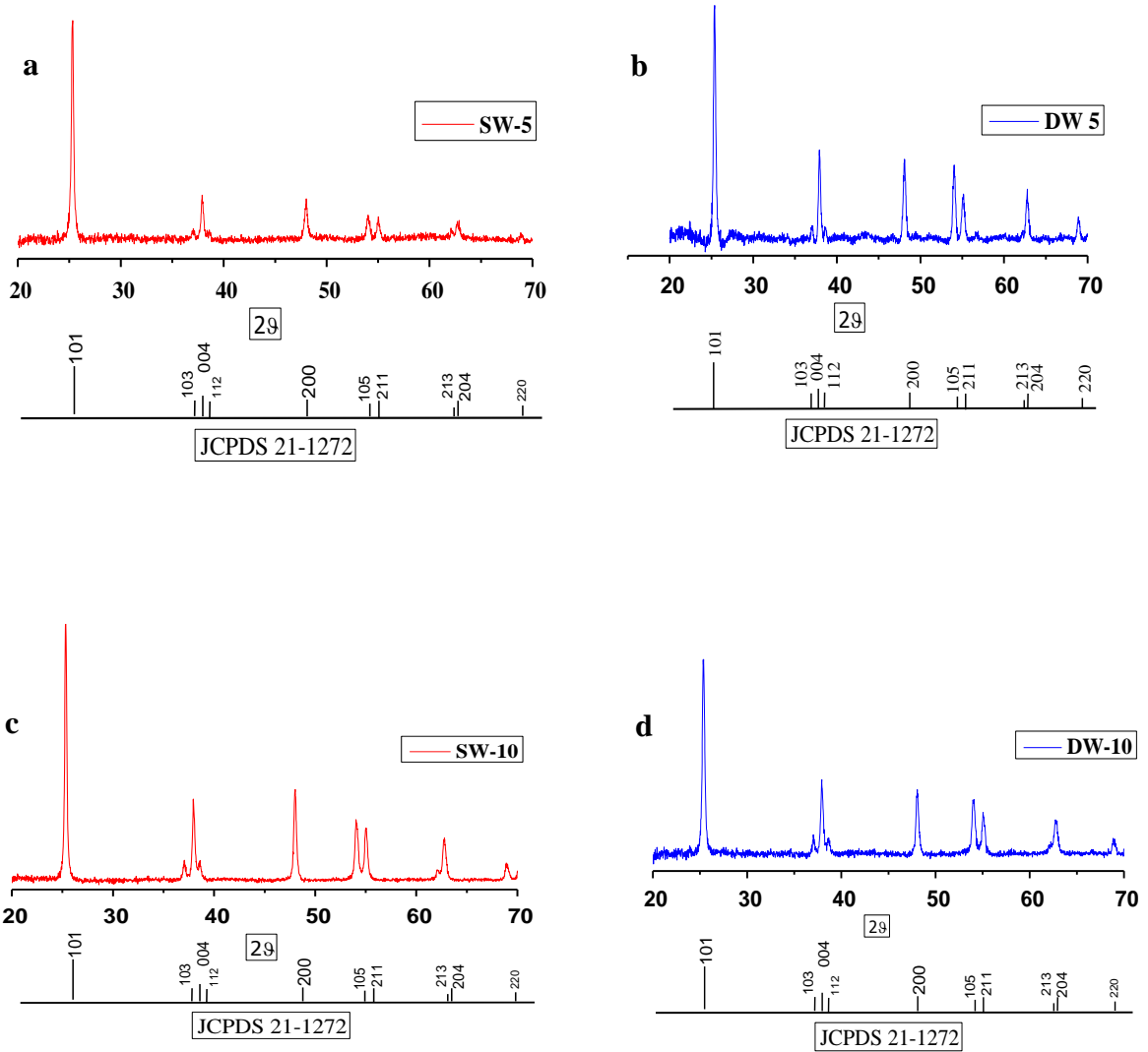


Figure 5-7 XRD patterns of removed a) single wall TiO₂ NTs heated at 5 °C /min, b) double wall nanotubes heated at 5 °C /min, c) single wall TiO₂ NTs heated at 10 °C /min, and d) double wall nanotubes heated at 10 °C /min. All samples are annealed at 500°C for 1 hour

Depth profile XPS characterization of as anodized nanotubes (Part 1-2) reveals that the amount of fluoride in the bottom of double wall nanotubes is much more

than single walls (Figure 5-8) . This may explain why the (004) peaks in double wall tubes are more intense than (101) peaks.

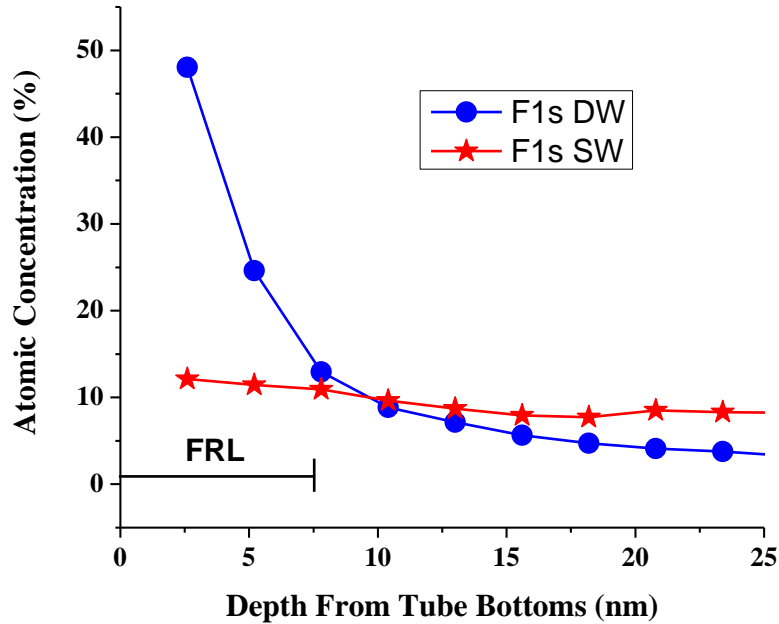


Figure 5-8 Comparison of XPS depth profiles of F1S in single and double wall tubes

Another important concern in the heat treatment of TiO_2 NTs is the formation of rutile phase. As the electron mobility in rutile phase is less than anatase, this phase is not desirable especially in the applications such as photovoltaics [2]. Some researchers reported the formation of rutile phase in nanotubes' walls [25], but others claimed that rutile phase forms just underneath the tubes (the compact oxide layer) at this temperature [50]. As can be seen in Figure 5-7, the present results show no evidence of formation of rutile phase in the removed nanotubes from the surface. Therefore the rutile peak detected in Figure 5-6 comes from the rather thick TiO_2 layer under the nanotubes.

5.4 Depth Profile XPS

XPS depth profile characterization studies of the as-anodized samples are a method proposed by some researchers to detect and measure the amount of contamination under the removed tubes from the foil. Sergiu *et al* showed that during anodization of Ti foil in electrolytes containing fluoride, a fluoride-rich layer (FRL) with stable titanium oxy-fluorides or titanium fluorides is formed between the bottom of double wall nanotubes and the Ti substrate [5].

This has been proposed to be because of the faster migration of fluoride ions by a factor of two with respect to oxygen ions towards Ti substrate in a high potential field during anodization [101]. Therefore, for a more precise comparison between single and double wall tubes, depth profile XPS was performed. In this case, the XPS profile of F1S for double wall tubes is similar to those in Sergiu's report [5], with FRL being 8 nm thick (Figure 5-9a). Therefore, assuming that the outer shell thicknesses of the tubes are about 16 nm (Figure 5-9 c), the total thickness of the nanotube *outer shell plus the FRL* could be estimated to be around 20 to 25 nm (internal wall region) as shown in Figure 5-9c.

The depth profile of C1S is shown in Fig 5-9b for the range of 20 to 50 nm (internal wall region) from the bottom of the removed double and single wall tubes. As can be seen there is no sign of carbon in this range for single wall tubes, while there is a considerable amount of carbon in this range in double wall tubes. This observation can be attributed to the lack of the inside shell in single wall nanotubes, whereas in case of double wall tubes it shows a level of carbon containing compounds entrapped inside the internal shell.

All in all, the depth profile XPS confirms the FTIR results that the synthesized single wall tubes are much cleaner than the double walls near the bottoms of the tubes (See *Section 5.1*).

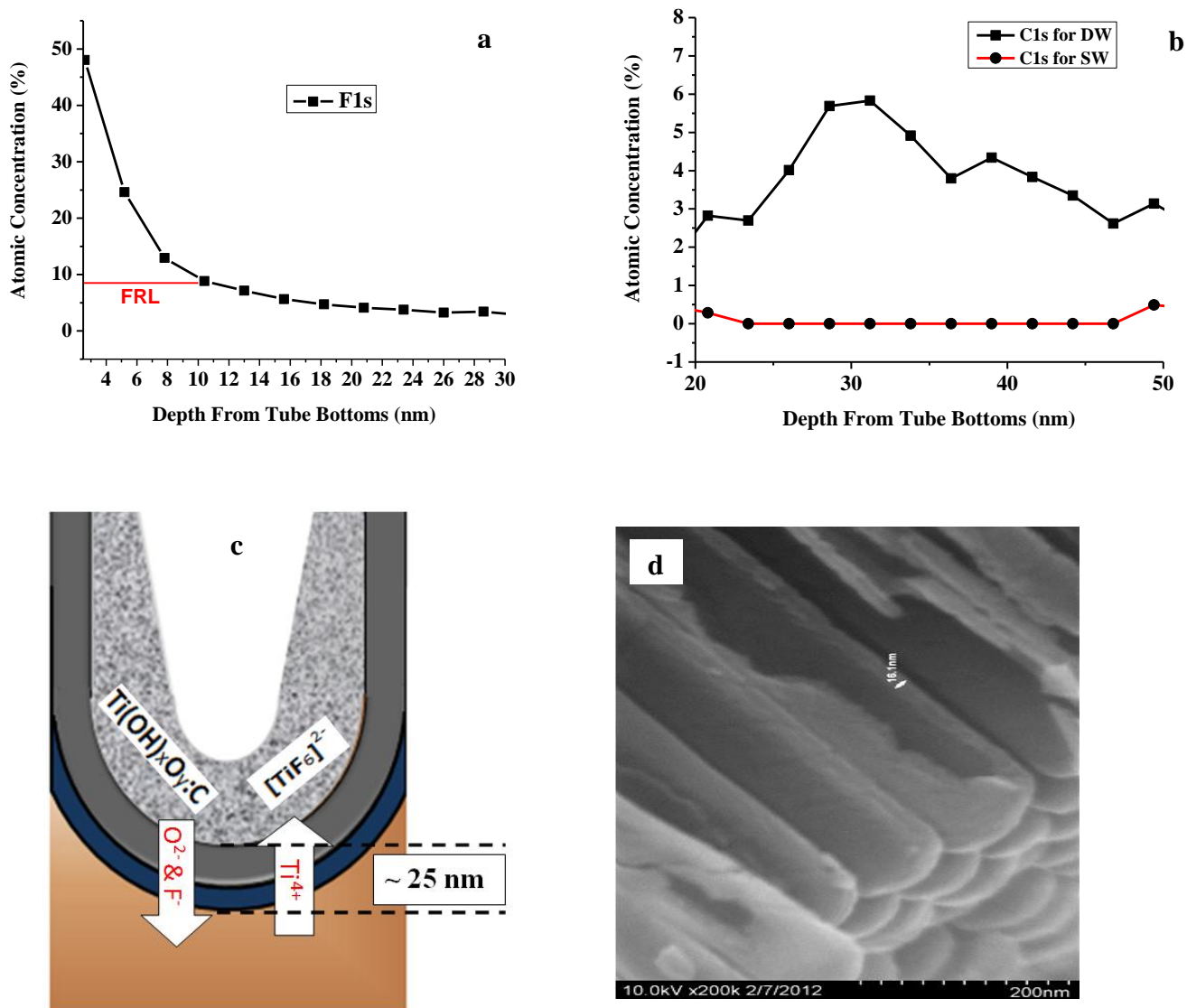


Figure 5-9a) XPS depth profile of F1S, b) XPS depth profile of C1S from the bottom of Double and Single Wall nanotubes, c) Schematic representation of different parts of TiO_2 nanotube layers, and d) The outer shell thickness near the bottom of the tubes.

5.5 Differential Scanning Calorimetric (DSC) Tests

The as-anodized TiO₂ nanotubes are in an amorphous form that must be transformed into crystalline through heat treatment to be used in applications such as photovoltaics. To investigate some parameters related to the annealing process, such as phase transformation temperatures and activation energies, differential scanning calorimetry (DSC) and thermogravimetric analysis (TGA) as thermoanalytical techniques are vastly used. Besides the known parameters, the interpretation of the DSC curves of a material might contain other useful information about its properties like its purity level and defect level.

The DSC profiles for the double wall and single wall nanotubes are shown in Figure 5-10a and 5-10c respectively. As can be seen from Figure 5- 10a double wall nanotubes show two sharp separate exothermic peaks. The first peak in double wall tubes ranging from 250 °C and 350 °C, could be related to the oxidative combustion of the ethylene glycol units as well as the degradation of the organic groups residue entrapped inside nanotubes [102-104]. The second exothermic DSC peaks of double walls, ranging from around 330 °C and 450 °C correspond to the amorphous to anatase transformation of titania [105, 106].

As another proof to the above discussion about the first DSC peaks for the double wall nanotubes, the comparable non-ambient XRD peaks of the DW tubes at different temperatures are shown in Figure 5-10.b. As is evident, there is no significant change in the peak heights around 300 °C, proving that the first exothermic DSC peak does not belong to a phase transformation in the structure

and is likely to be evidence for the presence and ignition of organic compounds during the heat treatment in DW tubes in this temperature range.

For the single wall TiO₂ NTs the first peak is negligible (Figure 5-10c) and the two peaks are almost merged together. This can be attributed to less decomposition of EG and entrapment of decomposition products inside the nanotubes confirming the FTIR results discussed in *Section 5.1*.

The weight change percent of the nanotubes are shown in Figure 5-10d. As can easily be distinguished the weight change in case of double wall tubes (~25%) is much more than single wall tubes with about 12% weight loss up to 400 °C. The sharp weight change slopes is another confirmation to the high amount of organics entrapped inside the tube after anodization at high voltages.

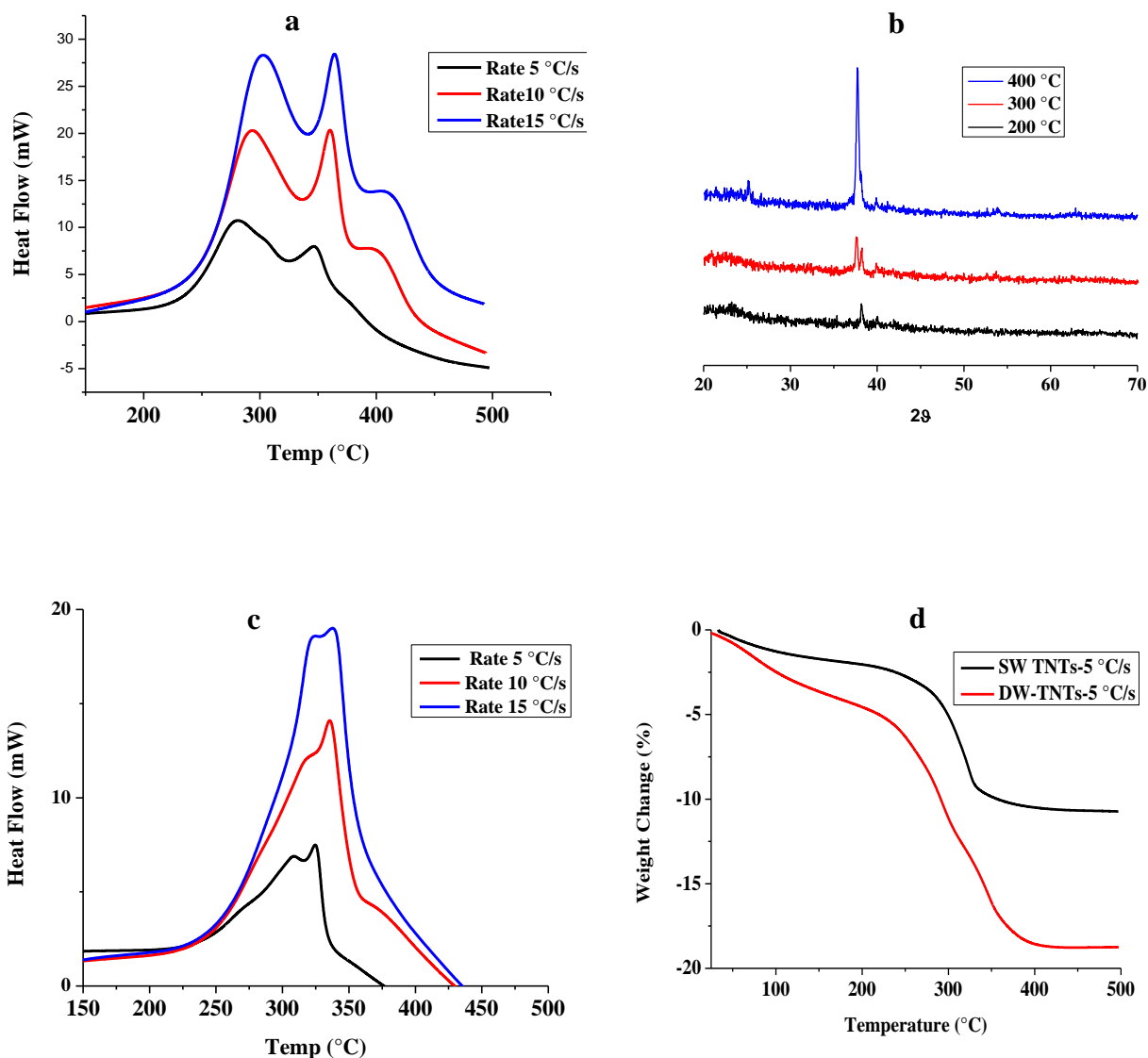


Figure 5-10 a) DSC profile for double wall TiO₂ NTs, b) Non-ambient XRD of double wall TiO₂ NTs at different temperatures, (heating rate: 5 °C/s), c) DSC profile for the single wall TiO₂ NTs, and d) The weight change of nanotubes with temperature (heating rate: 5 °C/s)

Since the two main DSC peaks overlap for both SW and DW nanotubes, a mathematical deconvolution based on Lorentzian approach was executed to fit the peaks. Figure 5-11 shows the DSC peaks of DW and SW tubes (heated at 15 °C/s), with their deconvoluted peaks shown in red using Origin 8.5 software.

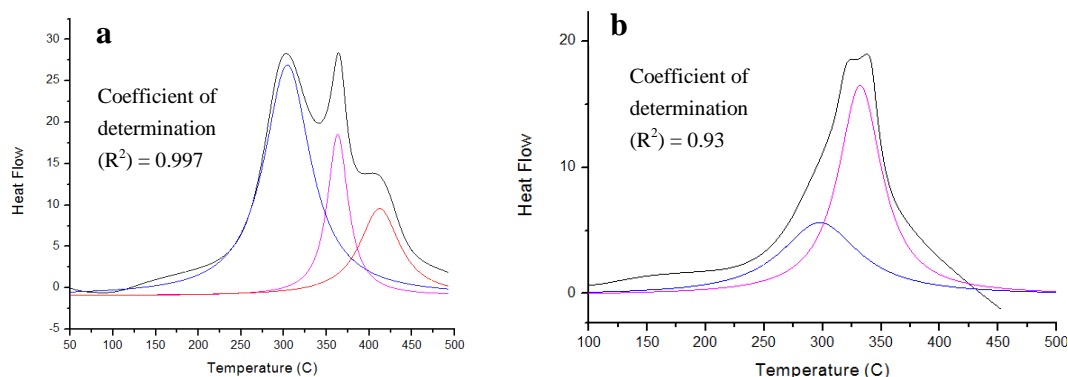


Figure 5-11 DSC peaks (Black) and the deconvoluted peaks from the mathematical curve fitting technique (colorful) of a) DW and b) SW nanotubes (heating rate:15°C/s)

Based on the fitted DSC curves shown in Figure 5-11, the organic removal peaks (first peak), start rising from about 150 °C to 200 °C. The onset of the anatase peak is about 280 °C for SW tubes while it is about 320°C for double walls. The range is very similar to that stated in the literature (See *Section 2.6*).

It should be noted that a third peak is evident in DSC of DW tubes at about 450 °C at higher heating rates (Figure 5-10a and Figure 5-11). It is evident from the TGA curve of the DW tubes at 15 °C/s (Figure 5-12) that the third peak is linked to a sharp and considerable weight change, while such a change is not seen in DSC of SW nanotubes. Thus it cannot be related to a phase transformation (like anatase to rutile) in the structure. It is likely correlated to the further combustion of organics to CO₂ and for evaporation of water from inside the tubes.

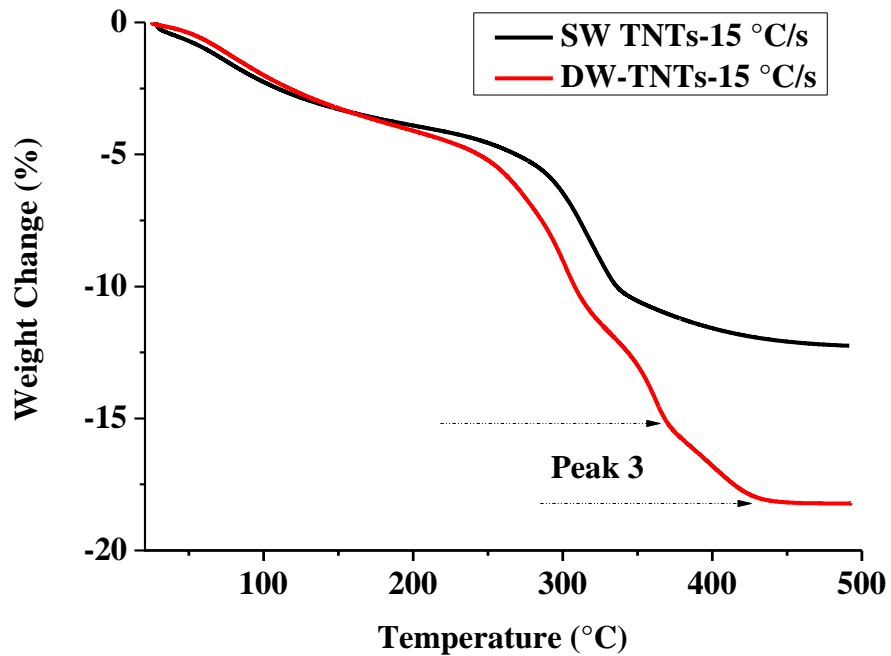


Figure 5-12 Weight change of double and single wall tubes during TGA; heating rate: 15 °C/s

To investigate in more detail, thermogravimetric analysis combined with a mass spectrometer (MS-TGA) experiments were conducted and results for single and double wall tubes are shown in Figure 5-13. The samples were heated at the 20 °C/min in air up to 600°C, kept at that temperature for an hour, and cooled with the same rate to the room temperature.

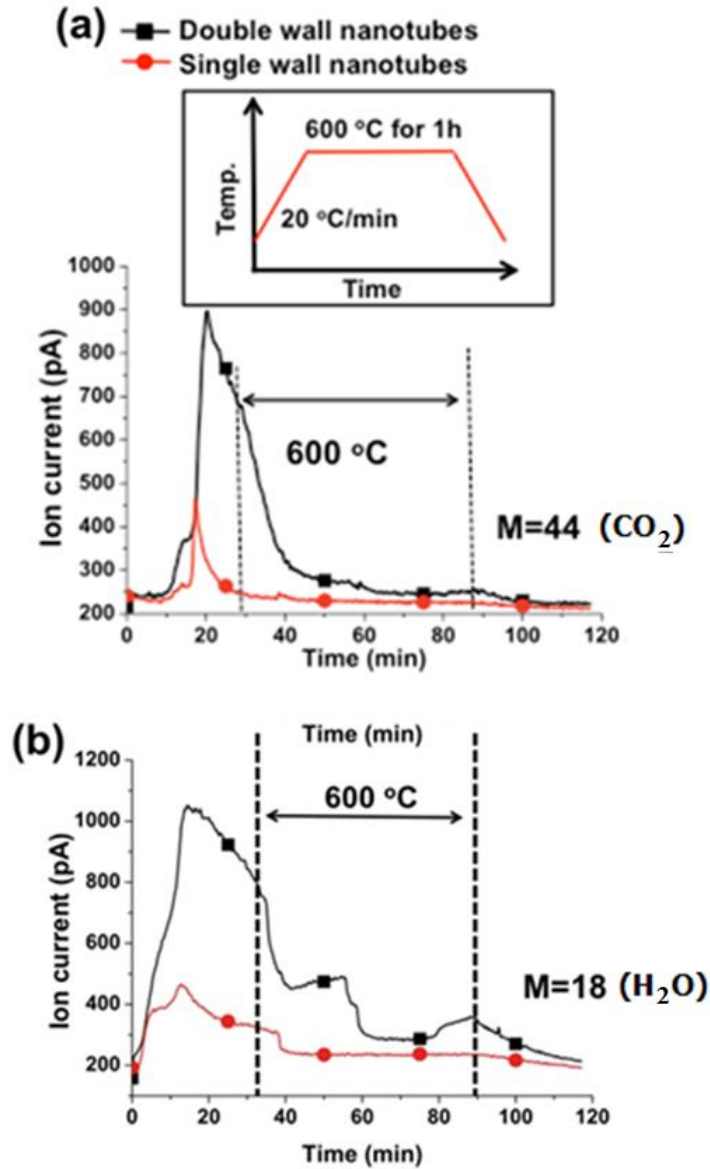


Figure 5-13 Thermal desorption profile for M=44 (CO₂), and M=18 (water) by TGA-MS analysis (from the author's previous publication) [7]

As can be distinguished from Figure 5-13a, the CO₂ (M=44) released from DW tubes has a sharp increase rate up to 400°C, and continues even after 20 minutes at 600°C. Water (M=18) discharge, (Figure 5-13b) has a sharp rate until about 300°C and even at 500 °C a considerable amount of water in DW tubes is

still being released. It is also noteworthy that a part of water is freed only at 600°C. The above MS-TGA results show that SW tubes are much cleaner than its rival, DW tubes. As the significant releases of CO₂ and water (H₂O) of DW nanotubes continue to about 400 and 300 °C respectively (Figure 5-13), the third peak in higher rate DSC curves of DW tubes (Figure 5-10a and Figure 5-11a) can be related to the further removal of remaining organics and water. It should be noted that in slower heating conditions (e.g. 5 °C/s), the liberation of these contaminating compounds mostly happens at lower temperatures; therefore no distinguishable peak is seen in DSC plot of 5 °C/s.

Another fact from the DSC curves is the phase transformation peak onset and the maximum heat flows of single wall tubes are less than double walls. This difference can be because of the wall thickness effect [105] . The single walls are thinner compared to double wall tubes so the transformation happens at lower temperatures.

5.6 Comparison of activation energies of amorphous to anatase transformations of DW and SW nanotubes from DSC results

The activation energy of amorphous to crystalline phase transformation can be derived from the Kissinger equation that is a derivative of Avrami equation for non-isothermal processes as follows:

$$\ln \frac{\phi}{T_p^2} = -\frac{Q}{RT_p} + \text{const.} \quad \text{Equation 17}$$

where T_p is the amorphous to anatase peak temperature (K) , ϕ is the heating scan rate ($^{\circ}\text{C/s}$), R is the universal gas constant, and Q is the activation energy for anatase formation in KJmol^{-1} [107].

To calculate Q , $\ln \frac{T_p^2}{\phi}$ is plotted against $\frac{1}{T_p}$ for single and double wall tubes in

Figure 5-14 heated with different rates.

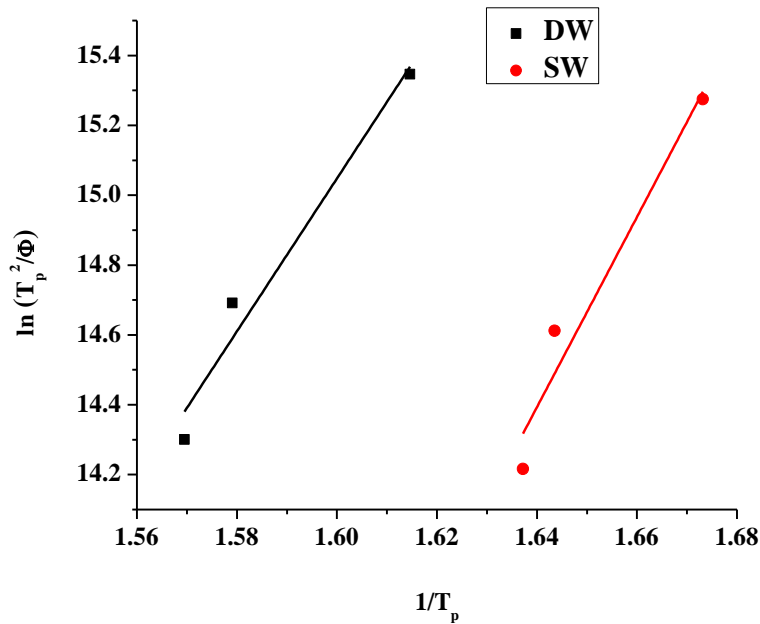


Figure 5-14 The Kissinger plots of single and double wall nanotubes calculated from DSC data (Each experiment was repeated at least three times and error bars are too small to be seen)

From the slope of the linearly fitted lines, the activation energy of the amorphous to anatase phase transformation of the tubes can be calculated to be 243 kJ/mol for SW and 196 kJ/mol for DW nanotubes. The activation energy of the transformation of double wall tubes is in a good agreement with the reported energy by other researchers for similar nanotubes [105, 108].

The probable reason for the difference between the activation energies of the SW and DW nanotubes can be the defects level. As shown in TEM pictures, the inside wall in double wall nanotubes is a highly porous layer and moreover the grain size of Titania in the outer shell of the DW tubes is shown to be much smaller than that of its SW counterpart (Figure 5-15 and Figure 5-16). These two factors increase the density of defects in double wall tubes, resulting in a highly heterogeneous nucleation and hence lower activation energy [105].

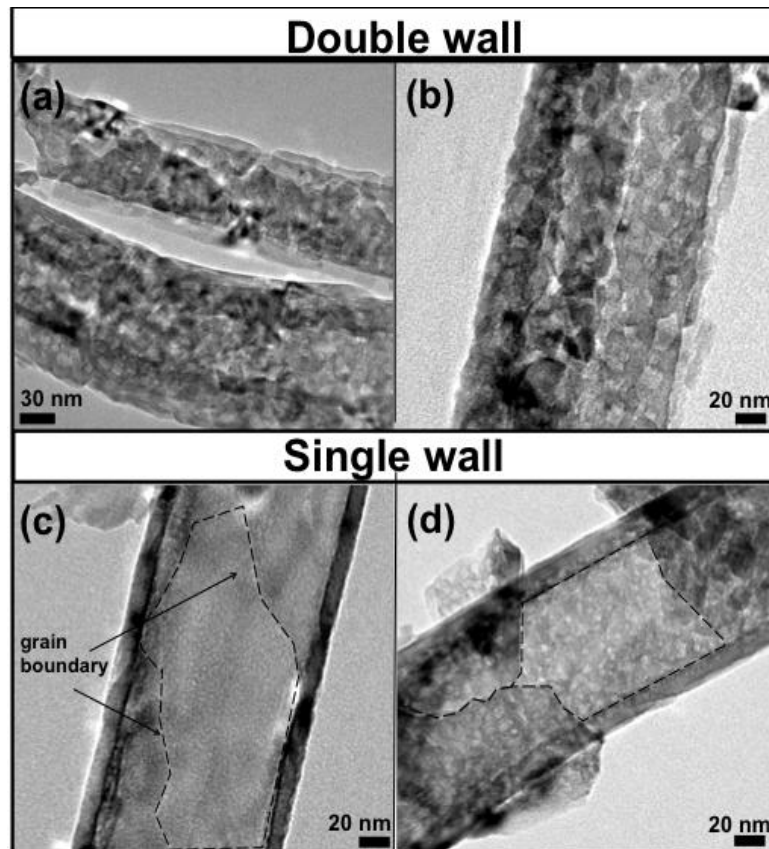


Figure 5-15 TEM images of heat treated double wall (a,b) and single wall (c,d) nanotubes at 500 °C for 1 hour (from the author's previous publication) [7].

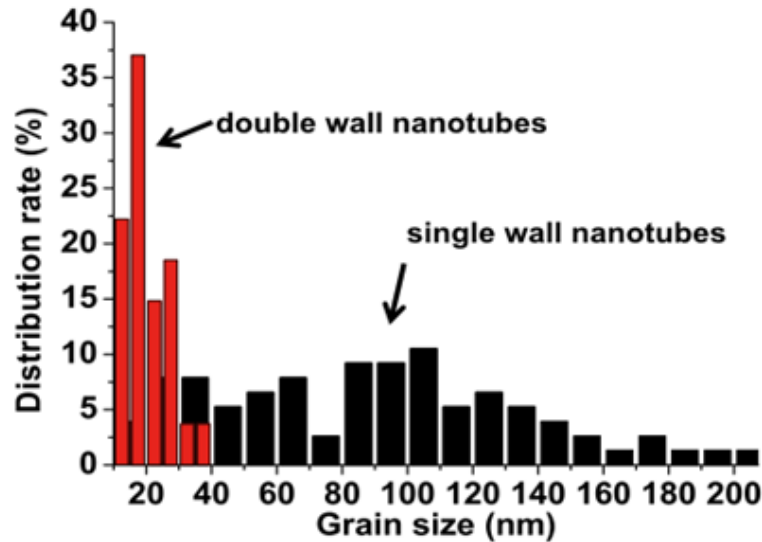


Figure 5-16 The distribution of grain sizes of single and double wall tubes (from the author's previous publication) [7].

5.7 Effect of heat treatment temperature on the conductivity of single wall nanotubes:

5.7.1 Variation of conductivity of amorphous nanotubes with temperature

The electrical conductivity of crystalline TiO₂ nanotubes plays an important role in many applications such as photovoltaic devices. However, there are only a small number of investigations published on the effect of annealing on the electrical conductivity of TiO₂ NTs [52, 56, 109]. In order to compare the conductivity of nanotubes, two-point measurements by simple top-bottom contacting were performed in at different temperatures. Alexei *et al* argued that for longer than 1 μm nanotubes the Van der Pauw measurement method (4-point approach) is not feasible because of the increasing overall resistance [52].

The result of the *in situ* measurement of the resistance of double and single wall tubes are shown in Figure 5-17a. The first point to be mentioned is that for most of temperatures, the single wall tubes are more conductive compared to their double wall rival. The resistance plots in both cases can be divided into 6 regions. The regions are numbered from I to VI for both samples' plots in Figure 5-17a. The first increase in resistance (region I) can be attributed to the low temperature evaporation of adsorbed water [52]. The resistance of the tubes remains roughly constant with increasing temperature in the second region (region II) followed by a slow decrease in region III for the double walls (between 120 °C and 180 °C). This temperature range (III) is the range that most probably the evaporation and oxidation of adsorbed organics and residual electrolyte in tubes occurs [110]. Therefore the resistance drops significantly in double wall TiO₂ NTs as they are shown to be more contaminated as confirmed by FTIR and DSC tests (See *Sections 5.1 and 5.5*), while there is a little change in resistance of SW tubes (region III)⁶.

⁶ It should be noted that generally we have $\rho = R \frac{A}{l}$, where ρ is the electrical resistivity, R is the electrical resistance, A is the cross-sectional area, and l is the length of the piece of material. In our samples, if the hollowness of the tubes is ignored as in Asmatulu *et al's* work [3], A is almost $1.77 \text{ cm}^2 \left(\pi \frac{(1.5 \text{ cm})^2}{4} \right)$, and l is almost 15 μm , so $\rho = 1180 \text{ R}$

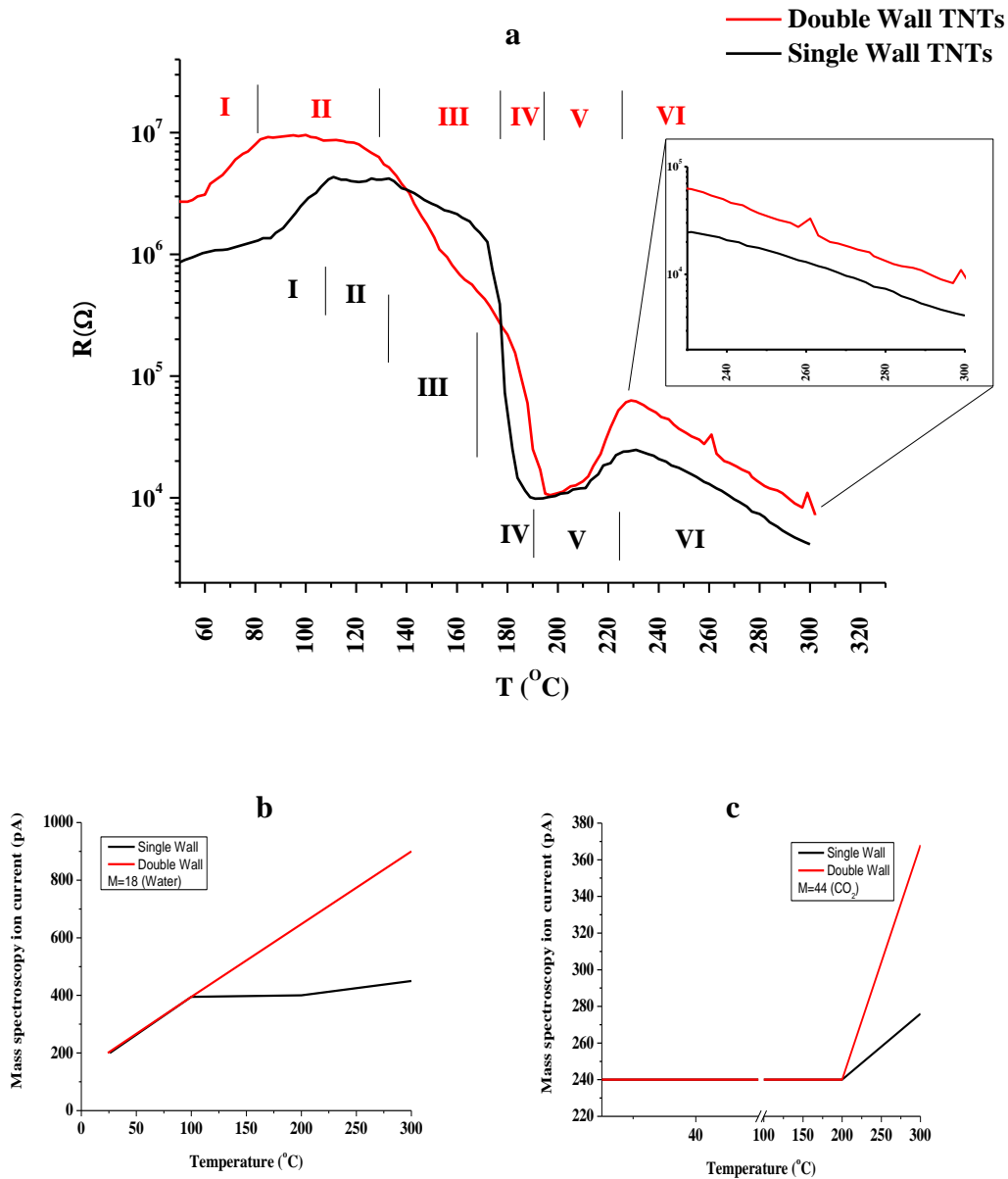


Figure 5-17 a) Variation of the resistivity of as prepared double and single wall tubes with temperature, and linearly fitted curves of thermal desorption profiles of double and single wall nanotubes for b) Water and c) CO₂ under 300 $^{\circ}\text{C}$ (Re-plotted of the Figure 5-1)

The re-plotted and linearly fitted curves of thermal desorption profiles (Figure 5-13) in Section 5.6 of double and single wall nanotubes (MS-TGA) up to 300 $^{\circ}\text{C}$

are also shown in Figure 5-17 b and c. In case of water it is evident (Figure 5-17 b) that the release from DW tubes (in black) is almost linear up to 300°C. In contrast, the water in SW tubes discharges in 3 steps. First the water release rate is linear up to 100°C following the same trend of DW release. Second, there is almost no H₂O release between 100 and 200 °C, but continue to a third step with much lower rate than the DW nanotubes between 200 and 300 °C. Unlike water, there is no CO₂ formation under 200 °C in both tubes. Therefore the CO₂ observed may come from the decomposition of organics during the anodization. The CO₂ level increases linearly between 200 and 300 °C in both tubes, but much faster in double wall tubes than SW nanotubes.

Therefore the sharp fall in resistance followed by a short stable progress in region IV for both SW and DW tubes from about 180°C to about 210°C in Figure 5-17a can be explained as in this temperature region the sudden and very fast release of CO₂ starts (Figure 5-17c).

Alexei *et al* have reported a similar drop in resistance starting from about 200°C. They related the resistance drop to crystallization of the amorphous phase to the anatase form [52]. This change is also shown by Ramazan *et al* [49]. They correlated it to a “nanoporous” anatase formation without considering the probable effect of any contamination in this temperature range. However, DSC analyses confirmed by XRD results show that the phase transformation starts at higher temperatures (Figure 5-10b). Nevertheless the first peak in DSC results (related to the combustion of organics) starts its sharp rise from about 200 °C (Figure 5-10 and 5-11). Moreover, the MS-TGA plot (Figure 5-17c) illustrates the

start of CO₂ release at about 200°C. Therefore, the sharp fall in resistance of tubes about 200°C is more likely due to the start of the combustion of remaining organic contaminations left in the tubes from anodization.

The drops in resistance continue at temperatures higher than 230°C (region VI, Figure 5-17a) with slower rates compared to region IV, but similar for both SW and DW tubes correlates to the sharp release of CO₂ in this range (Figure 5-17c) as well as the start of anatase phase formation which activates in this region (second peak in DSC peaks of the tubes (Figure 5- 10 and 5-11).

The short increase in resistance in region V could arise from the fast removal of water of crystallization between 250 and 300 °C (Figure 5-17b) besides the oxidation of the substrate metal occurs in this temperature range.

As can be seen in the inset of Figure 5-17a, there is a linear correlation between ln(R) and temperature. From this region's data, the activation energy for conductivity of the anatase phase can be found. Based on Arrhenius correlations [49]: $R \propto \exp\left(\frac{-Q}{RT}\right)$ in which Q is the activation energy , R is the universal gas constant, and T is the temperature. Assuming that the two lines are completely linear, for each two points on a line we have

$$\frac{R_2}{R_1} = \exp\left(\frac{Q}{R} \left(\frac{1}{T_2} - \frac{1}{T_1}\right)\right) \quad \text{Equation 18}$$

Supposing that $R = 5.189 \times 10^{19} \text{ eV.K}^{-1}.\text{mol}^{-1}$ (universal gas constant equal to $8.3144621 \text{ J K}^{-1} \text{ mol}^{-1}$), Q for the double wall tubes will be 0.78 eV which is near

to what reported by Ramazan *et al.*[49], while it is 0.6 eV for single wall tubes. This shows that the energy needed to transfer an electron in anatase SW tubes is almost 23% less.

5.7.2 Variation of conductivity of annealed nanotubes with temperature

5.7.2.1. Effect of heating / cooling rate on the conductivity of nanotubes

The conductivity of TiO₂ nanotubes has been shown to depend strongly on heat treatment temperatures [52, 109, 111]. The electrical DC-resistance measurement of samples also reveals a strong dependence on heat treatment temperature of the tubes as well as heating / cooling rates. As can be seen in Figure 5-18, single wall nanotubes are much more conductive at all test temperatures compared with double wall ones. This phenomenon is attributable to the negative effect of the higher level of organic contaminations detected in conventional double wall nanotubes. The ignition and degradation of organics will result in diffusion of carbon inside the tubes, which according to Kar *et al* and Tu *et al* makes the rutile phase formation more favourable yielding in higher resistance [105]. Although Kar *et al* discussed that decrease of anatase to rutile phase change temperature in carbon doped nanotubes might be related to the effect of carbon atoms on the grain sizes and thickness of the nanotubes, this phenomenon may be due to the crystallographic effects of carbon atoms on the Titania lattice structure [105]. Furthermore, as shown before (*Figure 5-15 in Section 5-5 and Figure 5-6 in Section 5.2*), the inside wall of the double wall TiO₂ NTs has is a highly porous phase. This inside layer can drastically decrease the electron mobility [11] and

increase its electrical resistance as well as the probability of charge recombination in photovoltaic devices [7].

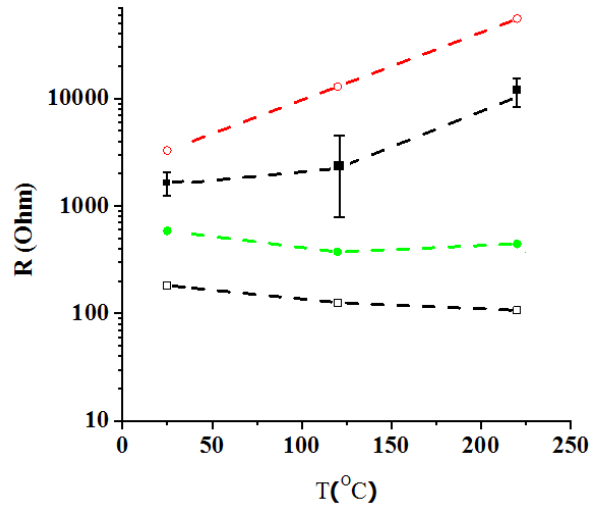


Figure 5-18 Comparison of the electrical resistance of crystalline single wall and double wall nanotube layers of 15 μm thickness at different temperatures, a) single wall nanotube, treated at 500°C, with 1 °C/s heating/cooling rate, b) single wall nanotube, treated at 500°C, with 0.1 °C/s heating/cooling rate, c) double wall nanotube, treated at 500°C, with 1 °C/s heating/cooling rate, and d) double wall nanotube, treated at 500°C, with 0.1 °C/s heating/cooling rate. The dashed lines in the figure are a “guide to the eye”.

The room temperature conductivity of single wall tubes heat treated at 500 °C, with the same ramp rates, are almost 1 order of magnitude higher than double wall tubes. Beside the abovementioned reasons, the smaller average grain size of double walls, which means they have a higher defect density, may also contribute in this effect (Figure 5-16).

It should also be noted that for the SW tubes an almost temperature independent resistance is obtained. However the resistance of double wall TiO₂ NTs increases with increasing temperatures above 200 °C.

The other fact that can be found from Figure 5-18 is the higher the heating ramp rate the more conductive the nanotubes. As reported before for double wall tubes [5], this effect can be attributed to the fact that higher heating/cooling rates lead to bigger nanocrystallites of TiO_2 , and hence less grain boundaries in the nanostructure. Besides, with the lower ramp rates rutile phase comes to existence as can be seen in XRD patterns for the samples heat treated at 500°C (Figure 5-19). Rutile formation decreases the density of states, resulting in lower conductivity [111]. Moreover, at higher annealing rates, the thickness of the underlying oxide layer between the nanotubes and the foil would be less resulting in higher conductivities [50, 52, 112].

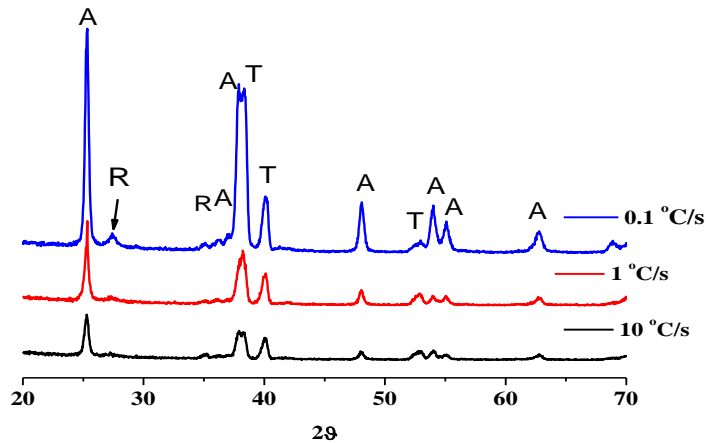


Figure 5-19 XRD spectra of the annealed single wall TiO_2 nanotubes (A = anatase, R = rutile and T = titanium) annealed at 500°C with different heating/cooling rates.

5.7.2.2. Effect of annealing temperature on the conductivity of single wall nanotubes

The variation of conductivity of single wall tubes annealed at different temperatures with different heating / cooling rates are shown in Figure 5-20.

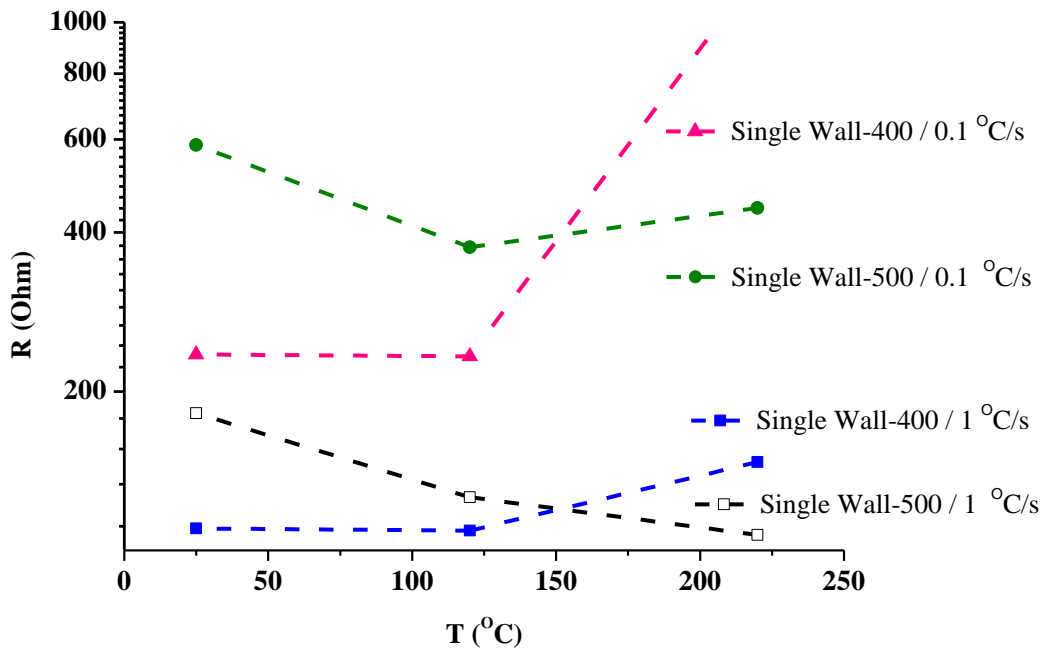


Figure 5-20 Comparison of the electrical resistance of crystalline single wall nanotube layers of 15 μm thickness at different temperatures, a) single wall nanotube, treated at 500°C, with 1 °C/s heating/cooling rate, b) single wall nanotube, treated at 400°C, with 1 °C/s heating/cooling rate, c) single wall nanotube, treated at 500°C, with 0.1 °C/s heating/cooling rate, and d) single wall nanotube, treated at 400°C, with 0.1 °C/s heating/cooling rate. The dashed lines in the figure are a “guide to the eye”.

Heat treatment at 400 °C, as evident from Figure 5-20, yields tubes that are 15 times more conductive at room temperature than their 500 °C annealed double wall counterparts.

It has been shown that the rutile formation temperature can be as low as 430 °C [49, 50, 52]. Therefore the lower conductivity of the tubes treated at 500 °C can be due to the formation and growth of the rutile phase (Figure 5-21), and hence a lower level of density of states [111] at higher heat treatment temperatures in the metal-oxide interface because of the direct oxidation of the underlying Ti metal. Furthermore it has been shown by Albu *et al* that annealing at higher temperatures creates defects (such as nanoscopic cracks) in the walls of the nanotubes that in addition to the formation of rutile can decrease the electron mobility in tubes annealed at higher temperatures [50].

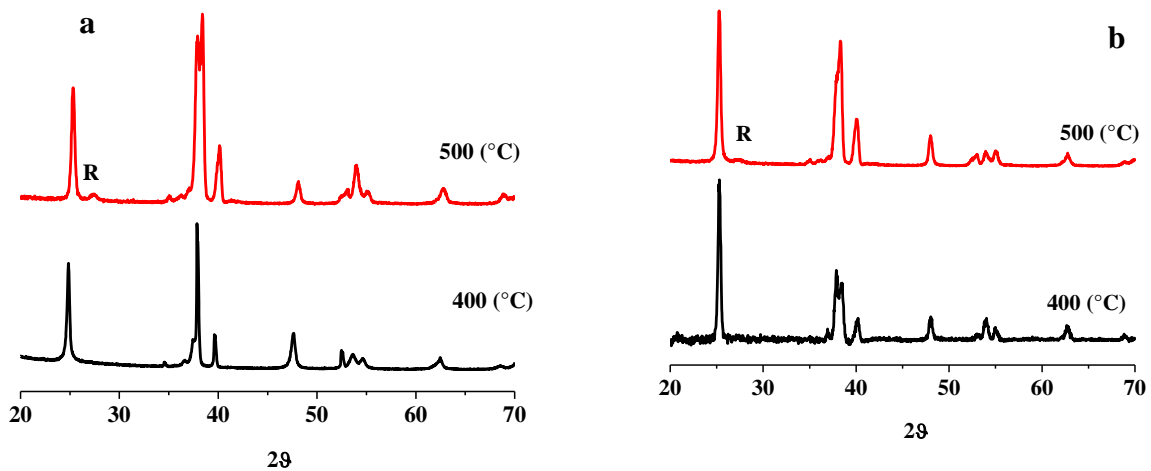


Figure 5-21 Comparison of the XRD patterns of annealed a) double wall, and b) single wall nanotubes at 400 and 500 °C

The reason for the increase in the resistance of the 400 single wall tubes at high test temperatures is not entirely clear.

The final point to note for 400 °C annealing is that the higher heating/cooling rates yield higher conductivities, likely due to a thinner oxide layer forming

beneath the nanotubes and/or the effect of the grain size. This is the same phenomenon that is seen with the 500 °C samples and discussed in *Section 5.6*.

5.8 Diffuse reflectance UV-VIS of SW and DW nanotubes

5.8.1 Calculation of optical bandgap of SW and DW- TiO₂ NTs

The minimum energy difference between the valance band and the conduction band of a semiconductor (optical bandgap) can be estimated from diffuse reflectance UV-VIS data. For this purpose *Tauc law* is usually utilized to predict the bang gap. Based on this law the *absorption* or *extinction* coefficient of a semiconductor for a transition near the band-gap is well described as:

$$\alpha(h\nu) = B (h\nu - E_g)^n \quad \text{Equation 19}$$

where α is the *extinction coefficient*, $h\nu$ is the photon energy, B is the absorption constant and E_g is the material's optical gap [113, 114].

The extinction coefficient, α , is proportional to the *reflectance* of the material given by the *Kubelka-Munk (K-M) function*:

$$F(R_\infty) = \frac{(1-R_\infty)^2}{2R_\infty} \quad \text{Equation 20}$$

So,

$$F(R_\infty) (h\nu) \propto B (h\nu - E_g)^n \quad \text{Equation 21}$$

where R_∞ is the reflectance of a thick enough film that will not change by further increasing the film thickness. The power n in Equation 3 and Equation 5 is assumed to be 2 for amorphous materials and those with indirect allowed

transition bandgap and $\frac{1}{2}$ for semiconductors with direct allowed transition bandgaps [115].

Following the literature, n is assumed to be 2 for anatase TiO_2 (indirect allowed transition) [25, 43, 114]. Deploying the *Tauc method*, to estimate the E_g of a material graphically, $F(R_\infty) (h\nu)^{\frac{1}{2}}$ should be plotted against $h\nu$. The plot contains a linear part related to the absorption edge of a semiconductor. The material's E_g can be estimated from the extrapolation of the linear part to $F(R_\infty) = 0$ [114, 116].

The UV-VIS reflectance spectra of single and double wall nanotubes are shown in Figure 5-22.

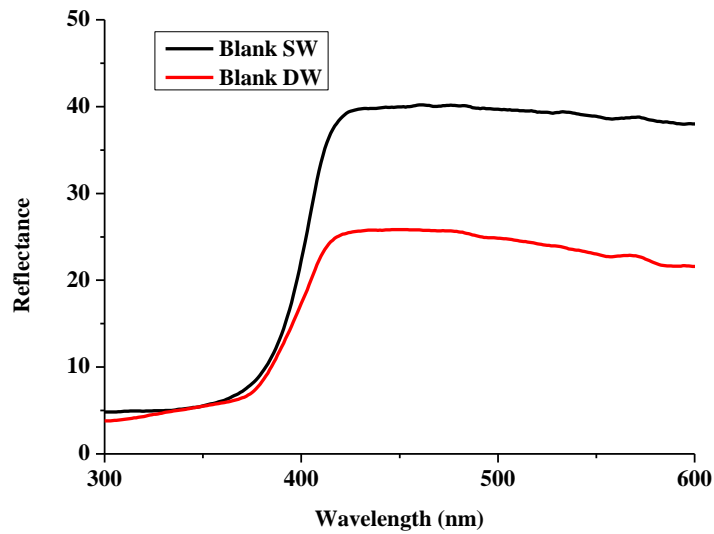


Figure 5-22 Diffuse reflectance UV-VIS spectra of single and double wall nanotubes heat treated at 500 °C for one hour.

To determine the optical bandgap of the SW and DW nanotubes, their Tauc plot are constructed from their diffuse reflectance UV-VIS data (Figures 5-23 and 5-24). Figures 5-23a and 5-24-a show the Tauc plots for SW and DW nanotubes respectively. Extrapolation of the linear part of the curve to $F(R) = 0$ yields 2.97 eV as the bandgap for SW nanotubes (Figure 5-23a). However for the DW tubes, the reflectance curves in Figure 5-24a reveals that the curve in the middle linear part is composed of two linear parts. Extrapolation of the two lines to $F(R)=0$ in Figure 5-24a for DW nanotubes yields 2.97 , and 2.89 eV. To analyze this (double-slope linearity) in more detail and prove, the derivatives of $[F(R_{\infty})(h\nu)]^{\frac{1}{2}}$ versus photon energy are plotted in Figure 5-23b and Figure 5-24b. For the SW tubes Figure 5-23b shows an approximately one step flat level between 3.1 and 3.2 eV related to the linear “middle” part in Figure 5-23a .

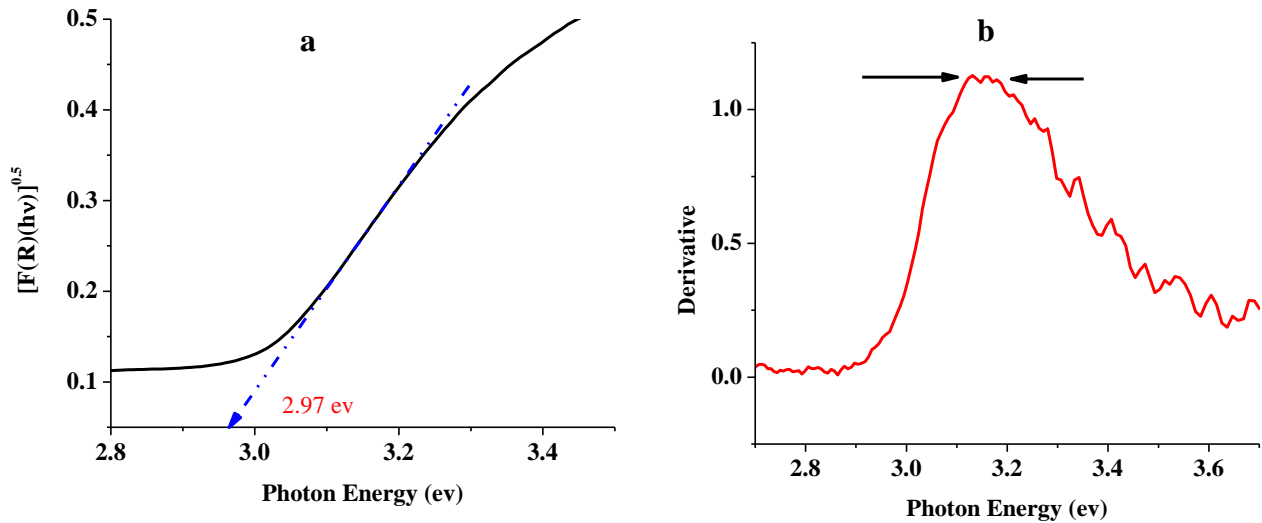


Figure 5-23 Tauc plot and b) derivative of $[F(R_{\infty})(h\nu)]^{\frac{1}{2}}$ versus photon energy for SW nanotubes

Furthermore, Figure 5-24b is the first derivative of $[F(R_{\infty})(h\nu)]^{\frac{1}{2}}$ versus photon energy for DW tubes showing a *two step* roughly flat level between 3.05 and 3.08 eV and 3.2 and 3.25 eV related to the two linear parts in Figure 5-24a.

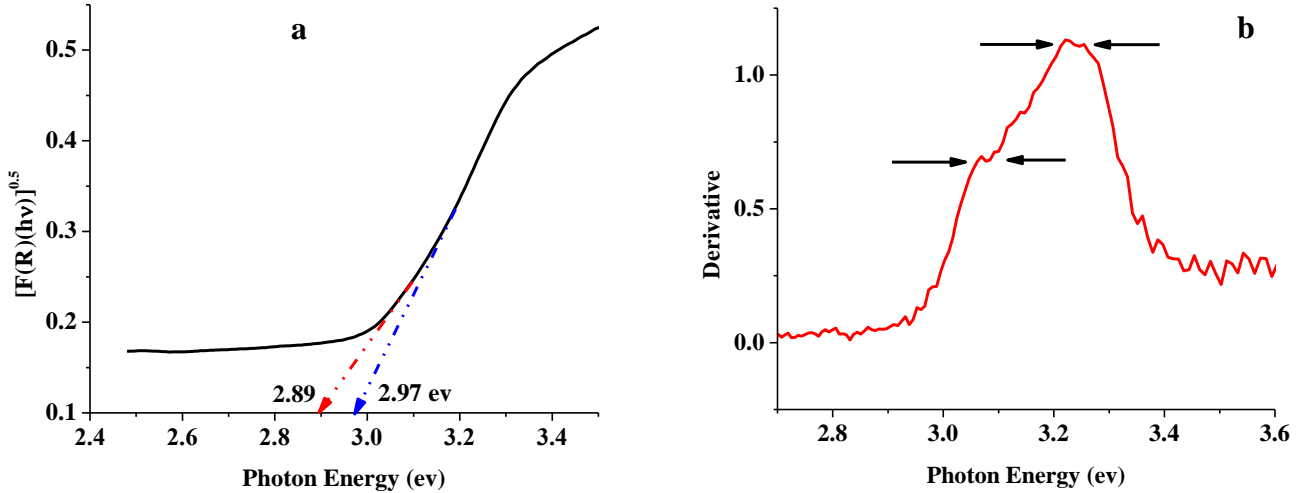


Figure 5-24 a) Tauc plot and b) derivative of $[F(R_{\infty})(h\nu)]^{\frac{1}{2}}$ versus photon energy for DW nanotubes

The optical bandgap of bulk anatase TiO_2 is reported to be 3.2 eV [2]. However, according to Schmuki *et al*, unlike aqueous electrolytes, anodization of nanotube arrays in organic solvents results in a lower bandgap of 2.85 eV and a tail in photoresponse owing to carbon remnants [112]. This result is confirmed also by Mahajan for nanotubes grown in ethylene glycol [117]. Grimes and Mor have also shown that the linear part of the Tauc plot of the tubes has two slopes resulting in two different bandgaps a bigger and a smaller gap [25]. They related the smaller bandgap to the high degree of lattice distortion in nanotubes. Hence, the high density of vacancies increases the trapping states yielding in a lower

bandgap. Yet they have not discussed why such a phenomenon is seen for the nanotubes from organic electrolytes.

However, the results in this work show that the division of the linear part of the Tauc plot for DW tubes into two parts can be related to its nanostructure. The higher bandgap of 2.97 eV for DW tubes is similar to the bandgap of the SW tubes (Figure 5-23a). This could be the bandgap of the outer wall of DW tubes.

Moreover the lower bandgap of DW nanotubes (2.89 eV) could be due to the bandgap of the porous internal, which was shown to have a rather high amount of carbon. So, carbon doping is very likely to happen in the porous layer inside tubes, resulting in a slightly lower bandgap [112, 118].

It is noteworthy that Li *et al* believe that carbon doping may change the nature of the bandgap of TiO₂ from indirect to direct. They used $[F(R_{\infty}) (h\nu)]^2 - h\nu$ curve to estimate the bandgap [119].

5.8.2 Diffuse reflectance UV-VIS of CdSe sensitized SW and DW nanotubes:

Semiconductor sensitized solar cells are of the interest of many researchers as they have exciting opto-electronic properties. Tunable bandgap, high extinction coefficients and improved light absorption properties are some of their interesting properties. In this study the optical property of a semiconductor (CdSe) sensitized SW nanotubes are investigated using UV-VIS experiments and a comparison is also made with CdSe sensitized DW nanotubes.

To enhance the light absorption of TiO₂, small bandgap inorganic nanocrystals such as CdSe are widely used. The most convenient method to sensitize TiO₂ with these particles is the successive ionic layer adsorption and reaction method (SILAR) [82, 120]

In general CdSe is a direct bandgap II-VI semiconductor. Variation from the bulk semiconductor to small the quantized size crystals results in a quantum confinement effects and size-dependent bandgap. The band-gap energy increases as the particle size decreases and therefore, the quantum sized CdSe has greater bandgap than the bulk material (1.74eV) [82] which arises from very small grain and the resulting quantum confinement of electronic states [121]

Figure 5-25 shows the UV-VIS spectra of DW and SW nanotubes coated with CdSe by 10 SILAR cycles. As can be seen, the onset of light absorption for SW nanotubes occurs at about 665 nm which is equivalent to a bandgap energy of 1.86 eV. However, the sensitized DW nanotube (Figure 5-25a) shows a double slope linear part (similar to the simple DW tubes). The first absorption onset for sensitized DW nanotubes is about 665 nm, which is similar to SW tubes, and the second linear part yields to about 640 nm (representing 1.93 eV bandgap) as the second absorption onset.

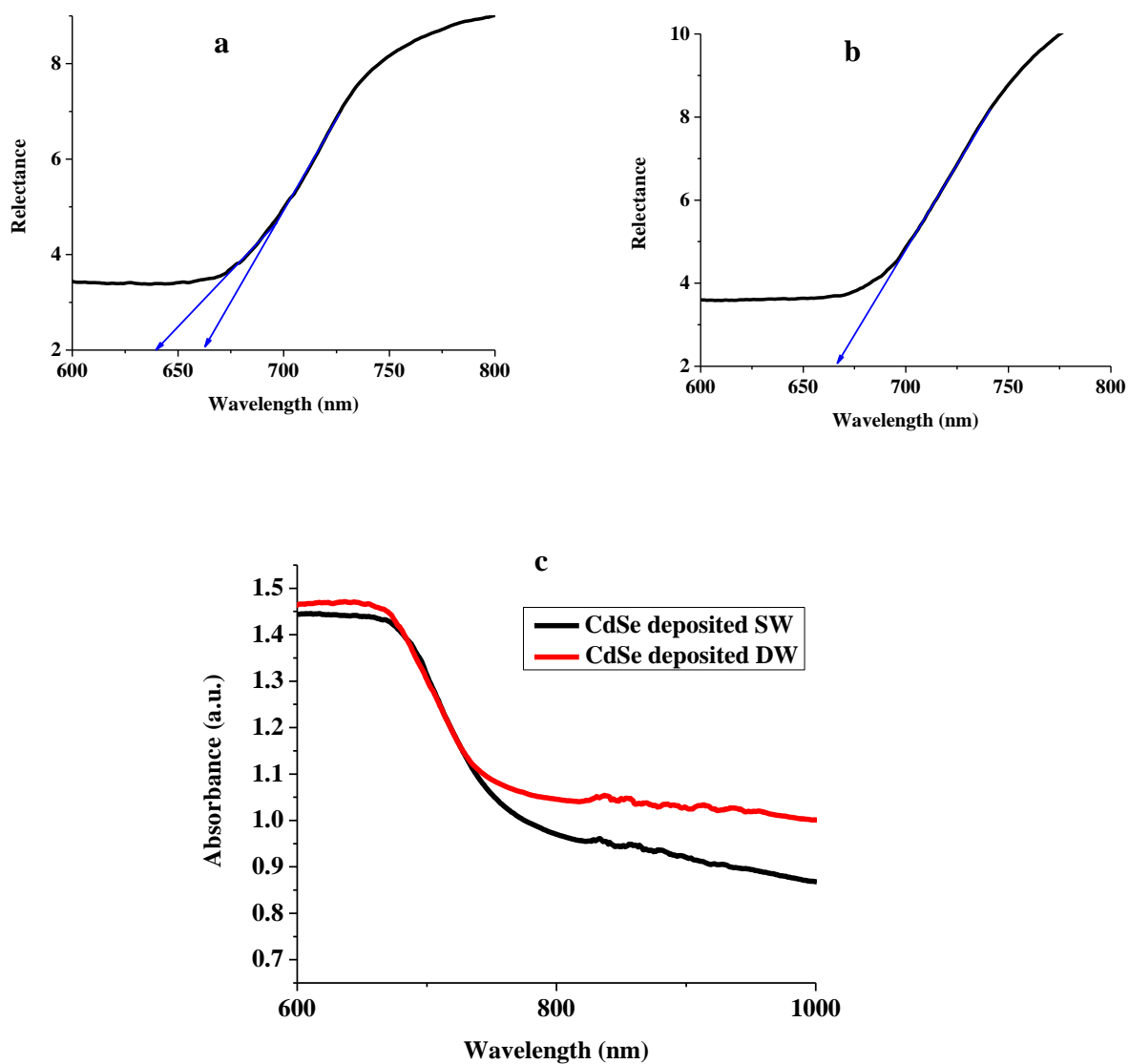


Figure 5-25 UV-VIS spectra of CdSe sensitized a) DW, b) SW nanotubes, and c) absorbance of 10 cycle CdSe sensitized SW and DW- TiO₂ NTs

This experience and the difference between the two nanotube structures could be again related to the double wall nanostructure of the common EG-nanotubes. The internal shell of the nanotubes, as observed before, is a highly porous layer as a result of the decomposition and evaporation of the organic residue. Therefore, because of the much higher surface energy of the internal shell compared to the

flat surface of the outer shell, deposited CdSe particles would be smaller on the inside shell as very small curvature favors heterogeneous nucleation. Thus quantum confinement increases in the CdSe and this yields to bigger bandgap of 1.93 eV. Though the outer shell is similar in both DW and SW, showing a 1.86 eV bandgap.

5.9 Conclusion

The anodically synthesized TiO₂ single walls from mixed EG:DMSO-based electrolytes have been characterized and compared to their more common double wall counterparts from EG-based electrolytes. In the first part of the chapter the differences between the chemical compositions and crystalline nanostructure of single and double wall TiO₂ NTs were discussed.

FTIR analysis of electrolytes before and after anodization, on the one hand show much higher loss of C-O and C-H stretches and more water in EG compared to EG:DMSO. This suggests that electro-oxidation of EG occurs during the high voltage anodization leading to carbonaceous organic compounds and water. On the other hand, FTIR of the as-formed double wall TiO₂ NTs shows a significant level of carbon containing compounds compared to the single wall TiO₂ NTs from EG:DMSO-based electrolytes. Therefore it is concluded that DMSO suppresses the decomposition of EG.

The XRD investigations of the nanotubes on foils and the nanotubes removed from foils confirm the formation of anatase phase. However, a difference was found in the preferential orientations between SW and DW tubes on the foil as

well as between the tubes on the foil and detached from it. The differences are explained based on XPS depth profile results. They show that DW- TiO₂ NTs contain more fluoride under the TiO₂ NT layer which is thought to be adsorbed to one of the surfaces decreasing its surface energy, hence promoting the probability of preferential growth in a special direction.

Besides, XPS depth profiles of as-formed TiO₂ NTs proved that the DW nanotubes hold much more carbon contamination arising from their internal layer. Based on these findings a completed mechanism of the formation of an internal shell inside the outer shell of double wall nanotubes has been proposed.

In the second part of the chapter, the characteristic properties of the single wall were investigated and comparisons made with the properties of double wall TiO₂ NTs.

The exact transformation temperatures and the activation energies of amorphous to anatase Titania were calculated for SW and DW nanotubes by DSC experiments. MS-DSC experiments were also performed to check the levels of contamination of SW and DW- TiO₂ NTs. This revealed that SW nanotubes are purer and burning of carbon containing organics may happen up to temperatures as high as 400 °C in DW- TiO₂ NTs resulting in probable doping while this phenomenon is not significant in SW nanotubes.

Electrical conductivities of tubes (SW and DW) were also measured and reported. The outcomes showed that single wall nanotubes are 10 to 100 times more conductive with conductivities varying with heat treatment temperature and

with heating/cooling rates. These are discussed to be because of smaller grain sizes, higher amounts of the rutile phase formed during annealing and the nanoporous nature of the internal shell in DW nanotubes.

Finally UV-VIS of the annealed tubes was reported and their bandgaps calculated. Analysis of DW and SW nanotubes showed that both of them have a bandgap of 2.97 e.V, however DW nanotubes have an additional bandgap of about 2.89 e.V which can arise from the diffusion of carbon to the internal nanoporous shell of DW TiO₂ NTs during the heat treatment.

5.10 Effect of heat treatment ramping rates on the morphology of nanotubes

In a preliminary study it was found that unlike the common double wall nanotubes, single wall nanotubes cannot survive high heating/cooling rates and the tubes' walls break in to particles. Figures 5-26 and 5-27 show preliminary results of the effect of heat treatment ramping rates on the morphology of single wall and double wall nanotubes. As can be seen in Figure 5-27a,b, the heating/cooling rate of 0.1 °C/s results in very smooth tube walls with open tops, however 1 °C/s rate makes the walls rougher and less smooth (Figure 5-27c). With increasing the rates to 10 °C/s nanotubes lose their shape, some break and small TiO₂ particles emerge on tubes' walls (Figure 5-27d). Furthermore, as can be seen in Figure 5-27 e, a thick layer of anatase phase covers the surface of the tubes and blocks them. Further rising of the heating/cooling rates to 50 °C/s deforms the whole nanotubular structure to a totally mesoporous TiO₂ particles with a thick top layer consisted of big anatase particles (Figure 5-27f,g,h). It

should be mentioned that such deformation of nanotubular nanostructure was not seen in DW NTs. This may be because the inside wall of double wall tubes helps them resist against thermal stresses.

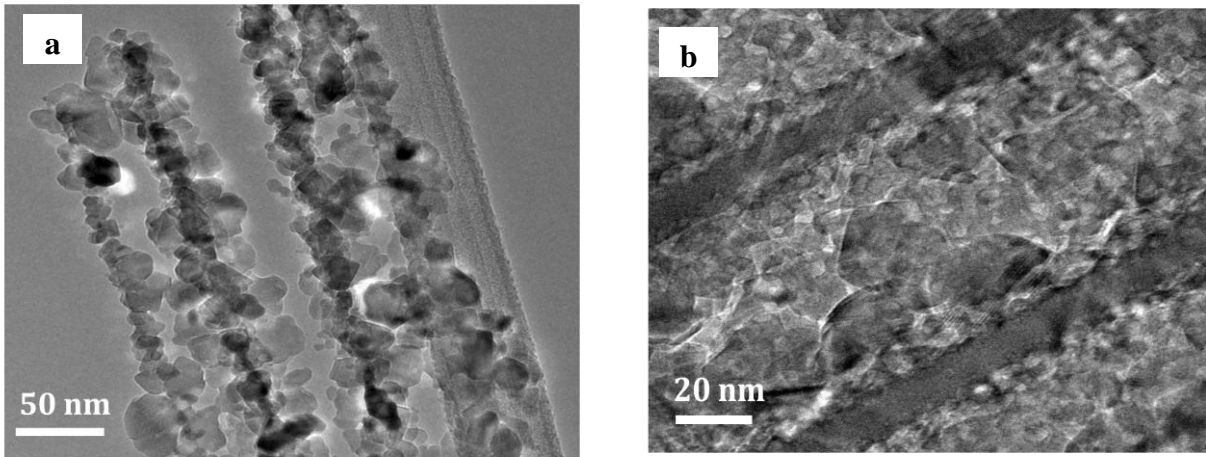
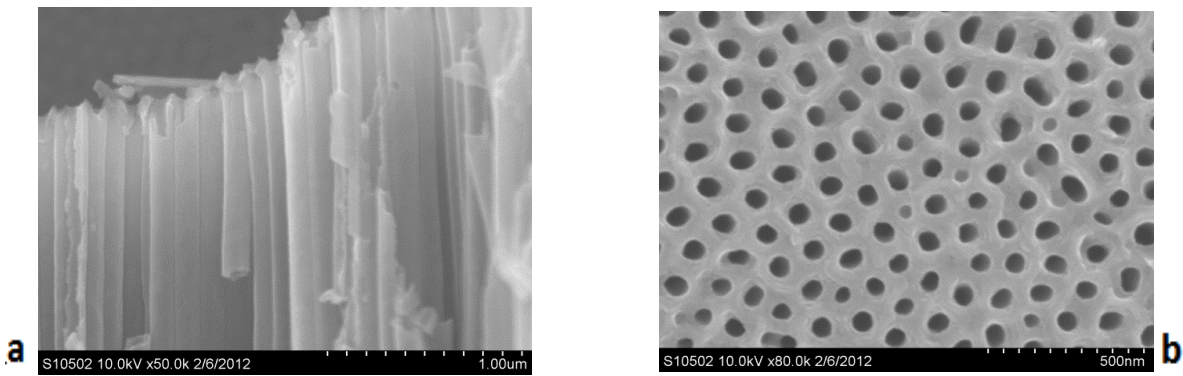


Figure 5-26 Effect of annealing with 10 °C/s ramp rates on the nanostructure of a) SW and b) DW nanotubes.



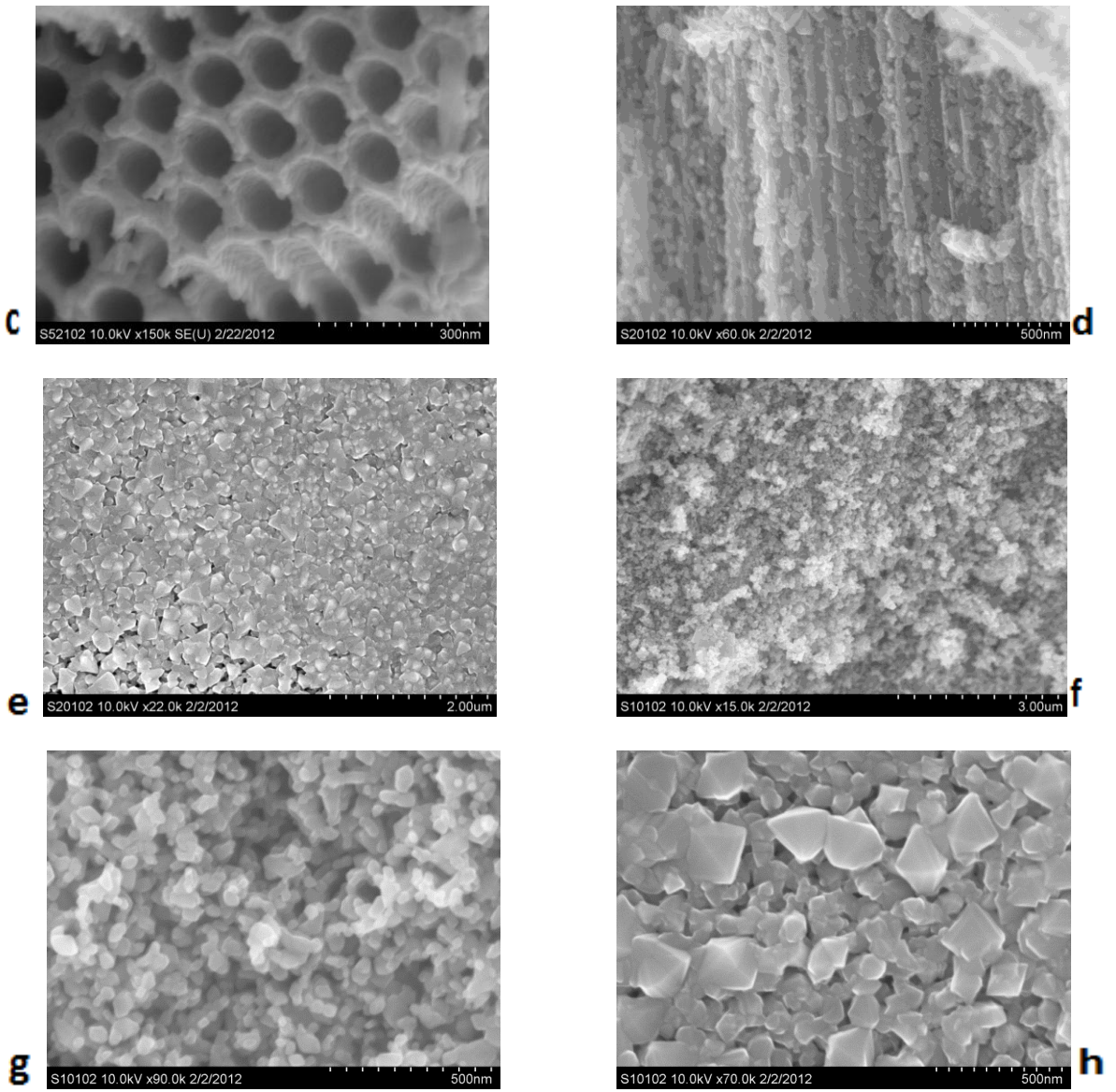


Figure 5-27 Effect of heating/cooling rates on the nanostructure of single walled nanotubes. a,b) 0.1 °C/s. c) 1 °C/s, d,e) 10 °C/S, and f,g,h) 50 °C/s. The tubes are all kept at 500 °C, for 30 minutes.

Chapter 6

Single wall nanotubes in dye and semiconductor sensitized solar cells

In the present chapter the details of the application of SW- TiO₂ NTs in dye and CdSe sensitized solar cells will be presented and a comparison between the cells made from SW and DW nanotubes will be made. It will be discussed how the elimination of the internal wall of DW- TiO₂ NTs affects the dynamics of charge transfer/transport in these solar cells.

6.1 SW and DW nanotubes in dye sensitized solar cells

6.1.1 *j*-*V* characterization of SW and DW-DSSCs

In order to study the properties of single wall TiO₂ nanotubes in DSSC application, cells were fabricated with single wall and common double wall nanotubes and heat treated at 500°C (See *Chapter 3* for more details). A comparison between plain nanotubes and TiCl₄ treated ones following the well developed method [122], were made as well. Figure 6-1 and Table 6-1 show the *j*-*V* characteristics for the fabricated DSSCs. As can be seen, although the amount of dye loading to single wall nanotubes is less, they show a higher short circuit current density and efficiency compared with their double wall counterparts. The lower amount of the adsorbed dye in single wall nanotubes can be attributed to the elimination of the inner rough shell. It is discussed and shown in the following sections that the improved properties of the single wall nanotubes can be

attributed to their better charge collection efficiency and higher conductivity in the absence of the inner shell. The other point to be mentioned is that TiCl_4 treatment has a larger effect on SW nanotubes than DW- TiO_2 NTs (Figure 6-1 and Table 6-1). This is because the SW- TiO_2 NTs have a larger hollow space inside compared to DW nanotubes, so the amount of TiO_2 particles attach to nanotubes' walls through TiCl_4 treatment is more, therefore the dye loading amount of SW nanotubes has been increased by 55%, while the increase in dye loading of DW nanotubes is about 39% (Table 6-1). It should be mentioned that the length of both SW and DW nanotube layers are 15 μm and the outer diameter of both types are between 100 to 120 nm (Figures 4-25 and 4-26).

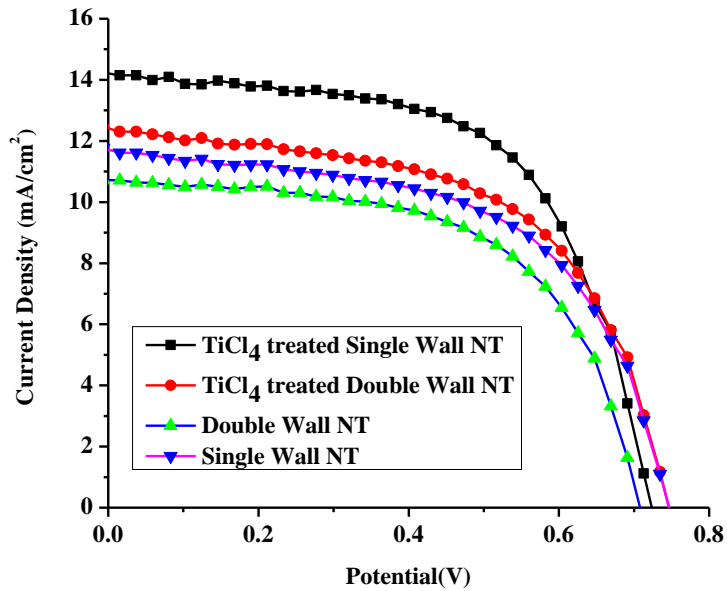


Figure 6-1 *j*-*V* characteristics of DSSCs fabricated from plain and TiCl_4 treated single and double wall nanotubes heat treated at 500°C with ramping rate of 1°C/s .

Table 6-1 The photovoltaic parameters of the DSSCs fabricated from plain and TiCl₄ treated single and double wall nanotubes heat treated at 500°C with ramping rate of 1°C/s. (J_{sc} = short-circuit current density, V_{oc} = open-circuit voltage, ff = fill factor, and η = efficiency)

	J _{sc} (mA/cm ²)	V _{oc} (V)	ff (%)	η (%)	L _{dye} (a.u.)
Double Wall NT	10.32±0.4	0.69±0.01	55.49±1.4	4.16±0.1	10.3
Single Wall NT	11.26±0.43	0.72±0.02	54.5±0.8	4.76±0.05	8.4
TiCl₄ treated Double Wall NT	12 ±0.4	0.72 ±0.01	52.7 ± 1.2	4.64 ±0.3	14.3
TiCl₄ treated Single Wall NT	13.9 ± 0.2	0.71 ±0.01	57.8 ± 0.93	5.88 ± 0.1	13

It has been shown by Roy *et al* that the properties of DSSCs are influenced by the ramping rates of the heat treatment of the nanotubes [11]. To find the best heating/cooling rate, comparisons were made between the *j-V* curves for cells with 500°C single wall nanotubes. As can be evidenced in Figure 6-2, the best ramping rate for single wall nanotubes is 1°C/s, which results in higher short circuit current density as well as efficiency. At the slower ramp rate of 0.1°C/s more rutile phase formed in the tubes, or in between the nanotubes and the substrate metal as evidenced by the XRD profiles in Figure 6-3. It is known that rutile phase is detrimental to the TiO₂ electronic properties. Increasing the heating rate to 10 °C/s damages the structure of the nanotubes and leaves a thick layer on top of the tubes (Figure 6-4), which could be the reason for the poor properties of the 10 °C/s tubes compared with the other two [5]. For comparison, an SEM of a sample annealed with a slow heating rate can be seen in Figure 4-4.

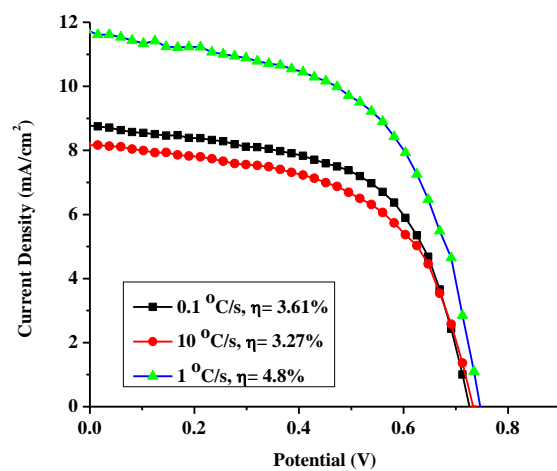


Figure 6-2 j - V characteristics of DSSCs fabricated from single wall nanotubes heat treated at 500°C with different ramping rates.

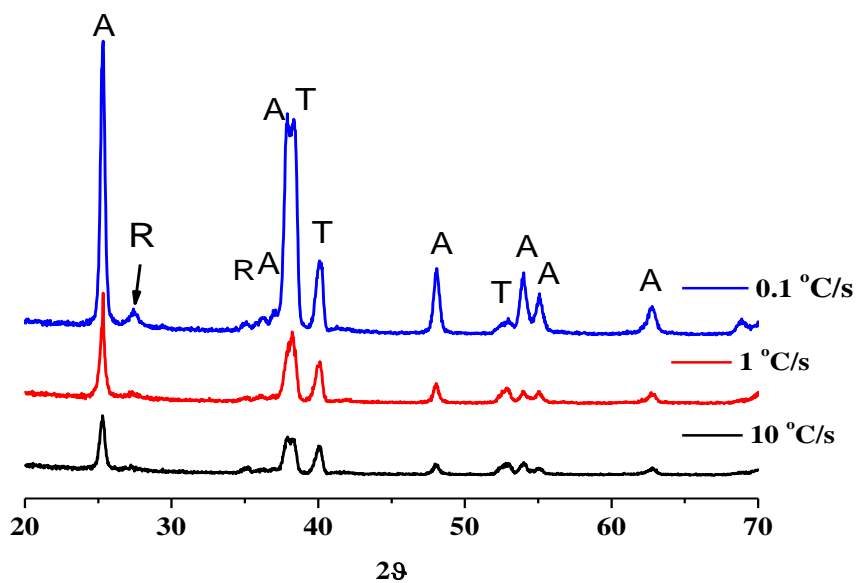


Figure 6-3 XRD spectra of the annealed single wall TiO_2 nanotubes (A = anatase, R = rutile and T = titanium) annealed at 500 °C/s with different heating/cooling rates.

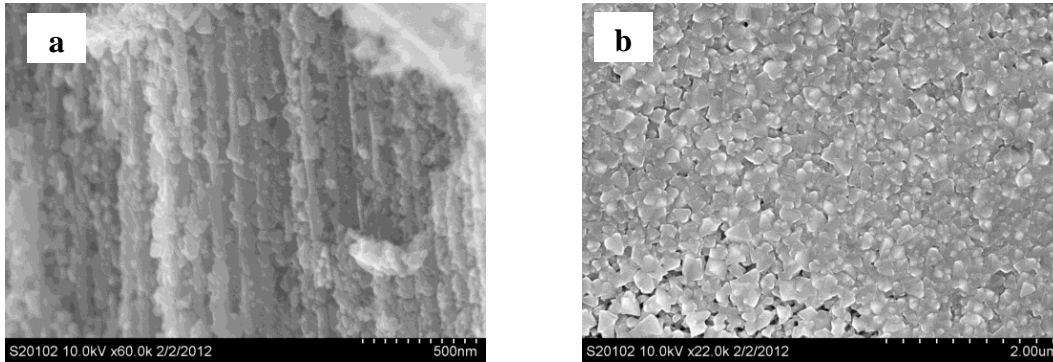


Figure 6-4 SEM images showing the effect of high (10 °C/s) ramp rate on the nanostructure of SW- TiO₂ NTs. a) Ttubes' walls and b) The top (almost) blocked surface. For comparison, an SEM of a sample annealed with a slow heating rate can be seen in Figure 4-4.

6.1.2 Intensity modulated photocurrent spectroscopy (IMPS) and photovoltage spectroscopy (IMVS) of SW and DW-DSSCs

As stated in the previous section, the higher efficiency of the SW-DSSC in the absence of the inner shell can be attributed to their better conductivity (see *Sections 5.7.2 and 6.1.1*) and charge collection efficiency. To study this issue two frequency domain methods; intensity modulated photovoltage (IMVS) and intensity modulated photocurrent (IMPS) experiments were performed. In these methods, the responses from the solar cells to modulation of light intensity are measured as a voltage or a current density. The results of IMVS and IMPS are usually represented as inverted semicircles in a complex plane (in-phase against 90° out of phase) from which, charge recombination time and transport time (from dye to TiO₂ surface) at a certain photon flux can be calculated. Figures 6-5 and 6-6 provide the IMPS and IMVS response curves of SW and DW based DSSCs at different photon fluxes.

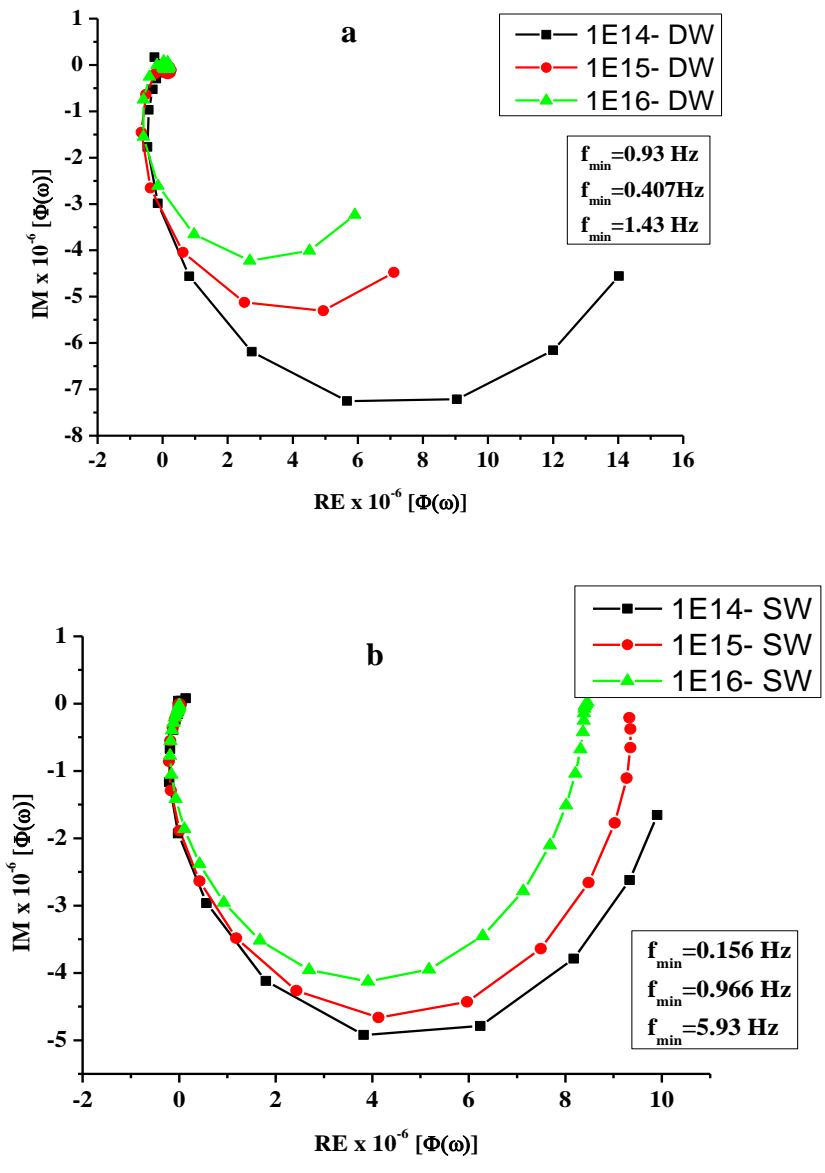


Figure 6-5 IMPS responses of a) DW- TiO₂ NT and b) SW- TiO₂ NT DSSCs under different photon fluxes of 10¹⁴, 10¹⁵, and 10¹⁶ photons.cm⁻².s⁻¹. f_{\min} is the frequency of the minimum imaginary component of each curve

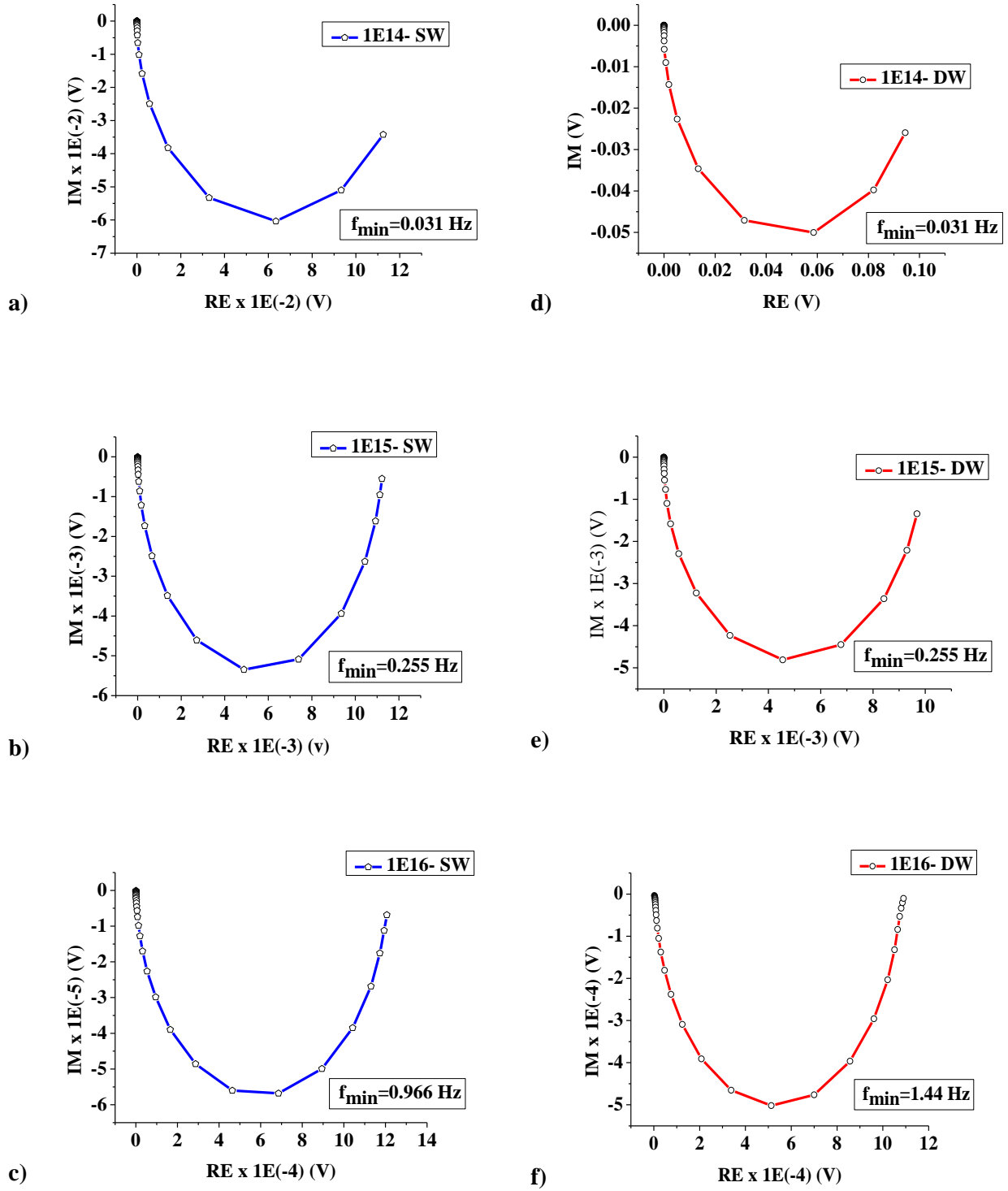


Figure 6-6 IMVS responses of SW and DW-DSSCs under different photon fluxes of a,d) 10^{14} , b, e) 10^{15} , and c, f) 10^{16} photons.cm⁻².s⁻¹. f_{\min} is the frequency of the minimum imaginary component of each curve.

To calculate the *transport time constant* (τ_t) and the *recombination time constant* (τ_r) from the IMVS and IMPS data we have:

$$\tau_t = 1/2\pi f_t \quad \text{Equation 22}$$

$$\tau_r = 1/2\pi f_r \quad \text{Equation 23}$$

in which f_t and f_r are the frequencies of the minimum imaginary components of IMPS and IMVS inverted semicircles respectively [3].

Figure 6-7a shows that the recombination time constant τ_r , is approximately the same in both tubes and hence independent of the inner shell of the nanotubes. However, Figure 6-7b shows that the elimination of the internal shell clearly leads to a shorter transport time constant τ_t . To calculate *charge collection efficiency* ($\eta_{coll,\tau}$) we have [3]:

$$\eta_{coll,\tau} = 1 - (\tau_t/\tau_r) \quad \text{Equation 24}$$

Therefore from the data in Figure 6-7, the SW- TiO₂ NTs can be shown to have a 40 to 50 percent higher $\eta_{coll,\tau}$ at the higher incident photon fluxes. The reason for this phenomenon may be the elimination of the internal nano-porous shell allowing a better directionality in the charge path and the considerable larger crystallite sizes in SW- TiO₂ NTS which causes less defects in the tube walls (due to fewer grain boundaries).

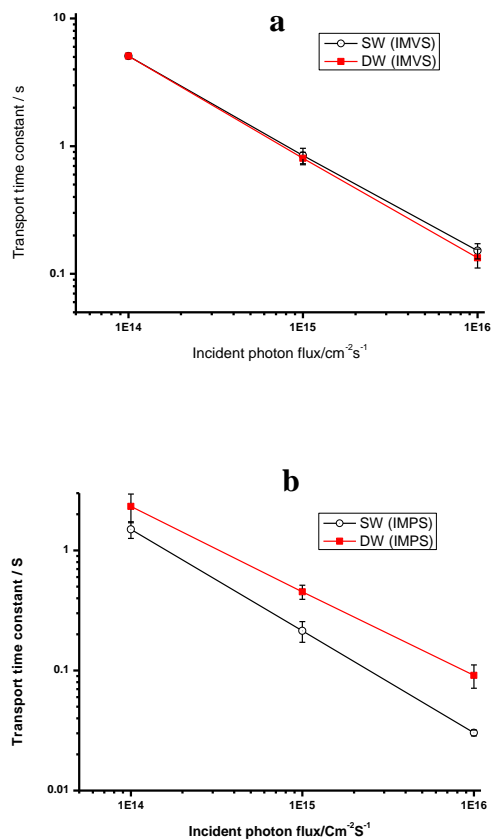


Figure 6-7 Recombination time (a) and transport time (b) constants calculated from IMVS and IMPS for single and double walled DSSCs.

6.1.3 Electrochemical Impedance spectroscopy

Electrochemical Impedance spectroscopy (EIS) under illumination was used to further investigate the charge transport and charge recombination processes occurring in blank SW and DW-TiO₂ nanotube (non-TiCl₄ treated) based DSSCs. For this purpose the equivalent circuit (EC) model was used to fit the experimental EIS data. The equivalent circuit of the system that represents the current path (or low resistance path) is a common method to describe EIS measured data in electrochemistry.

When light or forward bias is applied to the DSSC, electrons are injected into TiO₂ and the charge is transported through the semiconductor film. Meanwhile, a fraction of the generated electrons is recombined with the acceptor states in the electrolyte. Equivalent circuit fitting has proved to be an appropriate tool to describe the details of these electronic processes in the DSSC [58, 67].

For analysis of EIS data of DSSC device the equivalent circuit contains combination of transmission line with other elements representing several interfaces that exists in the device [58, 65, 67, 123].

Impedance measurements were carried out in order of descending light intensity using an Autolab potentiostat/galvanostat and the Nova 1.6 software package. Experiments were performed with cells under illumination provided by a red LED (centre wavelength $\lambda = 627$ nm) and biased at the V_{oc} induced by the illumination. The highest light intensity used was sufficient to produce a V_{oc} approximately equal to that obtained under AM 1.5 1 Sun illumination and the incident photon flux was of the order of 10^{17} cm⁻² s⁻¹. A 15 mV RMS voltage perturbation was used and the frequency range was 10⁵–0.1 Hz. To assess solar cell performance at several bias conditions, different illumination intensities were achieved using neutral density filters mounted in an automated filter wheel system (Newport), which was controlled by the Nova 1.6 software.

Figure 6-8a, b and c show representative Nyquist, Bode and phase angle preliminary plots for both SW and DW TiO₂ solar cells and a schematic illustration of equivalent circuit used to model the solar cell devices in this study is depicted in Figure 6-8d. For both samples as can be seen from the Bode plots in

Figure 6-8b, excellent fits to the most of the spectra can be obtained using the equivalent circuit shown in Figure 6-8d which is based upon the diffusion-reaction model as described by de Levie [124] and applied to the DSSC by Bisquert *et al* [63]. In these spectra, experimental data are shown by dots and solid line presents the fitted data.

In this model R_s is the series resistance associated with the Ti foil, external connections and load, R_t is the TiO_2 film charge transport resistance, R_{ct} is the charge transfer resistance at the photoanode/electrolyte interface, C_μ is the TiO_2 film chemical capacitance, C_{sub} is the substrate capacitance, r_t is the distributed transport resistance of electrons in TiO_2 , c_μ is the distributed chemical capacitance of the oxide layer, r_{ct} is the distributed charge transfer resistance at photoanode/electrolyte interface, R_{Pt} is the charge transfer resistance at the platinumized FTO cathode/electrolyte interface and C_{Pt} is its corresponding double layer capacitance.

The distributed resistances and capacitances are related to total resistances and capacitances by the following equations:

$$r_t = \frac{A}{d} \cdot R_t \quad \text{Equation 25}$$

$$r_{ct} = A \cdot d \cdot R_{ct} \quad \text{Equation 26}$$

$$c_\mu = \frac{C_\mu}{A \cdot d} \quad \text{Equation 27}$$

where d and A are the thickness and projected area of the TiO_2 electrode respectively. The units for the distributed parameters r_t , r_{ct} , and c_μ are $\Omega \text{ cm}$, $\Omega \text{ cm}^3$ and F cm^{-3} respectively.

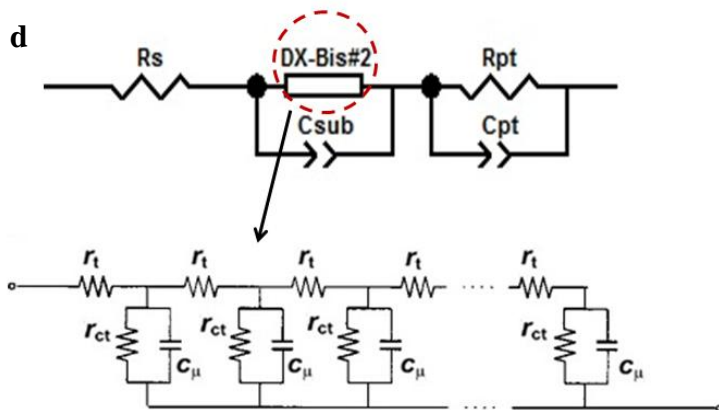
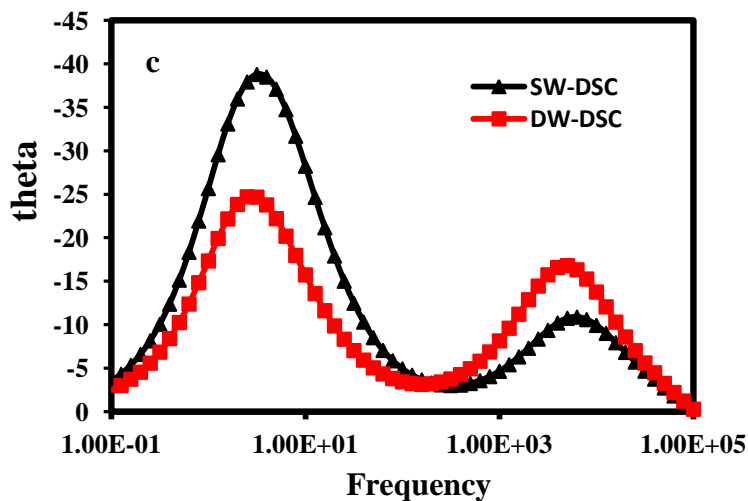
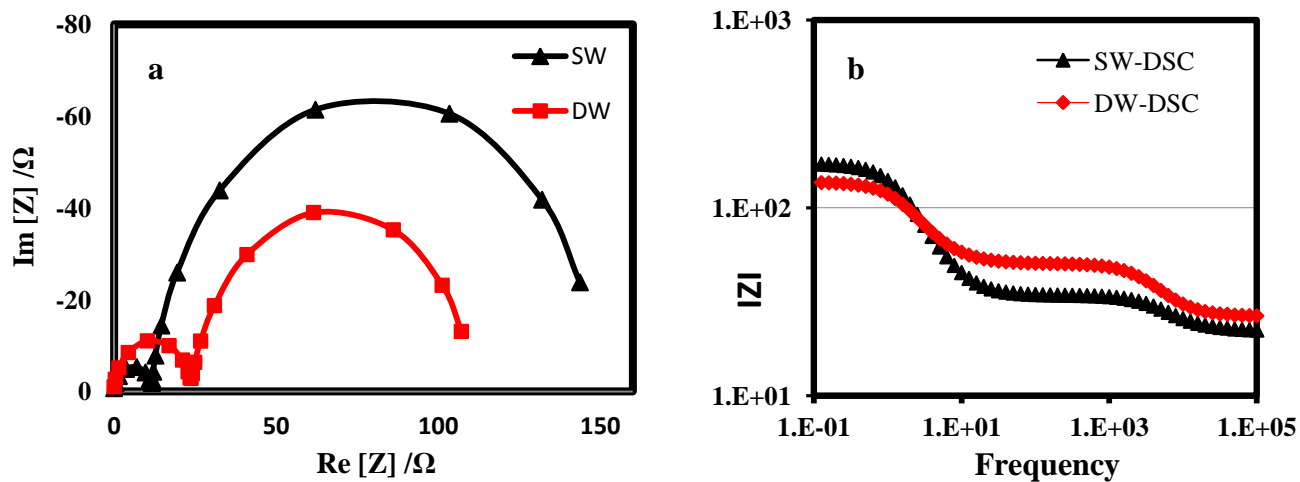


Figure 6-8 a) Nyquist, b) Bode and c) phase angle plots of single and double walled nanotube DSSC. d) Equivalent circuit used to fit the data; (dots represent experimental data and solid lines present the fitted data)

When presented in the Nyquist format, electrochemical impedance spectra of a dye sensitized solar cell typically contains three time constants that represent the internal impedances. The highest frequency semi-circle relates to the charge transfer at the platinum counter electrode. The middle frequency semi-circle attributes to the electron transport in the $\text{TiO}_2/\text{dye}/\text{electrolyte}$ interface and the low frequency "depressed semi-circle" with a 45° take off angle presents the Nernstian diffusion within the electrolyte. [67]. It should be mentioned that as the electrolytes used for both SW-SSSCs and DW-SSSCs contained high iodide/iodine concentrations, the low frequency Warburg impedance related to diffusion in the electrolyte are not apparent in the Nyquist plots of the solar cells (Figure 6-8a) [64].

In section 6.1.1 it was shown that the SW-based device has better photocurrent and photo- conversion efficiency than the DW-device, despite the former having a lower light harvesting ability due to its lower dye loading (Table 6-1). Since the solar cell performance is defined by charge injection, recombination resistance and charge collection processes, it can be most plausibly concluded that either charge injection into SW-based DSSCs system is faster leading to a better charge separation than in its DW counterpart; or the recombination is slower in the SW-DSSC. To verify which hypothesis is the more likely, an attempt was made to compare the electron injection, charge recombination and charge collection processes in both samples.

Figure 6-9 presents the calculated chemical capacitance for both SW and DW samples based on the equivalent circuit used to fit the EIS data (Figure 6-8b). The

measured chemical capacitance is directly related to the density of states around the quasi-Fermi level [80]. Thus, it is reasonable to assume that a device with a higher C_{μ} , i.e. a higher density of electron acceptor states, should have enhanced electron injection. Figure 6-9 shows that at any identical V_{oc} , C_{μ} for DW-based device is larger than C_{μ} of SW-based DSSC. As a result, better charge injection into SW-based DSSC could not be anticipated and thus is not the reason for the formers better performance. Besides the injection, lower charge recombination or better charge collection can result in better performances. Therefore, both recombination and charge collection have to be carefully scrutinized to investigate the phenomenon that the better performance stems from.

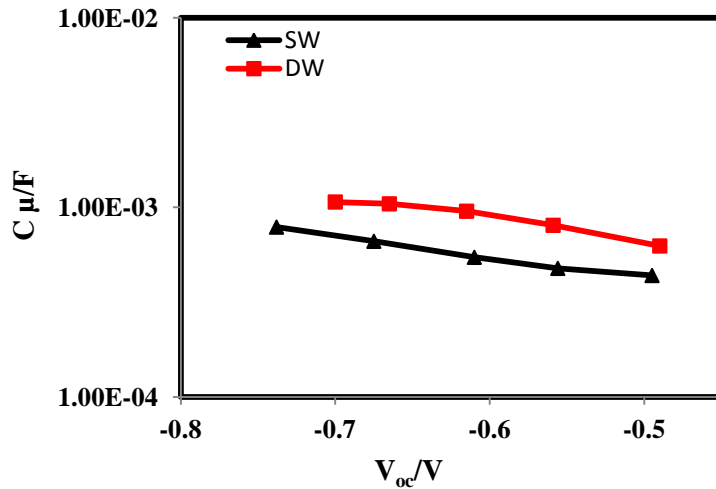


Figure 6-9 Chemical capacitances of DW and SW DSSCs calculated from EIS spectra

Figures 6-10a and b present the carrier transport resistance and charge transfer resistance obtained from the fitting of EIS spectra, respectively. For both SW and DW devices R_{ct} is much greater than the R_t (Warburg impedance at zero hertz for the titania/electrolyte interface) which suggests that both devices exhibits near

unity carrier collection efficiency. The collection efficiency (η_{coll}) being calculated from:

$$\eta_{coll} = 1 - \frac{R_t}{R_{ct}} \quad \text{Equation 28}$$

Moreover, the effective electron diffusion length (L_n) can be determined from R_{ct} and R_t as follows:

$$L_n = d \sqrt{\frac{R_{ct}}{R_t}} \quad \text{Equation 29}$$

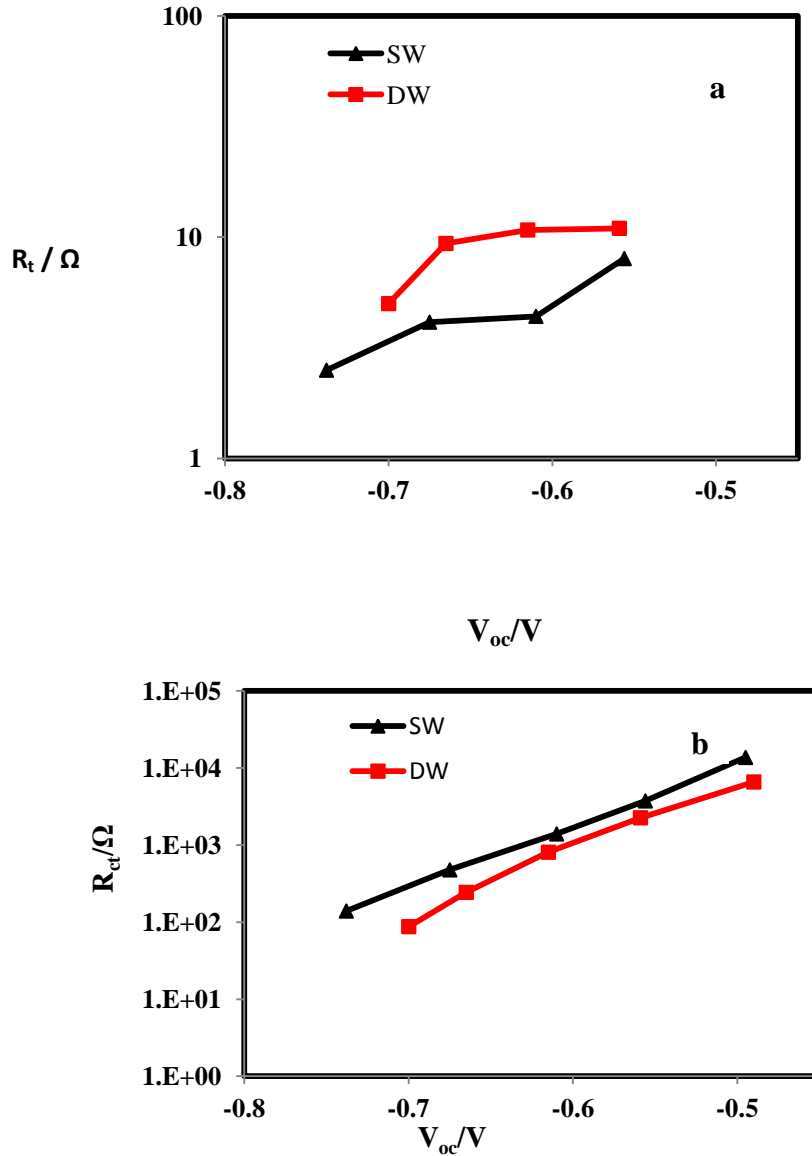


Figure 6-10 SW and DW DSSCs (a) Charge transport resistance and (b) charge transfer resistance

It is also clear from Figure 6-10a that at any given photovoltage value, the electron transport resistance is higher in DW-DSSC than SW-DSSC. This implies that electron transport has been facilitated by modifying the TiO_2 nanotube from double wall to single wall structure. Moreover, comparison of the electron transfer resistance (R_{ct}) shows that it exhibits higher value for SW-DSSCs than

that of DW-DSSCs (Figure 6-10b). The electron transfer resistance is inversely attributed to the recombination rate, e.g. the higher the R_{ct} the lower the recombination, which is more favorable for the device performance.

Figure 6.11 shows that the calculated electron diffusion length (L_n) in both cells are several orders of magnitude greater than the TiO_2 film thickness ($15 \mu m$), which is sufficient to ensure unity charge collection.

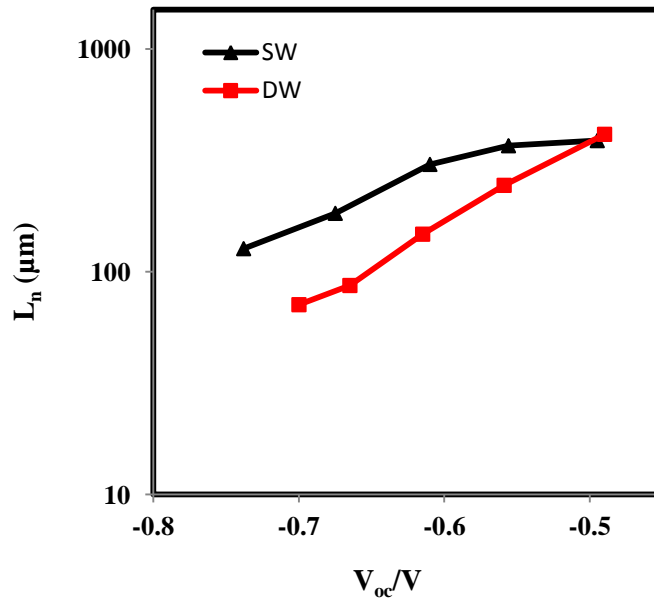


Figure 6-11 Calculated electron Diffusion length (L_n) for SW and DW based DSSC at different V_{oc}

The electron lifetime (τ) is the product of the $C\mu$ and the R_{ct} . The electron lifetime for both SW and DW based DSSC is calculated and plotted in Figure 6-12. It can be seen that the electron lifetime in the SW-DSSC is slightly longer than DW-DSSC at typical V_{oc} of device e.g. -0.7. The longer electron lifetime in the SW based DSSC device indicates reduced recombination and is consistent with a larger V_{oc} . This is very similar to the conclusions drawn from the

recombination time constants calculated from the IMVS experiments of DSSCs
(See Section 6.1.2).

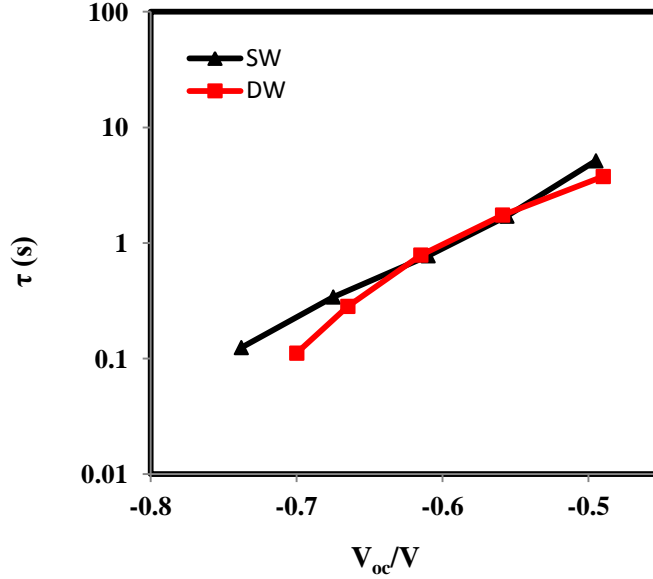


Figure 6-12 Electron lifetime in SW and DW-DSSCs

All in all assuming that the comparison of charge injection in both cells based on chemical capacitances is accurate enough and charge injection into SW-DSC is not better than DW-DSC, it is likely that the causes for better performance of SW-DSC are either less recombination or better charge separation or a combination of the two. According to the EIS spectra fitting data, the recombination resistance in SW-DSC is about 1.7 times higher than DW-DSC. Thus, less recombination could result in better performance. Moreover, despite using identical electrolytes and sensitizer in both cells, the amount of dye loading in DW is higher than SW cell; it is plausible that geminate recombination is faster in the DW-SSC counterpart.

6.2 SW and DW nanotubes in CdSe sensitized solar cells

6.2.1 j - V characterization of SW and DW-DSSCs

To prepare CdSe sensitized solar cells, the SILAR method with 5, 7, 10 and 12 number of cycles was used to sensitize the tubes. As can be seen in Figure 6-13 and presented in Table 6-2, it was found that 10 cycles of CdSe deposition results in the best efficiency for solar cells among all SEM characterizations showed that with more than 10 cycles, blockage of the tubes by CdSe layer happens (Figure 6-14). It should be noted that the j - V measurements had to be done immediately after the cell fabrication, as the SW-SSC cell is not stable. This might be due to detachment of CdSe over time when the electrolyte is injected into the cell as the surfaces of the tubes are very smooth with lower surface energies.

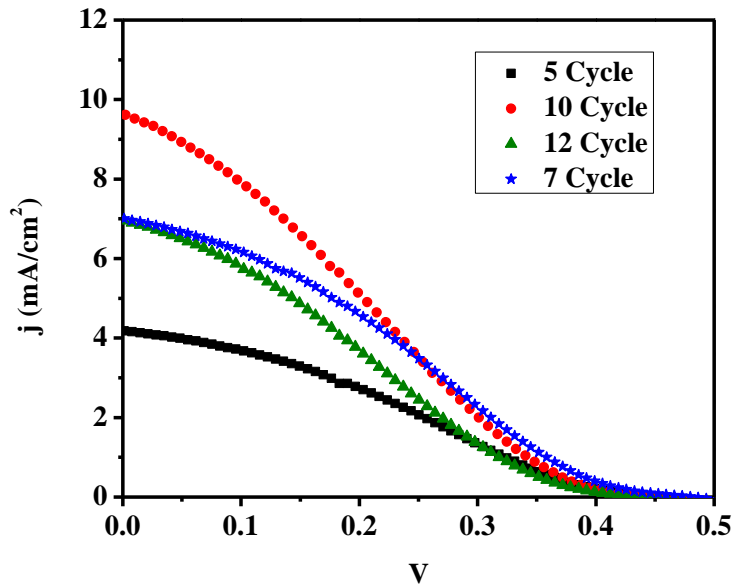


Figure 6-13 j - V characteristics of SSSCs fabricated from single nanotubes sensitized with different SILAR cycles of CdSe deposition.

Table 6-2 The photovoltaic parameters of the SSSCs fabricated from single nanotubes sensitized with different SILAR cycles of CdSe deposition. (J_{sc} = short-circuit current density, V_{oc} = open-circuit voltage, ff = fill factor, and η = efficiency)

Sample	V_{oc} (V)	J_{sc} (mA/cm ²)	ff (%)	η (%)
5 Cycle CdSe	0.45	4.18	29	0.55
7 Cycle CdSe	0.46	6.9	30.4	0.91
10 Cycle CdSe	0.45	9.5	24	1.01
12 Cycle CdSe	0.45	6.9	24.1	0.75

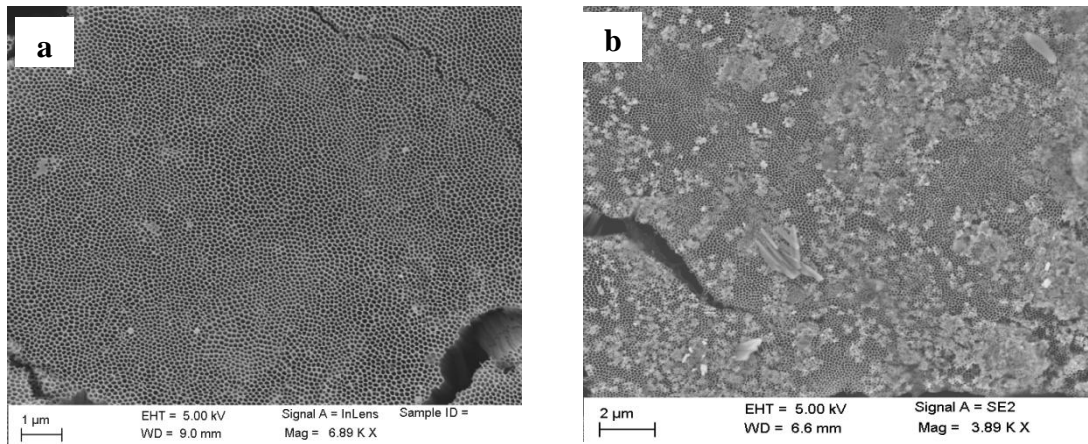


Figure 6-14 Top view SEM images of a) heat treated blank SW nanotubes and b) 12 cycle CdSe deposited SW- TiO₂ NTs showing blockage of the tubes in some parts

To make comparisons, the j - V characterization of the solar cells made from 10 SILAR cycle deposited CdSe single and double wall TiO₂ NTs are shown in Figure 6-15 and the data are presented in Table 6-3. The SW nanotubes show slightly better efficiencies and photocurrent than the DW cells, while the fill factors and open circuit voltages are almost the same. In accordance with the j - V measurements, the IPCE measurements also show a better incident photon to current efficiency for SW-SSSC than DW-SSSC. The IPCE spectra of both cells are depicted in Figure 6-18 in *Section 6.2.3*.

Table 6-3 The data related to *j-V* characterization of SW and DW SSSCs sensitized by 10 SILAR cycles of CdSe deposition

Sample	V_{oc} (V)	J_{sc} (mA/cm ²)	ff (%)	η (%)
SW-SSSC	0.44 ± 0.01	8.45 ± 0.95	26.5 ± 2.5	0.98 ± 0.03
DW-SSSC	0.44 ± 0.01	6.61 ± 0.21	25 ± 2	0.73 ± 0.03

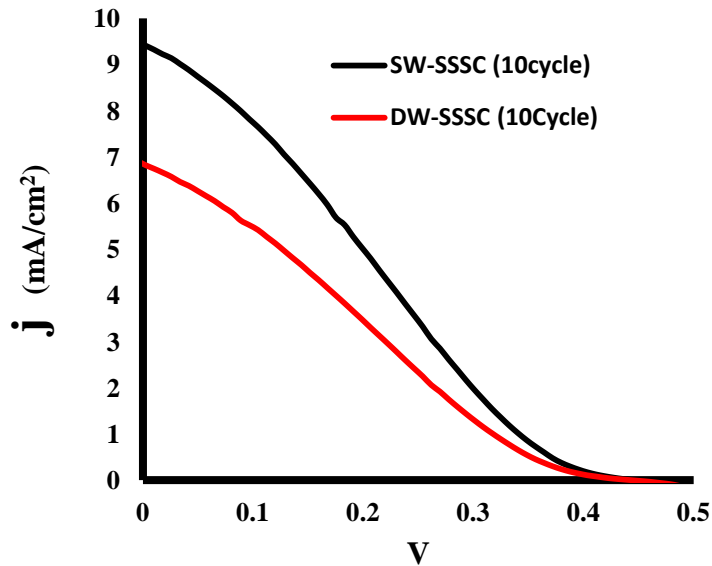


Figure 6-15 *j-V* characterization of SW and DW- TiO₂ NT based solar cells sensitized by 10 SILAR cycles of CdSe deposition

6.2.2 Electrochemical Impedance spectroscopy of SSSCs

To explore the photophysical features of SW and DW devices, EIS spectra were fitted and interpreted using the same equivalent circuit used for DSSCs (Figure 6.8b). It is worth mentioning that identical electrolytes and sensitizer were used (10 SILAR cycles of CdSe deposition) for both types of SSSCs.

Preliminary EIS spectra (Nyquist and Bode plots) of SW and DW TiO₂ solar cells sensitized by 10 SILAR cycles of CdSe are depicted in Figure 6-16. It is clear that the EIS spectra of SW and DW are similar. For all SSSCs equivalent circuit (Figure 6-8 d) is applied to fit the EIS spectra that provide an excellent fit as can be seen from the Bode plot in Figure 6-16b. [63, 124]. All associated parts of the equivalent circuit model have been explained in *Section 6.1.3*.

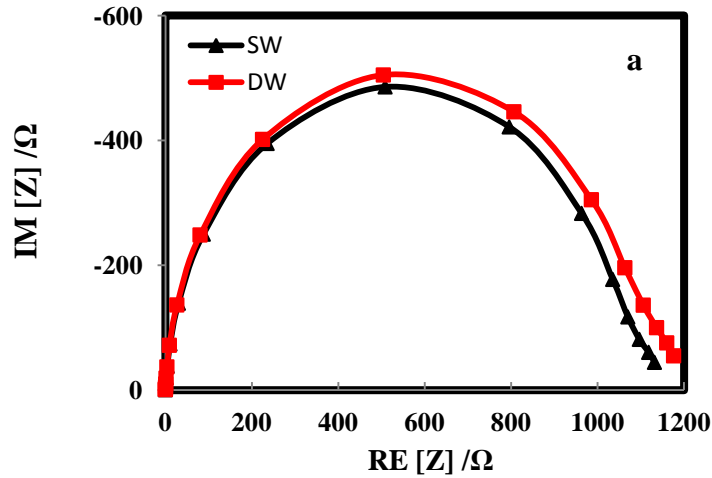


Figure 6-16 Nyquist (a), Bode (b) and phase angle (c) plots of single and double walled nanotube SSSC sensitized by 10 SILAR cycles of CdSe deposition; (dots represent experimental data and solid lines present the fitted data). (To be continued in the next page)

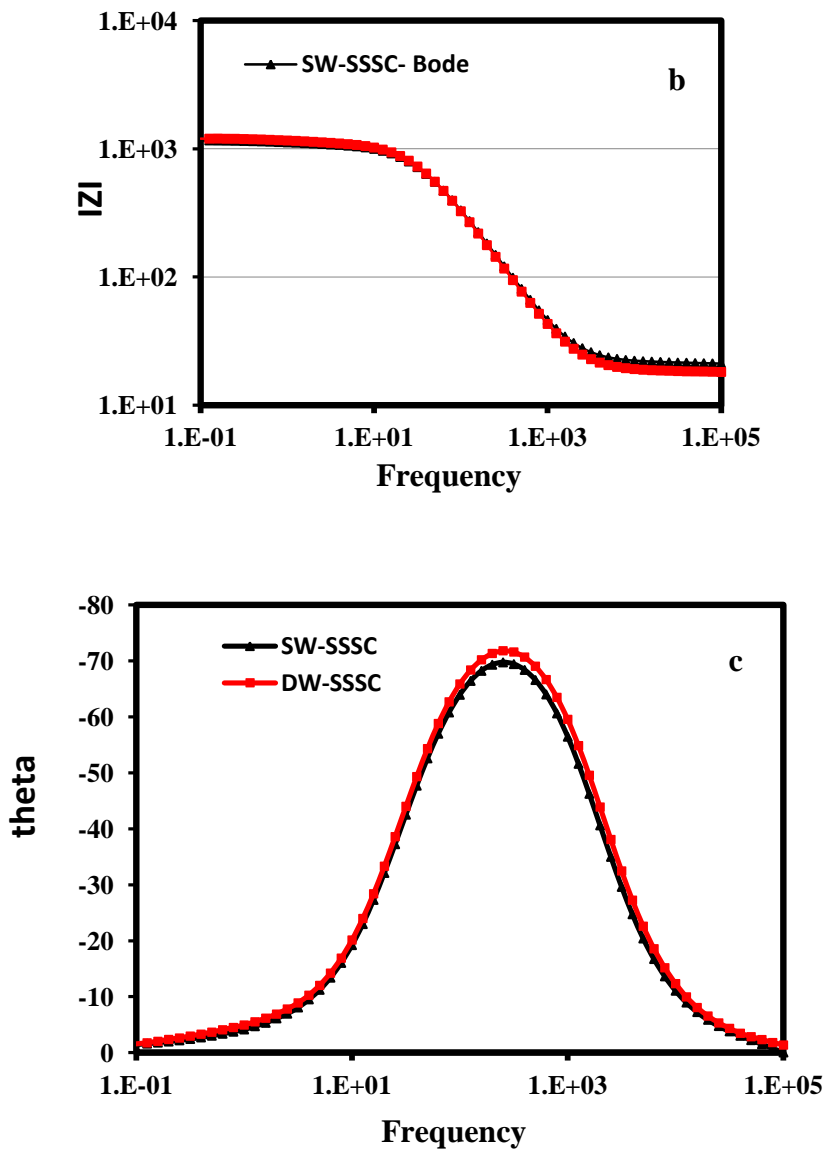


Figure 6-16 (Continued) Nyquist (a), Bode (b) and phase angle (c) plots of single and double walled nanotube SSSC sensitized by 10 SILAR cycles of CdSe deposition; (dots represent experimental data and solid lines present the fitted data).

Figure 6-17 presents the charge transfer resistance (R_{ct}) for both DW and SW based device obtained from the fitting of EIS spectra to the equivalent circuit model in Figure 6-8b. Comparison of R_{ct} at any given photovoltage value reveals a slightly higher value for DW-SSSC than that of SW-SSSC. Higher charge

transfer resistance is in favor of device performance as it is inversely attributed to the recombination rate.

For both SW and DW devices only one semi-circle is obvious in EIS spectra. Consequently, when the spectra are fitted to the applied equivalent circuit model (Section 6.1.3, Figure 6-8d) the error of extracted value for charge transport resistance (R_t) was noticeably high and thus it was not sufficiently accurate to calculate meaningful R_t from the fitted EIS spectra. In other words, deconvolution of the transport time constant with reasonable degree of accuracy was impossible. Thus it was not possible to obtain any useful information regarding the charge transport and its comparison in SSSCs. As stated in Section 6.1, both R_t and R_{ct} values are required to calculate the carrier collection efficiency ($\eta_{COL}(\lambda)$) and electron diffusion length. Therefore, carrier collection efficiency and electron diffusion lengths cannot be calculated for SW-SSSC and DW-SSSC devices.

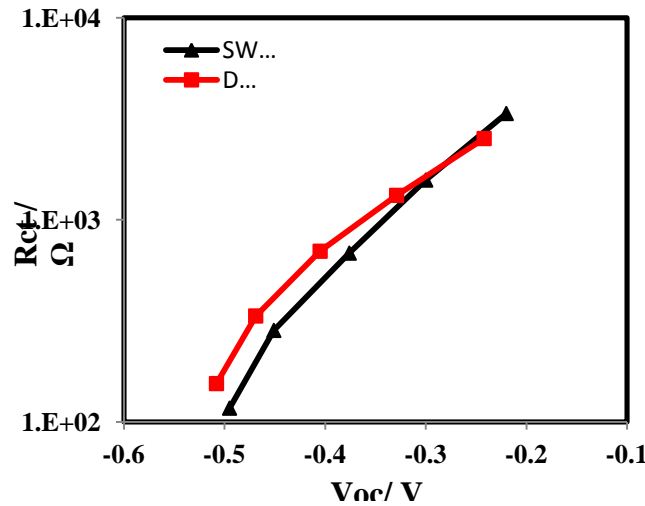


Figure 6-17 Charge transfer resistance in both SW and DW SSSCs sensitized by 10 SILAR cycles of CdSe deposition

6.2.3 IPCE of SSSCs

An alternative approach to acquire useful information about the charge transport features in the SSSCs is to analyze the incident photon to current efficiency (IPCE) of cells. IPCE is referred to the external quantum efficiency (EQE) of the solar cell, and it is defined as the number of photogenerated electrons in the external circuit divided by the number of incident photons at different wavelength. The IPCE of SSSCs can be analyzed in terms of the light harvesting ($\eta_{\text{LH}}(\lambda)$), the injection ($\eta_{\text{INJ}}(\lambda)$) and collection efficiencies ($\eta_{\text{COL}}(\lambda)$) indicated by Equation 30:

$$\eta_{\text{IPCE}}(\lambda) = \eta_{\text{LH}}(\lambda)\eta_{\text{INJ}}(\lambda)\eta_{\text{COL}}(\lambda) \quad \text{Equation 30}$$

$\eta_{\text{LH}}(\lambda)$ can be estimated from the optical density (OD) spectra of the photoanode at each wavelength [80]. $\eta_{\text{INJ}}(\lambda)$ depends on the carrier injection efficiency from the excited sensitizer into the conduction band of TiO_2 and can be assumed identical when the same sensitizer and same metal oxide film are used. $\eta_{\text{COL}}(\lambda)$ measures how efficiently the injected carrier is collected at the external circuit, which can be examined by the effective diffusion length of electrons in the sensitized electrode.

Considering approximately similar charge injection efficiencies for SW and DW devices (due to the application of identical sensitizer and electrolyte in both cases and as studies performed by other groups indicate almost 100% injection efficiency from CdSe into TiO_2 particles), the IPCE ratio of SW and DW devices

depends solely on light harvesting and collection efficiencies as shown in Equation 31:

$$\frac{IPCE_{SW}}{IPCE_{DW}} = \frac{(\eta_{LHE} \cdot \eta_{col})_{SW}}{(\eta_{LHE} \cdot \eta_{col})_{DW}} \quad \text{Equation 31}$$

Furthermore, the light harvesting efficiency for counter electrode side illumination (CE) can be calculated by Equation 32 [80].

$$\eta_{LH} = T_{CE}T_{EL}(1 - e^{-\alpha}) \quad \text{Equation 32}$$

Where;

T_{CE} = Transmittance of the counter electrode

T_{EL} = Transmittance of the electrolyte

α = absorption coefficient of photoelectrode

As T_{CE} and T_L should be almost identical in both single walled and double walled samples, equation 30 is re-written as:

$$\frac{IPCE_{SW}}{IPCE_{DW}} = \frac{((1 - e^{-\alpha}) \cdot \eta_{col})_{SW}}{((1 - e^{-\alpha}) \cdot \eta_{col})_{DW}} \quad \text{Equation 33}$$

From the optical measurement (*Section 5.8.2*) the absorption coefficient (α) can be estimated. As the light absorption of double walled sample is higher than single walled sample we have:

$$\frac{(1 - e^{-\alpha.d})_{SW}}{(1 - e^{-\alpha.d})_{DW}} \leq 1 \quad \text{Equation 34}$$

and if we call equation 34 as constant K then :

$$\frac{IPCE_{SW}}{IPCE_{DW}} = K \cdot \left(\frac{\eta_{col_{SW}}}{\eta_{col_{DW}}} \right) \quad \text{Equation 35}$$

where K is smaller than one. However, as can be observed from the IPCE measurement the ratio $\frac{IPCE_{SW}}{IPCE_{DW}}$ is bigger than 1, so it can be simply inferred that the $\frac{\eta_{col_{SW}}}{\eta_{col_{DW}}}$ ratio must be greater than one. In other words, it is informing that the SW-SSSC has better charge collection in comparison with DW-SSSC.

From the above study it is concluded that CdSe-sensitized SW- TiO₂ solar cells possess better charge collection efficiency than DW-TiO₂ SSSC which is similar to better charge collection efficiency of SW-DSSCs calculated from IMVS/IMPS experiments discussed in *Section 6.2.1*. The higher charge collection efficiency results in better photocurrent generation and better IPCE of SW-SSSC despite its lower light absorption caused by lower surface area onto which CdSe can be deposited

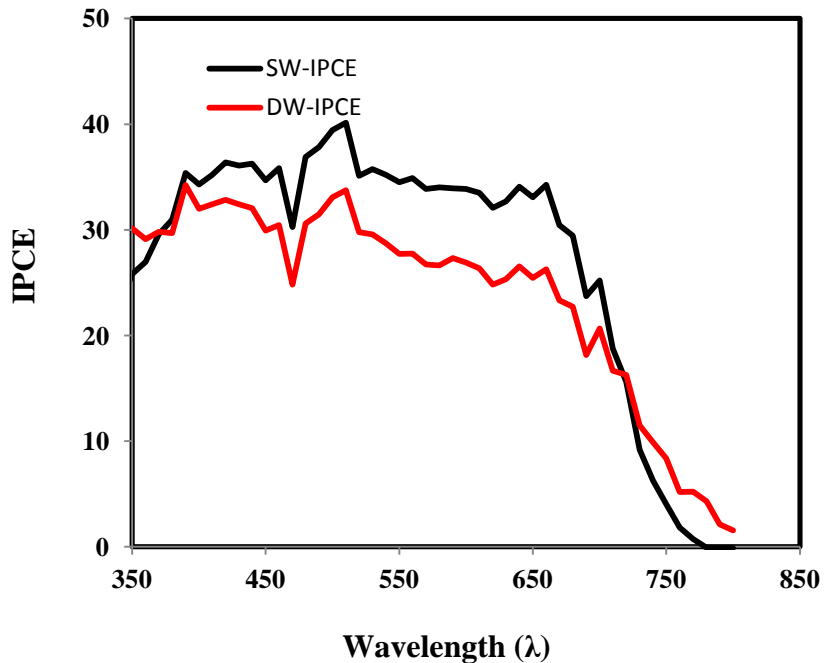


Figure 6-18 IPCE of DW and SW-SSSC sensitized by 10 SILAR cycles of CdSe deposition at different wavelengths

It should be noted that as the deposition method was SILAR and no characteristic excitonic peak could be observed in both OD (optical density) spectra in Figure 5-25, they show a *dispersed size distribution* of the deposited semiconductor nanocrystallites with no clear evidence of different particle sizes. Besides, the absorption onsets for both structures are almost similar (~ 750 nm) and the differences in OD spectra in figure 5-25 are mostly at long wavelengths where CdSe is normally not absorbing light. Therefore, their difference could be due to uncorrected light scattering losses and rigorous corrections for light scattering [80].

6.3 Conclusion

The newly synthesized SW-nanotubes were used to fabricate dye and semiconductor (CdSe) sensitized solar cells.

Although the amounts of dye adsorbed to single wall and TiCl₄ treated single wall TiO₂ NTs are less, the efficiencies of their DSSC is higher compared to the DSSC fabricated from double wall and TiCl₄ treated double wall TiO₂ NTs. This is mainly due to the negative effect of the internal shell (IST) of double wall TiO₂ NTs on the charge transfer from dye to TiO₂ in DSSCs. Besides, the efficiency of the SW nanotubes synthesized from mixed DMSO:EG solvent in a backside illumination configuration, is amongst the highest efficiencies reported for non-decorated nanotubes in the literature [2, 11, 77, 125]. Moreover, The electron diffusion length for SW NTs is considerably higher than the what previously reported by Jennings *et al* for common NTs [71] (See *section 2.11* for more details).

To support the abovementioned reason, modulated photocurrent and photovoltage spectroscopy measurements) were investigated. The results show similar recombination time constants, τ_r for both single wall and double wall nanostructures. Conversely, the elimination of the inner shell is shown to clearly shorten the *transport time constant* τ_t by a factor of 2, i.e. a faster carrier transport in SW-DSSCs. Consequently, SW-DSSCs have a 40 to 50 percent higher *charge collection efficiency* (η_{cc}) at higher incident photon fluxes

To study the charge transport and collection efficiencies in more detail, EIS experiments were performed for SW and DW –DSSCs. The EIS spectra of both gave excellent fits to the standard equivalent circuit model proposed by previous workers [63, 124]. Both SW and DW devices exhibited near unity carrier collection efficiency. The better photocurrent and photo-conversion efficiency of SW-based devices than their DW-based counterparts was shown by EIS studies to stem from the lower electron transport resistance and facilitated charge transport as well as higher recombination resistance of SW-DSSCs. Likewise, the electron lifetime in SW DSSCs is slightly longer than that in the DW devices which is in favor of device performance.

To examine the application of SW- TiO₂ NT in semiconductor sensitized solar cells, the SILAR method was used to deposit CdSe into SW and DW based TiO₂ layers. Among all, the best efficiency was achieved from 10 SILAR cycles of CdSe deposition with further deposition of CdSe resulting in tube blockage. Therefore, all characterization experiments were performed for 10 SILAR cycle deposited CdSe. Despite similar fill factors and open circuit photo-voltages, SW-SSSCs displayed better photocurrent, better incident photon to current efficiency (IPCE) and slightly better photo-conversion efficiencies than the DW-SSSCs.

To explore the detailed properties of DW-SSSC and SW-SSSC, EIS was performed and again good fits were obtained for the spectra to the equivalent circuit model for both types of cell. Comparison of photo-physical properties showed that the DW-SSSC has slightly higher charge transfer resistance (R_{ct}) than SW-SSSC. However, no data could be retrieved for the charge transport

resistance (R_t) due to the large error of the fitted value for both devices. Thus, analysis of IPCE spectra was used as an alternative approach to acquire useful information about the charge transport features in the SSSCs. This showed that although the charge injection efficiency is similar for both devices and light harvesting efficiency is slightly higher for DW-SSSC, the IPCE value of SW-SSSC was larger than DW-SSSC at any defined wavelength. Considering that $\eta_{IPCE}(\lambda) = \eta_{LH}(\lambda)\eta_{INJ}(\lambda)\eta_{COL}(\lambda)$, from the IPCE ratio ($\frac{IPCE_{SW}}{IPCE_{DW}} > 1$) it can be inferred that the $\frac{\eta_{col_{SW}}}{\eta_{col_{DW}}}$ is greater than one, or SW-SSSC has better charge collection efficiency than DW-SSSC. This is in agreement with the results of IMVS/IMPS data for DSSCs. Most plausibly, the better charge collection of SW-SSSC resulted in its better photocurrent and photo-conversion efficiency.

Chapter 7

Conclusions and Future Work

7.1 Conclusions

The key objective of this investigation was to study the fabrication of self organized “single wall” TiO₂ nanotubes (TiO₂ NTs) through anodization, characterization and the application of these in dye and semiconductor sensitized solar cells (DSSCs and SSSCs).

It has been shown in several studies by Sergiu *et.al* that one of the main problems in the well known TiO₂ NTs from EG electrolytes is their double wall nanostructure [5, 6, 50]. Their observations and arguments are supported only by several high resolution SEM and TEM images and EDX characterizations. In agreement with Sergiu *et.al*'s results, FTIR characterizations of the anodization electrolytes and the as-formed nanotubes conducted for the present thesis demonstrated that the inside walls of double wall TiO₂ NTs are rich in organic compounds resulted from the decomposition of EG during anodization at high voltages to organic compounds. The unwanted carbon from carbonaceous organics entrapped inside tubes can diffuse in to the TiO₂ atomic structure during the higher temperature heat treatments of TiO₂ NTs and change its atomic composition and physical properties such as its bandgap. Moreover, detailed SEM and TEM studies of these TiO₂ NTs showed that decomposition of EG results in an extra internal nanoporous layer. This double wall nanostructure was shown to

have a negative effect on the electron transition/transfer in photo-voltaic applications of TiO₂ NTs.

Based on these findings and their probable drawbacks, nanotubes without the internal shell – so called “single wall” TiO₂ NTs- were expected to show better electronic properties in photo voltaic applications like dye sensitized solar cells.

As an alternative, DMSO -a solvent with higher ability than EG in capturing radicals- is shown to result in single wall nanotubes (SW- TiO₂ NTs). However, the SW- TiO₂ NTs from DMSO electrolytes are not advantageous especially for application in photovoltaics. This is because the nanotubes are not robust enough, the nanostructure is not uniform, the anodization time is too long and the tubes are very likely to be clogged by a thick layer.

To find a way to synthesize better “single wall TiO₂ NTs” a mixed EG:DMSO solvent was used; making use of the benefits of both EG and DMSO [59]. In a systematic study in fifty different experimental conditions it was found that anodization of Ti foil in the equi-volumetric solution of EG and DMSO results in the best “single wall” TiO₂ NT nano array. The details of the effects of the ratio of EG to DMSO, water and fluorine contents of the electrolyte and the voltage and temperature of the anodization process on the nanostructure of the TiO₂ NT film has been presented and the best route to grow SW- TiO₂ NTs is proposed to be anodization in 1.5 M H₂O, 0.1 M NH₄F in 1:1 EG and DMSO at 60 °C, following by a post anodization step in the same electrolyte at the same temperature.

SEM and TEM studies prove the complete elimination of the internal shell. Moreover, the amount of the electro-oxidation of EG in the presence of DMSO during the anodization and organic compounds in “single wall” TiO₂ NTs measured by FTIR were shown to be much less compared to pure EG-based electrolytes and those “double wall” ones with similar tube lengths. Besides, single wall nanotubes show a drastically reduced carbon content in EDX and XPS depth profile investigations compared to double wall TiO₂ NTs with high carbon amounts similar to Sergiu *et al*'s report [5]. The strongly reduced carbon content is also evident from the reported thermal desorption measurements (TGA-MS), which is likely because in single wall TiO₂ NTs no carbon burn off takes place during thermal crystallization.

One of the remarkable features of this study is that after annealing “single wall” TiO₂ NTs exhibit a drastic improvement in electrical conductivity by about 10-100 times. The resistivity of single wall tubes is almost temperature independent, whereas an increase can be seen for double wall TiO₂ NTs with increasing the temperature. This phenomenon can be attributed to the negative effect of the inside shell on the electron transfer through the internal shell of the double wall TiO₂ NTs. These findings could be of crucial importance as this study is the first successful investigation in synthesis of “single wall” TiO₂ NTs with considerably better electronic properties.

Finally, UV-VIS results of the annealed tubes were reported and their bandgaps calculated. Analysis of DW and SW nanotubes showed that both of them have a bandgap of 2.97 eV, however DW nanotubes have an additional

adsorption at about 2.89 eV which can arise from the diffusion of carbon to the internal nanoporous shell of DW TiO₂ NTs during the heat treatment.

In order to reveal the beneficial use of single wall TiO₂ NTs in photovoltaic applications, dye and semiconductor (CdSe) sensitized solar cells were fabricated from both single and double wall TiO₂ NTs. The effect of TiCl₄ decoration of the TiO₂ NTs in DSSCs was studied as well. It is demonstrated that although the amount of dye adsorption is less in single wall and TiCl₄ treated single wall TiO₂ NTs, the efficiency of their DSSCs is higher compared to the DSSCs fabricated from double wall and TiCl₄ treated double wall TiO₂ NTs. This improvement shows the negative effect of the nanoporous internal shell of double wall TiO₂ NTs on the electron transfer from dye to TiO₂ in DSSCs. To additionally support this justification, about the negative role of the internal wall of double wall TiO₂ NTs, modulated photocurrent and photovoltage spectroscopy measurements were investigated. The results show that DSSCs made of both tube types have the same recombination time constant τ_r and hence this is independent of the inner shell of the nanotubes. However, the elimination of the inner shell leads to a clearly *shorter transport time constant* τ_t , by a factor of 2, i.e. a faster carrier transport. Accordingly, for the charge collection efficiency (η_{cc}), the single wall nanostructure shows a 40 to 50 percent higher value (at higher incident photon fluxes).

For DSSC based solar cells, EIS spectra of both SW and DW TiO₂ gave excellent fits to a standard equivalent circuit model. Both SW and DW devices exhibit near unity carrier collection efficiency. The better photocurrent and photo-

conversion efficiency of SW-based devices than their DW-based counterparts was shown by EIS studies to stem from the lower electron transport resistance and facilitated charge transport as well as higher recombination resistance of SW-DSSCs. Likewise, the electron lifetime in SW DSSCs is slightly longer than that in the DW devices which is in favor of device performance.

To examine the application of SW- TiO₂ NT in semiconductor sensitized solar cells, the SILAR method was used to deposit CdSe into SW and DW based TiO₂ layers. Among all, the best efficiency was achieved from 10 SILAR cycles of CdSe deposition with further deposition of CdSe resulting in tube blockage. Therefore, all characterization experiments were performed for 10 SILAR cycle deposited CdSe. Despite similar fill factors and open circuit photo-voltages, SW-SSSCs displayed better photocurrent, better incident photon to current efficiency (IPCE) and slightly better photo-conversion efficiencies than the DW-SSSCs.

To explore the detailed properties of DW-SSSC and SW-SSSC, EIS was performed and again good fits were obtained for the spectra to the equivalent circuit model for both types of cell. Comparison of photo-physical properties showed that the DW-SSSC has slightly higher charge transfer resistance (R_{ct}) than SW-SSSC. However, no data could be retrieved for the charge transport resistance (R_t) due to the large error of the fitted value for both devices. Thus, analysis of IPCE spectra was used as an alternative approach to acquire useful information about the charge transport features in the SSSCs. This showed that although the charge injection efficiency is similar for both devices and light harvesting efficiency is slightly higher for DW-SSSC, the IPCE value of SW-

SSSC was larger than DW-SSSC at any defined wavelength. Considering that $\eta_{IPCE}(\lambda) = \eta_{LH}(\lambda)\eta_{INJ}(\lambda)\eta_{COL}(\lambda)$, from the IPCE ratio ($\frac{IPCE_{SW}}{IPCE_{DW}} > 1$) it can be inferred that the $\frac{\eta_{col_{SW}}}{\eta_{col_{DW}}}$ is greater than one, or SW-SSSC has better charge collection efficiency than DW-SSSC. This is in agreement with the results of IMVS/IMPS data for DSSCs. Most plausibly, the better charge collection of SW-SSSC resulted in its better photocurrent and photo-conversion efficiency.

Finally, it is worth mentioning that although the efficiency of DSSCs compared with the commercial silicon panels (with 14 to 17% efficiency) seems too low, DSSCs - based on their low cost and better properties in some cases- would be a good replacement for silicon solar cells in "low density" applications like rooftop collectors. Due to the DSSCs' different kinetic of electron-hole travelling, these types of solar cells can easily work in low-light condition (cloudy sky, non-direct sunlight and indoor applications), while silicon cells would suffer a cutout. This is mainly because of recombination and charge carrier mobility problems in silicon solar cells, however the problem is much less significant in DSSCs.

Moreover, the present investigation resulted in NTs with better recombination and electron lifetime properties compared to nanoparticle DSSCs as well as conventional NT-DSSCs. Thus, synthesis of SW-NTs would be a step forward in synthesis of renewable energy materials.

All in all, the major contributions of the work in this thesis can be summarized as:

- (i) Production of high quality single wall TiO₂ NTs via anodization in a mixed EG:DMSO solvent.
- (ii) Production of TiO₂ NTs with electrical high electrical conductivity of more than 10x that of common TiO₂ NTs from EG solvents.
- (iii) Determination of the role of DMSO in reduction of carbon contamination of the TNTs due to its higher resistance to oxidation and excellent radical scavenging ability.
- (iv) Study of bandgaps and phase transformations of DW/SW TNTs in detail.
- (v) Improvement of sensitized solar cells due to the better recombination resistance of SW TNTs.

7.2 Future Work

Based on all the observations of the better properties of SW- TiO₂ NTs (like conductivity), further study of the application of them in other photovoltaic devices such as water splitting devices and photocatalysts could result in attractive improvements.

It should be pointed out that the results of this study are based on the “twice anodized” foils which have been shown to result in clean top TiO₂ NTs [11]. However, the observations show that in “twice anodization” process, the TiO₂ NTs may become preferentially oriented. Further research is therefore needed to investigate the probable effect of “preferential orientation” of TiO₂ NT walls on their electrical properties such as electron transfer/transition.

An important limitation in synthesis of SW- TiO₂ NTs from EG:DMSO electrolytes is the limited solubility of NH₄F in DMSO. This restriction in addition to the low TiO₂ NT growth rate was the main reason to choose high temperatures for anodization. Alternatively, there is a possibility to use fluoride containing salts that are more soluble in organic solvents such as Tetrabutylammonium Fluoride (TBAF). This is known as a source of organic soluble fluorine ion and in the absence of water, the solution of TBAF in DMSO is stable. By this, the amount of fluorine ion can be increased resulting in higher anodization rates and elimination of the internal shell of DW- TiO₂ NTs without using high temperature processes for that.

Another important field for further investigations with regard to SW- TiO₂ NTs would be studying the effect of high to very high ramp rates in the heat treatment process. The preliminary results offered and discussed in *section 5.10* show that unlike the common double wall nanotubes, single wall nanotubes cannot survive high heating/cooling rates and the tubes' walls break in to particles. By developing this method, it may be possible to get fine nanoporous structures on the foil which might show interesting properties in applications that need charge transfer due to the excellent attachment of the film to the backside electrode.

Based on the better performance and IPCE spectra of SW based CdSe sensitized TiO₂ nanotube solar cells (SW-SSSCs) than DW counterparts, surface treatments could be a promising way to further enhance the charge transfer and reduce the recombination. This method in addition to the application of new

sensitizer materials are two main approaches that can result in breakthrough enhancements [60].

As mentioned by Ruhl *et al*, existence of surface states in the semiconductor sensitizer is the main difference between DSSCs and SSSCs [12]. Thus, reducing the recombination caused by the sensitizer surface state is one of the most attempted strategies thus far. Particularly, ZnS treatment after deposition of sensitizer and fabrication of cascade sensitizers e.g. CdS/CdSe can be applied in SW-SSSCs to suppresses the recombination and enhanced IPCE and photoconversion efficiency. In addition to commonly used ZnS and cascade treatments, insightful fundamental studies to define the loss mechanisms in SW-SSSCs and judicious interfacial engineering are indispensable.

Finally, employment of other types of sensitizer such as PbS to expand the light absorption window and enhance the light absorption efficiency as well as application of efficient redox electrolytes instead of commonly used polysulfide may result in enhanced performance of SSSCs.

Chapter 8

References

- [1] S. Iijima, "Helical microtubules of graphitic carbon," *Nature*, 354, 56-58, 1991.
- [2] P. Roy, S. Berger, and P. Schmuki, "TiO₂ Nanotubes: Synthesis and Applications," *Angewandte Chemie International Edition*, 50, 2904-2939, 2011.
- [3] K. Zhu, N. R. Neale, A. Miedaner, and A. J. Frank, "Enhanced Charge-Collection Efficiencies and Light Scattering in Dye-Sensitized Solar Cells Using Oriented TiO₂ Nanotubes Arrays," *Nano Letters*, 7, 69-74, 2006.
- [4] C. M. Lieber, "One-dimensional nanostructures: Chemistry, physics & applications," *Solid State Communications*, 107, 607-616, 1998.
- [5] S. P. Albu, A. Ghicov, S. Aldabergenova, P. Drechsel, D. LeClere, G. E. Thompson, J. M. Macak, and P. Schmuki, "Formation of Double-Walled TiO₂ Nanotubes and Robust Anatase Membranes," *Advanced Materials*, 20, 4135-4139, 2008.
- [6] S. P. Albu and P. Schmuki, "TiO₂ Nanotubes Grown in Different Organic Electrolytes," *physica status solidi (RRL) – Rapid Research Letters*, 4, 215-217, 2010.
- [7] H. Mirabolghasemi, N. Liu, K. Lee, and P. Schmuki, "Formation of 'single walled' TiO₂ nanotubes with significantly enhanced electronic properties for higher efficiency dye-sensitized solar cells," *Chemical Communications*, 49, 2067-2069, 2013.
- [8] N. A. o. Engineering. (2013). Available: <http://www.engineeringchallenges.org/>
- [9] Research Cell Efficiency Records [Online]. Available: <http://www.nrel.gov/ncpv/>
- [10] B. O'Regan and M. Gratzel, "A low-cost, high-efficiency solar cell based on dye-sensitized colloidal TiO₂ films," *Nature*, 353, 4, 1991.
- [11] P. Roy, D. Kim, K. Lee, E. Spiecker, and P. Schmuki, "TiO₂ nanotubes and their application in dye-sensitized solar cells," *Nanoscale*, 2, 45-59, 2010.
- [12] S. Rühle, M. Shalom, and A. Zaban, "Quantum-Dot-Sensitized Solar Cells," *Chemical Physics and Physical Chemistry*, 11, 2290-2304, 2010.
- [13] A. J. Nozik, "Quantum dot solar cells," *Physica E: Low-dimensional Systems and Nanostructures*, 14, 115-120, 2002.
- [14] R. Vogel, P. Hoyer, and H. Weller, "Quantum-Sized PbS, CdS, Ag₂S, Sb₂S₃, and Bi₂S₃ Particles as Sensitizers for Various Nanoporous Wide-Bandgap Semiconductors," *The Journal of Physical Chemistry*, 98, 3183-3188, 1994.
- [15] D. Liu and P. V. Kamat, "Photoelectrochemical behavior of thin cadmium selenide and coupled titania/cadmium selenide semiconductor films," *The Journal of Physical Chemistry*, 97, 10769-10773, 1993.
- [16] J. Yan and F. Zhou, "TiO₂ nanotubes: Structure optimization for solar cells," *Journal of Materials Chemistry*, 21, 9406-9418, 2011.
- [17] G. K. Mor, O. K. Varghese, M. Paulose, K. Shankar, and C. A. Grimes, "A review on highly ordered, vertically oriented TiO₂ nanotube arrays: Fabrication, material properties, and solar energy applications," *Solar Energy Materials and Solar Cells*, 90, 2011-2075, 2006.
- [18] S. P. Albu, P. Roy, S. Virtanen, and P. Schmuki, "Self-organized TiO₂ Nanotube Arrays: Critical Effects on Morphology and Growth," *Israel Journal of Chemistry*, 50, 453-467, 2010.

- [19] P. Hoyer, "Formation of a titanium dioxide nanotube array," *Langmuir*, 12, 1411-1413, 1996.
- [20] S. Kobayashi, N. Hamasaki, M. Suzuki, M. Kimura, H. Shirai, and K. Hanabusa, "Preparation of helical transition-metal oxide tubes using organogelators as structure-directing agents," *Journal of the American Chemical Society*, 124, 6550-6551, 2002.
- [21] T. Kasuga, M. Hiramatsu, A. Hoson, T. Sekino, and K. Niihara, "Formation of titanium oxide nanotube," *Langmuir*, 14, 3160-3163, 1998.
- [22] C. Lee, S. Rhee, and H. Choi, "Preparation of TiO₂ nanotube/nanoparticle composite particles and their applications in dye-sensitized solar cells," *Nanoscale Research Letters*, 7, 1-5, 2012.
- [23] V. Zwillling, M. Aucouturier, and E. Darque-Ceretti, "Anodic oxidation of titanium and TA6V alloy in chromic media. An electrochemical approach," *Electrochimica Acta*, 45, 921-929, 1999.
- [24] A. Ghicov, H. Tsuchiya, J. M. Macak, and P. Schmuki, "Titanium oxide nanotubes prepared in phosphate electrolytes," *Electrochemistry Communications*, 7, 505-509, 2005.
- [25] C. A. Grimes and G. K. Mor, *TiO₂ Nanotube Arrays: Synthesis, Properties, and Applications*. USA: Springer, 2009.
- [26] J. M. Macak, H. Tsuchiya, L. Taveira, S. Aldabergerova, and P. Schmuki, "Smooth Anodic TiO₂ Nanotubes," *Angewandte Chemie International Edition*, 44, 7463-7465, 2005.
- [27] S. Yoriya, M. Paulose, O. K. Varghese, G. K. Mor, and C. A. Grimes, "Fabrication of Vertically Oriented TiO₂ Nanotube Arrays Using Dimethyl Sulfoxide Electrolytes," *The Journal of Physical Chemistry C*, 111, 13770-13776, 2007.
- [28] K. Lee, J. Kim, H. Kim, Y. Lee, Y. Tak, D. Kim, and P. Schmuki, "Effect of Electrolyte Conductivity on the Formation of a Nanotubular TiO₂ Photoanode for a Dye-Sensitized Solar Cell," *Journal of the Korean Physical Society*, 54, 4, 2009.
- [29] S. Yoriya, G. K. Mor, S. Sharma, and C. A. Grimes, "Synthesis of ordered arrays of discrete, partially crystalline titania nanotubes by Ti anodization using diethylene glycol electrolytes," *Journal of Materials Chemistry*, 18, 3332-3336, 2008.
- [30] M. Paulose, K. Shankar, S. Yoriya, H. E. Prakasam, O. K. Varghese, G. K. Mor, T. A. Latempa, A. Fitzgerald, and C. A. Grimes, "Anodic Growth of Highly Ordered TiO₂ Nanotube Arrays to 134 μm in Length," *The Journal of Physical Chemistry B*, 110, 16179-16184, 2006.
- [31] M. Paulose, H. E. Prakasam, O. K. Varghese, L. Peng, K. C. Popat, G. K. Mor, T. A. Desai, and C. A. Grimes, "TiO₂ Nanotube Arrays of 1000 μm Length by Anodization of Titanium Foil: Phenol Red Diffusion," *The Journal of Physical Chemistry C*, 111, 14992-14997, 2007.
- [32] Y.-Y. Song, P. Roy, I. Paramasivam, and P. Schmuki, "Voltage-Induced Payload Release and Wettability Control on TiO₂ and TiO₂ Nanotubes," *Angewandte Chemie International Edition*, 49, 351-354, 2010.
- [33] O. Hammerich and B. Svensmark, *Organic Electrochemistry*. New York: Marcel Dekker Inc., 1991.
- [34] K. Matsuoka, Y. Iriyama, T. Abe, M. Matsuoka, and Z. Ogumi, "Electrocatalytic Oxidation of Ethylene Glycol in Alkaline Solution," *Journal of the Electrochemical Society*, 152, A729-A731, 2005.

- [35] M. Enachi, I. Tiginyanu, V. Sprincean, and V. Ursaki, "Self-Organized Nucleation Layer for the Formation of Ordered Arrays of Double-Walled TiO₂ Nanotubes with Temperature Controlled Inner Diameter," *physica status solidi (RRL) – Rapid Research Letters*, 4, 100-102, 2010.
- [36] Z. B. Xie and D. J. Blackwood, "Effects of anodization parameters on the formation of titania nanotubes in ethylene glycol," *Electrochimica Acta*, 56, 905-912, 2010.
- [37] Y.-Y. Song, P. Roy, I. Paramasivam, and P. Schmuki, "Voltage-Induced Payload Release and Wettability Control on TiO₂ and TiO₂ Nanotubes," *Angewandte Chemie*, 122, 361-364, 2010.
- [38] L. Wang, H. Meng, P. K. Shen, C. Bianchini, F. Vizza, and Z. Wei, "In situ FTIR spectroelectrochemical study on the mechanism of ethylene glycol electrocatalytic oxidation at a Pd electrode," *Physical Chemistry Chemical Physics*, 13, 2667-2673, 2011.
- [39] P. Krtil, L. Kavan, I. Hoskovcová, and K. Kratochvilová, "Anodic oxidation of dimethyl sulfoxide based electrolyte solutions: An in situ FTIR study," *Journal of Applied Electrochemistry*, 26, 523-527, 1996.
- [40] *Silicon-on-Insulator Technology and Devices X*: The Electrochemical Society, 2001.
- [41] P. Schmuki and L. E. Erickson, "Selective High-Resolution Electrodeposition on Semiconductor Defect Patterns," *Physical Review Letters*, 85, 2985-2988, 2000.
- [42] P. Schmuki, L. E. Erickson, and D. J. Lockwood, "Light Emitting Micropatterns of Porous Si Created at Surface Defects," *Physical Review Letters*, 80, 4060-4063, 1998.
- [43] H. Tsuchiya, J. M. Macak, A. Ghicov, A. S. Räder, L. Taveira, and P. Schmuki, "Characterization of electronic properties of TiO₂ nanotube films," *Corrosion Science*, 49, 203-210, 2007.
- [44] S. R. Morrison, *Electrochemistry at Semiconductor and Oxidized Metal Electrodes*. New York: Plenum, 1980.
- [45] M. Tooley, *Electronic Circuits: Fundamentals and Applications*: Taylor & Francis, 2012.
- [46] D. Regonini, A. Jaroenworuluck, R. Stevens, and C. R. Bowen, "Effect of heat treatment on the properties and structure of TiO₂ nanotubes: phase composition and chemical composition," *Surface and Interface Analysis*, 42, 139-144, 2010.
- [47] A. Jaroenworuluck, D. Regonini, C. R. Bowen, and R. Stevens, "Nucleation and early growth of anodized TiO₂ film," *Journal of Materials Research*, 23, 2116-2124, 2008.
- [48] A. Rothschild, A. Levakov, Y. Shapira, N. Ashkenasy, and Y. Komem, "Surface photovoltage spectroscopy study of reduced and oxidized nanocrystalline TiO₂ films," *Surface Science*, 532-535, 456-460, 2003.
- [49] O. K. Varghese, D. Gong, M. Paulose, C. A. Grimes, and E. C. Dickey, "Crystallization and high-temperature structural stability of titanium oxide nanotube arrays," *Journal of Materials Research*, 18, 156-165, 2003.
- [50] S. P. Albu, H. Tsuchiya, S. Fujimoto, and P. Schmuki, "TiO₂ Nanotubes – Annealing Effects on Detailed Morphology and Structure," *European Journal of Inorganic Chemistry*, 2010, 4351-4356, 2010.
- [51] A. Jaroenworuluck, D. Regonini, C. R. Bowen, and R. Stevens, "A microscopy study of the effect of heat treatment on the structure and properties of anodised TiO₂ nanotubes," *Applied Surface Science*, 256, 2672-2679, 2010.

- [52] A. Tighineanu, T. Ruff, S. Albu, R. Hahn, and P. Schmuki, "Conductivity of TiO₂ nanotubes: Influence of annealing time and temperature," *Chemical Physics Letters*, 494, 260-263, 2010.
- [53] J. M. Low, B. Curtain, M. Philipps, Z. Q. Liu, and M. Ionescu, "High temperature diffraction study of in-situ crystallization of nanostructured TiO₂ photocatalysts," *Journal of the Australian Ceramics Society*, 48, 7, 2012.
- [54] B. D. Cullity and S. R. Stock, *Elements of X-Ray Diffraction*: Prentice Hall, 2001.
- [55] H. Zhang and J. F. Banfield, "Phase transformation of nanocrystalline anatase-to-rutile via combined interface and surface nucleation," *Journal of Materials Research*, 15, 437-448, 2000.
- [56] R. Asmatulu, A. Karthikeyan, D. Bell, S. Ramanathan, and M. Aziz, "Synthesis and Variable Temperature Electrical Conductivity Studies of Highly Ordered TiO₂ Nanotubes," *Journal of Materials Science*, 44, 4613-4616, 2009.
- [57] F. Fabregat-Santiago, G. Garcia-Belmonte, I. Mora-Sero, and J. Bisquert, "Characterization of nanostructured hybrid and organic solar cells by impedance spectroscopy," *Physical Chemistry Chemical Physics*, 13, 9083-9118, 2011.
- [58] K. Kalyanasundaram, *Dye-sensitized Solar Cells*: Eapl Press, 2010.
- [59] W. P. Gomes and D. Vanmaekelbergh, "Impedance spectroscopy at semiconductor electrodes: Review and recent developments," *Electrochimica Acta*, 41, 967-973, 1996.
- [60] M. Tomkiewicz, "Impedance spectroscopy of rectifying semiconductor-electrolyte interfaces," *Electrochimica Acta*, 35, 1631-1635, 1990.
- [61] H. Gerischer, "The impact of semiconductors on the concepts of electrochemistry," *Electrochimica Acta*, 35, 1677-1699, 1990.
- [62] J. Bisquert, G. Garcia-Belmonte, F. Fabregat-Santiago, N. S. Ferriols, P. Bogdanoff, and E. C. Pereira, "Doubling Exponent Models for the Analysis of Porous Film Electrodes by Impedance. Relaxation of TiO₂ Nanoporous in Aqueous Solution," *The Journal of Physical Chemistry B*, 104, 2287-2298, 2000.
- [63] J. Bisquert, "Theory of the Impedance of Electron Diffusion and Recombination in a Thin Layer," *The Journal of Physical Chemistry B*, 106, 325-333, 2001.
- [64] F. Fabregat-Santiago, J. Bisquert, G. Garcia-Belmonte, G. Boschloo, and A. Hagfeldt, "Influence of electrolyte in transport and recombination in dye-sensitized solar cells studied by impedance spectroscopy," *Solar Energy Materials and Solar Cells*, 87, 117-131, 2005.
- [65] I. Mora-Seró and J. Bisquert, "Impedance Characterization of Quantum Dot Sensitized Solar Cells," in *Frontiers of Quantum Dot Solar Cells*, ed: CMC Publishing Co., Ltd., 2012, 162-175.
- [66] A. Hauch and A. Georg, "Diffusion in the electrolyte and charge-transfer reaction at the platinum electrode in dye-sensitized solar cells," *Electrochimica Acta*, 46, 3457-3466, 2001.
- [67] *Solar Cells (Dye Sensitized Devices)*: InTech, 2011.
- [68] F. Fabregat-Santiago, J. Bisquert, L. Cevey, P. Chen, M. Wang, S. M. Zakeeruddin, and M. Grätzel, "Electron Transport and Recombination in Solid-State Dye Solar Cell with Spiro-OMeTAD as Hole Conductor," *Journal of the American Chemical Society*, 131, 558-562, 2008.
- [69] J. Bisquert, F. Fabregat-Santiago, I. n. Mora-Seró, G. Garcia-Belmonte, and S. Giménez, "Electron Lifetime in Dye-Sensitized Solar Cells: Theory and Interpretation of Measurements," *The Journal of Physical Chemistry C*, 113, 17278-17290, 2009.

- [70] J. M. Macák, H. Tsuchiya, A. Ghicov, and P. Schmuki, "Dye-sensitized anodic TiO₂ nanotubes," *Electrochemistry Communications*, 7, 1133-1137, 2005.
- [71] J. R. Jennings, A. Ghicov, L. M. Peter, P. Schmuki, and A. B. Walker, "Dye-Sensitized Solar Cells Based on Oriented TiO₂ Nanotube Arrays: Transport, Trapping, and Transfer of Electrons," *Journal of the American Chemical Society*, 130, 13364-13372, 2008.
- [72] D. Kim, A. Ghicov, and P. Schmuki, "TiO₂ Nanotube arrays: Elimination of disordered top layers ("nanograss") for improved photoconversion efficiency in dye-sensitized solar cells," *Electrochemistry Communications*, 10, 1835-1838, 2008.
- [73] P. Xuan, C. Changhong, Z. Kai, and F. Zhaoyang, "TiO₂ nanotubes infiltrated with nanoparticles for dye sensitized solar cells," *Nanotechnology*, 22, 235402, 2011.
- [74] S. P. Albu, D. Kim, and P. Schmuki, "Growth of Aligned TiO₂ Bamboo-Type Nanotubes and Highly Ordered Nanolace," *Angewandte Chemie International Edition*, 47, 1916-1919, 2008.
- [75] J. H. Park, T.-W. Lee, and M. G. Kang, "Growth, detachment and transfer of highly-ordered TiO₂ nanotube arrays: use in dye-sensitized solar cells," *Chemical Communications*, 2867-2869, 2008.
- [76] K. Zhu, T. B. Vinzant, N. R. Neale, and A. J. Frank, "Removing Structural Disorder from Oriented TiO₂ Nanotube Arrays: Reducing the Dimensionality of Transport and Recombination in Dye-Sensitized Solar Cells," *Nano Letters*, 7, 3739-3746, 2007.
- [77] N. Mir, K. Lee, I. Paramasivam, and P. Schmuki, "Optimizing TiO₂ Nanotube Top Geometry for Use in Dye-Sensitized Solar Cells," *Chemistry – A European Journal*, 18, 11862-11866, 2012.
- [78] L. KANGLE, "All-solid-state front illuminated Titania nanotube-based dye sensitized solar cells," PhD, Materials Science and Engineering, National University of Singapore, Singapore, 2012.
- [79] Newport solar diverging simulator Available:
<http://engineering.case.edu/centers/sdle/SDLE-Capabilities-and-Equipment/Newport-1-50x-suns-solar-simulator>
- [80] M. A. Hossain, J. R. Jennings, Z. Y. Koh, and Q. Wang, "Carrier Generation and Collection in CdS/CdSe-Sensitized SnO₂ Solar Cells Exhibiting Unprecedented Photocurrent Densities," *ACS Nano*, 5, 3172-3181, 2011.
- [81] M. A. Hossain, G. Yang, M. Parameswaran, J. R. Jennings, and Q. Wang, "Mesoporous SnO₂ Spheres Synthesized by Electrochemical Anodization and Their Application in CdSe-Sensitized Solar Cells," *The Journal of Physical Chemistry C*, 114, 21878-21884, 2010.
- [82] H. J. Lee, J. Bang, J. Park, S. Kim, and S.-M. Park, "Multilayered Semiconductor (CdS/CdSe/ZnS)-Sensitized TiO₂ Mesoporous Solar Cells: All Prepared by Successive Ionic Layer Adsorption and Reaction Processes," *Chemistry of Materials*, 22, 5636-5643, 2010.
- [83] H. Masuda and K. Fukuda, "Ordered Metal Nanohole Arrays Made by a Two-Step Replication of Honeycomb Structures of Anodic Alumina," *Science*, 268, 1466-1468, 1995.
- [84] G. Zhang, H. Huang, Y. Zhang, H. L. W. Chan, and L. Zhou, "Highly ordered nanoporous TiO₂ and its photocatalytic properties," *Electrochemistry Communications*, 9, 2854-2858, 2007.

- [85] S. P. Albu and P. Schmuki, "Highly Defined and Ordered Top-Openings in TiO₂ Nanotube Arrays," *physica status solidi (RRL) – Rapid Research Letters*, 4, 151-153, 2010.
- [86] J. M. Macak, S. P. Albu, and P. Schmuki, "Towards ideal hexagonal self-ordering of TiO₂ nanotubes," *physica status solidi (RRL) – Rapid Research Letters*, 1, 181-183, 2007.
- [87] N. Liu, H. Mirabolghasemi, K. Lee, S. P. Albu, A. Tighineanu, M. Altomare, and P. Schmuki, "Anodic TiO₂ nanotubes: Double Walled vs. Single Walled," *Faraday Discussions*, 2013.
- [88] G. V. Buxton, C. L. Greenstock, W. P. Helman, and A. B. Ross, "Critical Review of rate constants for reactions of hydrated electrons, hydrogen atoms and hydroxyl radicals (OH/O in Aqueous Solution)," *Journal of Physical and Chemical Reference Data*, 17, 513-886, 1988.
- [89] W. Wei, S. Berger, C. Hauser, K. Meyer, M. Yang, and P. Schmuki, "Transition of TiO₂ nanotubes to nanopores for electrolytes with very low water contents," *Electrochemistry Communications*, 12, 1184-1186, 2010.
- [90] S. M. Sze, *Physics of Semiconductor Devices*: John Wiley & Sons, 1981.
- [91] I. Tiginyanu, S. Langa, H. Foll, and Ursachi, *Porous III-V Semiconductors*, 2009.
- [92] D. H. Williams and I. Fleming, *Spectroscopic methods in organic chemistry*: McGraw-Hill, 1995.
- [93] J. Zou, J. Gao, and F. Xie, "An amorphous TiO₂ sol sensitized with H₂O₂ with the enhancement of photocatalytic activity," *Journal of Alloys and Compounds*, 497, 420-427, 2010.
- [94] P. Huang, A. Dong, and W. S. Caughey, "Effects of dimethyl sulfoxide, glycerol, and ethylene glycol on secondary structures of cytochrome c and lysozyme as observed by infrared spectroscopy," *Journal of Pharmaceutical Sciences*, 84, 387-392, 1995.
- [95] H.-t. Zhu, Y.-s. Lin, and Y.-s. Yin, "A novel one-step chemical method for preparation of copper nanofluids," *Journal of Colloid and Interface Science*, 277, 100-103, 2004.
- [96] G. G. Miller and J. A. Raleigh, "Action of some hydroxyl radical scavengers on radiation-induced haemolysis," *Int J Radiat Biol Relat Stud Phys Chem Med*, 43, 411-419, 1983.
- [97] M. K. Eberhardt and R. Colina, "The reaction of OH radicals with dimethyl sulfoxide. A comparative study of Fenton's reagent and the radiolysis of aqueous dimethyl sulfoxide solutions," *The Journal of Organic Chemistry*, 53, 1071-1074, 1988.
- [98] M. Liu, H. Li, Y. Zeng, and T. Huang, "Anatase TiO₂ single crystals with dominant 001 facets: Facile fabrication from Ti powders and enhanced photocatalytic activity," *Applied Surface Science*, 274, 117-123, 2013.
- [99] U. Diebold, "The Surface Science of Titanium Dioxide," *Surface Science Reports*, 48, 53-229, 2003.
- [100] H. G. Yang, C. H. Sun, S. Z. Qiao, J. Zou, G. Liu, S. C. Smith, H. M. Cheng, and G. Q. Lu, "Anatase TiO₂ single crystals with a large percentage of reactive facets," *Nature*, 453, 638-641, 2008.
- [101] H. Habazaki, K. Fushimi, K. Shimizu, P. Skeldon, and G. E. Thompson, "Fast migration of fluoride ions in growing anodic titanium oxide," *Electrochemistry Communications*, 9, 1222-1227, 2007.
- [102] V. G. Pol, Y. Langzam, and A. Zaban, "Application of Microwave Superheating for the Synthesis of TiO₂ Rods," *Langmuir*, 23, 11211-11216, 2007.

- [103] P. S. Archana, R. Jose, T. M. Jin, C. Vijila, M. M. Yusoff, and S. Ramakrishna, "Structural and Electrical Properties of Nb-Doped Anatase TiO₂ Nanowires by Electrospinning," *Journal of the American Ceramic Society*, 93, 4096-4102, 2010.
- [104] T. X. Huaqing XIE, Qinghong ZHANG, Qingren WU, "Study on the Phase Transformation Behavior of Nanosized Amorphous TiO₂," *J. Mater. Sci. Technol.*, 19, 463-466, 2003.
- [105] P. Kar, K. S. Raja, M. Misra, and B. N. Agasanapur, "Formation and stability of anatase phase of phosphate incorporated and carbon doped titania nanotubes," *Materials Research Bulletin*, 44, 398-402, 2009.
- [106] H.-J. Oh, S. Lee, B. Lee, Y. Jeong, and C.-S. Chi, "Surface characteristics and phase transformation of highly ordered TiO₂ nanotubes," *Metals and Materials International*, 17, 613-616, 2011.
- [107] Y.-M. Sung, J.-S. Park, and T. G. Kim, "Anatase phase formation kinetics in Ti and TiO_x nanoparticles produced by gas-phase condensation," *Journal of Non-Crystalline Solids*, 358, 182-187, 2012.
- [108] H.-J. Oh, R. Hock, R. Schurr, A. Hölzing, and C.-S. Chi, "Phase transformation and photocatalytic characteristics of anodic TiO₂ nanotubular film," *Journal of Physics and Chemistry of Solids*, 74, 708-715, 2013.
- [109] N. Vaenas, M. Bidikoudi, T. Stergiopoulos, V. Likodimos, A. G. Kontos, and P. Falaras, "Annealing effects on self-assembled TiO₂ nanotubes and their behavior as photoelectrodes in dye-sensitized solar cells," *Chemical Engineering Journal*, 224, 121-127, 2013.
- [110] J. C. Kennedy Iii and A. K. Datye, "Photothermal Heterogeneous Oxidation of Ethanol over Pt/TiO₂," *Journal of Catalysis*, 179, 375-389, 1998.
- [111] P. P. Vijayan, M. Thomas, and K. C. George, "Effect of calcinations on electrical properties of TiO₂ nanotubes," *Journal of Applied Physics*, 112, 104308-104308, 2012.
- [112] R. P. Lynch, A. Ghicov, and P. Schmuki, "A Photo-Electrochemical Investigation of Self-Organized TiO₂ Nanotubes," *Journal of The Electrochemical Society*, 157, G76-G84, 2010.
- [113] R. F. Bunshah, "Handbook of Deposition Technologies for Films and Coatings - Science, Technology and Applications (2nd Edition)," ed: William Andrew Publishing/Noyes, 1994.
- [114] R. López and R. Gómez, "Band-gap energy estimation from diffuse reflectance measurements on sol-gel and commercial TiO₂: a comparative study," *Journal of Sol-Gel Science and Technology*, 61, 1-7, 2012.
- [115] J. Tauc, "Optical Properties of Amorphous Semiconductors," in *Amorphous and Liquid Semiconductors*, J. Tauc, Ed., ed: Springer US, 1974, 159-220.
- [116] J. Tauc, "Optical properties and electronic structure of amorphous Ge and Si," *Materials Research Bulletin*, 3, 37-46, 1968.
- [117] V. K. Mahajan, "Ordered titanium dioxide nanotubular arrays: Synthesis, characterization and photoelectrochemical behavior," Ph.D., University of Nevada, Reno, Ann Arbor, 2008.
- [118] L. Mai, C. Huang, D. Wang, Z. Zhang, and Y. Wang, "Effect of C doping on the structural and optical properties of sol-gel TiO₂ thin films," *Applied Surface Science*, 255, 9285-9289, 2009.
- [119] Q. Li, R. Xie, Y. W. Li, E. A. Mintz, and J. K. Shang, "Enhanced Visible-Light-Induced Photocatalytic Disinfection of E. coli by Carbon-Sensitized Nitrogen-Doped Titanium Oxide," *Environmental Science & Technology*, 41, 5050-5056, 2007.

- [120] V. González-Pedro, X. Xu, I. Mora-Seró, and J. Bisquert, "Modeling High-Efficiency Quantum Dot Sensitized Solar Cells," *ACS Nano*, 4, 5783-5790, 2010.
- [121] R. Vogel, K. Pohl, and H. Weller, "Sensitization of highly porous, polycrystalline TiO₂ electrodes by quantum sized CdS," *Chemical Physics Letters*, 174, 241-246, 1990.
- [122] D. Kim, P. Roy, K. Lee, and P. Schmuki, "Dye-sensitized solar cells using anodic TiO₂ mesosponge: Improved efficiency by TiCl₄ treatment," *Electrochemistry Communications*, 12, 574-578, 2010.
- [123] Q. Wang, S. Ito, M. Grätzel, F. Fabregat-Santiago, I. Mora-Seró, J. Bisquert, T. Bessho, and H. Imai, "Characteristics of High Efficiency Dye-Sensitized Solar Cells†," *The Journal of Physical Chemistry B*, 110, 25210-25221, 2006.
- [124] R. d. Levie, *Advances in Electrochemistry and Electrochemical Engineering* vol. 6. New York: Interscience.
- [125] J. Wang and Z. Lin, "Dye-Sensitized TiO₂ Nanotube Solar Cells: Rational Structural and Surface Engineering on TiO₂ Nanotubes," *Chemistry – An Asian Journal*, 7, 2754-2762, 2012.

List of Publications and Presentations:

1. **H. Mirabolghasemi**, Ning Liu, Kiyoung Lee and Patrik Schmuki, "Formation of 'Single Wall' TiO₂ nanotubes with Significantly Enhanced Electronic Properties", Chem. Commun., 2013,49, 2067-2069.
2. Ning Liu , **H. Mirabolghasemi**, Kiyoung Lee , Sergiu P. Albu, Alexei Tighineanu , Marco Altomare and Patrik Schmuki, "Anodic TiO₂ nanotubes: Double Walled vs. Single Walled", Faraday Discussions (2013). [Link](#)
3. **H. Mirabolghasemi**, Ning Liu, Kiyoung Lee, Patrik Schmuki, Daniel John Blackwood, " Application of "Single Wall" TiO₂ Nanotubes in Dye Sensitized Solar Cells and Effect of Heat Treatment on Their Photovoltaic Properties ", Oral Presentation, MRS conference, ICMAT 2013, Singapore.
4. **H. Mirabolghasemi**, Ning Liu, Kiyoung Lee, Patrik Schmuki, Daniel John Blackwood, " Synthesis and Properties of "Single Wall" Anodic TiO₂ Nanotubes", Oral Presentation, MRS conference, ICMAT 2013, Singapore.
5. **H. Mirabolghasemi**, D.J.Blackwood, "FTIR and differential Scanning Calorimetry studies of Single Wall TiO₂ nanotubes", In preparation for submission.